

**Azimuthal Anisotropy  
Measurements For Identified Particles Produced  
In Au+Au Collisions At  $\sqrt{s_{NN}} = 7.7-200$  GeV**

by  
**Md Nasim**

Enrolment No. : PHYS07200904007

National Institute of Science Education and Research

Bhubaneswar -751005, India.

A thesis submitted to the  
Board of Studies in **Physical Sciences**  
in partial fulfillment of requirements  
for the degree of  
**DOCTOR OF PHILOSOPHY**  
of  
**HOMI BHABHA NATIONAL INSTITUTE**



April, 2014

**HOMI BHABHA NATIONAL INSTITUTE**  
**Recommendations of the Viva Voce Board**

As members of the Viva Voce Board, we certify that we have read the dissertation prepared by Md Nasim entitled **Azimuthal Anisotropy Measurements For Identified Particles Produced In Au+Au Collisions At  $\sqrt{s_{NN}} = 7.7-200$  GeV** and recommend that it may be accepted as fulfilling the dissertation requirement for the Degree of Doctor of Philosophy.

Ajit M. Srivastava Date: 22-4-14  
Chairman- Prof. Ajit Mohan Srivastava

Bedangadas Mohanty Date: 22/4/2014  
Guide/Convener- Dr. Bedangadas Mohanty

Sanjay Swain Date: 22/04/2014  
Member 1- Dr. Sanjay Kumar Swain

Subhasish Basak Date: 22/4/14  
Member 2- Dr. Subhasish Basak

Sourendu Gupta Date: 22/4/2014  
Member 3 (External Examiner)- Prof. Sourendu Gupta

Final approval and acceptance of this dissertation is contingent upon the candidates submission of the final copies of the dissertation to HBNI.

I hereby certify that I have read this dissertation prepared under my direction and recommend that it may be accepted as fulfilling the dissertation requirement

Date: 22/4/2014

Bedangadas Mohanty  
(Dr. Bedangadas Mohanty)

Place: Bhubaneswar

# Statement by Author

This dissertation has been submitted in partial fulfillment of requirements for an advanced degree at Homi Bhabha National Institute (HBNI) and is deposited in the Library to be made available to borrowers under rules of the HBNI.

Brief quotations from this dissertation are allowable without special permission, provided that accurate acknowledgement of source is made. Requests for permission for extended quotation from or reproduction of this manuscript in whole or in part may be granted by the Competent Authority of HBNI when in his or her judgment the proposed use of the material is in the interests of scholarship. In all other instances, however, permission must be obtained from the author.

(Md Nasim)

# Declaration

I, Md Nasim, hereby declare that the investigation presented in the thesis has been carried out by me. The work is original and has not been submitted earlier as a whole or in part for a degree/diploma at this or any other Institution/University.

(Md Nasim)

*To*  
*My Family & Friends*

# Acknowledgements

Here I would like to mention my appreciation to all the peoples who have been the instrumental in supporting my thesis work. My apologies if I miss someone who deserves to be listed here.

First and foremost, I would like to extend very special thanks to my supervisor Dr. Bedangadas Mohanty for giving me the opportunity to work on this interesting topic for my Ph.D thesis, and for all the advice, guidance, and support he has given me. His constructive criticism on my research work, was essential to the successful completion of this thesis. From the last four years, he provided me all necessary resources to complete my research work. I am really thankful to him. Finally, I greatly appreciate the wealth of opportunities given to me by Dr. Mohanty to attend several international conferences and visits to many national laboratory inside and outside India, each of which had a profound impact upon my work.

I would like to thanks Dr. Chitrasen Jena and Dr. Nihar Ranjan Sahoo for introducing me about the STAR analysis frame work at the beginning of my Ph.D carrier, and for lots physics discussions.

I would like to express my thanks to Prof. T. K. Chandrashekar (Director of NISER), Prof. D. K. Srivastava (Director of VECC), Dr. Y. P. Viyogi and HBNI for helping me to transfer from VECC to NISER. I take this opportunity to thank all the members of my doctoral committee at VECC and NISER. I consider it an honor to work with all the members of physics group at VECC, NISER and IOP. Thanks to Prof. D. P. Mahapatra and Dr. P. K. Sahoo for allowing me to work at PMD laboratory of IOP. I thank the academic and computing sections of NISER for helping the smooth conduct of the thesis work.

Thanks to everyone of the LBNL-RNC group mainly Prof. Nu Xu, Prof. Art Poskanzer and Dr. Xin Dong for giving me support and opportunity to work at

LBNL. Thanks to Prof. Feng Liu and all members of CCNU-IOPP for providing me support and opportunity to work on flow analysis at IOPP.

I would also like to thanks Dr. Shusu Shi, Dr. Hiroshi Masui, Dr. Xiaoping Zhang and Dr. Alexander Schmah for their help and valuable discussions in flow analysis.

My warm and sincere thanks to all the conveners of STAR physics working group (PWG) and members of STAR collaboration for giving me valuable comments and suggestions on my analysis.

I would like to express my sincere thanks to the RHIC Operations Group and RACF at BNL, the NERSC Center at LBNL and Grid Computing Facilities at VECC and NISER for providing resources and support.

I would like to thank Mr. Subhash Singha, Mr. Rihan Haque, Mr. Ranbir Singh, Dr. Lokesh Kumar, Mr. Shreekanth Tripathy, Mr. Shikshit Gupta, Mr. Mukesh Sharma, Mrs. Sabita Das and all classmates in VECC, NISER and IOP for many useful discussions. I would like to express my thanks to all the members of PMD collaborations.

I gratefully acknowledge the financial support from DST Swarnajyanti project for my fellowship at NISER and also DST for supporting my trip on conference.

Last but most importantly, I would like to thank my parents and all other family members for the understanding and support during the past 4 years.

(Md Nasim)

## Publications

### List of Publications Related to Thesis (As a Primary Authors):

1. **Using  $\phi$ -meson elliptic flow to map the strength of the partonic interaction.** \*  
Md. Nasim, Phys. Rev. C **89** (2014) 034909.
2. **Observation of an energy-dependent difference in elliptic flow between particles and anti-particles in relativistic heavy ion collisions.** \*  
L. Adamczyk *et al.* (STAR Collaboration)  
Phys. Rev. Lett. **110** (2013) 142301.
3. **Elliptic flow of identified hadrons in Au+Au collisions at  $\sqrt{s_{NN}} = 7.7-62.4$  GeV.** \*  
L. Adamczyk *et al.* (STAR Collaboration), Phys. Rev. C **88** (2013) 014902.
4. **Elliptic flow of  $\phi$ -meson a sensitive probe for onset of de-confinement transition in high energy heavy-ion collisions.** \*  
Md. Nasim, B. Mohanty and N. Xu, Phys. Rev. C **87** (2013) 014903.
5. **Inclusive charged hadron elliptic flow in Au + Au collisions at  $\sqrt{s_{NN}} = 7.7-39$  GeV.** \*  
L. Adamczyk *et al.* (STAR Collaboration), Phys. Rev. C **86** (2012) 054908.
6. **Longitudinal scaling of observables in heavy-ion collision models.** \*  
Md. Nasim, C. Jena, L. Kumar, P. K. Netrakanti and B. Mohanty.  
Phys. Rev. C **83** (2011) 054902.
7. **Energy dependence of elliptic flow from heavy-ion collision models.**\*  
Md. Nasim, L. Kumar, P. K. Netrakanti and B. Mohanty.  
Phys. Rev. C **82** (2010) 054908.

8. **Systematic study of the elliptic flow parameter using a heavy-ion collision model \***

Md. Nasim and B. Mohanty.

e-Print: arXiv:1402.6093 [nucl-ex].

## List of Conference Proceedings :

1. **Systematic investigation of partonic collectivity through centrality dependence of elliptic flow of multi-strange hadrons in Au+Au collisions at  $\sqrt{s_{NN}} = 200$  GeV in STAR. \***  
Md. Nasim for the STAR Collaboration.  
Nucl. Phys. **A 904** (2013) 413c.
2. **Energy dependence of  $\phi$ -meson production and elliptic flow in Au+Au collisions at STAR. \***  
Md. Nasim for the STAR Collaboration.  
Pos (CPOD 2013) 049.
3. **Energy dependence of elliptic flow of  $\phi$ -meson in STAR at RHIC. \***  
Md. Nasim for the STAR Collaboration.  
Acta Phys.Polon.Supp. **5** (2012) 317.
4. **Probing the QCD phase diagram with the measurements of  $\phi$ -meson production and elliptic flow in the heavy-ion collision at STAR. \***  
Md. Nasim for the STAR Collaboration.  
e-Print: arXiv:1309.7784 [nucl-ex].  
Will be published in Journal of Physics: Conference Series (JPCS).

## List of Other Publications (As a Primary Authors) :

1. **Elliptic and Triangular flow in asymmetric heavy-ion collisions.**  
Md. R. Haque, Md. Nasim and B. Mohanty, Phys. Rev. **C 84** (2011) 067901.
2. **Energy dependence of inclusive photon elliptic flow in heavy-ion collision models.**  
R. Singh, Md. Nasim, B. Mohanty and S. S. Sambyal  
J. Phys. **G 39** (2012) 055002.

## Paper Under Review in STAR Collaboration (As a Primary Authors):

1. **Centrality dependence of multi-strange hadrons  $v_2$  in Au+Au collisions at  $\sqrt{s_{NN}} = 200$  GeV. \***

Intended for Physical Review Letter (under preparation in physics working group).

2. **Probing parton dynamics of QCD matter with  $\Omega$  and  $\phi$  production. \***

Intended for Physical Review Letter (in collaboration review).

(\*) indicates papers on which this thesis is based.

## List of Collaboration Papers :

1.  **$J/\psi$  polarization in  $p+p$  collisions at  $\sqrt{s} = 200$  GeV in STAR.**

L. Adamczyk *et al.* (STAR Collaboration), e-Print: arXiv:1311.1621 [nucl-ex].

2.  **$J/\psi$  production at low  $p_T$  in Au+Au and Cu+Cu collisions at  $\sqrt{s_{NN}} = 200$  GeV at STAR.**

L. Adamczyk *et al.* (STAR Collaboration), e-Print: arXiv:1310.3563 [nucl-ex].

3. **Energy Dependence of Moments of Net-proton Multiplicity Distributions at RHIC.**

L. Adamczyk *et al.* (STAR Collaboration), e-Print: arXiv:1309.5681 [nucl-ex].

Accepted for publication in Phys. Rev. Lett.

4. **Neutral pion cross section and spin asymmetries at intermediate pseudo-rapidity in polarized proton collisions at  $\sqrt{s} = 200$  GeV.**

L. Adamczyk *et al.* (STAR Collaboration), e-Print: arXiv:1309.1800 [nucl-ex].

5. **Measurement of charge multiplicity asymmetry correlations in high energy nucleus-nucleus collisions at 200 GeV.**  
L. Adamczyk *et al.* (STAR Collaboration), e-Print: arXiv:1303.0901 [nucl-ex].
6. **Jet-hadron correlations in  $\sqrt{s_{NN}} = 200$  GeV Au+Au and  $p+p$  collisions.**  
L. Adamczyk *et al.* (STAR Collaboration), e-Print: arXiv:1302.6184 [nucl-ex].
7. **Fluctuations of charge separation perpendicular to the event plane and local parity violation in  $\sqrt{s_{NN}} = 200$  GeV Au+Au collisions at RHIC.**  
L. Adamczyk *et al.* (STAR Collaboration), e-Print: arXiv:1302.3802 [nucl-ex].
8. **Freeze-out dynamics via charged kaon femtoscopy in  $\sqrt{s_{NN}} = 200$  GeV central Au+Au collisions.**  
L. Adamczyk *et al.* (STAR Collaboration), Phys. Rev. C **88** (2013) 034906.
9. **System size dependence of transverse momentum correlations at RHIC.**  
L. Adamczyk *et al.* (STAR Collaboration), Phys. Rev. C **87** (2013) 064902.
10. **Third harmonic flow of charged particles in Au+Au collisions at  $\sqrt{s_{NN}} = 200$  GeV.**  
L. Adamczyk *et al.* (STAR Collaboration), Phys. Rev. C **88** (2013) 014904.
11. **Measurement of  $J/\psi$  azimuthal anisotropy in Au+Au collisions at  $\sqrt{s_{NN}} = 200$  GeV.**  
L. Adamczyk *et al.* (STAR Collaboration), e-Print: arXiv:1212.3304 [nucl-ex].
12. **Studies of di-jets in Au+Au collisions using angular correlations with respect to back-to-back leading hadrons.**  
L. Adamczyk *et al.* (STAR Collaboration), e-Print: arXiv:1212.1653 [nucl-ex].

13.  **$J/\psi$  production at high transverse momenta in p+p and Au+Au collisions at  $\sqrt{s_{NN}} = 200$  GeV.**  
L. Adamczyk *et al.* (STAR Collaboration), Phys. Lett. **B 722** (2013) 55.
14. **Single spin asymmetry AN in polarized proton-proton elastic scattering at  $\sqrt{s_{NN}} = 200$  GeV.**  
L. Adamczyk *et al.* (STAR Collaboration), Phys. Lett. **B 719** (2013) 62.
15. **Transverse single-spin asymmetry and cross-section for  $\pi^0$  and  $\eta$  mesons at large Feynman-x in polarized p+p collisions at  $\sqrt{s}=200$  GeV.**  
L. Adamczyk *et al.* (STAR Collaboration), Phys. Rev. **D 86** (2012) 051101.
16. **Longitudinal and transverse spin asymmetries for inclusive jet production at mid-rapidity in polarized p+p collisions at  $\sqrt{s}=200$  GeV.**  
L. Adamczyk *et al.* (STAR Collaboration), Phys. Rev. **D 86** (2012) 032006.
17. **Measurements of  $D^0$  and D production in p+p collisions at  $\sqrt{s} = 200$  GeV.**  
L. Adamczyk *et al.* (STAR Collaboration), Phys. Rev. **D 86** (2012) 072013.
18. **Di-electron spectrum at mid-rapidity in p+p collisions at  $\sqrt{s}=200$  GeV.**  
L. Adamczyk *et al.* (STAR Collaboration), Phys. Rev. **C 86** (2012) 024906.
19. **Directed flow of identified particles in Au+Au collisions at  $\sqrt{s_{NN}} = 200$  GeV at RHIC**  
L. Adamczyk *et al.* (STAR Collaboration), Phys. Rev. Lett. **108** (2012) 202301.
20. **Identified hadron compositions in p+p and Au+Au collisions at high transverse momenta at  $\sqrt{s_{NN}} = 200$  GeV.**  
G. Agakishiev *et al.* (STAR Collaboration).  
Phys. Rev. Lett. **108** (2012) 072302.

# SYNOPSIS

The quantum chromodynamics (QCD), a theory of strong interaction between quarks and gluons, predicts that at very high temperature and/or high density quarks and gluons will be no longer confined within the hadrons [1]. This de-confined state is known as Quark-Gluon-Plasma (QGP). It is believed that just after Big-Bang the universe was consisted of free quarks and gluons. The main aim of the Relativistic Heavy Ion Collider (RHIC) at Brookhaven National Laboratory (BNL) is to create such de-confined state in laboratory and measure its properties.

After observing the clear signatures of the formation of QGP matter in Au+Au collisions at centre-of-mass energy ( $\sqrt{s_{NN}}$ ) of 62.4 and 200 GeV, attempts are being made to vary the colliding beam energy and to search for the transition region in terms of colliding beam energy between the partonic and/or hadronic dominant interactions in the QCD phase diagram. This is one of the main goals of the Beam Energy Scan (BES) program at RHIC [2]. In this program study of azimuthal anisotropy (known as elliptic flow) of produced particles will play a crucial role, since it is sensitive to the early dynamics of system created in the heavy-ion collision [7]. At top RHIC energy in Au+Au collisions,  $\phi$  meson has played an important role to establish that matter formed in such collisions is partonic i.e de-confined phase of quarks and gluons [36, 5]. Due to the small hadronic interaction cross-section, the yield and elliptic flow of the  $\phi$  meson are primarily controlled by the partonic interaction in the relativistic heavy-ion collisions [6, 17]. Therefore study of  $\phi$  meson will be the key measurement at RHIC BES program.

This thesis includes the study of elliptic flow of  $\phi$ -meson and inclusive charged hadrons in Au+Au collisions at RHIC energies ( $\sqrt{s_{NN}} = 7.7-200$  GeV) in STAR experiment. The measurement of transverse momentum spectra of  $\phi$  meson at RHIC BES energies ( $\sqrt{s_{NN}} = 7.7-39$  GeV) has been presented. It also includes systematic measurement of centrality dependence of multi-strange hadrons ( $\phi$ ,  $\Xi$ , and  $\Omega$ )  $v_2$  in Au+Au collisions at  $\sqrt{s_{NN}} = 200$  GeV. In addition, various models (Transport and Hydro) have been used to explain the experimental data. The content of this thesis is as follows. We will present the beam energy dependence of invariant yield and elliptic flow ( $v_2$ ) of

$\phi$  meson in Au+Au collisions, data collected in the years 2010 and 2011 by the STAR experiment. The observed number-of-constituent quark (NCQ) scaling of identified hadrons  $v_2$  was considered as signature for the formation of de-confined matter [8]. This NCQ scaling, mainly for multi-strange hadrons ( $\phi$ ,  $\Xi$  and  $\Omega$ ), has been considered as a necessary signature for the formation of QGP [6, 17, 9]. In this thesis NCQ scaling of  $\phi$ -meson  $v_2$  will be presented for different beam energies to search for the turn-off of the QGP signature.

The nuclear modification factor ( $R_{CP}$ ), defined as the particle yields in central nucleus-nucleus collisions to those in peripheral collisions, is also an important observable for studying QGP. For the QGP state,  $R_{CP}$  is expected to be less than unity at the high  $p_T$  due to energy loss of high- $p_T$  partons in the dense medium created in central collisions [12]. In addition,  $R_{CP}$  of identified hadrons shows particle type dependence (i.e baryon-meson separation) at intermediate  $p_T$  similar to  $v_2$ . To confirm this baryon-meson separation,  $\phi$  meson is considered as an essential probe, since it is a meson but it has a mass comparable to the mass of the lightest baryons (such as proton). The measurement of  $\phi$ -meson  $R_{CP}$  as a function of  $p_T$  for different centre-of-mass energies will be presented in this thesis.

We will also discuss particle ratio to shed light on  $\phi$ -meson production mechanism in the heavy-ion collisions. The ratio of yield of the  $\phi$  meson to the yield of the kaon,  $N(\phi)/N(K)$ , can be used to determine whether kaon coalescence is the dominant process for  $\phi$ -meson production. The ratios  $N(\phi)/N(K)$  as function of collision centrality and centre-of-mass energy will be shown. The ratio of yield of the  $\Omega$  baryon to the yield of the  $\phi$  meson,  $N(\Omega)/N(\phi)$ , are also observed to be sensitive to the particle production mechanism. At  $\sqrt{s_{NN}} = 200$  GeV, the ratios  $N(\Omega)/N(\phi)$  can be well explained by the quark recombination model for particle production [12, 11]. In this thesis, we will present the  $N(\Omega)/N(\phi)$  as function of  $p_T$  for various new beam energies in RHIC BES program.

In addition, we will explore the early dynamics of the system created in the heavy-ion collision by studying the elliptic flow of charged hadrons. In this thesis the measurement of inclusive charged hadron  $v_2$  as function of transverse momentum, collision

centrality and beam energy will be shown. These measurements will be compared to various models calculations and results from top RHIC and LHC energy.

Like  $\phi$  meson, other multi-strange hadrons i.e.  $\Xi$  and  $\Omega$  also have small hadronic interaction cross sections and they freeze-out close to the quark-hadron transition temperature predicted by lattice QCD [13, 14, 15, 16]. Hence, the multi-strange hadrons are expected to provide information from the partonic stage of the evolution in the heavy-ion collisions. Due to limited statistics, from the earlier measurements on  $v_2$  of multi-strange hadrons at RHIC, it was not possible to make strong physics conclusions. With high statistics data set collected by STAR experiment at top RHIC energy in the years 2010 and 2011, it is now possible to have high-precision measurements of multi-strange hadrons  $v_2$ . In this thesis we will present systematic measurements of centrality dependence of multi-strange hadrons  $v_2$ . Number-of-constituent quark scaling will be presented for different collision centrality classes to see how the partonic collectivity changes with different system size. Other possibility is to study the effect of the late-stage hadronic re-scattering on  $v_2$  low  $p_T$ . Initial simulations using a hybrid model (Hydro+Cascade) showed that the usual mass ordering trend of  $v_2(\phi) < v_2(p)$  will be reversed due to the late-stage hadronic re-scattering [16]. In this thesis we will investigate this effects by comparing  $v_2$  of proton and  $\phi$  meson at low  $p_T$  in experimental data.

# Bibliography

- [1] G. Baym, Nucl. Phys. **A 698** (2002) XXIII.
- [2] B. I. Abelev *et al.* (STAR Collaboration), Phys. Rev. **C 81** (2010) 024911.
- [3] P.F. Kolb *et al.* Nucl. Phys. **A 715** (2003) 653c.
- [4] B. I. Abelev *et al.* (STAR Collaboration), Phys. Rev. Lett. **99** (2007) 112301.
- [5] B. I. Abelev *et al.* ( STAR Collaboration), Phys. Lett. **B 673** (2009) 183.
- [6] Md. Nasim, B. Mohanty and N. Xu, Phys. Rev. **C 87** (2013) 014903.
- [7] B. Mohanty and N. Xu, J. Phys. **G 36** (2009) 064022.
- [8] D. Molnar and S. A. Voloshin, Phys. Rev. Lett. **91** (2003) 092301.
- [9] K. J. Wu *et al.* Nuclear Physics **A 834** (2010) 303c.
- [10] J. Adams *et al.* (STAR Collaboration), Nucl. Phys. **A 757** (2005) 102.
- [11] R.C. Hwa and C.B. Yang, Phys. Rev. **C 75** (2007) 054904.
- [12] J. Adams *et al.* (STAR Collaboration), Phys. Lett. **B 595** (2004) 143.
- [13] J. Adams *et al.* (STAR Collaboration), Phys. Rev. **C 70** (2004) 041901.
- [14] J. Adams *et al.* (STAR Collaboration), Phys. Lett. **B 612** (2005) 181.
- [15] J. Adams *et al.* (STAR Collaboration), Phys. Rev. Lett. **92** (2004) 182301 .
- [16] T. Hirano *et al.*, Phys. Rev. **C 77** (2008) 044909.

# Contents

<b>1</b>	<b>Introduction</b>	<b>1</b>
1.1	The Standard Model of Particle Physics . . . . .	1
1.2	Quantum Chromodynamics . . . . .	3
1.3	Quark-Gluon Plasma : QCD Phase Transition . . . . .	5
1.4	Relativistic Heavy Ion Collisions . . . . .	7
1.4.1	Space-time evolution . . . . .	7
1.4.2	Kinematics of heavy ion collisions . . . . .	8
1.4.2.1	Transverse momentum: . . . . .	8
1.4.2.2	Rapidity: . . . . .	9
1.4.2.3	Pseudo-rapidity: . . . . .	9
1.4.2.4	Multiplicity: . . . . .	9
1.4.2.5	Invariant distribution: . . . . .	10
1.4.2.6	Collision centrality: . . . . .	10
1.4.2.7	Units and conversion factors: . . . . .	11
1.5	Experimental Observables . . . . .	11
1.5.1	Hadron yields . . . . .	12
1.5.2	Jet quenching . . . . .	14
1.5.3	High $p_T$ probes . . . . .	14
1.5.4	Strangeness enhancement . . . . .	18
1.5.5	Particle ratio . . . . .	18
1.5.6	Elliptic flow : A collective phenomena . . . . .	20
1.5.6.1	Number-of-constituent quark scaling: . . . . .	22

1.5.6.2	$p_T$ integrated $v_2$ : . . . . .	24
1.6	Thesis Motivation . . . . .	25
1.6.1	Measurement of inclusive charged hadrons $v_2$ . . . . .	25
1.6.2	Measurement of $\phi$ -meson invariant yield and elliptic flow . . . . .	26
1.6.3	Measurement of multi-strange hadrons $v_2$ . . . . .	26
<b>2</b>	<b>Experimental Facilities at RHIC</b>	<b>32</b>
2.1	Solenoidal Tracker At RHIC (STAR) . . . . .	33
2.1.1	Time projection chamber . . . . .	35
2.1.2	Time-of-flight . . . . .	41
2.1.3	The trigger detectors . . . . .	42
<b>3</b>	<b>Energy Dependence of <math>\phi</math>-meson <math>v_2</math></b>	<b>48</b>
3.1	Data Sets and Cuts . . . . .	48
3.1.1	Event selection . . . . .	48
3.1.2	Centrality determination . . . . .	50
3.1.3	Particle identification . . . . .	52
3.1.3.1	Using TPC . . . . .	52
3.1.3.2	Using TOF . . . . .	55
3.2	Elliptic flow measurement methods . . . . .	55
3.2.1	Detector acceptance correction . . . . .	57
3.2.2	Event plane resolution correction . . . . .	59
3.2.3	The event plane method . . . . .	63
3.2.4	The $\eta$ -sub event plane method . . . . .	64
3.2.5	Extraction of $\phi$ -meson $v_2$ . . . . .	64
3.2.5.1	The $\phi$ -binning method: . . . . .	65
3.2.5.2	The $v_2$ vs. $m_{inv}$ method: . . . . .	66
3.3	Systematic uncertainties . . . . .	66
3.3.1	Uncertainty in particle identification . . . . .	66
3.3.2	Uncertainty from residual background . . . . .	68
3.4	Results & Discussion . . . . .	68

3.4.1	Differential $\phi$ -meson $v_2$ . . . . .	69
3.4.2	Mass ordering of $\phi$ $v_2$ at low $p_T$ . . . . .	71
3.4.3	Number-of-constituent quark scaling . . . . .	71
3.4.4	Centrality dependence of $\phi$ -meson $v_2$ . . . . .	73
3.4.5	$p_T$ integrated $\phi$ -meson $v_2$ . . . . .	75
3.4.6	Transport model comparison . . . . .	78
3.5	Summary . . . . .	81
3.6	Appendix . . . . .	85
3.6.1	Centrality selection condition using $N_{ch}^{raw}$ or refmult . . . . .	85
3.6.2	Data points of $\phi$ -meson $v_2$ . . . . .	86
3.6.2.1	$\sqrt{s_{NN}} = 62.4$ GeV: . . . . .	86
3.6.2.2	$\sqrt{s_{NN}} = 39$ GeV: . . . . .	86
3.6.2.3	$\sqrt{s_{NN}} = 27$ GeV: . . . . .	86
3.6.2.4	$\sqrt{s_{NN}} = 19.6$ GeV: . . . . .	87
3.6.2.5	$\sqrt{s_{NN}} = 11.5$ GeV: . . . . .	87
3.6.2.6	$\sqrt{s_{NN}} = 7.7$ GeV: . . . . .	87
3.6.3	Figures and fit parameter for integrated $v_2$ calculation . . . . .	88
3.6.3.1	Au+Au 200 GeV: . . . . .	88
3.6.3.2	Au+Au 62.4 GeV: . . . . .	89
3.6.3.3	Au+Au 27 GeV: . . . . .	90
3.6.3.4	Au+Au 19.6 GeV: . . . . .	91
3.6.3.5	Au+Au 11.5 GeV: . . . . .	92
3.6.4	TPC event plane distributions . . . . .	93
<b>4</b>	<b>Energy Dependence of <math>\phi</math>-meson Invariant Yields</b>	<b>94</b>
4.1	Data Sets and Cuts . . . . .	94
4.2	Transverse Momentum Spectra Measurement Methods . . . . .	95
4.2.1	$\phi$ -meson reconstruction . . . . .	95
4.2.2	Combinatorial background estimation . . . . .	95
4.2.3	Extraction of raw $\phi$ -meson yield . . . . .	96
4.2.4	Efficiency and acceptance corrections . . . . .	97

4.2.4.1	Kaon efficiency from embedding : . . . . .	97
4.2.4.2	Short lived resonance efficiency from single particle embedding: . . . . .	100
4.2.4.3	Energy loss correction for kaon: . . . . .	103
4.3	Systematic Error Study . . . . .	104
4.3.1	Uncertainty in particle identification . . . . .	105
4.3.2	Uncertainty from residual background . . . . .	105
4.3.3	Statistical uncertainty on efficiency . . . . .	106
4.4	Results & Discussion . . . . .	107
4.4.1	Mass and width of $\phi$ meson . . . . .	107
4.4.2	Invariant transverse momentum spectra . . . . .	110
4.4.3	$\phi$ -meson yield per unit rapidity . . . . .	111
4.4.4	Nuclear modification factor . . . . .	113
4.4.5	Particle ratios . . . . .	116
4.4.5.1	$\phi/\pi^-$ : . . . . .	116
4.4.5.2	$\phi/K^-$ : . . . . .	117
4.4.6	$\phi$ -meson $\langle p_T \rangle$ . . . . .	118
4.4.7	Strange quark dynamics . . . . .	119
4.5	Summary . . . . .	121
4.6	Appendix . . . . .	124
4.6.1	(signal+background)/background ratio . . . . .	124
4.6.2	$\phi$ -meson yield per unit rapidity . . . . .	129
4.6.3	Parameters of Levy and exponential fit to the $\phi$ -meson $p_T$ spectra	132
4.6.3.1	Levy fit parameters: . . . . .	132
4.6.3.2	Exponential fit parameters: . . . . .	134
4.6.4	Results from Glauber model simulation . . . . .	137
<b>5</b>	<b>Energy Dependence of Charged Hadron Elliptic Flow and Heavy-Ion Collision Model Results</b>	<b>147</b>
5.1	Data Sets . . . . .	147
5.2	Elliptic Flow Measurement Methods . . . . .	148

5.2.1	The cumulant method . . . . .	148
5.2.1.1	The cumulant method with generating function: . . .	149
5.2.1.2	The Q-cumulant method: . . . . .	149
5.2.2	The scalar product method . . . . .	154
5.3	Results & Discussion . . . . .	156
5.3.1	Energy dependence of charged hadron $v_2$ . . . . .	156
5.3.2	Centrality dependence of charged hadron $v_2(p_T)$ . . . . .	158
5.3.3	Model comparison . . . . .	159
5.4	Systematic Study on $v_2$ Using Transport Models . . . . .	163
5.4.1	Longitudinal scaling of $v_2$ : . . . . .	163
5.4.2	Effect of centrality determination procedure on measured $v_2$ : .	168
5.4.3	Effect of detector efficiency on measured $v_2$ . . . . .	169
5.4.4	Resonance decay effect . . . . .	173
5.5	Summary . . . . .	176
5.6	Appendix . . . . .	182
5.6.1	Color Glass Condensate Simulation . . . . .	182
5.6.2	Glauber Model Simulation . . . . .	183
5.6.3	Inputs Parameters of AMPT and UrQMD Model . . . . .	184
5.6.3.1	Inputs parameters of AMPT model: . . . . .	184
5.6.3.2	Inputs parameters of UrQMD model: . . . . .	185
<b>6</b>	<b>Centrality Dependence of Multi-strange Hadron <math>v_2</math> in Au+Au Col-</b>	
	<b>lisions at 200 GeV</b>	<b>186</b>
6.1	Data Sets and Event Selection Cuts . . . . .	186
6.2	Procedure to obtain multi-strange hadron $v_2$ . . . . .	187
6.2.1	Multi-strange hadron reconstruction . . . . .	187
6.2.1.1	$\Lambda$ reconstruction: . . . . .	188
6.2.1.2	$\Xi$ and $\Omega$ reconstruction: . . . . .	189
6.2.2	Combinatorial background estimation . . . . .	191
6.2.3	Elliptic flow measurement methods . . . . .	194
6.2.4	Event plane resolution correction . . . . .	196

6.2.5	Systematic error study . . . . .	197
6.2.5.1	Cut details for $\Xi$ and $\Omega$ : . . . . .	197
6.2.5.2	Cut details for $\phi$ meson: . . . . .	200
6.2.6	Efficiency correction . . . . .	201
6.2.7	Event bias correction . . . . .	203
6.3	Results & Discussion . . . . .	205
6.3.1	Comparison with previous published results . . . . .	205
6.3.2	Signature of partonic collectivity . . . . .	205
6.3.3	Centrality dependence of multi-strange hadron $v_2$ . . . . .	206
6.3.4	Centrality dependence of number-of-constituent quark scaling	208
6.3.5	Hadronic re-scattering effect on $v_2$ . . . . .	211
6.4	Summary . . . . .	216
6.5	Appendix . . . . .	220
6.5.1	Data points . . . . .	220
<b>7</b>	<b>Summary and Conclusions</b>	<b>228</b>

# List of Figures

1.1	(Color online) A standard info-graphic for the standard model. . . . .	2
1.2	(Color online) Various measurements on the strong coupling constant $\alpha_S$ as function of energy scale $Q$ . The curves are the QCD predictions. Figure has been taken from Ref. [9]. . . . .	4
1.3	(Color online) Lattice QCD calculations for energy density as a function of temperature [13]. Stefan-Boltzmann ideal gas limits are also shown. . . . .	5
1.4	(Color online) Schematic QCD phase diagram for nuclear matter [16]. The solid lines show the phase boundaries for the indicated phases. The solid circle depicts the critical point [14]. . . . .	6
1.5	(Color online) The space-time evolution of a heavy-ion collision. . . . .	8
1.6	(Color online) A geometrical picture of the heavy ion collision. . . . .	10
1.7	(Color online) Ratios of $p_T$ integrated mid-rapidity yields for different hadron species measured in STAR for central Au+Au collisions at $\sqrt{s_{NN}} = 200\text{GeV}$ . The horizontal bars represent statistical model fits to the measured yield ratios for stable and long-lived hadrons. The variation of $\gamma_s$ with centrality is shown in the inset, including the value (left most point) from fits to yield ratios measured by STAR for 200 GeV $p+p$ collisions [12]. . . . .	13

1.8	(Color online) The $1\sigma$ and $2\sigma$ $\chi^2$ contour for $T_{fo}$ and $\langle\beta_T\rangle$ extracted from thermal and radial flow fits to $\pi$ , $K$ , $p$ data in 9 centrality bins for Au+Au collisions at $\sqrt{s_{NN}} = 200$ GeV and for $\sqrt{s_{NN}} = 200$ GeV $p+p$ collisions [12]. . . . .	13
1.9	(Color online) Jets: Expectation from Au+Au and $p+p$ collisions. . .	14
1.10	(Color online) Dihadron azimuthal correlations in Au+Au, d+Au and $p+p$ collisions [12]. . . . .	15
1.11	(Color online) Left panel: $R_{AA}$ (also known as $R_{AB}$ ) measured in central Au+Au and d+Au collisions with $\sqrt{s_{NN}} = 200$ GeV for charged hadrons. Right panel: $R_{AA}$ measured in central Au+Au at $\sqrt{s_{NN}} = 200$ GeV for $\eta$ , $\pi^0$ and photons. The grey error band reflects the uncertainty in the number of binary collisions for central Au+Au collisions [12].	16
1.12	(Color online) $R_{CP}$ of identified hadrons at mid-rapidity in Au+Au collisions at $\sqrt{s_{NN}} = 200$ GeV. The shaded bands represent the uncertainties in the Glauber model calculations for $\langle N_{bin} \rangle$ and $\langle N_{part} \rangle$ [11].	17
1.13	(Color online) The ratio of the yields of $K^-$ , $\phi$ , $\bar{\Lambda}$ , and $\Xi + \bar{\Xi}$ normalized to $\langle N_{part} \rangle$ nucleus-nucleus collisions to corresponding yields in inelastic proton-proton collisions as a function of $\langle N_{part} \rangle$ at 62.4 and 200 GeV [8].	19
1.14	(Color online) Left panel: $\phi/K^-$ ratio as a function number of participants. Right panel: $\phi/K^-$ ratio as a function of centre-of-mass energies [7]. . . . .	20
1.15	(Color online) $\Omega/\phi$ as a function of $p_T$ in Au+Au collision at $\sqrt{s_{NN}} = 200$ GeV [7]. . . . .	21
1.16	(Color online) Schematic views of a non-central nucleus-nucleus collision.	22
1.17	(Color online) Measurements of $v_2(p_T)$ for identified particles for 0 – 80% centrality at RHIC. The lines are the results from hydrodynamic model calculation [38]. . . . .	22
1.18	(Color online) The $v_2$ scaled by number-of-constituent quarks ( $n_q$ ) as a function of $p_T/n_q$ and $(m_T - m_0)/n_q$ for identified hadrons in Au+Au collisions at $\sqrt{s_{NN}} = 200$ GeV [39]. . . . .	23

1.19	$\langle v_2 \rangle$ for charged particles at mid-rapidity for minimum bias collisions at $\sqrt{s_{NN}} = 9.2, 19.6, 62.4$ and $200$ GeV [15, 37, 38] compared to corresponding results from AMPT and UrQMD model calculations [37].	24
2.1	(Color online) Summary of RHIC Runs [1]. The nucleon-pair luminosity is defined as $L_{NN} = A_1 A_2 L$ , where where $L$ is the luminosity, and $A_1$ and $A_2$ are the number of nucleons of the ions in the two beam respectively. . . . .	33
2.2	(Color online) A layout of RHIC. . . . .	34
2.3	(Color online) Three dimensional view of STAR detector system. Figure has been taken from Alexander Schmah. . . . .	36
2.4	(Color online) Cutaway side view of STAR detector system. . . . .	37
2.5	STAR coordinate system. . . . .	38
2.6	Three dimensional schematic diagram indicating the main structural elements of the STAR TPC. . . . .	39
2.7	A sector of the TPC anode plane indicating the inner and outer sub-sectors and their respective padrows. . . . .	40
2.8	(Color online) The energy loss distribution for charged particles in the STAR TPC as a function of momentum. . . . .	41
2.9	(a) Cross section of the $6 \times 220 \mu\text{m}$ MRPC module for TOF. (b) Top view of the printed circuit board (PCB) with a $1 \times 6$ readout pads array. The PCB is $94 \text{ mm} \times 212 \text{ mm}$ area. The projection of the glass layers on the readout pads is also shown. . . . .	43
2.10	(Color online) $1/\beta$ as a function of momentum in Au+Au collisions at $\sqrt{s_{NN}} = 200$ GeV. . . . .	44
2.11	(Color online) A schematic figure of a nucleus-nucleus collision and STAR trigger systems. . . . .	45
3.1	The distribution of Z-positions of vertex for the events selected for the analysis at six different centre-of-mass energies. . . . .	49

3.2	(Color online) The distribution of X and Y-positions of vertex for $\sqrt{s_{NN}} = 7.7$ GeV in Au+Au collisions. Red dashed circle represent the circumference of beam pipe and solid red curve is a circle of radius equal to 2 cm. . . . .	50
3.3	(Color online) The uncorrected multiplicity distribution of reconstructed charged particles per unit pseudo-rapidity interval at mid-rapidity for the six different centre-of-mass energies. The solid black points depict the measured data and a GlauberMonte Carlo simulation is overlaid as the solid red curve. Three different centrality classes of 0 – 10%, 10 – 40% and 40 – 80% from the right of the distributions respectively are indicated by the different shaded regions. . . . .	52
3.4	(Color online) The mean specific energy loss, $dE/dx$ , of reconstructed tracks within a pseudo-rapidity range of $ \eta  < 1$ in the TPC in Au+Au collisions at $\sqrt{s_{NN}} = 39$ GeV. The Bichsel functions used to determine the $n\sigma$ values are shown as a line for each particle. The black line corresponds to Bichsel function for kaons. . . . .	54
3.5	(Color online) The ratio of $\phi$ -meson raw yield, normalized by events, (left panel) and signal to background ratio (right panel) for $Dca < 3$ cm and $Dca < 1.5$ cm for 20-30% centrality at $\sqrt{s_{NN}} = 39$ GeV. . . .	55
3.6	(Color online) The mass squared, $m^2$ , as a function of momentum within a pseudo-rapidity range of $ \eta  < 0.9$ in Au+Au collisions at $\sqrt{s_{NN}} = 39$ GeV. The red line corresponds to PDG mass value for kaons. . . . .	56
3.7	(Color online) TPC event plane distributions in Au+Au collisions at $\sqrt{s_{NN}} = 7.7$ GeV. Left panel and right panel show event plane constructed using flow tracks with $-1.0 < \eta < -0.05$ and $0.05 < \eta < 1.0$ , respectively. . . . .	59
3.8	(Color online) The event plane resolution of TPC using $\eta$ -sub events in Au+Au collisions at $\sqrt{s_{NN}} = 7.7 - 200$ GeV. . . . .	60

3.9	(Color online) The elliptic flow of charged particles as function of $p_T$ for 0-80% centrality in Au+Au collisions at $\sqrt{s_{NN}}= 200$ GeV from AMPT model. The $v_2$ values with different methods of resolution correction compared to results from true reaction plane. . . . .	62
3.10	(Color online) The raw $\phi$ -meson yield for different $(\phi - \Psi_2)$ bin at $\sqrt{s_{NN}} = 39$ GeV in Au+Au collisions for 0-80% centrality fitted with function shown in Eq. 3.24. . . . .	65
3.11	(Color online) Upper left panel: Invariant mass of $K^+$ and $K^-$ pairs in a same event (shown by blue line) and in a mixed event after normalization (shown by red line) for $2.1 < p_T < 2.7$ GeV/c in Au+Au collisions at $\sqrt{s_{NN}} = 39$ GeV for 0-80% centrality. Upper right panel: Background (mixed event) subtracted invariant mass of $K^+$ and $K^-$ pairs, i.e $\phi$ -meson signal fitted with Breit-Wigner function (B.W) + 1st order polynomial. (Details of $\phi$ -meson signal extraction will be discussed in chapter 3). Bottom left panel: $v_2^{S+B}$ as function of invariant mass fitted with function shown in Eq. 6.1. Bottom right panel: The $\phi$ -meson $v_2$ obtained from $v_2$ vs. $m_{inv}$ method are compared with $(\phi - \Psi_2)$ bin method for $\sqrt{s_{NN}} = 39$ GeV and 0-80% centrality. Errors are statistical. . . . .	67
3.12	(Color online) $\phi$ -meson $v_2$ using different cuts in Au+Au collisions at $\sqrt{s_{NN}} = 39$ GeV. The ratios with default value are shown in bottom panels. Error bars are statistical. . . . .	69
3.13	(Color online) The $\phi$ -meson $v_2(p_T)$ at mid-rapidity ( $ y  < 1.0$ ) in Au+Au collisions at $\sqrt{s_{NN}} = 7.7 - 62.6$ GeV for 0-80% centrality [13]. The systematic uncertainties are shown by the shaded areas attached to the data points, while the global systematic uncertainties are shown as the shaded horizontal bar near $v_2 = 0$ and the vertical lines are statistical uncertainties. . . . .	70

3.14 (Color online) The elliptic flow, $v_2(p_T)$ , in 0-80% central Au+Au collisions for selected identified particles plotted only for the transverse momentum up-to 1.5 GeV/c to emphasize the mass ordering at low $p_T$ [13]. Only statistical error bars are shown. Systematic errors are much smaller than the statistical errors. The lines connecting $v_2(p_T)$ data points for $\pi^-$ , $K^-$ and $\bar{p}$ is just to guide the eye of the reader. . . . .	72
3.15 (Color online) The NCQ-scaled elliptic flow, $v_2/n_q$ , versus $p_T/n_q$ for 0-80% central Au+Au collisions for selected identified particles [13]. Only statistical error bars are shown. . . . .	73
3.16 (Color online) The NCQ-scaled elliptic flow, $v_2/n_q$ , versus $(m_T - m)/n_q$ for 0-80% central Au+Au collisions for selected identified particles [13]. Only statistical error bars are shown. . . . .	74
3.17 (Color online) The $\phi$ -meson $v_2(p_T)$ for 0-30% and 30-80% centrality bins. Error bars represent statistical errors. . . . .	75
3.18 (Color online) The $\phi$ -meson $v_2(p_T)$ scaled by $\varepsilon_{part}\{2\}$ for 0-30% and 30-80% centrality bins. The systematic errors on $\varepsilon_{part}\{2\}$ are added in quadrature to the statistical error of $v_2$ . . . . .	76
3.19 (Color online) Left panel: The $\phi$ -meson $v_2(p_T)$ at $\sqrt{s_{NN}} = 39$ GeV for 0-80% centrality bin is fitted with $3^{rd}$ order polynomial and with function described in Eq. 3.27. Right panel: The $\phi$ -meson $dN/dp_T$ vs $p_T$ at $\sqrt{s_{NN}} = 39$ GeV for 0-80% centrality bin is fitted with Levy function. Bottom panel: Statistical errors on $v_2(p_T)$ at $\sqrt{s_{NN}} = 39$ GeV for 0-80% centrality bin are fitted with $4^{th}$ order polynomial. . . . .	78
3.20 (Color online) The $p_T$ integrated $\phi$ -meson $v_2$ for various centre of mass energies for 0-80% centrality in Au+Au collisions. Vertical lines are the statistical error and systematic error are shown by cap symbol. The details of $\phi$ $v_2$ analysis at 200 GeV will be discussed in chapter 6. . . . .	79

3.21	(Color online) The $\phi$ -meson $v_2(p_T)$ for Au+Au minimum-bias collisions at mid-rapidity ( $ \eta  < 1.0$ ) from the STAR experiment at RHIC compared to the corresponding AMPT model calculation at various beam energies. The errors shown are statistical. . . . .	80
3.22	(Color online) The $p_T$ integrated $\phi$ -meson $v_2$ for Au+Au minimum-bias collisions at mid-rapidity ( $ \eta  < 1.0$ ) from the STAR experiment at RHIC are compared to the corresponding AMPT model calculation at various beam energies. Details of $\phi v_2$ analysis at 200 GeV will be discussed in chapter 6. . . . .	81
3.23	(Color online) Left panel: The $\phi$ -meson $v_2(p_T)$ at $\sqrt{s_{NN}} = 200$ GeV for 0-80% centrality bin is fitted with $3^{rd}$ order polynomial and with function described in Eq. 3.27. Right panel: The $\phi$ -meson $dN/dp_T$ vs $p_T$ at $\sqrt{s_{NN}} = 200$ GeV for 0-80% centrality bin is fitted with levy function. Bottom panel: Statistical errors on $v_2(p_T)$ at $\sqrt{s_{NN}} = 200$ GeV for 0-80% centrality bin are fitted with $4^{th}$ polynomial. . . . .	88
3.24	(Color online) Left panel: The $\phi$ -meson $v_2(p_T)$ at $\sqrt{s_{NN}} = 62.4$ GeV for 0-80% centrality bin is fitted with $3^{rd}$ order polynomial and with function described in Eq. 3.27. Right panel: The $\phi$ -meson $dN/dp_T$ vs $p_T$ at $\sqrt{s_{NN}} = 62.4$ GeV for 0-80% centrality bin is fitted with levy function. Bottom panel: Statistical errors on $v_2(p_T)$ at $\sqrt{s_{NN}} = 62.4$ GeV for 0-80% centrality bin are fitted with $4^{th}$ order polynomial. . . . .	89
3.25	(Color online) Left panel: The $\phi$ -meson $v_2(p_T)$ at $\sqrt{s_{NN}} = 19.6$ GeV for 0-80% centrality bin is fitted with $3^{rd}$ order polynomial and with function described in Eq. 3.27. Right panel: The $\phi$ -meson $dN/dp_T$ vs $p_T$ at $\sqrt{s_{NN}} = 19.6$ GeV for 0-80% centrality bin is fitted with levy function. Bottom panel: Statistical errors on $v_2(p_T)$ at $\sqrt{s_{NN}} = 19.6$ GeV for 0-80% centrality bin are fitted with $4^{th}$ order polynomial. . . . .	90

3.26 (Color online) Left panel: The $\phi$ -meson $v_2(p_T)$ at $\sqrt{s_{NN}} = 19.6$ GeV for 0-80% centrality bin is fitted with 3 <sup>rd</sup> order polynomial and with function described in Eq. 3.27. Right panel: The $\phi$ -meson $dN/dp_T$ vs $p_T$ at $\sqrt{s_{NN}} = 19.6$ GeV for 0-80% centrality bin is fitted with levy function. Bottom panel: Statistical errors on $v_2(p_T)$ at $\sqrt{s_{NN}} = 19.6$ GeV for 0-80% centrality bin are fitted with 4 <sup>rd</sup> order polynomial. . . . .	91
3.27 (Color online) Left panel: The $\phi$ -meson $v_2(p_T)$ at $\sqrt{s_{NN}} = 11.5$ GeV for 0-80% centrality bin is fitted with 3 <sup>rd</sup> order polynomial and with function described in Eq. 3.27. Right panel: The $\phi$ -meson $dN/dp_T$ vs $p_T$ at $\sqrt{s_{NN}} = 11.5$ GeV for 0-80% centrality bin is fitted with levy function. Bottom panel: Statistical errors on $v_2(p_T)$ at $\sqrt{s_{NN}} = 11.5$ GeV for 0-80% centrality bin are fitted with 4 <sup>rd</sup> order polynomial. . . . .	92
3.28 (Color online) TPC event plane distributions in Au+Au collisions at $\sqrt{s_{NN}} = 11.5, 19.6, 27, 39$ and $62.4$ GeV. . . . .	93
4.1 (Color online) Same event invariant mass distribution (black curve) and mixed event invariant mass distribution (red curve) after proper normalisation in Au+Au collision (60-80%) at $\sqrt{s_{NN}} = 39$ GeV for different $p_T$ bins. . . . .	98
4.2 (Color online) $\phi$ -mesons signal after combinatorial background subtraction in Au+Au collision (60-80%) at $\sqrt{s_{NN}} = 39$ GeV for different $p_T$ bins. . . . .	99
4.3 (Color online) Values of (signal+background)/background for $\phi$ mesons in Au+Au collisions at $\sqrt{s_{NN}} = 39$ GeV for different centrality classes and $p_T$ bins. . . . .	100
4.4 (Color online) Distributions of Z-vertex and uncorrected reference multiplicity from Au+Au embedding data at $\sqrt{s_{NN}} = 7.7$ GeV. . . . .	101
4.5 (Color online) Distributions DCA and TPC hits of $K^+$ tracks in Au+Au embedding data (open blue circle) and real data (solid black line) at $\sqrt{s_{NN}} = 7.7$ GeV for $0.3 < p_T < 0.4$ GeV/c. The distributions have been normalized to unit area. . . . .	101

4.6	(Color online) Transverse momentum and pseudo-rapidity distribution of Monte-Carlo (MC) and reconstructed (RC) tracks in Au+Au embedding data (0-80%) at $\sqrt{s_{NN}} = 7.7$ GeV. Error bars are statistical.	102
4.7	(Color online) Efficiency $\times$ Acceptance of $K^+$ in Au+Au embedding data at $\sqrt{s_{NN}} = 7.7$ GeV for 0-80% centrality. Error bars are statistical.	102
4.8	(Color online) Left panel shows a comparison of $\phi$ -meson efficiency from single kaon efficiency and from embedding production in Au+Au collisions at 200 GeV and ratio of them are shown in right panel.	103
4.9	(Color online) Efficiency $\times$ Acceptance for $\phi$ mesons as a function of $p_T$ calculated for different centralities in Au+Au collisions at $\sqrt{s_{NN}}=7.7$ - 39 GeV.	104
4.10	(Color online) Energy loss effect for $K^+$ as a function of reconstructed transverse momentum at mid-rapidity ( $ y  < 0.5$ ) in 7.7 GeV 0-80% minimum bias collisions. Errors shown are statistical only.	105
4.11	(Color online) Systematic errors due to residual background, particle identification (PID), uncertainty in efficiency and total systematic errors in Au+Au collisions at $\sqrt{s_{NN}} = 39$ GeV for (a) 0-10% and (b) 60-80% centrality. Panel (c): Total systematic error for six different centrality at $\sqrt{s_{NN}} = 39$ GeV. Panel (d): Total systematic error for different centre-of-mass energies for 0-10% centrality.	107
4.12	(Color online) Mass of $\phi$ meson in Au+Au collisions at $\sqrt{s_{NN}} = 39$ GeV for 0-10% centrality before and after kaon energy loss correction. The error bars are statistical uncertainties. Red dashed line is the PDG mass value for $\phi$ meson [4].	108
4.13	(Color online) Left panel: Mass of $\phi$ meson in Au+Au collisions at $\sqrt{s_{NN}} = 39$ GeV for various centralities. Right panel: Mass of $\phi$ meson in Au+Au collisions (0-10%) for different beam energies. The error bars are statistical uncertainties. Dashed line is the PDG mass value for $\phi$ meson [4].	109

4.14	(Color online) Left panel: Width of $\phi$ meson in Au+Au collisions at $\sqrt{s_{NN}} = 39$ GeV for various centralities. Right panel: Width of $\phi$ meson in Au+Au collisions (0-10%) for different beam energies. The error bars are statistical uncertainties. Dash line is the PDG width value for $\phi$ meson [4]. . . . .	109
4.15	(Color online) Panel (a): Reconstructed $\phi$ -meson signal using $K^+$ and $K^-$ decay channel using AMPT data in Au+Au collisions at $\sqrt{s_{NN}} = 39$ GeV. Panel (b): Reconstructed $\phi$ -meson signal using $K^+$ and $K^-$ decay channel using AMPT data with momentum resolution $\sim 2\%$ in Au+Au collisions at $\sqrt{s_{NN}} = 39$ GeV. . . . .	110
4.16	(Color online) The invariant yield of $\phi$ -mesons as a function of $p_T$ measured for different centralities in Au+Au collision at $\sqrt{s_{NN}} = 7.7 - 39$ GeV. Shaded green bands are systematic errors, while the statistical errors are represented by error bars. The dashed(solid) line represents an exponential(Levy) function fit to the data. . . . .	112
4.17	(Color online) The $\phi$ meson mid-rapidity yield per participant pair $(dN/dy)/(0.5N_{part})$ as a function of number of participant ( $N_{part}$ ) in Au+Au collisions at $\sqrt{s_{NN}} = 7.7, 11.5, 19.6, 27, 39$ and $62.4$ GeV. The results at $\sqrt{s_{NN}} = 62.4$ GeV are taken from previous STAR measurements [7]. Systematic errors are added in quadrature with statistical errors. . . . .	114
4.18	(Color online) The $\phi$ meson mid-rapidity yield $(dN/dy)$ as a function of $\sqrt{s_{NN}}$ in central Au+Au collisions in STAR and in central Pb+Pb collisions in NA49 [9]. Systematic errors are added in quadrature with statistical errors. . . . .	114
4.19	(Color online) The $\phi$ -meson $R_{CP}$ as function of $p_T$ in the Au+Au collision at various beam energies. The $R_{CP}(0-05\%/40-60\%)$ at $\sqrt{s_{NN}} = 200$ GeV are taken from previous STAR measurements [7]. Error bars are only statistical uncertainties. Gray bands represents normalization error from $N_{bin}$ which is approximately 20% for all energies. . . . .	115

- 4.20 (Color online)  $R_{CP}$  of  $\phi$  mesons and  $K_S^0$  as function of  $p_T$  in Au+Au collisions at  $\sqrt{s_{NN}} = 7.7-39$  GeV. Error bars are statistical uncertainty. Gray bands represents normalization error from  $N_{bin}$ . . . . . 116
- 4.21 (Color online) Left panel:  $N_{part}$  dependence of ratio  $N(\phi)/N(\pi^-)$  in Au+Au collisions at different centre-of-mass energies. Systematic errors are added in quadrature with statistical errors. Right panel:  $N_{part}$  dependence of ratio  $N(\phi)/N(K^-)$  in Au+Au collisions at different centre-of-mass energies. Systematic errors are added in quadrature with statistical errors. In both panels, data points are shifted towards left and right by  $N_{part}$  value 10 for 11.5 and 39 GeV, respectively . . . 117
- 4.22 (Color online) Left panel:  $N_{part}$  dependence of  $\langle p_T \rangle$  of  $\phi$  mesons in Au+Au collisions at different centre-of-mass energies. Systematic errors are added in quadrature with statistical errors. The  $\langle p_T \rangle$  values at  $\sqrt{s_{NN}} = 62.4$  and 200 GeV are taken from previous STAR measurements [7]. Right panel:  $\langle p_T \rangle$  of  $\phi$ ,  $\pi^-$ ,  $K^-$  and  $p^-$  in Au+Au collisions at  $\sqrt{s_{NN}} = 39$  GeV. Systematic errors are added in quadrature with statistical errors. The data points of  $\phi$  are shifted towards right by  $N_{part}$  value of 10 in X-axis. . . . . 118
- 4.23 (Color online) Left panel: The baryon-to-meson ratio,  $N(\Omega^- + \bar{\Omega}^+)/2N(\phi)$ , as a function of  $p_T$  in mid-rapidity ( $|y| < 0.5$ ) from central Au+Au collisions at  $\sqrt{s_{NN}} = 11.5-200$  GeV. Green bands denote systematical errors. The solid and dashed lines represent recombination model calculations for central collisions at  $\sqrt{s_{NN}} = 200$  GeV with total and thermal strange quark contributions, respectively [12]. Right panel: Number-of-constituent-quark scaled  $N(\Omega^- + \bar{\Omega}^+)/2N(\phi)$  ratios, as a function of  $p_T/n_q$  in mid-rapidity ( $|y| < 0.5$ ) from central Au+Au collisions at  $\sqrt{s_{NN}} = 11.5-200$  GeV. Here  $n_q$  is the number of constituent quarks of each hadron. Green bands denote systematical errors. Dashed lines are blast-wave fits with fixed slope parameter  $T = 0.268$  GeV to data at 11.5 and 19.6 GeV, respectively. . . . . 120

4.24 (Color online) Same event invariant mass distribution (black curve) and mixed event invariant mass distribution (red curve) after proper normalisation in Au+Au collision (60-80%) at $\sqrt{s_{NN}}= 7.7$ GeV for different $p_T$ bins. . . . .	139
4.25 (Color online) $\phi$ -mesons signal after combinatorial background subtraction in Au+Au collision (60-80%) at $\sqrt{s_{NN}}= 7.7$ GeV for different $p_T$ bins. . . . .	140
4.26 (Color online) Same event invariant mass distribution (black curve) and mixed event invariant mass distribution (red curve) after proper normalisation in Au+Au collision (60-80%) at $\sqrt{s_{NN}}= 11.5$ GeV for different $p_T$ bins. . . . .	141
4.27 (Color online) $\phi$ -mesons signal after combinatorial background subtraction in Au+Au collision (60-80%) at $\sqrt{s_{NN}}= 11.5$ GeV for different $p_T$ bins. . . . .	142
4.28 (Color online) Same event invariant mass distribution (black curve) and mixed event invariant mass distribution (red curve) after proper normalisation in Au+Au collision (60-80%) at $\sqrt{s_{NN}}= 19.6$ GeV for different $p_T$ bins. . . . .	143
4.29 (Color online) $\phi$ -mesons signal after combinatorial background subtraction in Au+Au collision (60-80%) at $\sqrt{s_{NN}}= 19.6$ GeV for different $p_T$ bins. . . . .	144
4.30 (Color online) Same event invariant mass distribution (black curve) and mixed event invariant mass distribution (red curve) after proper normalisation in Au+Au collision (60-80%) at $\sqrt{s_{NN}}= 27$ GeV for different $p_T$ bins. . . . .	145
4.31 (Color online) $\phi$ -mesons signal after combinatorial background subtraction in Au+Au collision (60-80%) at $\sqrt{s_{NN}}= 27$ GeV for different $p_T$ bins. . . . .	146
5.1 (Color online) Second order event plane resolution as a function of centrality in Au+Au collisions at 200 GeV from AMPT model. . . . .	154

5.2	(Color online) The elliptic flow of charged particle as a function of centrality in Au+Au collisions at 200 GeV from AMPT model. . . . .	155
5.3	(Color online) The top panels show $v_2\{4\}$ vs. $p_T$ at mid-rapidity for various collision energies ( $\sqrt{s_{NN}} = 7.7$ GeV to 2.76 TeV). The results for $\sqrt{s_{NN}} = 7.7$ to 200 GeV are for Au+Au collisions and those for 2.76 TeV are for Pb+Pb collisions. The dashed red curves show the empirical fits to the results from Au+Au collisions at $\sqrt{s_{NN}} = 200$ GeV. The bottom panels show the ratio of $v_2\{4\}$ vs. $p_T$ for all $\sqrt{s_{NN}}$ with respect to the fit curve. The results are shown for three collision centrality classes: 10 – 20% (a1), 20 – 30% (b1) and 30 – 40% (c1). Error bars are shown only for the statistical uncertainties. . . . .	157
5.4	(Color online) Average elliptic flow ( $\langle v_2 \rangle$ ) as a function of beam energy. The results are shown for charged particles from, LHC experiments of ALICE [11], RHIC experiments of STAR [15], PHENIX [16] and PHOBOS [17], SPS experiments of CERES [18], AGS experiments of E877 [19] and E895 [20] (proton). . . . .	158
5.5	(Color online) The $v_2$ over $\varepsilon_{\text{part}}\{2\}$ (Glauber) as a function of $p_T$ for various collision centralities (10–20%, 30–40% and 50–60%) in Au + Au collisions at mid-rapidity. Panels (a), (b), (c), (d) and (e) show the results for $\sqrt{s_{NN}} = 7.7, 11.5, 19.6, 27$ and 39 GeV respectively. The data are from $v_2\{\text{EtaSubs}\}$ . The error bars and shaded boxes represent the statistical and systematic uncertainties respectively.. . . . .	160
5.6	(Color online) The $v_2$ over $\varepsilon_{\text{part}}\{2\}$ (CGC) as a function of $p_T$ for various collision centralities (10 – 20%, 30 – 40% and 50 – 60%) in Au + Au collisions at mid-rapidity. Panels (a), (b), (c), (d) and (e) show the results for $\sqrt{s_{NN}} = 7.7, 11.5, 19.6, 27$ and 39 GeV respectively. The data are from $v_2\{\text{EtaSubs}\}$ . The error bars and shaded boxes represent the statistical and systematic uncertainties respectively. . . . .	161

5.7	(Color online) The $v_2\{4\}$ as a function of $p_T$ for 20 – 30% Au + Au collisions at $\sqrt{s_{NN}} = 7.7, 11.5, 39$ and 200 GeV compared to corresponding results from UrQMD, AMPT default version, and AMPT with string melting version (3 and 10 mb). The shaded boxes show the systematic uncertainties for the experimental data of 7.7, 11.5 and 39 GeV. The bottom panels show the ratio of data to the fit results of the models. . . . .	162
5.8	(Color online) The experimental data (symbols) are the same as in Fig. 5.3 (b2). The lines represent the viscous hydrodynamic calculations from Ref. [36] based on (a) MC-Glauber initial conditions and $\eta/s = 0.08$ (b) MC-KLN initial conditions and $\eta/s = 0.20$ . . . . .	163
5.9	(Color online) $dN_{ch}/d\eta$ versus $\eta$ - $y_{beam}$ for 0–6% central Au+Au collisions at $\sqrt{s_{NN}} = 19.6, 62.4$ and 200 GeV from (a) the PHOBOS experiment at RHIC [39], (b) UrQMD, (c) AMPT default and (d) AMPT-SM. Also shown are the model results from Pb+Pb collisions at $\sqrt{s_{NN}} = 2760$ GeV. . . . .	165
5.10	(Color online) $\langle p_T \rangle$ versus $\eta$ - $y_{beam}$ for minimum bias Au+Au collisions at $\sqrt{s_{NN}} = 19.6, 62.4$ and 200 GeV from (a) the UrQMD, (b) AMPT default and (c) AMPT-SM. Also shown are the model results from Pb+Pb collisions at $\sqrt{s_{NN}} = 2760$ GeV. . . . .	166
5.11	(Color online) $v_2$ for charged particles versus $\eta$ - $y_{beam}$ for 0–40% central Au+Au collisions at $\sqrt{s_{NN}} = 19.6, 62.4$ and 200 GeV from (a) the PHOBOS experiment at RHIC [41], (b) UrQMD, (c) AMPT default and (d) AMPT-SM. Also shown are the model results from Pb+Pb collisions at $\sqrt{s_{NN}} = 2760$ GeV. . . . .	167
5.12	(Color online) The elliptic flow of charged particles as function of centrality in Au + Au collisions from AMPT model. The black solid circle, red open circle and blue open square represents the charged particles $v_2$ corresponding centrality 1, 2 and 3, respectively. . . . .	169

5.13	(Color online) Left panel: Charged particles $v_2$ from AMPT model with finite particle track reconstruction efficiency $\varepsilon$ (as a function of $p_T$ and centrality) are compared with default $v_2$ ( $\varepsilon=1$ ) of AMPT. Centre-of-mass energy is 200 GeV and centrality is 0-80%. Right panel: Ratios of the $v_2$ as function of $p_T$ . . . . .	171
5.14	(Color online) Left panel: Charged particles $v_2$ from AMPT model with finite particle track reconstruction efficiency $\varepsilon$ (as a function of $p_T$ and centrality) and after efficiency correction are compared with default $v_2$ value ( $\varepsilon =1$ )of AMPT. Centre-of-mass energy is 200 GeV and centrality is 0-80%. Right panel: Ratios of the $v_2$ as function of $p_T$ .	172
5.15	(Color online) Left panel: Track reconstruction efficiency as function of $p_T$ for charged kaon and $K_S^0$ . Open symbol is for $K_S^0$ and filled symbol for charged kaons. Right panel: Yield as function of $p_T$ for kaon. Red line is yield of kaon directly obtained from AMPT model and black line correspond kaon yield obtained after modification with $K_S^0$ reconstruction efficiency values. Y-axis has arbitrary normalization.	173
5.16	(Color online) The elliptic flow of kaon as function of $p_T$ in Au+Au collision for 0-80% from AMPT model in three different condition: with 100% efficiency (labeled as default), with kaon reconstruction efficiency and with $K_S^0$ reconstruction efficiency. The centre-of-mass energy is 200 GeV per nucleon. . . . .	174
5.17	(Color online) The $v_2$ of $\pi$ , $K$ and $p$ as function of $p_T$ at 0-80% centrality with decay off and decay on condition in Au+Au collision at 200 GeV from UrQMD model. . . . .	175
5.18	(Color online) The elliptic flow of pions as a function of $p_T$ in Au+Au collisions at 200 GeV for 0-80% centrality from UrQMD model. . . .	176

6.1	(Color online) Distribution of uncorrected reference multiplicity (left panel) and Z position of vertex (right panel) in Au+Au collisions at $\sqrt{s_{NN}} = 200$ GeV. Blue and Red line corresponds to the data sets collected in the years 2010 (labeled as Run 10) and 2011 (labeled as Run 11), respectively. . . . .	187
6.2	(Color online) Decay diagram of $\Xi$ baryon. . . . .	188
6.3	(Color online) The topology of a $\Xi$ decay. The charged tracks are represented in the figure by solid lines, and the neutral $\Lambda$ track by a dashed line. All the geometrical variables used for $\Xi$ topological reconstruction are represented. . . . .	189
6.4	The topology of $V0$ decay. . . . .	190
6.5	(Color online) Reconstructed signal of $\Xi$ from $\Lambda$ and $\pi$ decay channel for 0-30% and 30-80% centrality in Au+Au collisions at $\sqrt{s_{NN}} = 200$ GeV integrated over $0 < p_T < 10$ GeV/c. In the upper panel red circles show rotational background. Background subtracted signal are shown in the bottom panel. Results obtained by combining both year 2010 and 2011 data sets. . . . .	193
6.6	(Color online) Reconstructed signal of $\Omega$ from $\Lambda$ and $K$ decay channel for 0-30% and 30-80% centrality in Au+Au collisions at $\sqrt{s_{NN}} = 200$ GeV integrated over $0 < p_T < 10$ GeV/c. In the upper panel red circles show rotational background. Background subtracted signal are shown in the bottom panel. Results obtained by combining both year 2010 and 2011 data sets. . . . .	194
6.7	(Color online) Reconstructed signal of $\phi$ meson from $K^+$ and $K^-$ decay channel for 0-30% and 30-80% centrality in Au+Au collisions at $\sqrt{s_{NN}} = 200$ GeV integrated over $0 < p_T < 10$ GeV/c. In the upper panel red circles show mixed event background. Background subtracted signal are shown in the bottom panel. Results obtained by combining both year 2010 and 2011 data sets. . . . .	195

6.8	(Color online) The TPC event plane angle distribution for TPC west and TPC East eta sub-events in Au+Au collisions at $\sqrt{s_{NN}} = 200$ GeV. Red lines are the fit function of the form $p_0(1 + 2 \times p_1 \times \cos(2 * x))$ . . . . .	196
6.9	(Color online) $v_2^{S+B}$ as function of invariant mass for $\Xi$ in minimum bias Au+Au collisions at $\sqrt{s_{NN}} = 200$ GeV for various $p_T$ bins. The distributions are fitted with function shown in Eq. 6.2. . . . .	198
6.10	(Color online) $v_2^{S+B}$ as function of invariant mass for $\Omega$ in minimum bias Au+Au collisions at $\sqrt{s_{NN}} = 200$ GeV for various $p_T$ bins. The distributions are fitted with function shown in Eq. 6.1. . . . .	199
6.11	(Color online) $v_2^{S+B}$ as function of invariant mass for $\phi$ meson in minimum bias Au+Au collisions at $\sqrt{s_{NN}} = 200$ GeV for various $p_T$ bins. The distributions are fitted with function shown in Eq. 6.1. . . . .	200
6.12	A comparison of $\Xi$ and $\Omega$ $v_2$ before and after efficiency correction for 0-80% centrality in Au+Au collisions at $\sqrt{s_{NN}} = 200$ GeV. Error bars are statistical only. . . . .	203
6.13	(Color online) Left panel: Particle yield as a function of uncorrected reference multiplicity in Au+Au collisions at $\sqrt{s_{NN}} = 200$ GeV. Right panel: Participants eccentricity calculated from Glauber model simulation as function of reference multiplicity in Au+Au collisions at $\sqrt{s_{NN}} = 200$ GeV. . . . .	204
6.14	(Color online) A comparison of $\phi$ , $\Xi$ and $\Omega$ $v_2$ between new analysis (using combined data sets of year 2010 and 2011, labelled as Run 10+11) and STAR published data (using data sets of year 2004, labeled as Run 4) in Au+Au collision at $\sqrt{s_{NN}} = 200$ GeV for 0-80% centrality. Error bars are statistical uncertainty. Systematic errors are shown by cap symbol on the new analysis. . . . .	206
6.15	(Color online) The $v_2$ as function of $p_T$ for $\pi$ , $p$ (panel a) and $\phi$ , $\Omega$ (panel b) in Au+Au minimum-bias collisions at $\sqrt{s_{NN}} = 200$ GeV. Only statistical errors are shown. $\phi$ and $\Omega$ $v_2$ are event bias corrected. . . . .	207

- 6.16 (Color online) The  $v_2$  as a function of  $p_T$  for multi-strange hadrons (a)  $\Xi^- + \bar{\Xi}^+$  (b)  $\Omega^- + \bar{\Omega}^+$  and (c)  $\phi$  in Au+Au collision at  $\sqrt{s_{NN}} = 200$  GeV for centrality 0-30% and 30-80%. Open bands are the systematic uncertainty and vertical lines are the statistical uncertainty. . . . . 208
- 6.17 (Color online) The  $v_2$  scaled by participant eccentricity  $\varepsilon_{part}\{2\}$  as a function of  $p_T$  for multi-strange hadrons (a)  $\Xi^- + \bar{\Xi}^+$  (b)  $\Omega^- + \bar{\Omega}^+$  and (c)  $\phi$  in Au+Au collision at  $\sqrt{s_{NN}} = 200$  GeV for centrality 0-30% and 30-80%. The participant eccentricity  $\varepsilon_{part}\{2\}$  was calculated from Glauber model simulation. Vertical lines are the statistical uncertainty only. . . . . 209
- 6.18 (Color online) The  $v_2$  scaled by number of constituent quarks ( $n_q$ ) as a function of  $p_T/n_q$  and  $(m_T - m)/n_q$  for identified hadrons in Au+Au collisions at  $\sqrt{s_{NN}} = 200$  GeV. The ratios with fit to  $\pi v_2$  to the other hadrons  $v_2$  are shown in corresponding lower panels. Statistical and systematic error are added in quadrature and propagated for the ratios for  $\phi$ ,  $\Xi$  and  $\Omega$  but for other particles only statistical errors are shown. 210
- 6.19 (Color online)  $\phi$  meson  $v_2$  for Au+Au minimum bias (0-80%) collisions at mid-rapidity ( $\pm 1.0$ ) at  $\sqrt{s_{NN}} = 200$  GeV from the AMPT model. Panels (a) and (b) shows the results as a function of  $p_T$  for parton-parton interaction cross section of 0 and 10 mb and calculations before and after relativistic transport (ART) calculations for hadrons, respectively. The lower panels (c) and (d) shows the difference in  $v_2$  shown in panels (a) and (b), respectively. The errors shown are statistical. . 212

6.20	(Color online) (a) $v_2$ of protons as a function of $p_T$ for Au+Au 0-80% collisions at $\sqrt{s_{NN}} = 200$ GeV from AMPT model at mid-rapidity. The results are shown for a parton-parton cross section of 10 mb and three different values of hadronic cascade time periods. (b) The same plot as (a) for the $\phi$ mesons. (c) Ratio of $v_2$ of protons for hadron cascade time of 0.6 fm/ $c$ to corresponding $v_2$ for time periods of 15 and 30 fm/ $c$ , and (d) same as in (c) for the $\phi$ mesons. The error bars shown are statistical. . . . .	214
6.21	(Color online) Ratio between $\phi$ and $p$ $v_2$ for 0-30% and 30-80% centrality in Au+Au collisions $\sqrt{s_{NN}} = 200$ GeV. Systematic uncertainties are shown by cap symbol and vertical lines are the statistical uncertainty.	215
6.22	(Color online) Ratio between $\phi$ and $p$ $v_2$ for 0-30% and 30-80% centrality in Au+Au collisions $\sqrt{s_{NN}} = 200$ GeV. Shaded bands are the results from the model calculations [20]. . . . .	216
6.23	(Color online) Ratio between $\phi$ and $p$ $v_2$ for 0-30% and 30-80% in Au+Au collisions $\sqrt{s_{NN}} = 200$ GeV. Shaded bands are the results from the AMPT and UrQMD model calculations for 0-30% centrality in Au+Au collisions $\sqrt{s_{NN}} = 200$ GeV.. . . .	217

# List of Tables

1.1	Mass, length and time in terms of Natural units. . . . .	11
3.1	Values of $n_{pp}$ and $\sigma_{nn}^{inel}$ with systematic uncertainties at $\sqrt{s_{NN}}= 7.7, 11.5, 19.6, 27, 39$ and $62.4$ GeV. . . . .	51
3.2	Kaons selection cuts using TPC for $\phi$ -meson reconstruction. . . . .	53
3.3	Track cuts for flow tracks selection. . . . .	57
3.4	Second order event plane resolution in TPC from $\eta$ -sub event method. Statistical error on resolution is less than 2% for all the centrality classes and all energies. . . . .	61
3.5	Values of $\varepsilon_{part}\{2\}$ with systematic uncertainties for 0-30% and 30-80% centrality bins at $\sqrt{s_{NN}}= 11.5, 19.6, 27, 39$ and $62.4$ GeV. . . . .	77
3.6	Values of $N_{ch}^{raw}$ or refmult for all the centrality classes and all energies. . . . .	85
4.1	Values of (signal+background)/background for $\phi$ mesons in Au+Au collisions at $\sqrt{s_{NN}} = 39$ GeV for different centrality classes and $p_T$ bins. . . . .	124
4.2	Values of (signal+background)/background for $\phi$ mesons in Au+Au collisions at $\sqrt{s_{NN}} = 27$ GeV for different centrality classes and $p_T$ bins. . . . .	125
4.3	Values of (signal+background)/background for $\phi$ mesons in Au+Au collisions at $\sqrt{s_{NN}} = 19.6$ GeV for different centrality classes and $p_T$ bins. . . . .	126
4.4	Values of (signal+background)/background for $\phi$ mesons in Au+Au collisions at $\sqrt{s_{NN}} = 11.5$ GeV for different centrality classes and $p_T$ bins. . . . .	127

4.5	Values of (signal+background)/background for $\phi$ mesons in Au+Au collisions at $\sqrt{s_{NN}} = 7.7$ GeV for different centrality classes and $p_T$ bins.	128
4.6	Summary of centrality bins, average number of participants $\langle N_{\text{part}} \rangle$ , and number of binary collisions $\langle N_{\text{coll}} \rangle$ , from MC Glauber simulations at $= 7.7, 11.5, 19.6, 27, 39$ and $62.4$ GeV. The errors are systematic uncertainties.	137
5.1	Summary of the parameters for the fit functions to the results of $v_2\{4\}$ vs. $p_T$ in Au+Au collisions at $= 200$ GeV.	159
5.2	The $\varepsilon_{\text{part}}\{2\}$ and transverse area $\langle S_{\text{part}} \rangle$ from the Color Glass Condensate (CGC) model [26, 27, 28, 29] calculations in Au + Au collisions at $\sqrt{s_{NN}} = 7.7, 11.5, 19.6, 27, 39, 62.4$ and $200$ GeV. The errors are systematic uncertainties.	182
5.3	The $\varepsilon_{\text{part}}\{2\}$ and transverse area $\langle S_{\text{part}} \rangle$ from the Glauber model calculations in Au + Au collisions at $\sqrt{s_{NN}} = 7.7, 11.5, 19.6, 27, 39, 62.4$ and $200$ GeV. The errors are systematic uncertainties.	183
6.1	Track selection cuts using TPC and TOF for $\Lambda^0$ reconstruction.	190
6.2	Track selection cuts for $\Xi$ and $\Omega$ reconstruction.	192
6.3	Summary of systematic error on $\phi$ -meson $v_2$ from different sources in Au+Au collisions at $\sqrt{s_{NN}} = 200$ GeV.	201
6.4	Summary of systematic error on $\Xi$ $v_2$ from different sources in Au+Au collisions at $\sqrt{s_{NN}} = 200$ GeV.	202
6.5	Summary of systematic error on $\Omega$ $v_2$ from different sources in Au+Au collisions at $\sqrt{s_{NN}} = 200$ GeV.	202
6.6	Event bias correction factors for different centrality in Au+Au collision at $\sqrt{s_{NN}} = 200$ GeV.	204

# Chapter 1

## Introduction

### 1.1 The Standard Model of Particle Physics

The Standard Model (SM), proposed by Glashow, Salam and Weinberg, attempts to explain properties of fundamental constituents of matter and their interactions [1, 2, 3]. The elementary particles are divided into three groups: Quarks, Leptons and Gauge Bosons [4]. All the leptons and quarks are fermions. The gauge bosons are the mediator of the interaction between quarks and leptons. They represent three of the four fundamental forces of nature; the electromagnetic force, the weak force and the strong force. There are six different gauge bosons: The massless photons ( $\gamma$ ) and gluons ( $g$ ), the massive  $W^\pm$  and  $Z^0$  bosons. The Standard Model also predicts the existence of Higgs (H) boson which is discovered recently [5, 6, 7, 8]. The leptons are divided into three generations in the SM : The electron and electron neutrino, the muon and muon neutrino, and the tau and tau neutrino. The leptons interact among them via the electromagnetic and the weak interaction. There are also six quarks in the SM and divided into three generations : The up (u) and down (d) quarks, the charm (c) and strange (s) quarks, and the top (t) and bottom (b) quarks. Figure 1.1 shows all the fundamental particles in the SM.

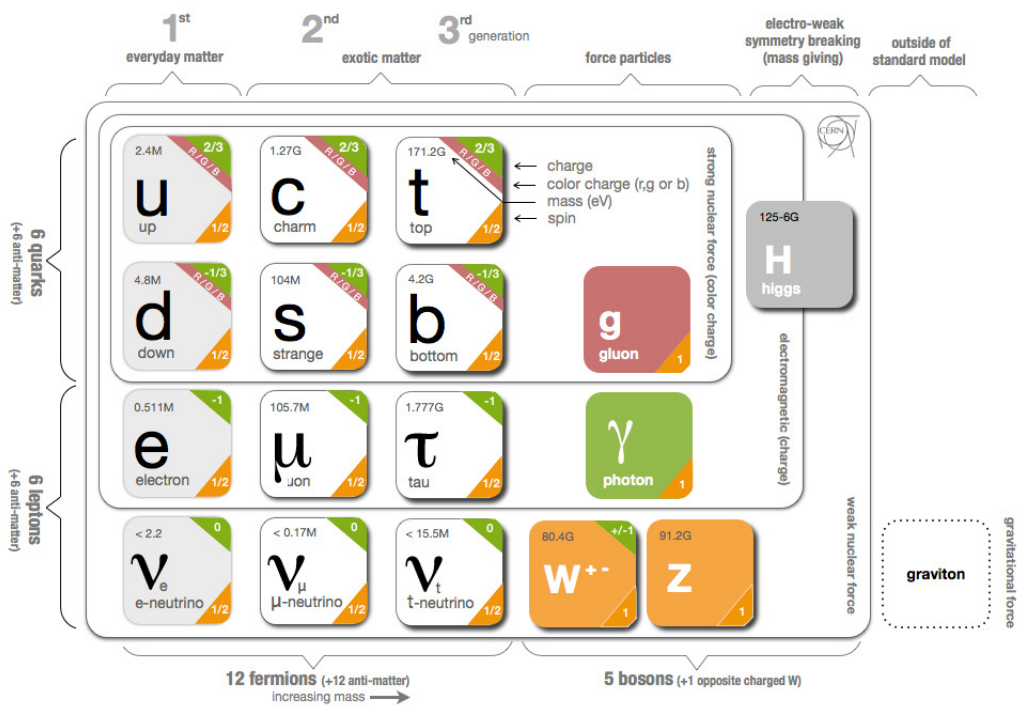


Figure 1.1: (Color online) A standard info-graphic for the standard model.

## 1.2 Quantum Chromodynamics

In the Standard Model the strong force is described by Quantum Chromodynamics (QCD). In QCD, the quarks and gluons are said to have color charge, similar to electric charge in electrodynamics, and they interact via strong force. The strong force is responsible for confinement of quarks in hadrons, such as proton and neutron. The strong interaction shows two interesting features: confinement and asymptotic freedom. The coupling strength ( $\alpha_S$ ) of the strong interaction is given by

$$\alpha_S(Q^2) = \frac{12\pi}{(11n - 2f)\ln(|Q^2|/\Lambda^2)}, \quad (1.1)$$

where  $Q^2$  is the momentum transfer,  $n$  is the number of colors and  $f$  is the number of flavors. The value of  $\Lambda$  appears to lie between the range  $100 \text{ MeV} < \Lambda < 500 \text{ MeV}$ . It is hard to determine  $\Lambda$  precisely from experimental data. The values of  $\alpha_S$  has been extracted from different experimental results and compared with perturbative QCD (pQCD) predictions as shown in Fig. 1.2. For small momentum transfer or at larger distance, the value of  $\alpha_s$  is very high and increases with increase in distance between quarks. This property, known as confinement, is responsible for binding of quarks inside the hadrons. On the other hand, when momentum transfers are large i.e distance between quarks are very small, the coupling between quarks are very small and quarks behaves like a free particle. This is known as Asymptotic freedom.

In general QCD is not a perturbative theory. But in case of interactions involving high momentum transfer (i.e. hard process), QCD can be calculated perturbatively. For soft process perturbative QCD is not a valid approximation. But soft process are the dominant process in the Universe. One of the main aim of high energy theoretical nuclear physics is to calculate QCD quantities using lattice gauge techniques in the non-perturbative regime. In Lattice QCD (lQCD) calculations are done on a discretized space-time lattice [10].

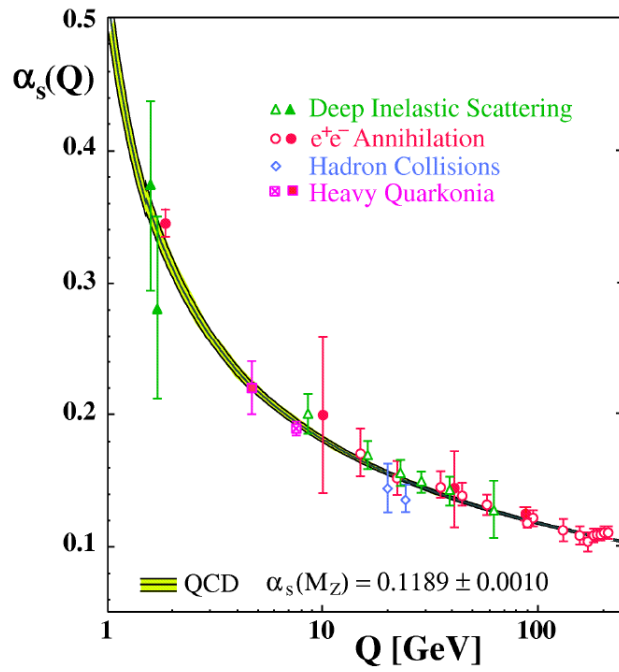


Figure 1.2: (Color online) Various measurements on the strong coupling constant,  $\alpha_s$  as function of energy scale  $Q$ . The curves are the QCD predictions. Figure has been taken from Ref. [9].

### 1.3 Quark-Gluon Plasma : QCD Phase Transition

The transformation of the system of hadrons into the system of free quark and gluon is called the de-confinement phase transition. When quarks are very close together then the force between two quarks are close to zero and the quarks stop interacting, they are, in a sense, free quarks. In the year 1974, T.D. Lee came out with a new idea. He suggested that by having high nucleon density over a relatively large volume, it might be possible to create very high dense states of nuclear matter which would contain asymptotically free quarks. Such dense nuclear matter of free quarks is known as the Quark-Gluon Plasma (QGP) [11]. Experimentally we define QGP as a (locally) thermally equilibrated state of matter in which quarks and gluons are de-confined from hadrons, so that color degrees of freedom become manifest over nuclear, rather than merely nucleonic, volumes [12]. Lattice QCD calculations also show that there

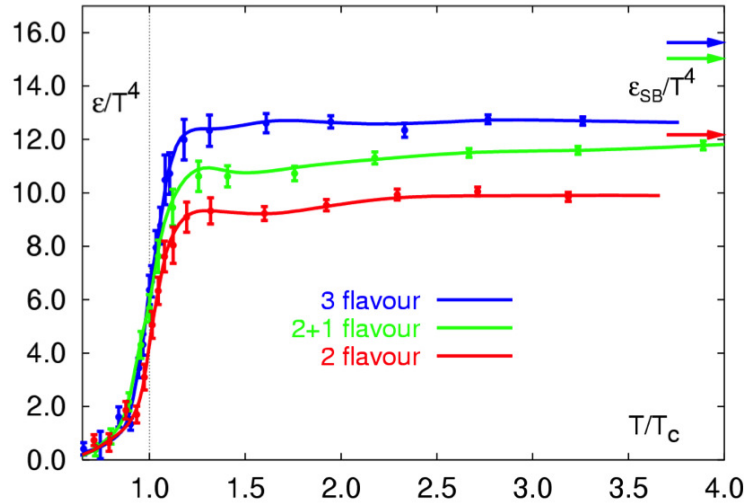


Figure 1.3: (Color online) Lattice QCD calculations for energy density as a function of temperature [13]. Stefan-Boltzmann ideal gas limits are also shown.

are two phases in the high temperature QCD calculations, which are identified with the hadron and quark-gluon phase, respectively. Fig. 1.3 shows the energy density ( $\epsilon$ ) as a function of temperature ( $T/T_c$ ) from lQCD calculations [13]. At a temperature

$T_c \sim 175$  MeV (at zero chemical potential  $\mu_B$ ), known as critical temperature, there is a sharp increase in energy density. This indicates sudden change in number of degree of freedom of the system i.e. de-confinement of hadrons into quarks and gluons. The

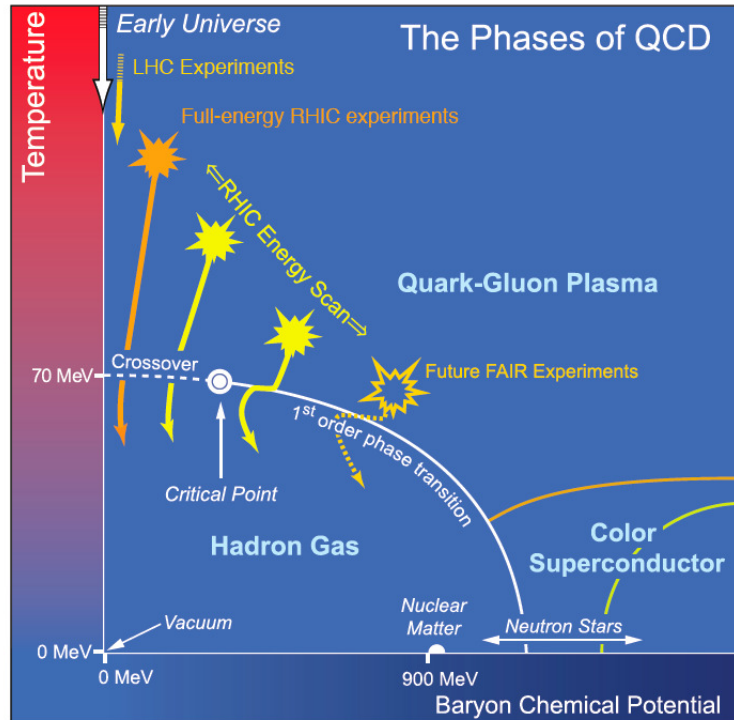


Figure 1.4: (Color online) Schematic QCD phase diagram for nuclear matter [16]. The solid lines show the phase boundaries for the indicated phases. The solid circle depicts the critical point [14].

different phases of QCD matter has been shown in the Fig. 1.4. This is a schematic phase diagram of QCD. At very high  $T$  and low  $\mu_B$ , a state of de-confined quarks and gluons is expected to be present while at low  $T$  and low  $\mu_B$  the quarks and gluons are known to be confined inside hadrons. QCD calculations suggest at low  $T$  and high  $\mu_B$  quarks form a colour super-conducting phase [15].

## 1.4 Relativistic Heavy Ion Collisions

The heavy-ion collisions provide a unique opportunity to study the quark-gluon plasma in the laboratory experiments. The main aim of the relativistic heavy-ion collisions is to create de-confined state of quarks and gluons and study the structure of the QCD phase diagram. At the Relativistic Heavy Ion Collider (RHIC) and now at the Large Hadron Collider (LHC) it is believed that creating a de-confined state of quarks and gluons has been accomplished. In the next section, results indicating a creation of QGP and some of its properties will be presented. But before that, a look into the evolution of the QCD matter after a collision and an introduction to the kinematics of the heavy ion collision is necessary.

### 1.4.1 Space-time evolution

Before the collision, two incoming nuclei accelerated to highly relativistic speeds will appear as two flat pancakes in the centre of mass frame due to Lorentz contraction along the beam direction. At time  $t = 0$ , the two nuclei hit each other and the interactions start developing in the overlapped region. Simply, as the heavy-ions collide they interact inelastically and lose kinetic energy. This loss of kinetic energy leads to the creation of matter in the vicinity of the collision which is often labelled as the *fireball*. If the *fireball* is hot enough, the QGP will be formed. The theoretically motivated space-time picture of a heavy ion collision (HIC) is depicted in Fig. 1.5. As shown in Fig. 1.5, the fireball will then expand due to pressure gradients. As it expands and cools, quarks and gluons will then form a hadron gas when the critical temperature  $T_c$  is reached. As the hadron gas expands, inelastic collisions will eventually cease at the *chemical freeze-out*, with a temperature  $T_{ch}$ . The chemical composition from this point onwards will remain the same. After further expansion, elastic collisions will cease and this is known as *kinetic freeze-out*, with a corresponding temperature  $T_{fo}$ .

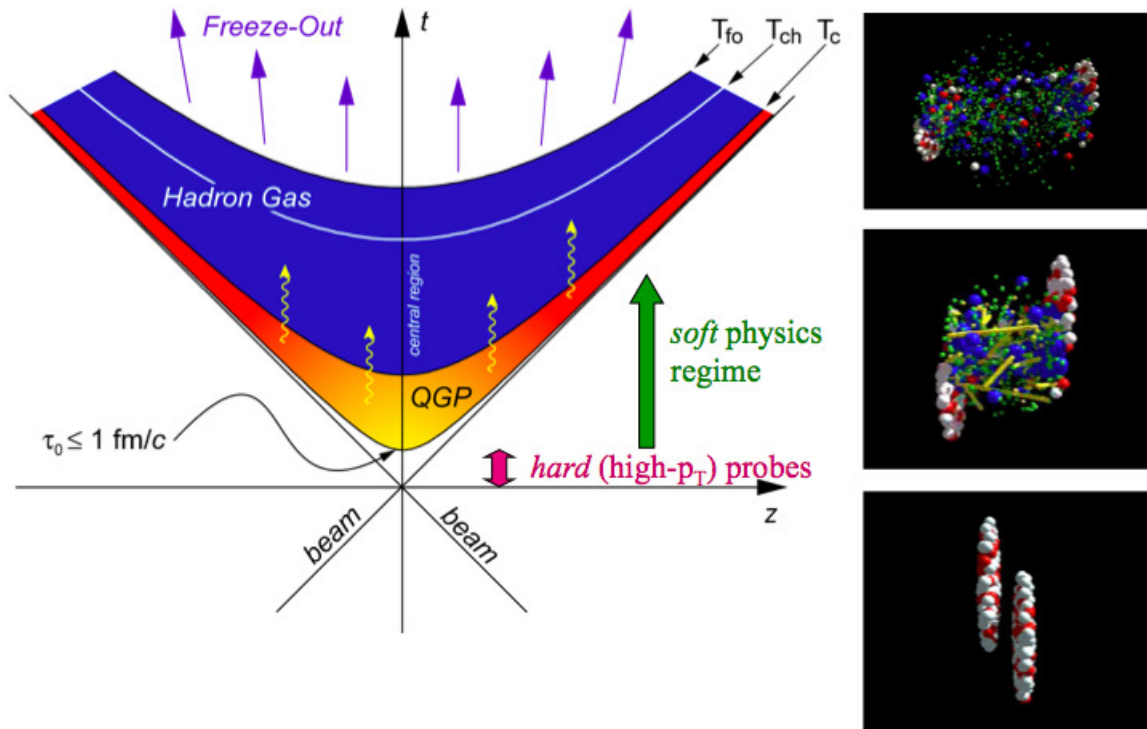


Figure 1.5: (Color online) The space-time evolution of a heavy-ion collision.

## 1.4.2 Kinematics of heavy ion collisions

At the RHIC, the coordinate system is such that the Z-axis is parallel to the collision axis (details will be shown in chapter 2). The nominal interaction point (IP) is at the (0, 0, 0)-coordinate. The beams are focused such that collisions take place around this point. Collisions do not always happen exactly at the IP. Thus the collision point also has to be measured, this is called the *primary vertex*.

### 1.4.2.1 Transverse momentum:

The total momentum is divided into two terms, a transverse momentum ( $p_T$ ), and a longitudinal momentum ( $p_z$ ). Transverse momentum is defined as:

$$p_T = \sqrt{p_x^2 + p_y^2}, \quad (1.2)$$

where  $p_x$  and  $p_y$  are the  $x$  and  $y$  components of total momentum ( $\mathbf{p}$ ). The transverse momentum has the advantage of being Lorentz invariant.

#### 1.4.2.2 Rapidity:

Actually  $p_z$  is rarely used by itself, rather it goes into defining the rapidity ( $y$ ) of a particle:

$$y = \frac{1}{2} \ln\left(\frac{E + p_z}{E - p_z}\right), \quad (1.3)$$

where  $E$  is the energy of the particle. Rapidity has the advantage of being additively invariant under Lorentz transformations, while  $p_z$  is not. In the non-relativistic limit,  $p \sim m$ , rapidity is equivalent to the velocity of the particle. Here  $m$  is the mass of the particle.

#### 1.4.2.3 Pseudo-rapidity:

Sometimes it is not possible to measure both energy and momentum. So experimentalists often use pseudo-rapidity ( $\eta$ ) for unidentified particles:

$$\eta = -\ln[\tan(\theta/2)], \quad (1.4)$$

where  $\tan(\theta) = \sqrt{x^2 + y^2}/z$ . Also  $\eta$  can be expressed in terms of  $y$  as:

$$\eta = \frac{1}{2} \ln\left[\frac{\sqrt{m_T^2 \cosh^2 y - m^2} + m_T \sinh y}{\sqrt{m_T^2 \cosh^2 y - m^2} - m_T \sinh y}\right]. \quad (1.5)$$

For massless particle, like photon, rapidity is equal to pseudo-rapidity.

#### 1.4.2.4 Multiplicity:

The multiplicity is defined as the number of particles produced in a single collision. In general the multiplicity will refer only to the number of charged particles and should really be called as the charged particle multiplicity.

#### 1.4.2.5 Invariant distribution:

The quantity  $E \frac{d^3\sigma}{dp^3}$ , invariant under Lorentz transformations, is called invariant cross section. In experiments, the invariant cross section is measured by using the equation

$$E \frac{d^3\sigma}{dp^3} = \frac{1}{L_{int}} E \frac{d^3N}{dp^3} = \frac{1}{L_{int} 2\pi p_T dp_T dy}, \quad (1.6)$$

where  $\sigma$  is the cross section,  $E$  is the energy and  $L_{int}$  is the integrated luminosity. Luminosity is defined as the number of particles per unit area per unit time times the opacity of the target.

#### 1.4.2.6 Collision centrality:

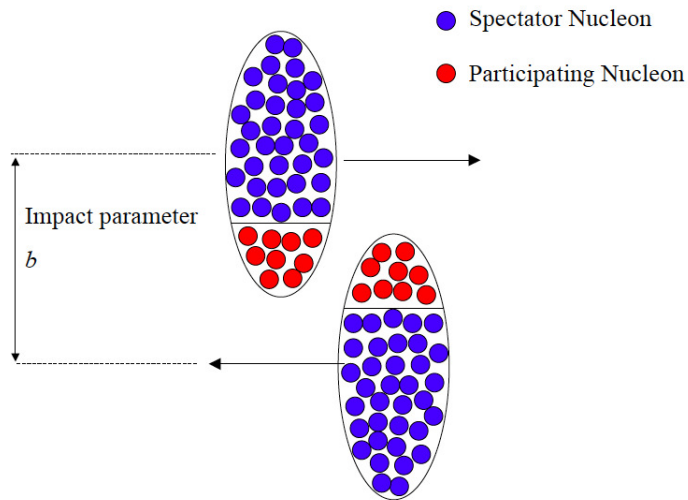


Figure 1.6: (Color online) A geometrical picture of the heavy ion collision.

Fig. 1.6 shows the geometry of a heavy-ion collision. The perpendicular distance  $\mathbf{b}$ , going from the centre of one nucleus to the centre of the other, is called impact parameter. It is a measurement of the overlap between the two colliding nuclei. The nucleons inside the overlap region is known as participant nucleons. The central

collisions are defined as having a small impact parameter thus a large amount of participating matter, peripheral collisions are defined as having a large impact parameter with a small amount of participating matter. As the impact parameter cannot be directly measured experimentally, the produced charged particle multiplicity is often used to characterize centrality. This can be done as one can assume that multiplicity is a monotonic function of the impact parameter. Higher values of multiplicity correspond to central collisions and lower values corresponds to peripheral collisions. The details of centrality determination technique will be discussed in chapter 3.

#### 1.4.2.7 Units and conversion factors:

In this thesis, all quantities are measured and expressed in terms of Natural units.

Quantity	Conversion	$\hbar = c = 1$ units
Mass	$1 \text{ kg} = 5.61 \times 10^{26} \text{ GeV}$	GeV
Length	$1 \text{ m} = 5.07 \times 10^{15} \text{ GeV}^{-1}$	$\text{GeV}^{-1}$
Time	$1 \text{ s} = 1.52 \times 10^{24} \text{ GeV}^{-1}$	$\text{GeV}^{-1}$

Table 1.1: Mass, length and time in terms of Natural units.

Some quantities often used in experimental heavy-ion physics are :

- $1 \text{ fm} = 10^{-15} \text{ m} = 5.07 \text{ GeV}^{-1}$
- $1 \text{ barn} = 10^{-28} \text{ m}^2$
- $\hbar c = 197 \text{ MeV fm}$

## 1.5 Experimental Observables

The medium created in the heavy-ion collision is very hot and dense and also extremely short-lived ( $\sim 5 - 10 \text{ fm}/c$ ). In experiments we only able to detect the freely streaming final state particles. Using these particles as probe we try to understand

the properties of the medium created in that collisions. In this section we will discuss few selected experimental observable at RHIC which can provide information about the properties of the medium created in heavy-ion collisions.

### 1.5.1 Hadron yields

At the *chemical freeze – out*, the inelastic collisions cease and the chemical abundances become fixed. So the measurement of particle yield will provide us information about the system at the *chemical freeze – out*. The  $p_T$  integrated particle yield ratios measured by the STAR experiment in Au+Au collisions at  $\sqrt{s_{NN}} = 200$  GeV is shown in Fig. 1.7 [12]. The horizontal bars are the statistical model fits to the particle ratios. There are mainly 3 parameters used in this model and their values are  $T_{ch} = 163 \pm 4$  MeV,  $\mu_B = 24 \pm 4$  MeV, and strangeness suppression factor ( $\gamma_s$ ) =  $0.99 \pm 0.07$ . The strangeness suppression factor is a measure of how far the system is from chemical equilibrium. The value of  $\gamma_s$  obtained from the statistical model fits is consistent with unity ( $0.99 \pm 0.07$ ) for most central collisions. This tells that the system created at RHIC is in chemical equilibrium. In this thesis we will be presenting the yields of  $\phi$ -mesons produced in Au+Au collisions at  $\sqrt{s_{NN}} = 7.7$  to 39 GeV.

At the *kinetic freeze – out*, the elastic collisions cease and the momentum distribution become fixed. So the measurement of particle transverse momentum distributions provide information about the system at the *kinetic freeze – out*. The particle spectra have been fitted with blast-wave model with fit parameters including the kinetic freeze-out temperature ( $T_{fo}$ ) and the mean collective expansion velocity ( $\langle\beta_T\rangle$ ). The results obtained by simultaneous fitting of  $\pi$ ,  $K$  and  $p$  spectra are shown in Fig. 1.8 [12]. For most central collision, the extracted  $\langle\beta_T\rangle$  is highest while  $T_{fo}$  is lowest, indicating that the system created in central collisions expands faster than peripheral collisions and freezes out at lower temperatures.



## 1.5.2 Jet quenching

A jet is a high  $p_T$  quark or gluon, which fragments into a number of highly correlated hadrons. Dihadron azimuthal correlations can be used to observe jets in high energy collisions. The idea is that if two jets are created near the fireball edge, one is emitted away from the fireball, while the other traverses the medium and appear on the other side. This is true in both  $p+p$  and  $d+Au$  collisions, but not in  $Au+Au$  collisions as illustrated in the Fig. 1.9. An example of a dihadron azimuthal correlation analysis

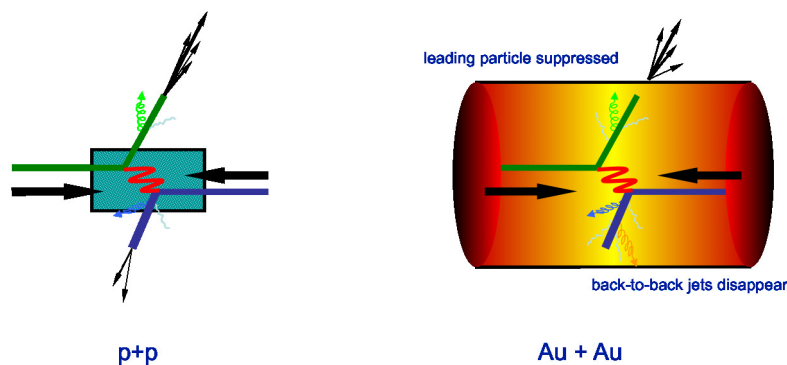


Figure 1.9: (Color online) Jets: Expectation from  $Au+Au$  and  $p+p$  collisions.

is shown in Fig. 1.10 [12]. The red points are from  $d+Au$  collisions, the black line is from  $p+p$  collisions and the blue points are from  $Au+Au$  collisions show a peak at  $\Delta\phi = 0$ , this is the near side jet, which is emitted away from the fireball. At  $\Delta\phi = \pi$ , only  $d+Au$  and  $p+p$  data shows a peak. This means the away side jet does not appear in  $Au+Au$  collisions. The theory is that the jet is completely quenched, i.e. it loses all its energy while traversing the medium. This has been considered as a signature of QGP at RHIC [12].

## 1.5.3 High $p_T$ probes

Bjorken first suggested that the QGP state should manifest itself by the suppression of the high momentum partons as they interact elastically with the medium [17]. It

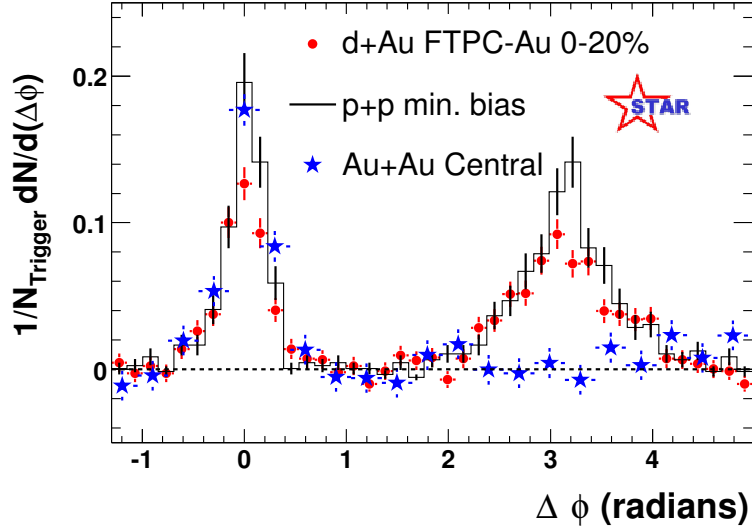


Figure 1.10: (Color online) Dihadron azimuthal correlations in Au+Au, d+Au and  $p+p$  collisions [12].

was then proposed that inelastic collisions would also lead to energy loss via gluon radiation [18, 19]. In relativistic nucleus-nucleus collisions, the main source of high momentum particle production is from scattered partons which fragment into hadron jets. In order to compare jet production rates in Au+Au and  $p+p$  (or d+Au) collisions, the  $R_{AA}$  is measured which is defined as follows:

$$R_{AA} = \frac{Yield_{A+A}/\langle N_{bin} \rangle}{Yield_{p+p}} \quad (1.7)$$

Where  $\langle N_{bin} \rangle$  is the average number of binary collisions.  $R_{AA}$  is known as a *Nuclear Modification Factor*. In addition to comparing to particle production in  $p+p$ , comparison can be made of the yields in central nucleus-nucleus collisions to those in peripheral collisions to quantify the differences between the systems created in collisions with different centralities:

$$R_{CP} = \frac{Yield_{central}}{Yield_{peripheral}} \times \frac{\langle N_{bin} \rangle_{peripheral}}{\langle N_{bin} \rangle_{central}} \quad (1.8)$$

The  $R_{AA}$  and  $R_{CP}$  measured at top RHIC energy is shown in Fig. 1.11 and Fig. 1.12 respectively [12, 11]. For nucleus nucleus collisions, the hadrons produced from hard

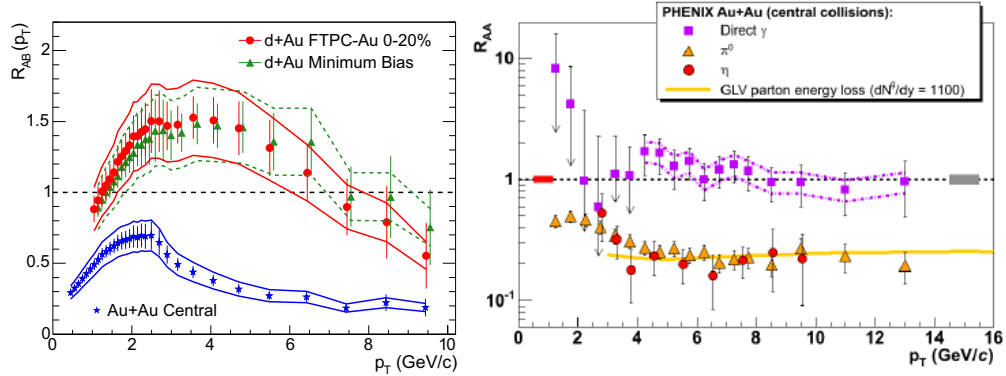


Figure 1.11: (Color online) Left panel:  $R_{AA}$  (also known as  $R_{AB}$ ) measured in central Au+Au and d+Au collisions with  $\sqrt{s_{NN}} = 200$  GeV for charged hadrons. Right panel:  $R_{AA}$  measured in central Au+Au at  $\sqrt{s_{NN}} = 200$  GeV for  $\eta$ ,  $\pi^0$  and photons. The grey error band reflects the uncertainty in the number of binary collisions for central Au+Au collisions [12].

processes are expected to scale with the number of binary collisions if there is no medium effects. In this case nucleus nucleus collisions is just simple superposition of nucleon nucleon collisions and  $R_{AA}$  will be equal to unity. The RHIC experiments report values for the nuclear modification factor below 1 for charged and identified hadrons for Au+Au collisions. This means that for intermediate to high  $p_T$  there is a suppression of particle production in central and mid-central Au+Au collisions compared to d+Au (or  $p+p$ ) collisions and in central Au+Au compared to peripheral Au+Au collisions. This suppression has been attributed to energy loss of high- $p_T$  partons in the dense medium created in central collisions. Moreover, for d+Au collisions where the QGP is not expected to form, an enhancement is observed. The enhancement is commonly attributed to the Cronin effect. The right panel of Fig 1.11 shows the  $R_{AA}$  of  $\eta$ ,  $\pi^0$  and photons in Au+Au central collisions. One can see that high  $p_T$  hadron ( $\eta$  and  $\pi^0$ ) production are suppressed but production of photons, which do not participate in strong interactions, is not suppressed. This again indicates the

effect of strong interactions in the hot and dense medium on the hadrons production in Au+Au collisions.

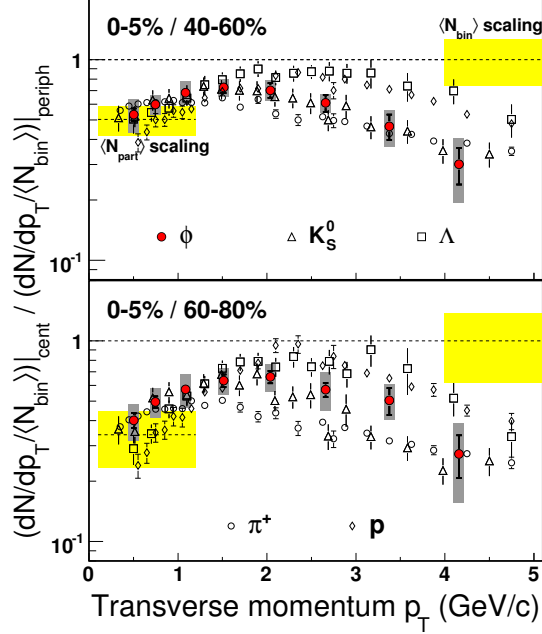


Figure 1.12: (Color online)  $R_{CP}$  of identified hadrons at mid-rapidity in Au+Au collisions at  $\sqrt{s_{NN}} = 200$  GeV. The shaded bands represent the uncertainties in the Glauber model calculations for  $\langle N_{bin} \rangle$  and  $\langle N_{part} \rangle$  [11].

From Fig. 1.12 one can see that at intermediate  $p_T$  the  $R_{CP}$  shows particle-type dependence. The mesons and baryons seem to follow different trends from each other as a function of  $p_T$ . This can be explained by considering particle production via recombination or coalescence of quarks [21, 22]. For 0 – 5%/60 – 80%, the  $R_{CP}$  of  $\phi$  sits between that for the  $K_S^0$  and the  $\Lambda$ . This may be attributed to the shape change of the  $\phi$  spectra from exponential at 40 – 60% centrality to Levy at 60 – 80%, which may be due to the change of the  $\phi$  production mechanism at intermediate  $p_T$  in different environments with different degrees of strangeness equilibration. In this thesis we will discuss the nuclear modification factor for  $\phi$  mesons produced in Au+Au collisions at  $\sqrt{s_{NN}} = 7.7, 11.5, 19.6, 27$  and  $39$  GeV.

### 1.5.4 Strangeness enhancement

Strange particle production is one of the observables expected to deliver detailed information on the reaction dynamics of relativistic nucleus-nucleus collisions [23]. In experiments at the CERN SPS accelerator it was found that the ratio of the number of produced kaons to that of pions is higher by a factor of about two compared to that in proton-proton reactions at the same energy [24, 25, 26, 27]. In the past, several possible reasons for this strangeness enhancement have been discussed. Firstly, if nucleus-nucleus reactions proceed through a de-confined stage, then strange-quark production should be abundant [28]. Alternative ideas of Canonical suppression of strangeness in small systems (proton-proton) as a source of strangeness enhancement in high energy nucleus-nucleus collisions have been proposed [29]. But  $\phi(s\bar{s})$  mesons due to its zero net strangeness is not subjected to Canonical suppression effects. Therefore measurements of  $\phi$  mesons in both nucleus-nucleus and proton-proton would give the answer for observed strangeness enhancement.

Figure 1.13 shows the ratio of strange hadron yields normalized to  $\langle N_{part} \rangle$  in nucleus-nucleus collisions relative to corresponding yields from proton-proton collisions as a function of  $\langle N_{part} \rangle$  at 62.4 and 200 GeV [8]. Enhancement of  $\phi$  ( $s\bar{s}$ ) production in Cu+Cu and Au+Au relative to  $p+p$  collisions clearly indicate the formation of a dense partonic medium in these collisions.

### 1.5.5 Particle ratio

Figure 1.14 shows the  $\phi/K^-$  ratio as function of number of participants and centre-of-mass energies [7]. The mechanism for  $\phi$ -meson production in high energy collisions has remained an open issue. In an environment with many strange quarks,  $\phi$  mesons can be produced readily through coalescence, bypassing the Okubo-Zweig-Iizuka (OZI) rule [32]. On the other hand, a naive interpretation of  $\phi$  meson production in heavy-ion collisions would be the  $\phi$  production via kaon coalescence. Models that include hadronic rescatterings such as RQMD and UrQMD [23] have predicted an increase of the  $\phi/K^-$  ratio at mid-rapidity as a function centrality [7]. This prediction was

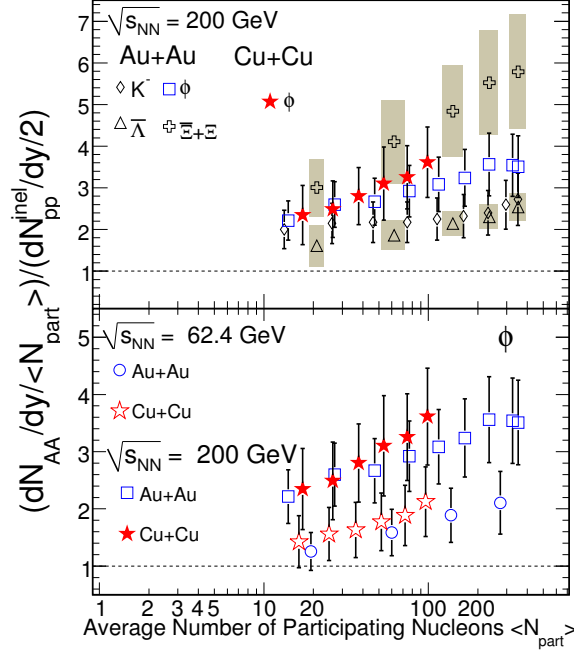


Figure 1.13: (Color online) The ratio of the yields of  $K^-$ ,  $\phi$ ,  $\bar{\Lambda}$ , and  $\Xi + \bar{\Xi}$  normalized to  $\langle N_{part} \rangle$  nucleus-nucleus collisions to corresponding yields in inelastic proton-proton collisions as a function of  $\langle N_{part} \rangle$  at 62.4 and 200 GeV [8].

disproved from experimental data in Au+Au collisions at  $\sqrt{s_{NN}} = 200$  GeV. It is clear from Fig. 1.14 that  $\phi/K^-$  is independent of centrality and also centre-of-mass energy. This measurements effectively rule out kaon coalescence as the dominant production mechanism for the  $\phi$  meson.

The production mechanism of multi-strange particle (e.g  $\phi$  and  $\Omega$ ) are predicted to be very sensitive to the early phase of nuclear collisions [34]. Therefore the ratio  $\Omega/\phi$  is expected to reflect the information about the early system created in the nucleus-nucleus collision [35]. In Fig. 1.15, the ratios of  $\Omega/\phi$  versus  $p_T$  are presented for different centralities [7]. Various theoretical predictions for the ratio  $\Omega/\phi$  are shown in the figure by different curves [35]. Experimental data can be well described by the model prediction by Hwa and Yang where they assume  $\phi$  and  $\Omega$  production via

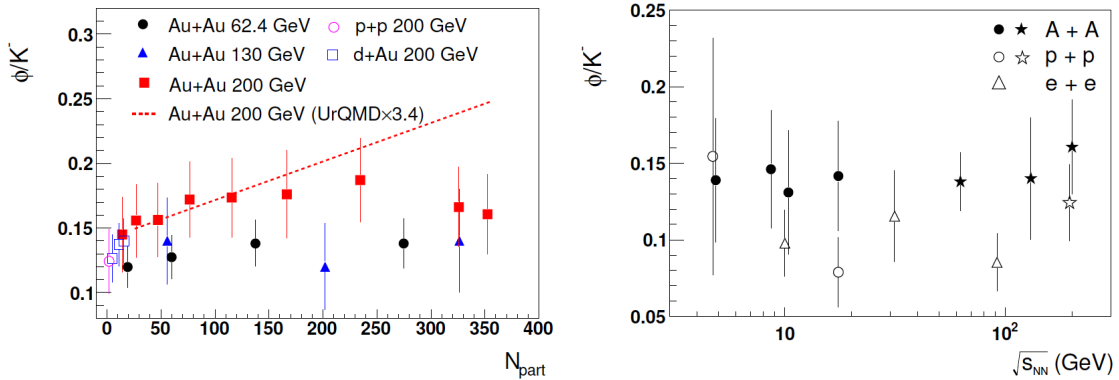


Figure 1.14: (Color online) Left panel:  $\phi/K^-$  ratio as a function number of participants. Right panel:  $\phi/K^-$  ratio as a function of centre-of-mass energies [7].

thermal  $s$  quarks in the medium. This may suggest that the production of  $\phi$  and  $\Omega$  at RHIC are via strange quarks coalescence and could be consider as signature of de-confinement matter produced in Au+Au collisions at  $\sqrt{s_{NN}} = 200$  GeV. In this thesis we will discuss the ratio of yields of  $\Omega$  baryon to  $\phi$  mesons as a function of  $p_T$  for Au+Au collisions at  $\sqrt{s_{NN}} = 7.7, 11.5, 19.6, 27,$  and  $39$  GeV.

### 1.5.6 Elliptic flow : A collective phenomena

In non-central nucleus nucleus collisions, the overlapping area is not spatially isotropic. This initial spatial anisotropy is then transformed into momentum anisotropy because of pressure gradient developed due to the subsequent interactions among the constituents. The elliptic flow ( $v_2$ ) is a measure of the anisotropy in momentum space [36]. For a nucleus-nucleus collision, the azimuthal distribution of produced particles can be described in terms of a Fourier series:

$$\frac{dN}{d\phi} \propto 1 + 2v_1 \cos((\phi - \Psi)) + 2v_2 \cos(2(\phi - \Psi)) + \dots \quad (1.9)$$

The second Fourier coefficient,  $v_2$ , is a known elliptic flow and can be defined as  $v_2 = \langle \cos(2(\phi - \Psi)) \rangle$  [17]. Where  $\phi$  is the azimuthal angle of the emitted particle and  $\Psi$  is the reaction plane angle. The reaction plane is defined as the plane described by

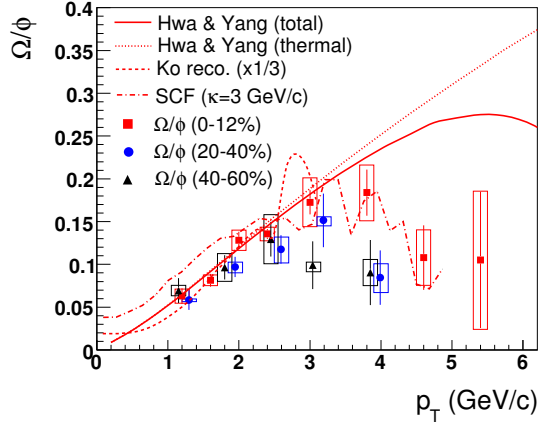


Figure 1.15: (Color online)  $\Omega/\phi$  as a function of  $p_T$  in Au+Au collision at  $\sqrt{s_{NN}} = 200$  GeV [7].

the vector between the centres of the colliding nuclei and the direction of the beam ( $Z$ ) axis. The angle between reaction plane and  $X$ -axis is known as reaction plane angle.

The elliptic flow has been measured in heavy ion collisions for a long time and results for identified particles from Au+Au collisions  $\sqrt{s_{NN}} = 200$  GeV measured by RHIC experiments are presented in Fig. 1.17 [38]. A characteristic of the hydrodynamic expansion is that the elliptic flow will vary for particles of different mass (smaller flow for heavier particles). This is seen in the data at low  $p_T$  as shown in Fig. 1.17, although the mass splitting is not necessarily of the exact magnitude suggested by hydrodynamics. A particle type (baryon versus meson) difference in  $v_2(p_T)$  was observed for identified hadrons ( $\pi$ ,  $p$ ,  $K_S^0$ ,  $\Lambda$ ) at the intermediate  $p_T$ . This particle type dependence of the  $v_2(p_T)$  can be explained by assuming hadronization via quark coalescence or recombination [21, 22]. In this thesis we will discuss in detail the mass ordering at low  $p_T$  using produced protons and  $\phi$  mesons in Au+Au collisions at  $\sqrt{s_{NN}} = 200$  GeV.

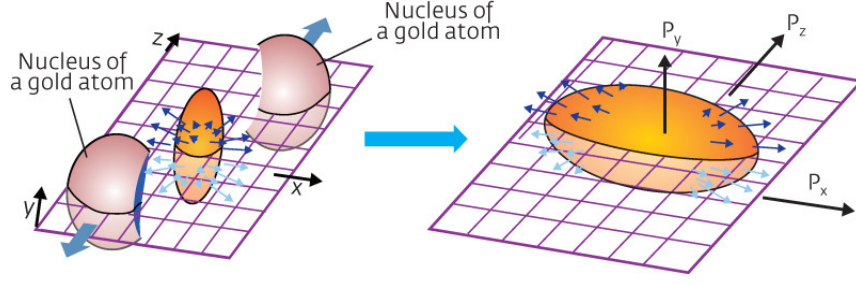


Figure 1.16: (Color online) Schematic views of a non-central nucleus-nucleus collision.

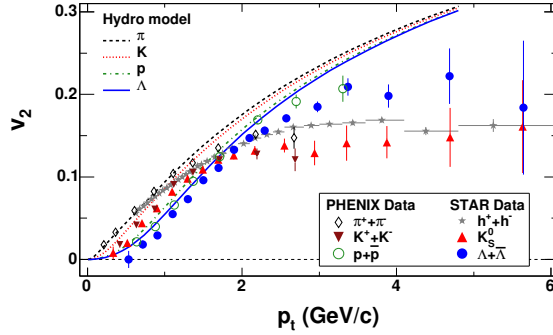


Figure 1.17: (Color online) Measurements of  $v_2(p_T)$  for identified particles for 0–80% centrality at RHIC. The lines are the results from hydrodynamic model calculation [38].

### 1.5.6.1 Number-of-constituent quark scaling:

At intermediate  $p_T$  the measured  $v_2$  values for identified particles appears to saturate as shown in Fig. 1.17. The  $v_2(p_T)$  shows a distinct grouping among the baryons and among the mesons. Now, if the  $v_2(p_T)$  values are divided by the number-of-constituent quarks ( $n_q$ ) a scaling has been observed for  $p_T/n_q > 1.0$  GeV/ $c$  as can be seen in Fig. 1.18 [39]. This is called number-of-constituent quark (NCQ) scaling [11, 21, 22]. In Fig. 1.18, left panel shows  $v_2/n_q$  as function of  $p_T/n_q$  and right panel shows  $v_2/n_q$  as function of  $(m_T - m_0)/n_q$ . Where  $m_T$  is transverse mass and  $m_0$  is the rest mass of

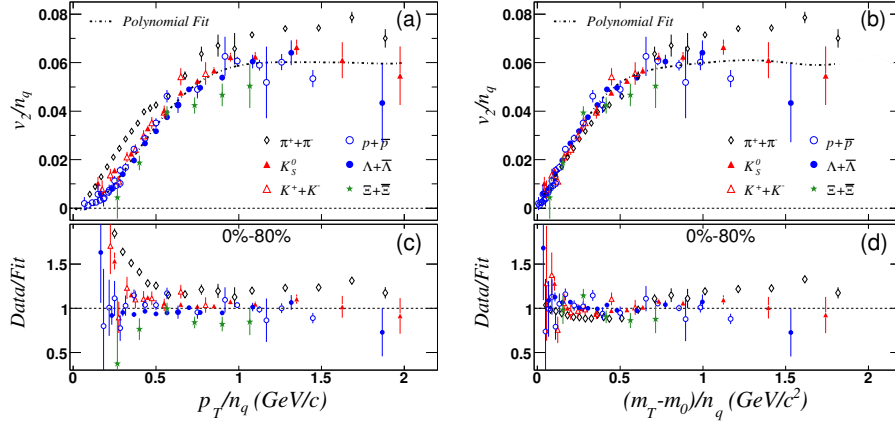


Figure 1.18: (Color online) The  $v_2$  scaled by number-of-constituent quarks ( $n_q$ ) as a function of  $p_T/n_q$  and  $(m_T - m_0)/n_q$  for identified hadrons in Au+Au collisions at  $\sqrt{s_{NN}} = 200$  GeV [39].

the hadron. The motivation of plotting  $v_2/n_q$  against  $(m_T - m_0)/n_q$  is just to remove difference in  $v_2$  due to mass effect and in this case scaling is observed for all  $p_T$ . The dash-dotted lines in the Fig. 1.18 are the polynomial fit to the data which is used as the denominator in the ratios shown in the bottom panels. The bottom panels show that the  $v_2$  for the identified particles scales with the number of constituent quarks since all the ratios (except the pions) fall on a common line. The large resonance decay contribution to pion production has been suggested as a possible explanation for their apparent violation. The quark recombination or coalescence models assume that the constituent quarks carry its  $v_2$  by themselves, before they start to form hadrons. After that the hadron  $v_2$  is developed by recombining constituent quarks into hadrons. The NCQ scaling can be explained by quark recombination or coalescence models [21, 22]. This indicates that that the system has been in the de-confined state prior to hadronization. In this thesis we will present results of  $\phi$  meson  $v_2$  viz-a-viz NCQ scaling for Au+Au collisions at  $\sqrt{s_{NN}} = 7.7, 11.5, 19.6, 27, 39, 62.4$  and 200 GeV.

### 1.5.6.2 $p_T$ integrated $v_2$ :

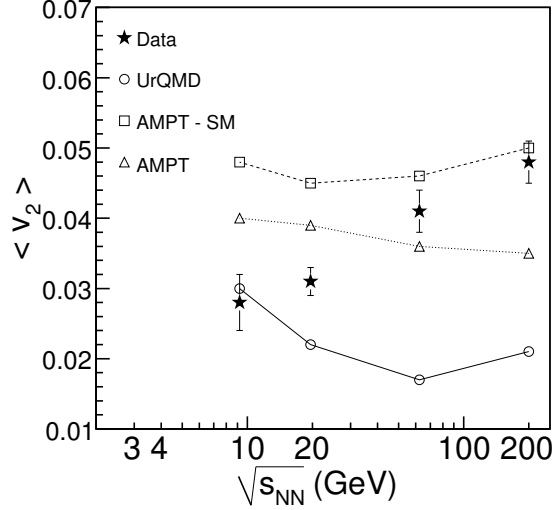


Figure 1.19:  $\langle v_2 \rangle$  for charged particles at mid-rapidity for minimum bias collisions at  $\sqrt{s_{NN}} = 9.2, 19.6, 62.4$  and  $200$  GeV [15, 37, 38] compared to corresponding results from AMPT and UrQMD model calculations [37].

Figure 1.19 shows the  $p_T$  integrated  $\langle v_2 \rangle$  for charged particles at mid-rapidity for various  $\sqrt{s_{NN}}$  for minimum bias (0-80%) collisions [15, 37]. The results for  $\sqrt{s_{NN}} = 9.2$  GeV are for minimum bias 0-60% collisions [38]. The  $\langle v_2 \rangle$  value increases linearly from about 3% at 9.2 GeV to about 5% at 200 GeV. The experimental data are compared to  $\langle v_2 \rangle$  calculated from UrQMD, AMPT and AMPT-SM with default settings [23, 22]. The centrality selection is same for data and the models. In contrast to observations from the data, the model  $\langle v_2 \rangle$  values either remain constant or decreases slightly with increasing  $\sqrt{s_{NN}}$ . The  $\langle v_2 \rangle$  value from UrQMD at 9.2 GeV and those from AMPT-SM at 200 GeV are in good agreement with the data. The  $\langle v_2 \rangle$  values from AMPT lie intermediate to those from UrQMD and AMPT-SM. If we assume the  $\langle v_2 \rangle$  values from UrQMD to be the contribution from hadronic phase, then this contribution ( $v_2^{UrQMD}/v_2^{data}$ ) varies from 100% to about 40% of the measured  $\langle v_2 \rangle$  as beam energy

increases from 9.2 GeV to 200 GeV. The higher values of  $\langle v_2 \rangle$  in data indicate the possible contribution that can come in such transport models due to inclusion of initial/final state scattering effects and/or due to partonic interactions. Comparison with AMPT-SM reflects that at 62.4 and 200 GeV, the  $\langle v_2 \rangle$  has contributions from partonic interactions. In this thesis a similar study will be carried out using the  $\langle v_2 \rangle$  of  $\phi$  mesons.

## 1.6 Thesis Motivation

### 1.6.1 Measurement of inclusive charged hadrons $v_2$

One of the main goals of the STAR experiment at RHIC is to study the properties of the QCD matter at extremely high energy and parton densities, created in the heavy-ion collisions [12]. Recently RHIC has undertaken a Beam Energy Scan (BES) program to look for changes in observation of various measurements as a function of beam energy to study the QCD phase structures. The BES program at RHIC allows to study elliptic flow at different baryonic chemical potential ( $\mu_B$ ) from 20 to about 400 MeV [44]. Lattice QCD calculations suggest that the quark-hadron transition is cross-over at small  $\mu_B$  or high  $\sqrt{s_{NN}}$  and other QCD based model calculations suggest that at higher  $\mu_B$  or lower  $\sqrt{s_{NN}}$  the transition is expected to be first order [45]. According to the reference [46], a non-monotonic behavior of  $v_2$  could be observed around the “softest point of the EOS”. Measurement of  $v_2$  as function of  $\sqrt{s_{NN}}$  and collision centrality could be used to search for the softest point of the EOS in the heavy ion collisions. In addition the  $v_2$  measurement using several methods would be helpful to understand non-flow contributions and flow fluctuations. In this thesis the measurement of inclusive charged hadron  $v_2$  using several methods in Au+Au collisions at  $\sqrt{s_{NN}}= 7.7, 11.5, 19.6, 27, 39, 62.4$  and 200 GeV will be presented. Transverse momentum, collision centrality and beam energy dependence of charged particle  $v_2$  will be discussed in chapter 5 of the thesis. A comparison with transport model calculations will be shown.

## 1.6.2 Measurement of $\phi$ -meson invariant yield and elliptic flow

The  $\phi$  vector meson is the lightest bound state of  $s$  and  $\bar{s}$  quarks. The interaction cross-section of the  $\phi$  meson with non-strange hadrons is expected to have a small value [12] and therefore its production should be less affected by the later stage hadronic interactions in the evolution of the system formed in heavy-ion collisions. The  $\phi$  meson seems to freeze out early compared to other light hadrons ( $\pi$ ,  $K$  and  $p$ ) [12]. The life time of the  $\phi$  meson is  $\sim 42$  fm/ $c$ . Because of longer life time the  $\phi$  meson will mostly decay outside the fireball and therefore its daughters will not have much time to re-scatter in the hadronic phase. The elliptic flow, a measure of the anisotropy in momentum space, for  $\phi$  meson can be used to probe the dynamics of the early stage of heavy-ion collisions [7]. For the  $\phi$ -meson  $v_2$ , effect of later stage hadronic interaction is small [16, 21]. Therefore, the  $\phi$  meson can be considered as a clean probe to study the QCD phase diagram in the Beam Energy Scan (BES) program at RHIC [50]. In this thesis energy dependence of  $\phi$ -meson invariant yield and elliptic flow in Au+Au collisions at  $\sqrt{s_{NN}} = 7.7, 11.5, 19.6, 27, 39, 62.4$  and 200 GeV will be presented in chapters 3 and 4.

## 1.6.3 Measurement of multi-strange hadrons $v_2$

The observed NCQ scaling of identified hadrons in experimental data can be well described by parton recombination or coalescence model [11, 21, 22]. Such scaling indicates that collective elliptic flow has been developed at the partonic phase. It has been already found by the previous measurements that  $\pi$ ,  $K$ ,  $p$ ,  $K_S^0$ ,  $\Lambda$ ,  $\Xi$  and  $\phi$  follows NCQ scaling fairly well at top RHIC energy [11]. The large statistics data collected by STAR detectors in the year of 2010 allows us to measure elliptic flow of multi-strange hadrons, especially the  $\phi$ -meson, consist of one strange and one anti-strange constituents quark, and  $\Omega$  baryon that made of pure strange or anti-strange constituents quarks. Because of their large mass and small hadronic interaction cross-section, the multi-strange hadrons are expected to be less sensitive to the late stage

hadronic re-scattering. In addition, a fit of the  $m_T$  spectra to a hydrodynamically inspired Blast Wave model suggests that the multi-strange hadrons freeze-out at a higher temperature, which is closer to the chemical freeze-out temperature, and with a smaller radial flow than the other lighter hadrons [34, 12, 13, 14, 15]. Therefore elliptic flow of multi-strange hadrons are good probes for the partonic phase of the system evolution. A systematic measurements of multi-strange hadrons  $v_2$  in Au+Au collisions at  $\sqrt{s_{NN}}= 200$  GeV will be presented in the chapter 6.

# Bibliography

- [1] S. L. Glashow, Nucl. Phys. **22**, 579 (1961).
- [2] A. Salam and J.C. Ward, Phys. Lett. **13**, 168 (1964).
- [3] S. Weinberg, Phys. Rev. Lett. **19**, 1264 (1967).
- [4] *Introduction to elementary particles* - by David Griffiths.
- [5] P. W. Higgs, Phys. Lett. **12**, 132 (1964);  
P. W. Higgs, Phys. Rev. Lett. **13**, 508 (1964).
- [6] F. Englert and R. Brout, Phys. Rev. Lett. **13**, 321 (1964).
- [7] G. Aad *et al.* (ATLAS Collaboration), Phys. Lett **B 716**, 1 (2012).
- [8] W. Adam *et al.* (CMS Collaboration), Phys. Lett **B 716**, 30 (2012).
- [9] S. Bethke, Prog. Part. Nucl. Phys. **58**, 351 (2007).
- [10] K. G. Wilson, Phys. Rev. **D 10**, 2445 (1974).
- [11] G. Baym, Nucl. Phys. **A 698**, XXIII (2002).
- [12] J. Adams *et al.* (STAR Collaboration), Nucl. Phys. **A 757**,102 (2005).
- [13] F. Karsch, Nucl. Phys. **A 698**, 199 (2002).
- [14] R. V. Gavai and S. Gupta, Phys. Rev. **D 71**, 114014 (2005).
- [15] Z. Fodor, Nucl. Phys. **A 715**, 319 (2003).

- [16] B. Mohanty, New Journal of Physics **13**, 065031 (2011).
- [17] J. D. Bjorken. Energy loss of energetic partons in quark-gluon plasma: Possible extinction of high momentum jets in hadron - hadron collisions. FERMILAB-PUB-82-059-THY.
- [18] R. Baier *et al.* Nucl. Phys. **B 483**, 291 (1997).
- [19] M. Gyulassy and M. Plumer, Phys. Lett. **B 243**, 432 (1990).
- [20] B. I. Abelev *et al.* (STAR Collaboration), Phys. Rev. Lett. **99**, 112301 (2007).
- [21] D. Molnar and S. A. Voloshin, Phys. Rev. Lett. **91**, 092301 (2003).
- [22] R. J. Fries *et al.* Phys. Rev. Lett. **90**, 202303 (2003).
- [23] P. Koch *et al.* Phys. Rep. **142**, 167 (1986).
- [24] T. Alber *et al.* (NA49 Collaboration), Z. Phys. **C 64**, 195 (1994).
- [25] P.G. Jones (for the NA49 Collaboration), Nucl. Phys. **A 610**, 188c (1996).
- [26] F. Sikler (for the NA49 Collaboration), Nucl. Phys. **A 611**, 45c (1996).
- [27] C. Hohne (for the NA49 Collaboration), Nucl. Phys. **A 611**, 485c (1996).
- [28] J. Rafelski and B. Muller, Phys. Rev. Lett. **48**, 1066 (1982).
- [29] K. Redlich and A. Tounsi, Eur. Phys. J. **C 24**, 589 (2002).
- [30] B.I. Abelev *et al.* (STAR Collaboration), Physics Letters **B 673**, 183 (2009).
- [31] B. I. Abelev *et al.* (STAR Collaboration), Phys. Rev. **C 49**, 064903 (2009).
- [32] N. Isgur and H. B. Thacker, Phys. Rev. **D 64**, 094507 (2001).
- [33] S. A. Bass *et al.* Prog. Part. Nucl. Phys. **41** 255 (1998);  
M. Bleicher *et al.* J. Phys. **G 25** 1859 (1999).
- [34] J. Adams *et al.* (STAR Collaboration), Phys. Rev. Lett. **92**, 182301 (2004).

- [35] R.C. Hwa and C.B. Yang, Phys. Rev. **C 75**, 054904 (2007).
- [36] J. Y. Ollitrault, Phys. Rev. **D 46**, 229 (1992);  
P. Huovinen *et al.* Phys. Lett. **B 503**, 58 (2001).
- [37] A. M. Poskanzer and S. A. Voloshin, Phys. Rev. **C 58**, 1671 (1998).
- [38] J. Adams *et al.* (STAR Collaboration), Phys. Rev. **C 72**, 014904 (2005).
- [39] B. I. Abelev *et al.* (STAR Collaboration), Phys. Rev. **C 75**, 054906 (2007).
- [40] J. Adams *et al.* ( STAR Collaboration), Phys. Rev. **C 72**, 014904 (2005);  
B. I. Abelev *et al.* ( STAR Collaboration), Phys. Rev. **C 75**, 054906 (2007);  
B. I. Abelev *et al.* ( STAR Collaboration), Phys. Rev. **C 77**, 054901 (2007).
- [41] Md. Nasim *et al.* Phys. Rev. **C 82**, 054908 (2010).
- [42] B. I. Abelev *et al.* (STAR Collaboration), Phys. Rev. **C 81**, 024911 (2010).
- [43] Zi-Wei Lin and C. M. Ko, Phys. Rev. **C 65**, 034904 (2002);  
Zi-Wei Lin *et al.* Phys. Rev. **C 72**, 064901 (2005);  
Lie-Wen Chen *et al.* Phys. Lett. **B 605**, 95 (2005).
- [44] J. Cleymans *et al.* Phys. Rev. **C 73**, 034905 (2006).
- [45] Y. Aoki *et al.* Nature **443**, 675 (2006).
- [46] P. F. Kolb *et al.* Phys. Rev. **C 62**, 054909 (2000).
- [47] P.F. Kolb *et al.* Nucl. Phys. **A715**, 653c (2003).
- [48] B. Mohanty and N. Xu, J. Phys. **G 36**, 064022 (2009).
- [49] Md. Nasim, B. Mohanty and N. Xu, Phys. Rev. **C 87**, 014903 (2013).
- [50] B. I. Abelev *et al.* (STAR Collaboration), STAR Internal Note -SN0493 (2009).
- [51] C. Adler *et al.* (STAR Collaboration), Phys. Rev. Lett. **89**, 092301 (2002).
- [52] J. Adams *et al.* (STAR Collaboration), Phys. Lett. **B 595**, 143 (2004).

- [53] J. Adams *et al.* (STAR Collaboration), Phys. Rev. **C 70**, 041901 (2004).
- [54] J. Adams *et al.* (STAR Collaboration), Phys. Lett. **B 612**, 181 (2005).

# Chapter 2

## Experimental Facilities at RHIC

After its first successful experimental operation in the year of 2000, the Relativistic Heavy Ion Collider (RHIC) has now been collecting data for 13 years. It is the first dedicated machine which can collide heavy ion beams at relativistic energies [1]. It is situated at Brookhaven National Laboratory, Upton, USA. Initially RHIC was designed for  $p+p$  collisions at  $\sqrt{s}= 500$  GeV and Au+Au at  $\sqrt{s_{NN}}= 200$  GeV. But in last decades, the collisions of gold, copper and uranium nuclei in the energy range  $\sqrt{s_{NN}}= 7.7 - 200$  GeV have been investigated to study the formation of the quark-gluon plasma. In addition to heavy-ion programme, RHIC was designed to run polarized  $p+p$  collisions as part of the spin physics programme with the aim of studying the spin structure of the nucleon. Figure 2.1 gives the brief information about luminosities and running period for the heavy-ion and polarized  $p+p$  collisions at RHIC.

A layout of RHIC is shown in Fig. 2.2. A brief description of the operations is as follows [2]. In heavy-ion mode, at first negatively charged ions are used as source in the Tandem Van de Graaff and the electrons are stripped from negatively charged ions. After that the ions are accelerated to an energy of 1 MeV per nucleon, and then travel towards the Booster. Ions are stripped again and accelerated further to

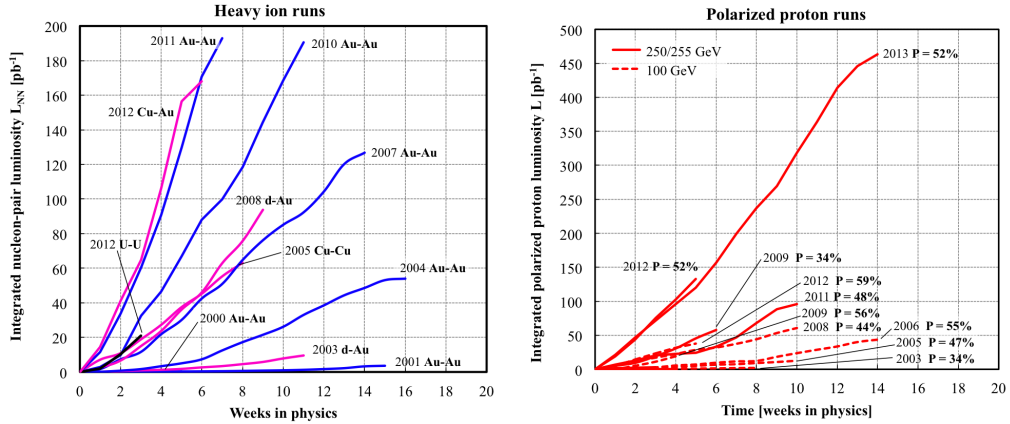


Figure 2.1: (Color online) Summary of RHIC Runs [1]. The nucleon-pair luminosity is defined as  $L_{NN} = A_1 A_2 L$ , where  $L$  is the luminosity, and  $A_1$  and  $A_2$  are the number of nucleons of the ions in the two beam respectively.

an energy 95 MeV per nucleon, and move towards the Alternating Gradient Synchrotron(AGS). In the AGS, the ions are fully stripped then the ions are bunched and accelerated to the RHIC injection energy of 10.8 GeV per nucleon. Finally ions are then transferred to RHIC via the AGS-to-RHIC Beam Transfer Line.

The Relativistic Heavy Ion Collider consists of two independent rings of superconducting magnets which bend and focus the ion beams. The RHIC rings have six interaction points, and four of these interaction points have been occupied by heavy ion experiments: BRAHMS detectors [3] located at 2 o'clock position, STAR detectors [4] located at 6 o'clock position, PHENIX detectors [5] located at 8 o'clock position and PHOBOS detectors [6] located at 10 o'clock position. Currently only STAR and PHENIX detectors are in an operational mode.

## 2.1 Solenoidal Tracker At RHIC (STAR)

All the results presented in this thesis are based on data collected using the STAR detector. STAR consist of a several detectors designed to measure different observ-

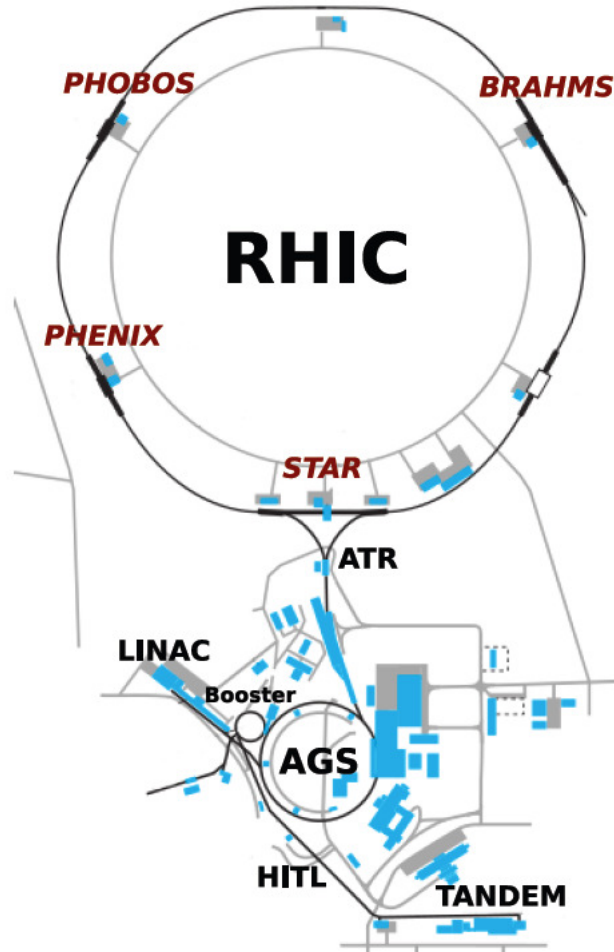


Figure 2.2: (Color online) A layout of RHIC.

ables as shown in Fig 2.3 and Fig 2.4. In the STAR coordinate system, Z-axis is along the beam direction as shown Fig. 2.5. The field from the STAR magnet which is applied in the z direction, bends the trajectories of charged particles enabling momentum measurements. STAR magnet can be maintained at magnetic fields of 0,  $\pm 0.25$  or  $\pm 0.5$  Tesla. The data are presented in this thesis were collected in  $\pm 0.5$  Tesla magnetic field. The Time Projection Chamber (TPC), is the main tracking detector and is capable of measuring charged particles within  $|\eta| < 1.8$  and full azimuthal coverage in the xy plane [7]. In 2010, a barrel Time-of-Flight (TOF) detector based on Multi-gap Resistive Plate Chamber (MRPC) technique was fully installed

in STAR [8]. The TOF consists of a total of 120 trays spanning a pseudo-rapidity range  $|\eta| < 0.9$  with full azimuth coverage. The trigger system of the TOF detector is the two upgraded Pseudo Vertex Position Detectors (VPDs), each staying 5.7 m away from the TPC center along the beam line. They provide the start timing information for TOF detectors. A Barrel Electromagnetic Calorimeters (BEMC) [9] and an Endcap Electromagnetic calorimeter (EEMC) [10] are used to measure the transverse energy deposited by electrons and photons. The full Barrel Electromagnetic Calorimeter (BEMC) covers  $|\eta| < 1.0$  and Endcap Electromagnetic Calorimeter (EEMC) covers  $1 < \eta < 2$ . Both BEMC and EEMC are azimuthally symmetric. There are two Forward Time Projection Chamber detectors (FTPCs) [11] with  $2.5 < \eta < 4.0$  and complete azimuthal coverage in the xy plane. The FTPCs extend STARs tracking capabilities in the forward and backward  $\eta$  direction. Two Zero-Degree Calorimeters (ZDCs), two Beam Beam Counters (BBCs) and two upgraded Pseudo Vertex Position Detectors (VPDs) are used for event triggering [1]. Photon Multiplicity Detector (PMD) [13] use to measure photon multiplicity at forward rapidity. The PMD covers a pseudo-rapidity range  $-3.7 < \eta < -2.3$  with full azimuthal coverage.

The TPC, and the TOF are the main detectors used in the analysis presented in this thesis, therefore we will only discuss these two detectors including trigger system in detail in the next section.

### 2.1.1 Time projection chamber

The Time Projection Chamber (TPC) [7] is the primary tracking device of STAR. It is also used to identify charged particles through measurements of their ionization energy loss ( $dE/dx$ ) as they traverse through the gas volume of the TPC. The schematic diagram of TPC is shown in Fig 2.6. Its acceptance covers  $\pm 1.8$  units of pseudo-rapidity with full azimuthal angle. It is 4.2 m long, 4 m in diameter, filled with P10 gas (90% Ar and 10%  $\text{CH}_4$ ) and divided into two drift chambers by central membrane, and with a uniform electric field of 135 V/m. It is surrounded by a uniform magnetic field in the z direction. Charged particles traversing the TPC will follow a curved

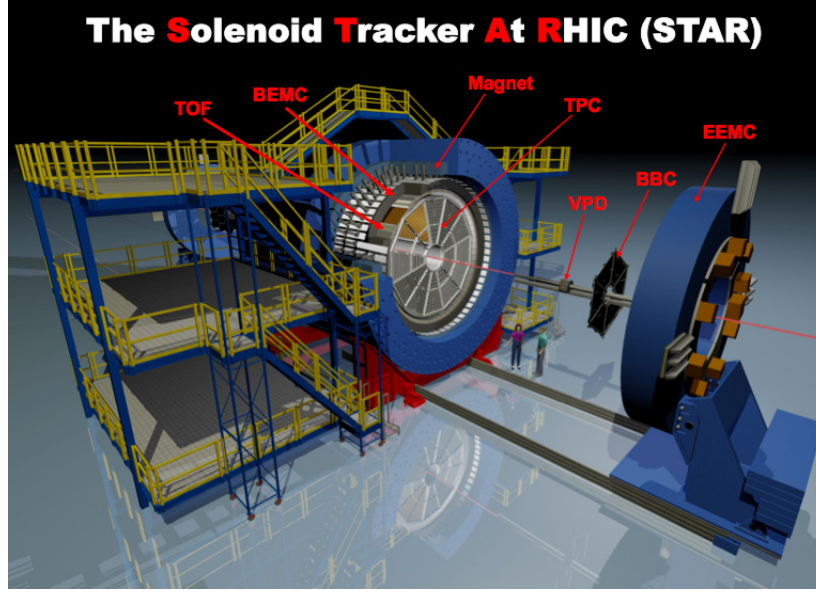


Figure 2.3: (Color online) Three dimensional view of STAR detector system. Figure has been taken from Alexander Schmah.

trajectory in the  $xy$  plane due the magnetic field, and subsequently leave a trail of ionized atoms in the active volume. P10 gas is used in the TPC due to its fast drift velocity which has a maximum value at low electric field strengths. Under the influence of the electric field, the liberated electron clouds drift with an average velocity  $5.45 \text{ cm}/\mu\text{s}$  towards the readout plane while positive ions drift towards the membrane.

The TPC readout endcap planes are multi-wire proportional counter (MWPC) chambers with pad readout and are positioned on the support wheels. The MWPC chambers consist of three wire planes and a pad plane each. For each endcap there are 12 readout modules (sectors) which are positioned radially with respect to the hole defined by the inner field-cage with 3 mm gaps between each sector. Each sector is subdivided into inner and outer subsectors characterized by a change in the readout padrow geometry. Each inner sector contains a large number of small pads, distributed in 13 pad rows, to maximize the position and two-track resolution in a region with

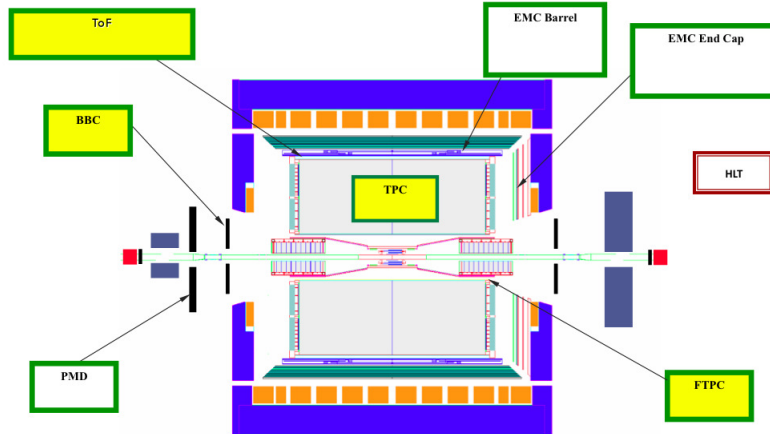


Figure 2.4: (Color online) Cutaway side view of STAR detector system.

high particle density. The pads of the outer sectors are densely packed in 32 rows per sector to optimize the measure of energy loss by ionization in a region with lower particle densities. Therefore, a track in the TPC can be sampled a maximum of 45 times if it crosses all 45 padrows. One full sector of the anode pad plane is shown in Fig 2.7. The central membrane cathode consists of  $70 \mu\text{m}$  thick carbon-loaded Kapton film. It also has 36 aluminium stripes attached to each side which are used as targets for the TPC laser calibration system [14].

**Track reconstruction:**

When a charged particle traverses through the volume of the TPC, it ionizes the gas atoms and molecules along its path leaving behind a cluster of electrons. The x-y position of each cluster is found by measuring the signal (charge) in adjacent pads (along a single padrow) and fitting to find the most likely position, assuming a gaussian pad response function. The z-coordinate of a cluster is found by measuring the drift time from the point of origin of the cluster to the endcap and dividing by the average drift velocity. Once the positions of the clusters are found, a Time Projection chamber Tracker (TPT) algorithm is used to reconstruct the tracks by a helical trajectory fit. Each track is a helix to first order, but there can be deviations

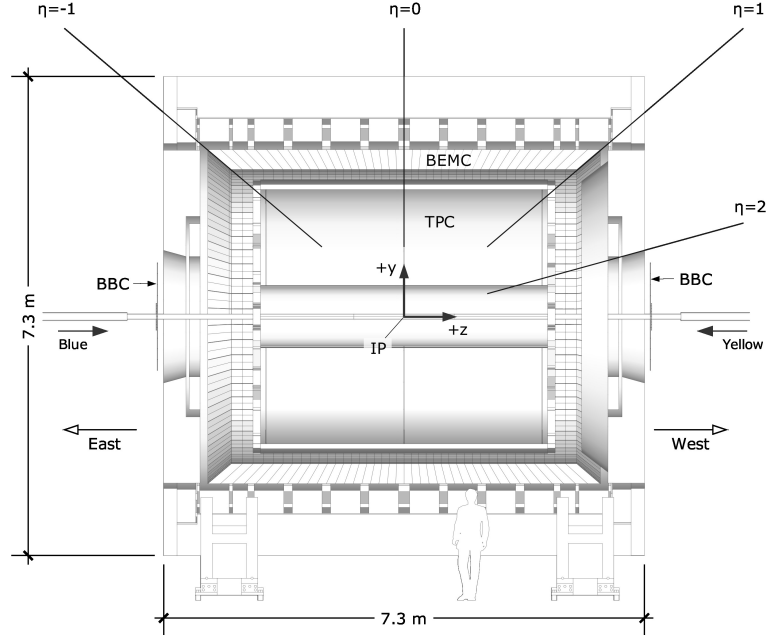


Figure 2.5: STAR coordinate system.

from the helical shape due to energy loss in the gas and multiple Coulomb scattering. The  $z$ -position of the primary collision vertex is determined by extrapolating the trajectories of the reconstructed global tracks back to the origin. If a global track has a distance of closest approach (dca) (with respect to the primary vertex), less than 3 cm, then the track is refitted to include the primary vertex as an additional space point. These tracks are called primary tracks. The reconstruction efficiency for primary tracks depends on the track quality cuts, particle type and track multiplicity. The tracking efficiency of the TPC is  $\sim 80\%$  for pions with transverse momentum ( $p_T$ )  $> 2.0$  GeV/ $c$ .

The transverse momentum of a track is calculated using radius of curvature of the track helix using following relation:

$$p_T = 0.3Brq \quad (2.1)$$

where  $B$  is the magnitude of the magnetic field,  $r$  the radius of curvature and  $q$  is

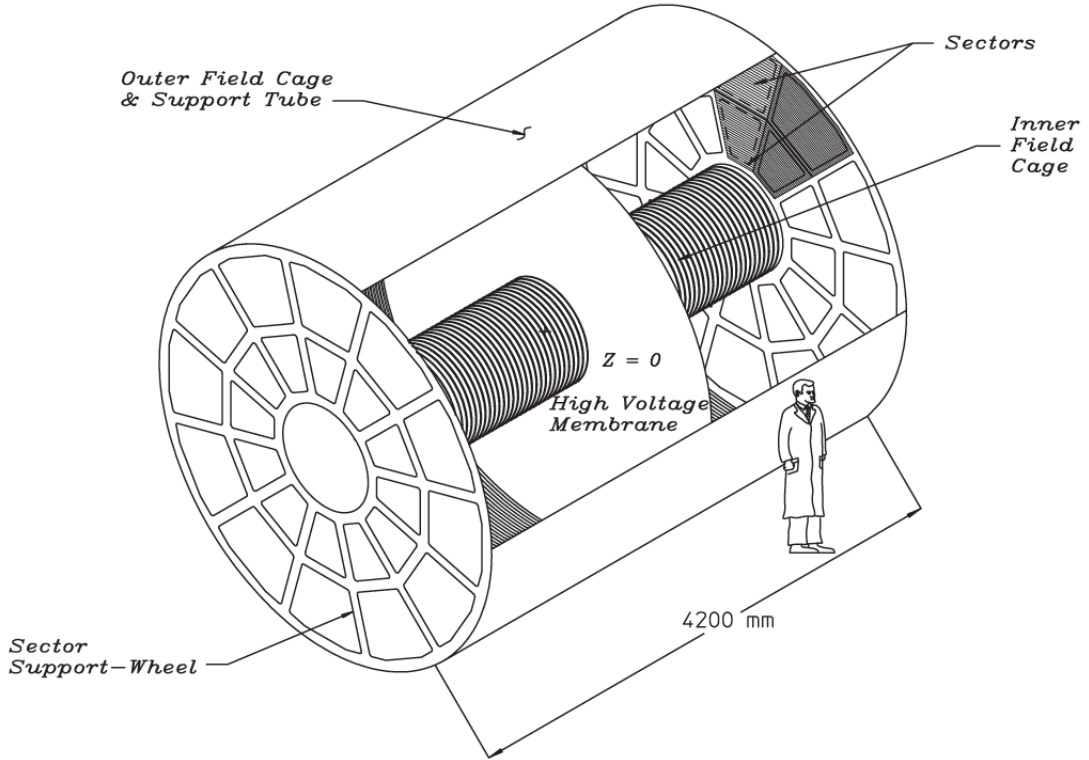


Figure 2.6: Three dimensional schematic diagram indicating the main structural elements of the STAR TPC.

the charge of the particle. After that all three momentum components of momentum can then be calculated using the angle that the track makes with respect to the z-axis of the TPC. This procedure works for all primary particles coming from the vertex, but for secondary decays, such as  $\Lambda$  or  $K_s^0$ , the circle fit must be done without reference to the primary vertex. To estimate the momentum resolution embedding technique was used. In which simulation tracks with known momentum are embedded in data and reconstructed back. The difference in momentum values of input and reconstructed track provides the momentum resolution. The momentum resolution depends on magnitude of momentum and also on the type of particle. The best momentum resolution obtained for pions is  $\sim 2\%$  for  $p_T \sim 0.5 \text{ GeV}/c$ .

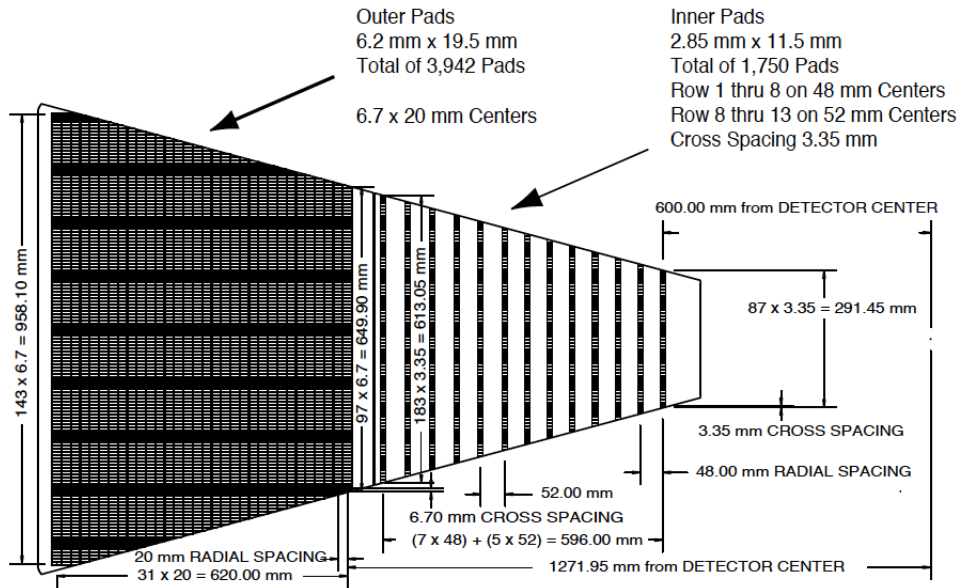


Figure 2.7: A sector of the TPC anode plane indicating the inner and outer subsectors and their respective padrows.

### Particle identification:

Identification of the charged particles can be done by TPC through their ionisation energy loss ( $dE/dx$ ) due to interactions in the medium inside the TPC. The  $dE/dx$  is extracted from the energy loss measured up to a maximum of 45 padrows. Since the length over which the particle energy loss is measured is short and ionization fluctuations are large, it is not possible to accurately measure the average  $dE/dx$ . Instead, the most probable energy loss is measured and used. This is done by calculating the truncated mean of 70% of the of the clusters (removing the 30% largest ionization clusters). Figure 2.8 shows the measured  $dE/dx$  as a function of momentum. The black lines are the theoretical predictions from Bichsel function [15] for different particle species and the bands represent the measured values of  $dE/dx$ . The typical resolution of  $dE/dx$  in Au+Au collisions is  $\sim 8\%$  which makes the  $\pi/K$  separation up

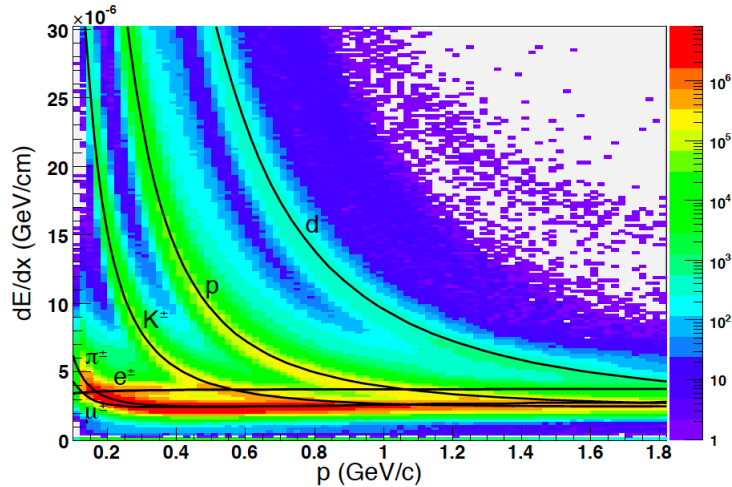


Figure 2.8: (Color online) The energy loss distribution for charged particles in the STAR TPC as a function of momentum.

to  $p \sim 0.6$  GeV/ $c$  and  $p/K$  separation up to  $p \sim 1.1$  GeV/ $c$ . The TPC is originally designed to identify particles at low momentum, but the separation of  $dE/dx$  of particles at relativistic rising region also allows to identify particles at high momentum ( $p > 3$  GeV/ $c$ ) [16].

### 2.1.2 Time-of-flight

The main goal of the STAR Time-of-Flight (TOF) [8] system is to extend particle identification capabilities of the experiment, mainly at high  $p_T$ . It consists of a highly-segmented cylindrical detector immediately surrounding the TPC and arranged in 120 trays. Each individual tray is 2.4 m long, 21.3 cm wide and 8.5 cm deep. Each tray covers 6 degree in azimuthal direction around the TPC. There are 32 Multigap Resistive Plate Chamber (MRPC) [17] modules in each tray, placed along beam ( $Z$ ) direction. The MRPC is basically a stack of resistive plates arranged in parallel. The intermediate plates create a series of gas gaps. Electrodes are applied to the outer surfaces of the two outer plates. A strong electric field is generated in each subgap

by applying a high voltage across these external electrode. A charged particle going through the chamber generates avalanches in the gas gaps. Since plates are resistive they are transparent to signal induced by avalanches, thus a signal induced in the pickup pad is the sum of signals from all the gas gaps. A cross-section view of the MRPC module is shown in Fig 2.9(a). The dimensions of the current module are 94 mm  $\times$  212 mm  $\times$  12 mm and the active area is 61 mm  $\times$  200 mm. The electrodes are made of graphite tape with a surface resistivity of 400 k $\Omega$ /square which covers the entire active area. The outer and inner glass plates are 1.8 and 0.55 mm thick, respectively. They are kept parallel by using 220  $\mu$ m diameter nylon fishing-line. The signal is read out with a 1  $\times$  6 array of copper pickup pads, each pad with an area of 63 mm  $\times$  31.5 mm, and the distance between pads is 3 mm. The pickup pad layers are separated from the outer electrodes by 0.35 mm of Mylar. Figure 2.9(b) shows the readout pad array.

TOF system consists of TOF trays and Vertex Position Detectors (VPDs) [18]. The TOF trays provide the stop time of each track. The VPD provides the common start time of the event. The difference of these two is the time of flight ( $\tau$ ) of the associated track. Time resolution of TOF is  $\sim$  80 to 100 ps. By measuring time of flight of each track we can calculate mass of the corresponding track using following relations

$$\beta = L/c\tau \quad (2.2)$$

$$\gamma = 1/\sqrt{1 - \beta^2} \quad (2.3)$$

$$m = p/\gamma\beta c \quad (2.4)$$

where  $L$  is the length traverse by the particle,  $c$  is the velocity of light,  $m$  is the mass of the particle and  $p$  is the momentum which can be measured by TPC. Figure 2.10 shows the  $1/\beta$  as function of momentum for few selected particles. Using information from TOF we can separate  $\pi/K$  and  $p/K$  up-to  $p \sim 1.6$  and 3.0 GeV/ $c$ , respectively.

### 2.1.3 The trigger detectors

The main trigger detectors are the Zero Degree Calorimeters (ZDCs), Beam Beam Counters (BBCs), the Vertex Position Detectors (VPDs), and the Electromagnetic

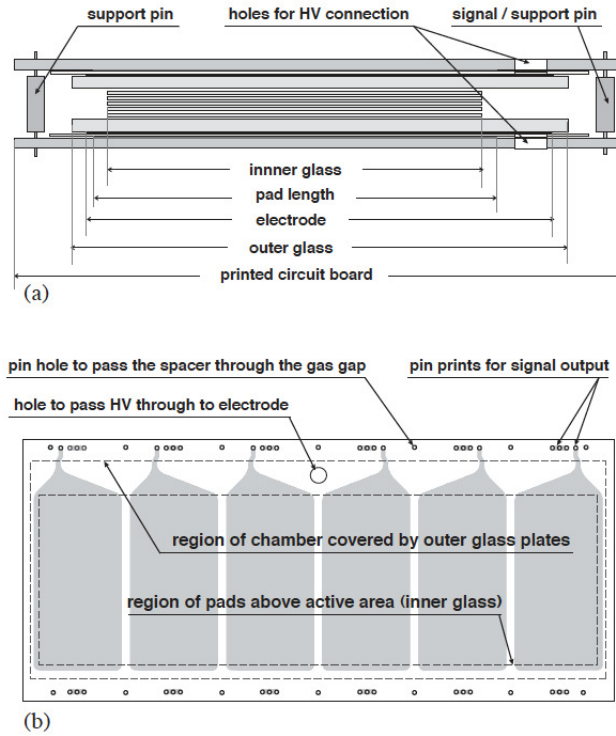


Figure 2.9: (a) Cross section of the  $6 \times 220 \mu\text{m}$  MRPC module for TOF. (b) Top view of the printed circuit board (PCB) with a  $1 \times 6$  readout pads array. The PCB is  $94 \text{ mm} \times 212 \text{ mm}$  area. The projection of the glass layers on the readout pads is also shown.

Calorimeter (EMC). The purpose of the STAR trigger is to instruct the slower detectors on when to record data. Since the various detector subsystems in STAR have different readout speeds. A schematic figure of a nucleus-nucleus collision and STAR trigger system are shown in Fig. 2.11.

The two ZDCs are positioned at  $\pm 18.25$  metres along the beam axis relative to  $z = 0$ . The ZDCs are hadronic calorimeters designed to measure the energy from the remaining neutrons from the colliding nuclei after collision in a small solid angle near zero degrees ( $\theta < 2 \text{ mrad}$ ). The energy deposited by the neutrons can be related to the multiplicity. For a minimum bias trigger, a coincidence between the two ZDCs is

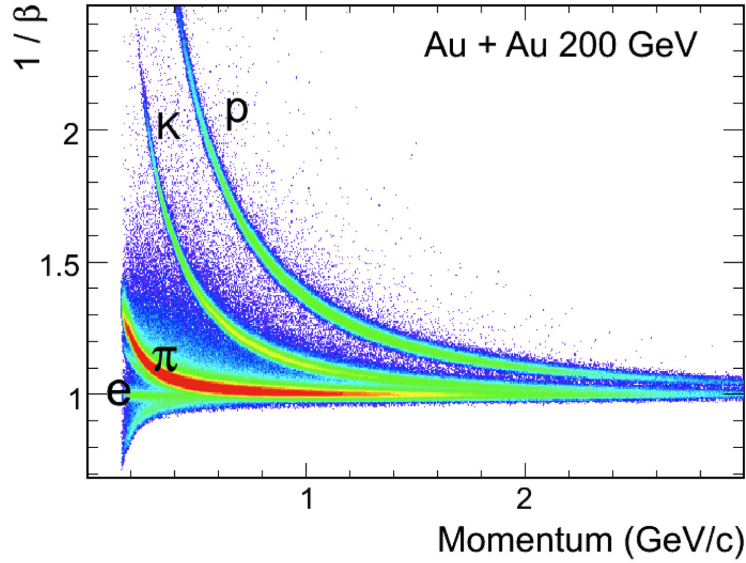


Figure 2.10: (Color online)  $1/\beta$  as a function of momentum in Au+Au collisions at  $\sqrt{s_{NN}} = 200$  GeV.

required with a summed signal greater than  $\sim 40\%$  of a single neutron signal.

The BBC [19] consists of a hexagonal scintillator array structure, located on each side of the interaction region covering the full azimuth and  $2.1 < |\eta| < 5.0$ . It is mounted around the beam pipe at a distance of 3.7 m from the interaction point. For a minimum bias trigger, a coincidence of signals is required between two BBC. The timing difference between the two counters is used to get information of the primary vertex position. BBC coincidences are also used to reject beam gas events. In addition, the small tiles of BBC are used to reconstruct the first order event plane for flow analysis [20].

Since 2009, a pair of Vertex Position Detectors (VPD) [18] was used to select events. Each VPD consists of 19 lead converters plus plastic scintillators with photomultiplier tube readout that are positioned very close to the beam pipe on each side of STAR. Each VPD is approximately 5.7 m from the interaction point and covers the pseudo-rapidity range  $4.24 < |\eta| < 5.1$ . Trigger for the minimum-bias (MB) events

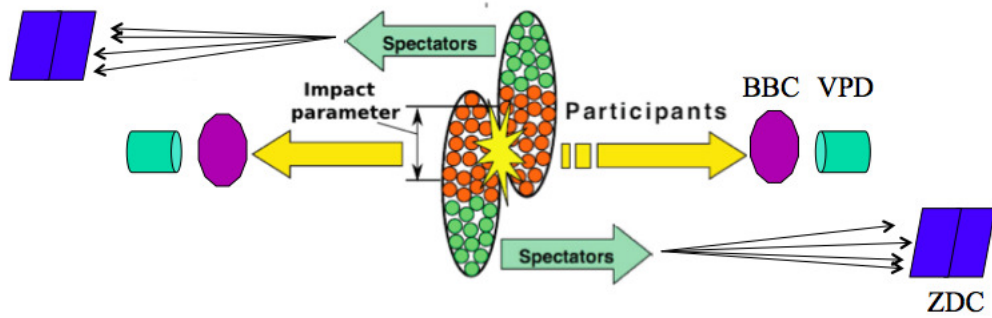


Figure 2.11: (Color online) A schematic figure of a nucleus-nucleus collision and STAR trigger systems.

using VPD is defined as a coincidence signal in the east and west VPD detectors. The VPD can also provide the information about the Z component of the vertex. The VPD has much better timing resolution than BBC.

The Electromagnetic Calorimeters (EMC) can be used to select events with rare probes such as high energy  $\gamma$  and  $\pi^0$  particles, or electrons from  $J/\psi$  decays.

# Bibliography

- [1] <http://www.bnl.gov/rhic/>.
- [2] M. Harrison *et al.*, Nucl. Inst. and Meth. **A 499**, 235 (2003).
- [3] M. Adamczyk *et al.* (BRAHMS Collaboration), Nucl. Inst. and Meth. **A 499**, 437 (2003).
- [4] K. H. Ackermann *et al.* (STAR Collaboration), Nucl. Inst. and Meth. **A 499**, 624 (2003).
- [5] K. Adcox *et al.* (PHENIX Collaboration), Nucl. Inst. and Meth. **A 499**, 469 (2003).
- [6] B. B. Back *et al.* (PHOBOS Collaboration), Nucl. Inst. and Meth. **A 499**, 603 (2003).
- [7] M. Anderson *et al.*, Nucl. Inst. and Meth. **A 499**, 659 (2003).
- [8] B. Bonner *et al.*, Nucl. Inst. and Meth. **A 508**, 181 (2003).
- [9] M. Beddo *et al.*, Nucl. Inst. and Meth. **A 499**, 725 (2003).
- [10] C. E. Allgower *et al.*, Nucl. Inst. and Meth. **A 499**, 740 (2003).
- [11] K. H. Ackermann *et al.*, Nucl. Inst. and Meth. **A 499**, 713 (2003).
- [12] C. Adler *et al.*, Nucl. Inst. and Meth. **A 499**, 778 (2003).
- [13] M. M. Aggarwal *et al.*, Nucl. Inst. and Meth. **A 499**, 751 (2003).

- [14] J. Abele *et al.*, Nucl. Inst. and Meth. **A 499**, 692 (2003).
- [15] H. Bichsel, Nucl. Instrum. Meth. **A562**, 154 (2006).
- [16] Y. Xu *et al.*, Nucl. Inst. and Meth. **A 614**, 28 (2010).
- [17] E. C. Zeballos *et al.*, Nucl. Inst. and Meth. **A 374**, 132 (1996).
- [18] W.J. Llope *et al.*, Nucl. Inst. and Meth. **A 522**, 252 (2005).
- [19] C. A. Whitten Jr (for the STAR Collaboration), AIP Conf. Proc. **980**, 390 (2008); J. Kiryluk (for the STAR Collaboration), arXiv:hep-ex[0501072].
- [20] L. Adamczyk *et al.* (STAR Collaboration), Phys. Rev. **C 86**, 054908 (2012).

# Chapter 3

## Energy Dependence of $\phi$ -meson $v_2$

In this chapter the results of  $\phi$ -meson  $v_2$  measured at mid-rapidity ( $|y| < 1.0$ ) for RHIC Beam Energy Scan data are presented.

### 3.1 Data Sets and Cuts

The results presented in this chapter are based on data collected from Au+Au collisions at  $\sqrt{s_{NN}} = 7.7, 11.5, 19.6, 27, 39$  and  $62.4$  GeV with the STAR detector for minimum bias trigger in the years of 2010 and 2011. The minimum-bias trigger condition for all six energies was based on a coincidence of the signals from the zero-degree calorimeters, vertex position detectors, and/or beam-beam counters.

#### 3.1.1 Event selection

Different cuts on primary vertex has been used for different collision energies for events selection. The cuts on primary vertex position along the longitudinal beam direction ( $V_z$ ) is 40 cm for 39 and 62.4 GeV data set, 50 cm for 11.5 and 19.6 GeV and 70 cm for 7.7 and 27 GeV data set. These vertex cuts were studied and optimized during the data taking using the online vertex reconstruction performed by the high-level trigger (HLT) and basic quality assurance performance plots. The distributions

of Z-positions of vertex are shown in Fig. 3.1 for  $\sqrt{s_{NN}} = 7.7, 11.5, 19.6, 27, 39$  and  $62.4$  GeV. The triggered events at the lowest beam energies may not solely originate

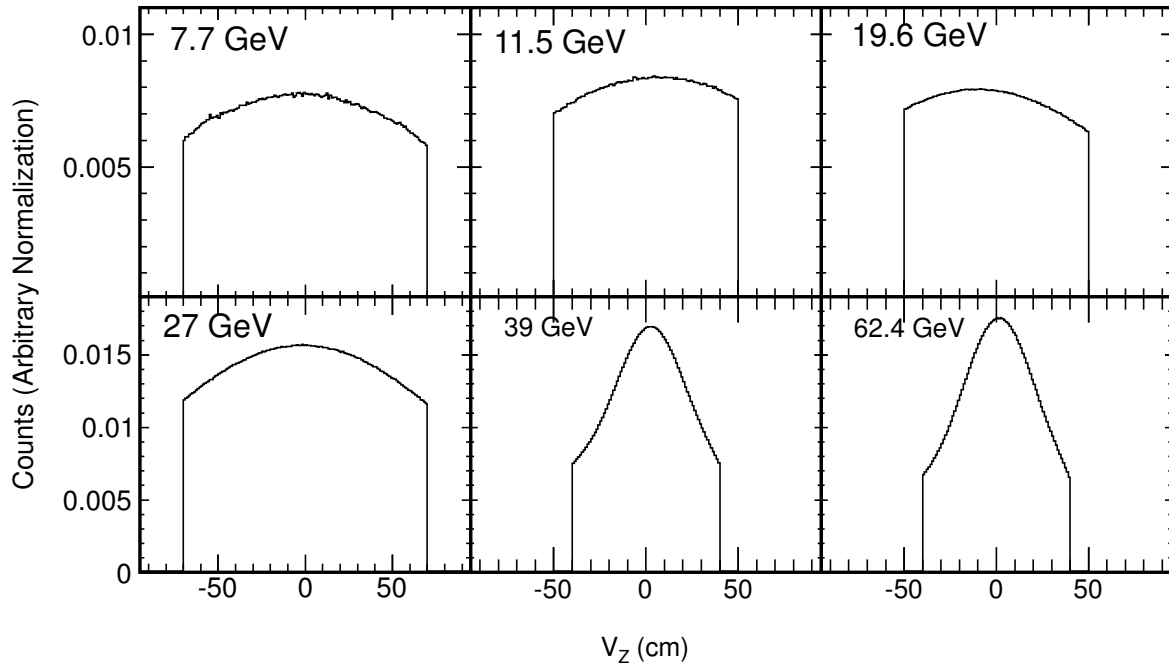


Figure 3.1: The distribution of Z-positions of vertex for the events selected for the analysis at six different centre-of-mass energies.

from Au+Au collisions in addition from the Au-plus-beam-pipe (or other material) collisions. This happens because of the large beam emittance at the lowest beam energies. The radius of the beam pipe is 3.95 cm. To reject the contamination from such events an additional cut on vertex radius ( defined as  $V_R = \sqrt{V_x^2 + V_y^2}$ , where  $V_x$  and  $V_y$  are the vertex positions along the x and y directions)  $< 2$  cm has been used. Figure 3.2 shows distribution of X and Y-positions of vertex for  $\sqrt{s_{NN}} = 7.7$  GeV. To remove pileup events, it was required that at least two tracks from the primary vertex were matched to the cells of the TOF detector (which has a timing resolution of  $\sim 80$  ps). After all events selection cuts, number of events for minimum bias centrality is about 4 million for 7.7 GeV, 12 million for 11.5 GeV, 36 million for 19.6 GeV, 70

million for 27 GeV, 130 million for 39 GeV and 64 million for 62.4 GeV.

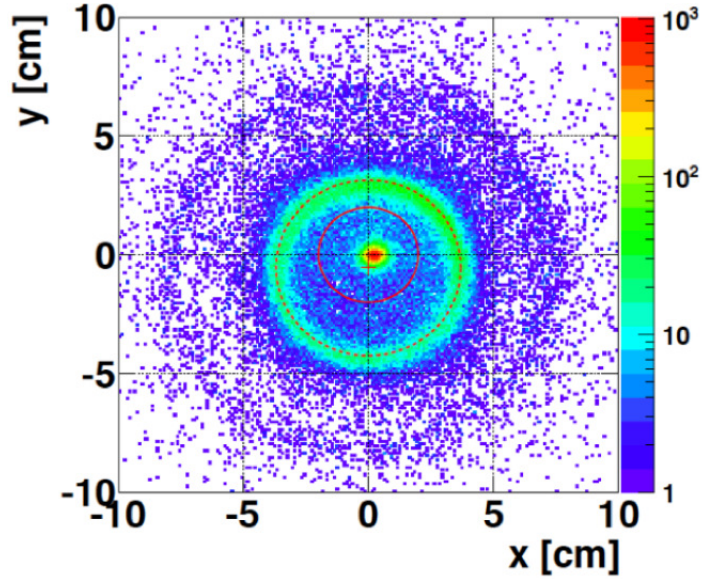


Figure 3.2: (Color online) The distribution of X and Y-positions of vertex for  $\sqrt{s_{NN}} = 7.7$  GeV in Au+Au collisions. Red dashed circle represent the circumference of beam pipe and solid red curve is a circle of radius equal to 2 cm.

### 3.1.2 Centrality determination

The collision centrality is determined by comparing the measured raw charged hadron multiplicity uncorrected for efficiency and acceptance effects (named as  $N_{ch}^{raw}$ ) from the TPC within a pseudo-rapidity window  $|\eta| \leq 0.5$  with Glauber Monte-Carlo simulations. The detailed procedures to obtain the simulated multiplicity are similar to that described in Ref. [10]. A two-component model [2] is used to calculate the simulated multiplicity distribution given by

$$\frac{dN_{ch}}{d\eta} = n_{pp} \left[ (1-x) \frac{N_{part}}{2} + x N_{coll} \right], \quad (3.1)$$

where  $N_{part}$  is the number of participant nucleons and  $N_{coll}$  is the number of binary nucleon-nucleon collisions in the Glauber Monte-Carlo simulations. The fitting parameter  $n_{pp}$  is the average multiplicity per unit of pseudorapidity in minimum-bias

$p+p$  collisions and  $x$  is the fraction of production of charged particles from the hard component. The  $x$  value is fixed at  $0.12 \pm 0.02$  based on the linear interpolation of the PHOBOS results at  $\sqrt{s_{NN}} = 19.6$  and 200 GeV [3]. Systematic errors on  $n_{pp}$  are evaluated by varying both  $n_{pp}$  and  $x$  within the quoted uncertainty of  $x$  to determine the minimum  $\chi^2$  to describe the multiplicity distribution of data. The inelastic nucleon-nucleon cross-section  $\sigma_{nn}^{inel}$  is extracted from fitting the results of available data for total and elastic  $p+p$  cross-sections from the Particle Data Group [4]. The parameters in the two-component model and  $\sigma_{nn}^{inel}$  in the MC Glauber simulations are summarized in table 3.1. Figure 3.3 shows the uncorrected charged multiplicity

$\sqrt{s_{NN}}$ (GeV)	$n_{pp}$	$\sigma_{nn}^{inel}$ (mb)
7.7	$0.89 \pm 0.04$	$30.8 \pm 1.20$
11.5	$1.07 \pm 0.05$	$31.2 \pm 1.13$
19.6	$1.29 \pm 0.05$	$32.0 \pm 1.11$
27	$1.39 \pm 0.06$	$33.0 \pm 1.10$
39	$1.52 \pm 0.08$	$34.0 \pm 1.10$
62.4	$1.60 \pm 0.09$	$36.0 \pm 1.00$

Table 3.1: Values of  $n_{pp}$  and  $\sigma_{nn}^{inel}$  with systematic uncertainties at  $\sqrt{s_{NN}} = 7.7, 11.5, 19.6, 27, 39$  and 62.4 GeV.

distribution for minimum-bias events and for three different centrality classes.

All the values of  $N_{ch}^{raw}$  or  $refmult$  for different centralities and different energies are listed in the Appendix section.

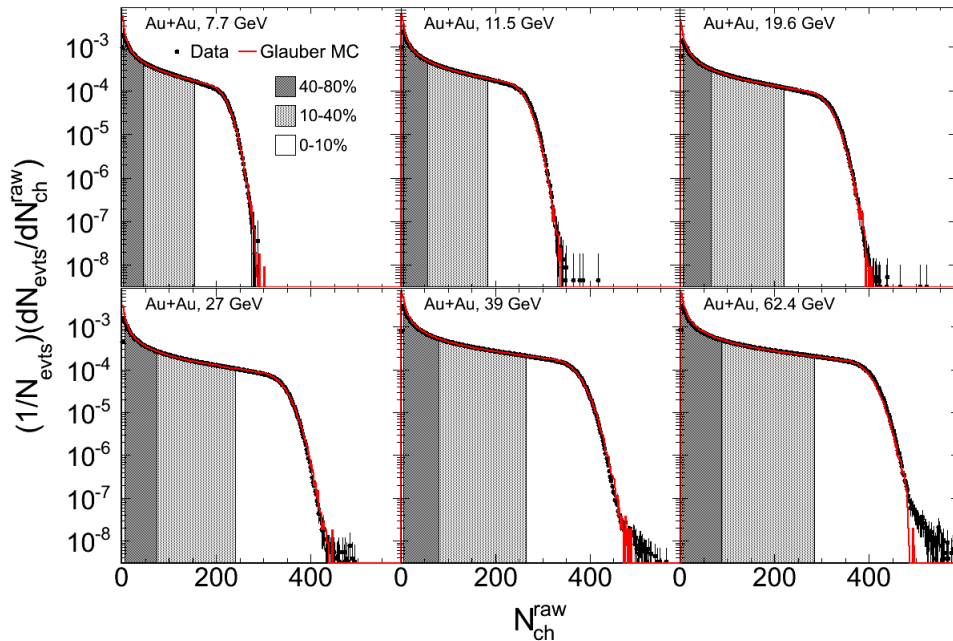


Figure 3.3: (Color online) The uncorrected multiplicity distribution of reconstructed charged particles per unit pseudo-rapidity interval at mid-rapidity for the six different centre-of-mass energies. The solid black points depict the measured data and a GlauberMonte Carlo simulation is overlaid as the solid red curve. Three different centrality classes of 0–10%, 10–40% and 40–80% from the right of the distributions respectively are indicated by the different shaded regions.

### 3.1.3 Particle identification

#### 3.1.3.1 Using TPC

In this analysis,  $\phi$  mesons were measured through the decay channel  $\phi \rightarrow K^+ + K^-$  (details will be discussed in chapter 4). The Time Projection Chamber (TPC) is the main tracking detector in the STAR experiment. Kaons are identified using information of the specific ionization energy loss as a function of momentum. The mean specific energy loss in the TPC for different particles as a function of rigidity (charge $\times$ momentum) are shown in Fig. 3.4. The Bichsel functions [5] used to

determine the  $n\sigma$  values are shown as a line for each particle. The  $n\sigma$  is defined as

$$n\sigma = \frac{1}{R} \times \frac{dE/dx_{measured}}{dE/dx_{theory}}, \quad (3.2)$$

where  $dE/dx$  is the specific ionization energy loss per unit path length and  $R$  is the  $dE/dx$  resolution. The black line corresponds to Bichsel function for kaons. The basic cuts for kaons selection using TPC are listed in the table 3.2. In order to ensure good

Number of fit points in TPC (nHits)	$\geq 15$
Ratio of fit points to possible points (nHits/Max. nHits)	$\geq 0.52$
Dca from primary vertex	$\leq 3.0$ cm
$n\sigma$ of kaon dE/dx	$\leq 2.0  \sigma $
$p_T$ of kaons	$\geq 0.15$ GeV/c
pseudo-rapidity ( $\eta$ ) of kaon	$\leq 1.0$
dip-angle between two kaon	$\geq 0.04$ rad

Table 3.2: Kaons selection cuts using TPC for  $\phi$ -meson reconstruction.

track momentum reconstruction, short tracks were eliminated from the analysis by requiring all tracks to have  $p_T > 0.15$  GeV/c and a minimum number of 15 fit points in TPC for each track. The effect of track-splitting due to the tracking algorithm is minimized by further requiring that the number of fit points is more than half of the number of total possible hit points for a track i.e.  $TPCnHits/Max.nHits \geq 0.52$ . In addition all kaon tracks with distance of closest approach (Dca) from primary vertex greater than 3 were removed to reject the tracks coming from sources other than primary vertex. Finally tracks with  $|\eta| \leq 1.0$ , where the acceptance of TPC is uniform, has been used in the analysis. The dip-angle  $\theta$  between two tracks  $a$  and  $b$  is defined as  $\cos\theta = \frac{(p_T^a p_T^b + p_z^a p_z^b)}{(|p^a||p^b|)}$ , where  $p_T$ ,  $p_z$  and  $p$  are the transverse momentum, z component of momentum and total momentum respectively. In order to exclude conversion electron pairs which may be misidentified as kaons in the  $p_T$  range where the dE/dx bands for kaons and electrons overlap, kaon-candidate pairs with a dip-

angle  $< 0.04$  rad were excluded as candidates for  $\phi$  meson [6]. In addition to the

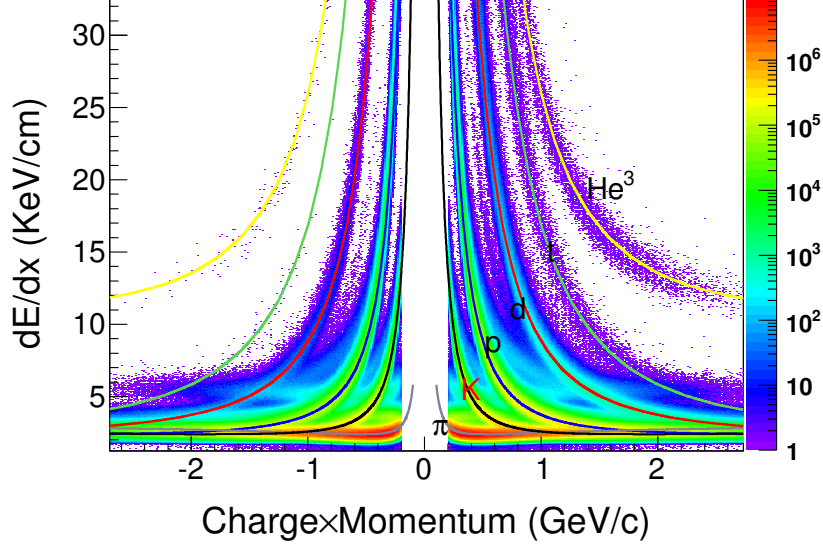


Figure 3.4: (Color online) The mean specific energy loss,  $dE/dx$ , of reconstructed tracks within a pseudo-rapidity range of  $|\eta| < 1$  in the TPC in Au+Au collisions at  $\sqrt{s_{NN}} = 39$  GeV. The Bichsel functions used to determine the  $n\sigma$  values are shown as a line for each particle. The black line corresponds to Bichsel function for kaons.

above reasons, the cuts were optimized by comparing  $\phi$ -meson raw yield and signal to background ratio for different sets of cuts. For example, cut on Dca was varied to 3, 2 and 1.5 cm. The comparison of raw  $\phi$ -meson yield, normalized by events, and signal to background ratio for  $Dca < 3$  and  $Dca < 1.5$  cm are shown in Fig. 3.5 for 20-30% centrality at  $\sqrt{s_{NN}} = 39$  GeV. One can see from Fig. 3.5 that by changing Dca from 3 to 1.5, there is no improvement in the signal to background ratio but it reduced the  $\phi$ -mesons raw yield causing larger statistical error. Hence  $Dca < 3$  is the best choice for the study of  $\phi$  mesons. Similar study was done for all other variables and for all other centre-of-mass energies.

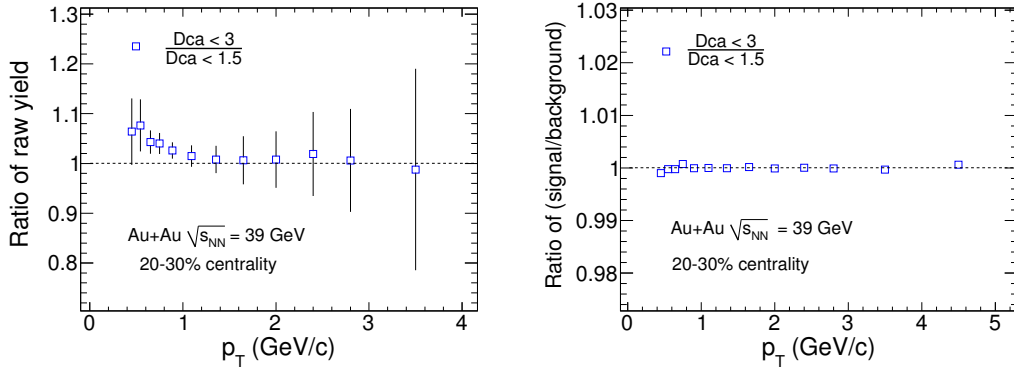


Figure 3.5: (Color online) The ratio of  $\phi$ -meson raw yield, normalized by events, (left panel) and signal to background ratio (right panel) for  $Dca < 3$  cm and  $Dca < 1.5$  cm for 20-30% centrality at  $\sqrt{s_{NN}} = 39$  GeV.

### 3.1.3.2 Using TOF

The time-of-flight (TOF) system was fully installed in STAR in the year 2010. The particle identification capability of STAR detector system improved significantly after the implementation of TOF. The particle mass squared,  $m^2$ , can be calculated using the measured time-of-flight and the reconstructed momentum from the TPC. The mass squared cut of  $0.16 < m^2 < 0.36$   $\text{GeV}^2/c^4$  were applied for kaons ( $m = 0.496$   $\text{GeV}/c^2$ ) selection. The mass squared,  $m^2$ , as a function of momentum for selected mass range is shown in Fig. 3.6.

## 3.2 Elliptic flow measurement methods

The elliptic flow parameter  $v_2$  is a good tool for studying the system formed in the early stages of high energy collisions at RHIC [7]. It describes the momentum anisotropy of particle emission from non-central heavy-ion collisions. It is defined as the second harmonic coefficient of the Fourier decomposition of azimuthal distribution with respect to the reaction plane angle ( $\Psi_r$ ) and can be written as

$$\frac{dN}{d\phi} \propto 1 + 2v_1 \cos((\phi - \Psi_r)) + 2v_2 \cos(2(\phi - \Psi_r)) + \dots, \quad (3.3)$$

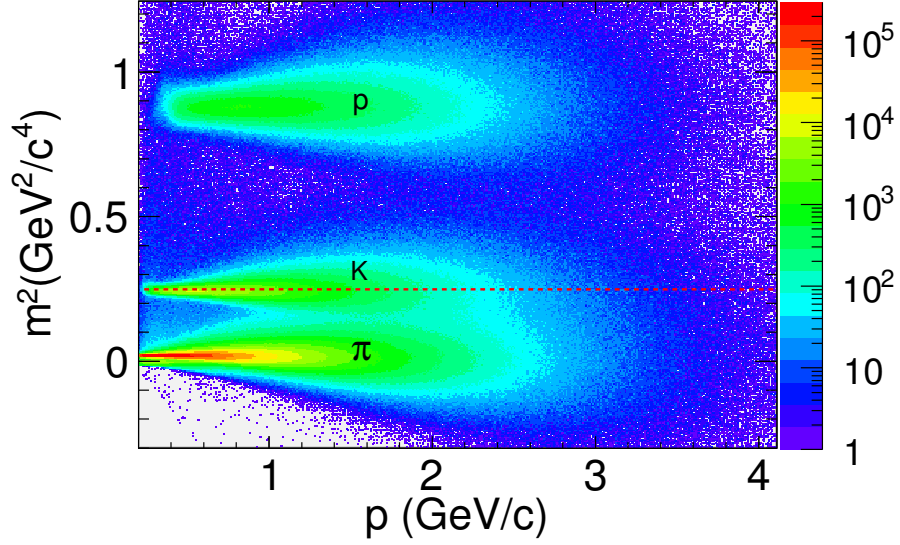


Figure 3.6: (Color online) The mass squared,  $m^2$ , as a function of momentum within a pseudo-rapidity range of  $|\eta| < 0.9$  in Au+Au collisions at  $\sqrt{s_{NN}} = 39$  GeV. The red line corresponds to PDG mass value for kaons.

where  $\phi$  is emission azimuthal angle. For a given rapidity window the second Fourier coefficient is

$$v_2 = \langle \cos(2(\phi - \Psi_r)) \rangle. \quad (3.4)$$

The  $\langle \rangle$  denote average over all particles in all events.

In order to measure the elliptic flow we have to calculate the reaction plane angle. Reaction plane is the plane which contains both beam (Z) axis and impact parameter (perpendicular distance between two centre of colliding nuclei). The angle between X-axis and reaction plane is called reaction plane angle. Since in experiment we can not measure the impact parameter between two colliding nuclei therefore the reaction plane angle is unknown. We used the method to estimate the reaction plane by using the anisotropic flow itself [8]. The estimated reaction plane is known as event plane. The first step is to calculate event flow vector  $Q_n$  which is defined as

$$Q_n \cos(n\Psi_n) = Q_X = \sum_{i=1}^N w_i \cos(n\phi_i) \quad (3.5)$$

$$Q_n \sin(n\Psi_n) = Q_Y = \sum_{i=1}^N w_i \sin(n\phi_i), \quad (3.6)$$

where  $w_i$  is the weight and  $N$  is the total number of particles in a event used for flow vector calculation. The  $n^{\text{th}}$  harmonic event plane angle can be calculated by

$$\Psi_n = \frac{1}{n} \tan^{-1} \left( \frac{\sum_i w_i \sin(n\phi_i)}{\sum_i w_i \cos(n\phi_i)} \right). \quad (3.7)$$

The choice of weights is to make the event plane resolution the best by maximizing the flow contributions to the flow vector. In this analysis weight  $w_i=p_{T_i}$  (for  $p_T < 2$  GeV/ $c$ ) has been taken for event plane reconstruction. The  $p_T$  of tracks were used as a weight to get good event plane resolution, since the  $v_2$  increases with  $p_T$ . The tracks selection criteria for event plane reconstruction is listed in table 3.3. Tracks with  $p_T$

Flow Tracks Selection Cuts	Value
nHits	$\geq 15$
nHits/Max. nHits	$\geq 0.52$ and $\leq 1.02$
Dca	$\leq 2$ cm
Transverse momentum	$0.15 < p_T < 2.0$ GeV/ $c$
Pseudo-rapidity	$ \eta  \leq 1.0$

Table 3.3: Track cuts for flow tracks selection.

$< 2.0$  GeV/ $c$  were used to minimize the contribution to the event plane determination from non-flow effects (the effect which are not necessarily correlated with the event plane, for example jets). Reason behind the other cuts has been already discussed above.

### 3.2.1 Detector acceptance correction

The event plane angle is random in the laboratory frame and therefore its distribution should be flat or uniform for a perfect detector. But in the experiments, the detectors have a finite acceptance which can lead to anisotropic particle distributions in the

lab frame. This anisotropy is not related to the true anisotropic flow arising due to pressure gradients developed in the system and we want to measure. Therefore it is necessary to ensure that event plane angle distribution should be flat or uniform in the laboratory frame. Several methods have been developed to correct the event plane angle distribution [8]. The most commonly used methods, is to use the distribution of the particles themselves as a measure of the correction for the acceptance effect. This is known as  $\phi$  weight method. In this method, one can accumulate the laboratory frame azimuthal distribution of the particles for all events and uses the inverse of this as weights in the calculation of the event planes. But this method will not work if the azimuthal distribution of the particles is zero or very low in some part of the phase-space. Exactly same problem happened for STAR detector system because of few dead sector in the TPC during data collection in the year of 2010. For this reason it was not possible to use  $\phi$  weight method for event plane correction. Another disadvantage of this method is that, it does not take into account the multiplicity fluctuations around the mean value. The second method, known as re-centering, is to recenter the distribution of flow vectors  $(Q_X, Q_Y)$  by subtracting the flow vectors averaged over all events.

$$Q_X = Q_X - \langle Q_X \rangle \quad (3.8)$$

$$Q_Y = Q_Y - \langle Q_Y \rangle \quad (3.9)$$

This method has been used for 2nd order event plane correction presented in this thesis. The main limitation of this method is that it does not eliminate the higher harmonics from the distribution of  $\Psi_2$ . To eliminate the higher harmonics the event plane has been further corrected by the shift method. In this method one has to fit the unweighted laboratory frame distribution of the event planes, summed over all events, to a Fourier expansion and devises an event-by-event shifting of the planes needed to make the final distribution isotropic. The equation for shift correction for  $n^{th}$  harmonic event plane is

$$\Delta\Psi_n = \frac{1}{n} \sum_{i=1}^{i_{max}} \frac{2}{i} [-\langle \sin(in\Psi_n) \rangle \cos(in\Psi_n) + \langle \cos(in\Psi_n) \rangle \sin(in\Psi_n)]. \quad (3.10)$$

The minimum value of  $i_{max} = 4/n$  where  $n$  is the harmonic number of interest. The final corrected event plane is

$$\Psi'_n = \Psi_n + \Delta\Psi_n. \quad (3.11)$$

The  $2^{nd}$  order event plane ( $\Psi_2$ ) distributions corrected by re-centering and shift method are shown in Fig. 3.7 for  $\sqrt{s_{NN}} = 7.7$  GeV in Au+Au collisions. Those event plane distributions has been fitted with a function

$$f = p_0[1 + 2p_1 \cos(2\Psi_2) + 2p_2 \sin(2\Psi_2)], \quad (3.12)$$

where  $p_0$ ,  $p_1$  and  $p_2$  are free parameters. Small values of parameters  $p_1$  and  $p_2$  indicates that event plane distributions are flat. Similar procedure is followed for other energies and some of those sample distributions are given in the Appendix.

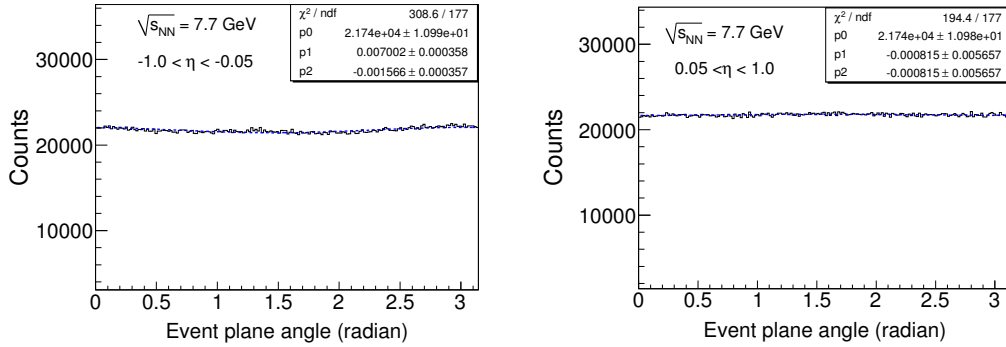


Figure 3.7: (Color online) TPC event plane distributions in Au+Au collisions at  $\sqrt{s_{NN}} = 7.7$  GeV. Left panel and right panel show event plane constructed using flow tracks with  $-1.0 < \eta < -0.05$  and  $0.05 < \eta < 1.0$ , respectively.

### 3.2.2 Event plane resolution correction

The finite multiplicity in a single event limits the resolution in estimating the angle of the reaction plane. Therefore the observed  $v_2^{obs}$  has to be corrected for the event plane resolution (R) as

$$v_2 = \frac{v_2}{R} = \frac{v_2^{obs}}{\langle \cos[2(\Psi_2 - \Psi_r)] \rangle}, \quad (3.13)$$

where  $\Psi_r$  is the true reaction plane angle. Since  $\Psi_r$  is unknown, the event plane resolution is estimated by the correlation of the events planes of two sub-events A and B and is given by

$$R = \langle \cos[2(\psi_2 - \psi_r)] \rangle = C \sqrt{\langle \cos[2(\psi_2^A - \psi_2^B)] \rangle}, \quad (3.14)$$

where  $C$  is a constant calculated from the known multiplicity dependence of the resolution [8]. For this analysis, the sub-events were constructed by dividing TPC acceptance into two  $\eta$ -sub group so that the multiplicity of each sub-event A and B are approximately the same and hence their respective resolutions should be equal.

Fig. 3.8 shows resolution for each sub event plane as function of centrality for different beam energies in Au+Au collisions. The event plane resolution has been calculated for nine different centrality individually (0-5%, 5-10%, 10-20%, 20-30%, 30-40%, 40-50%, 50-60%, 60-70% and 70-80%). As the event plane resolution depends on number

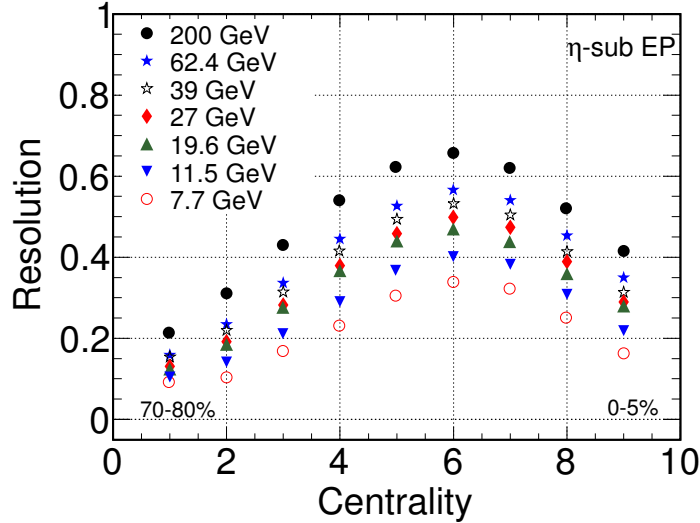


Figure 3.8: (Color online) The event plane resolution of TPC using  $\eta$ -sub events in Au+Au collisions at  $\sqrt{s_{NN}} = 7.7 - 200$  GeV.

of particles used for event plane reconstruction, therefore it should increase from pe-

ripheral to central collisions. On the other hand, since the event plane is calculated using the anisotropic flow of the event itself, it should degrades with more central collisions where flow values are small. Because of this two competing effects the final resolution first increases from peripheral to mid-central collision and then decreases. The values of second order TPC event plane resolution for  $\eta$ -sub events for all nine

<b>TPC <math>\eta</math>-sub event plane resolution</b>									
$\sqrt{s_{NN}}$	0-5%	5-10%	10-20%	20-30%	30-40%	40-50%	50-60%	60-70%	70-80%
200 GeV	0.4137	0.5192	0.6197	0.6550	0.6214	0.5397	0.4285	0.3104	0.2121
62.4 GeV	0.3493	0.4531	0.5403	0.5659	0.5261	0.4447	0.3367	0.2347	0.1587
39 GeV	0.3134	0.4135	0.5042	0.5319	0.4935	0.4148	0.3146	0.2199	0.1540
27 GeV	0.2896	0.3891	0.4736	0.4968	0.4584	0.3791	0.2825	0.1920	0.1308
19.6 GeV	0.2793	0.3595	0.4376	0.4677	0.4405	0.3668	0.2760	0.1850	0.1245
11.5 GeV	0.2185	0.3080	0.3823	0.4016	0.3648	0.2901	0.2085	0.1413	0.1042
7.7 GeV	0.1623	0.2496	0.3208	0.3379	0.3028	0.2302	0.1665	0.1016	0.0909

Table 3.4: Second order event plane resolution in TPC from  $\eta$ -sub event method. Statistical error on resolution is less than 2% for all the centrality classes and all energies.

centrality classes and all beam energies are shown in table 3.4.

Most commonly used method for resolution correction for an average  $v_2$  over a centrality range is

$$\langle v_2 \rangle = \frac{\langle v_2^{obs} \rangle}{\langle R \rangle}. \quad (3.15)$$

Here  $\langle R \rangle$  are the mean resolution in that wide centrality bin and can be calculated as

$$\langle R \rangle = \frac{\sum N_i \langle R \rangle_i}{\sum N_i}. \quad (3.16)$$

where  $N_i$  and  $\langle R \rangle_i$  is the multiplicity and resolution of the  $i^{th}$  narrow centrality bin, respectively. This procedure works well for narrow centrality bins, but fails for

wider centrality bins like for example 0 – 80%. There is another approach, known as event by event resolution correction, for event plane resolution correction for wide centrality bin [10]. In this method resolution correction for wide centrality bin has been done by dividing the term  $\cos(2(\phi - \Psi))$  by the event plane resolution ( $R$ ) for the corresponding centrality for each event.

$$\langle v_2 \rangle = \left\langle \frac{v_2^{obs}}{R} \right\rangle. \quad (3.17)$$

These two method do not give same  $\langle v_2 \rangle$  because

$$\frac{\langle v_2^{obs} \rangle}{\langle R \rangle} \neq \left\langle \frac{v_2^{obs}}{R} \right\rangle. \quad (3.18)$$

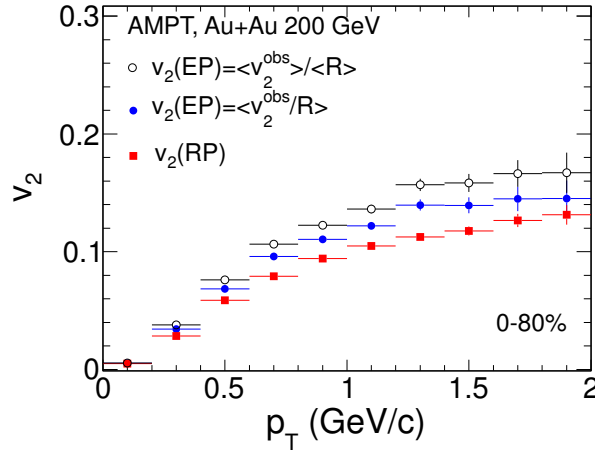


Figure 3.9: (Color online) The elliptic flow of charged particles as function of  $p_T$  for 0-80% centrality in Au+Au collisions at  $\sqrt{s_{NN}}= 200$  GeV from AMPT model. The  $v_2$  values with different methods of resolution correction compared to results from true reaction plane.

We have used the AMPT model [22] to show the difference in measured  $v_2$  from these two methods. Figure 3.9 shows charged particles  $v_2$  as function of  $p_T$  for 0-80% centrality bin in Au+Au collisions at  $\sqrt{s_{NN}}= 200$  GeV. The red marker corresponds

to  $v_2$  measured with respect to true reaction plane. Open black and solid blue circle corresponds to  $v_2$  measured with respect to event plane and resolution correction done using method described in equation 3.15 and 3.17, respectively. The  $v_2$  measured with respect to true reaction plane is the actual  $v_2$  in the AMPT model. One can see from the Fig. 3.9 that resolution correction using method described in equation 3.17 gives  $v_2$  closer to the actual  $v_2$  than other method. This observation is consistent with ref. [10]. In this thesis all the  $v_2$  results are corrected by method described by the equation 3.17.

### 3.2.3 The event plane method

The essence of the event plane method [8] (also known as full event plane method) is to first estimate the reaction plane by measuring event plane as discussed earlier. The observed  $v_2$  is the second harmonic of the azimuthal distribution of particles with respect to this second order event plane:

$$v_2^{obs} = \langle \cos(2(\phi - \Psi_2)) \rangle. \quad (3.19)$$

The final expression for resolution corrected  $v_2$  is

$$v_2 = \frac{v_2^{obs}}{R} = \frac{v_2^{obs}}{\langle \cos[2(\Psi_2 - \Psi_r)] \rangle}. \quad (3.20)$$

The event plane resolution for  $v_2$ , using the second harmonic event plane  $\Psi_2$ , can be expressed as [8]:

$$\langle \cos(2(\Psi_2 - \Psi_r)) \rangle = \frac{\sqrt{\pi}}{2\sqrt{2}} \chi_2 \exp(-\chi_2^2/4) [I_0(\chi_2^2/4) + I_1(\chi_2^2/4)], \quad (3.21)$$

where  $I_0$  and  $I_1$  are the modified Bessel function of order 0 and 1, respectively.

$$\chi_2 \equiv \frac{v_2}{\sigma} \quad \text{and} \quad \sigma^2 = \frac{1}{2N} \frac{\langle \omega^2 \rangle}{\langle \omega \rangle^2}, \quad (3.22)$$

where  $N$  is the number of particles used to calculate the event plane angle and  $\omega$  are the weights discussed previously. Equations 3.14 and 3.21 can be used to calculate the full event plane resolution, taking into account that the full event has twice as many particles as the sub-events. In the full event plane method the same tracks are used

to calculate the event plane and  $v_2$ . So there is self correlation. Therefore to remove auto(self)-correlation effect, the contribution of the each particle to flow vectors has been subtracted while calculating the  $v_2$  of that particle. The disadvantage of this method is that it is affected by non-flow correlations.

### 3.2.4 The $\eta$ -sub event plane method

The  $\eta$ -sub event plane method help to reduce the contribution from non-flow effects (mostly due to short-range correlations) by correlating particles separated in pseudo-rapidity. In this method [8], one defines the event flow vector for each particle based on their measurement in the opposite hemisphere in pseudo-rapidity:

$$v_2(\eta_{\pm}) = \frac{\langle \cos[2(\phi_{\eta_{\pm}} - \psi_{2,\eta_{\mp}})] \rangle}{\sqrt{\langle \cos[2(\psi_{2,\eta_{+}} - \psi_{2,\eta_{-}})] \rangle}}. \quad (3.23)$$

Here  $\psi_{2,\eta_{+}}(\psi_{2,\eta_{-}})$  is the second harmonic event plane angle defined for particles with positive(negative) pseudo-rapidity. An  $\eta$  gap of  $|\eta| < 0.05$  between positive and negative pseudo-rapidity sub-events has been introduced to suppress non-flow effects. In Eq. 3.23 the non-flow effects (correlations) are reduced in both the observed flow (numerator) and the event plane resolution (denominator). Depending on the nature of the remaining non-flow effects,  $v_2$  measured this way may have values that are either lower or higher than those obtained with the standard plane method [11]. But this method is not sufficient to reduce non-flow effects due to long-range correlations. The results presented in this thesis has been calculated using the  $\eta$ -sub event plane method.

### 3.2.5 Extraction of $\phi$ -meson $v_2$

There are two types of  $v_2$  measurement methods for resonance particle like  $\phi$  meson, one is  $\phi$ -binning [8] and another is  $v_2$  vs.  $m_{inv}$  method [5]. For the final results, the  $v_2$  vs.  $m_{inv}$  mass method has been used although consistency between the two methods is reported.

### 3.2.5.1 The $\phi$ -binning method:

In this method one has to measure the raw yield of the chosen particle as function of angle  $(\phi - \Psi)$ , where the  $\phi$  is the azimuthal angle of the particle in the lab-frame and  $\Psi$  is the event plane angle and finally it can be fitted with function

$$\frac{dN}{d(\phi - \Psi)} = p_0[1 + 2v_2 \cos(2(\phi - \Psi))], \quad (3.24)$$

where  $p_0$  and  $v_2$  are the parameters. The raw  $\phi$ -meson yields for different  $(\phi - \Psi_2)$  bin at  $\sqrt{s_{NN}} = 39$  GeV in Au+Au collisions for 0-80% centrality are shown in Fig. 3.10. The distribution is fitted with the function as described in Eq. 3.24 and the fit is shown by blue line. Here the measured  $v_2$  has been corrected by event by event resolution correction method [10].

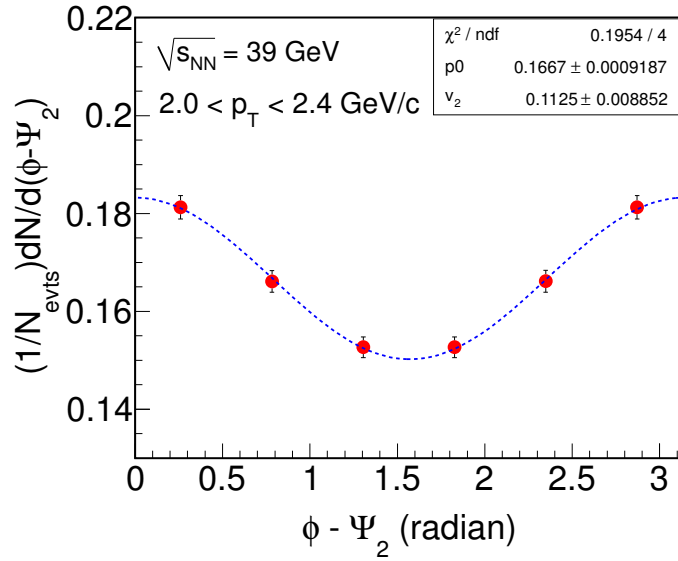


Figure 3.10: (Color online) The raw  $\phi$ -meson yield for different  $(\phi - \Psi_2)$  bin at  $\sqrt{s_{NN}} = 39$  GeV in Au+Au collisions for 0-80% centrality fitted with function shown in Eq. 3.24.

### 3.2.5.2 The $v_2$ vs. $m_{inv}$ method:

The  $v_2$  vs.  $m_{inv}$  method is quite useful to calculate  $v_2$  of the particles that are detected through their decay products, such as  $\phi \rightarrow K^+ + K^-$ ,  $\Xi^- \rightarrow \Lambda + \pi^-$  ( $\Xi^+ \rightarrow \bar{\Lambda} + \pi^+$ ) and  $\Omega^- \rightarrow \Lambda + K^-$  ( $\bar{\Omega}^+ \rightarrow \bar{\Lambda} + K^+$ ) and so on. The first step of this method is to calculate the  $v_2^{S+B} = \langle \cos[2(\phi - \Psi_2)] \rangle$  as a function of invariant mass  $m_{inv}$ . The  $v_2^{S+B}(m_{inv})$  can be decompose as

$$v_2^{S+B}(m_{inv}) = v_2^S \frac{S}{S+B}(m_{inv}) + v_2^B(m_{inv}) \frac{B}{S+B}(m_{inv}), \quad (3.25)$$

where S is the signal yield, B is background yield,  $v_2^S$ ,  $v_2^B$  and  $v_2^{S+B}$  are the  $v_2$  for signal, background and total particles, respectively. The ratios  $\frac{S}{S+B}$  and  $\frac{B}{S+B}$  are functions of invariant mass. The term  $v_2^B(m_{inv})$  is parametrized as a linear function in order to take care of the  $v_2^B$  value as a function of ( $m_{inv}$ ). Here  $v_2^B$  has been taken as a  $3^{rd}$  order polynomial function of invariant mass and its consistency has been verified by using  $1^{st}$  and  $2^{rd}$  order polynomial. The fit result  $v_2^S$  is the final  $v_2$ . The each term of Eq. 6.1 is shown in Fig. 3.11 for  $\phi$  meson at  $\sqrt{s_{NN}} = 39$  GeV in Au+Au collisions. The  $v_2$  obtained from fit is corrected for resolution event by event [10]. The consistency between  $(\phi - \Psi_2)$  bin and  $v_2$  vs.  $m_{inv}$  method is reported in the bottom right panel of Fig. 3.11.

## 3.3 Systematic uncertainties

The systematic uncertainties were evaluated by varying the methods and parameters used to determine the EP angles and particle yields. The differences between the  $v_2$  vs.  $m_{inv}$  method and  $\phi$ -binning method were taken into account in the systematic uncertainties. The main source of systematic uncertainty for  $\phi$ -meson yields are the following:

### 3.3.1 Uncertainty in particle identification

For systematic study, following cuts has been varied for kaon selection.

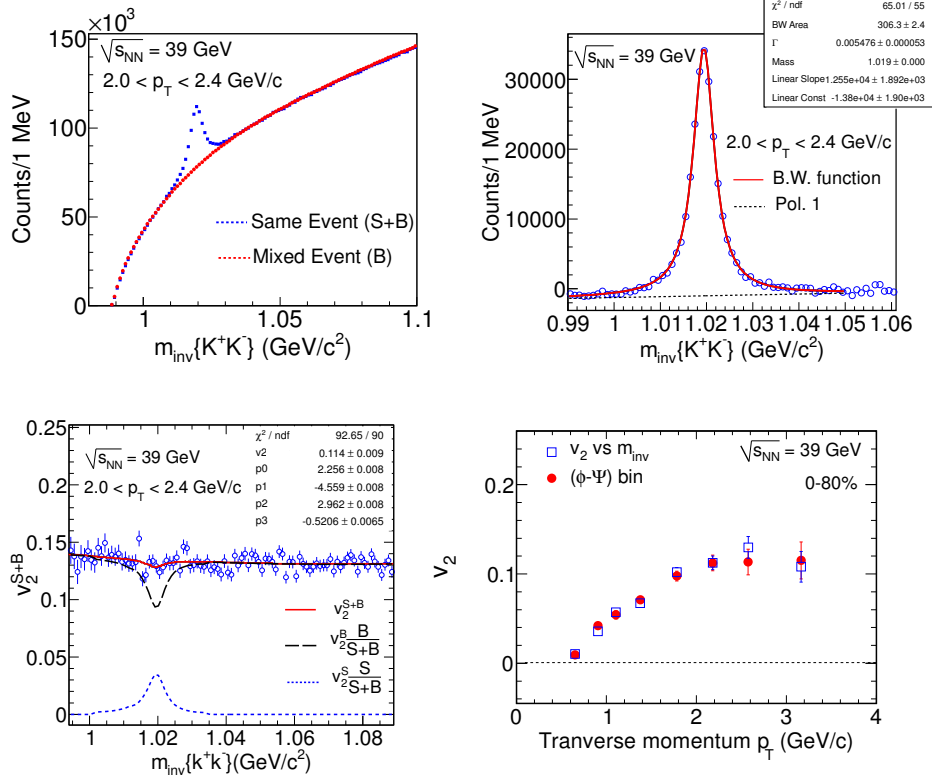


Figure 3.11: (Color online) Upper left panel: Invariant mass of  $K^+$  and  $K^-$  pairs in a same event (shown by blue line) and in a mixed event after normalization (shown by red line) for  $2.1 < p_T < 2.7$  GeV/c in Au+Au collisions at  $\sqrt{s_{NN}} = 39$  GeV for 0-80% centrality. Upper right panel: Background (mixed event) subtracted invariant mass of  $K^+$  and  $K^-$  pairs, i.e.  $\phi$ -meson signal fitted with Breit-Wigner function (B.W) + 1st order polynomial. (Details of  $\phi$ -meson signal extraction will be discussed in chapter 3). Bottom left panel:  $v_2^{S+B}$  as function of invariant mass fitted with function shown in Eq. 6.1. Bottom right panel: The  $\phi$ -meson  $v_2$  obtained from  $v_2$  vs.  $m_{inv}$  method are compared with  $(\phi - \Psi_2)$  bin method for  $\sqrt{s_{NN}} = 39$  GeV and 0-80% centrality. Errors are statistical.

Number of fit points	$\geq 15$	$\geq 20$	$\geq 25$
Dca	$\leq 3.0$ cm	$\leq 2.0$ cm	$\leq 1.5$ cm
Ratio of fit points to possible points	$\geq 0.52$	$\geq 0.54$	
$n\sigma$ cut on kaon dE/dx	$\leq 2.0  \sigma $	$\leq 1.5  \sigma $	

In addition, momentum dependent  $m^2$  cuts were used in TOF PID. The momentum dependent  $m^2$  cuts are  $0.18 < m^2 < 0.36$  GeV<sup>2</sup>/c<sup>4</sup> for  $p_T \leq 0.8$  GeV/c and  $0.15 < m^2 < 0.36$  GeV<sup>2</sup>/c<sup>4</sup> for  $p_T \geq 0.8$  GeV/c.

### 3.3.2 Uncertainty from residual background

The shape of residual background after mixed event subtraction varies with  $p_T$ . This is because of contamination in kaon selection. To estimate the effect different methods has been used for raw  $\phi$  yield extraction.

1. Varying fit function range for residual background.
2. Using different fit function for residual background
  - 1st order polynomial (Poly. 1)
  - 2nd order polynomial (Poly. 2)

The root-mean-square value of the distribution for each data point is consider as systematic error on this data point. Systematic error on  $\phi$ -meson  $v_2$  for different sources are shown in Fig. 3.12 for Au+Au collisions at  $\sqrt{s_{NN}} = 39$  GeV.

## 3.4 Results & Discussion

In this section the energy dependence of  $\phi$ -meson  $v_2$  will be discussed. As mentioned previously that all the results are from  $\eta$ -sub method and  $v_2$  vs.  $m_{inv}$  method.

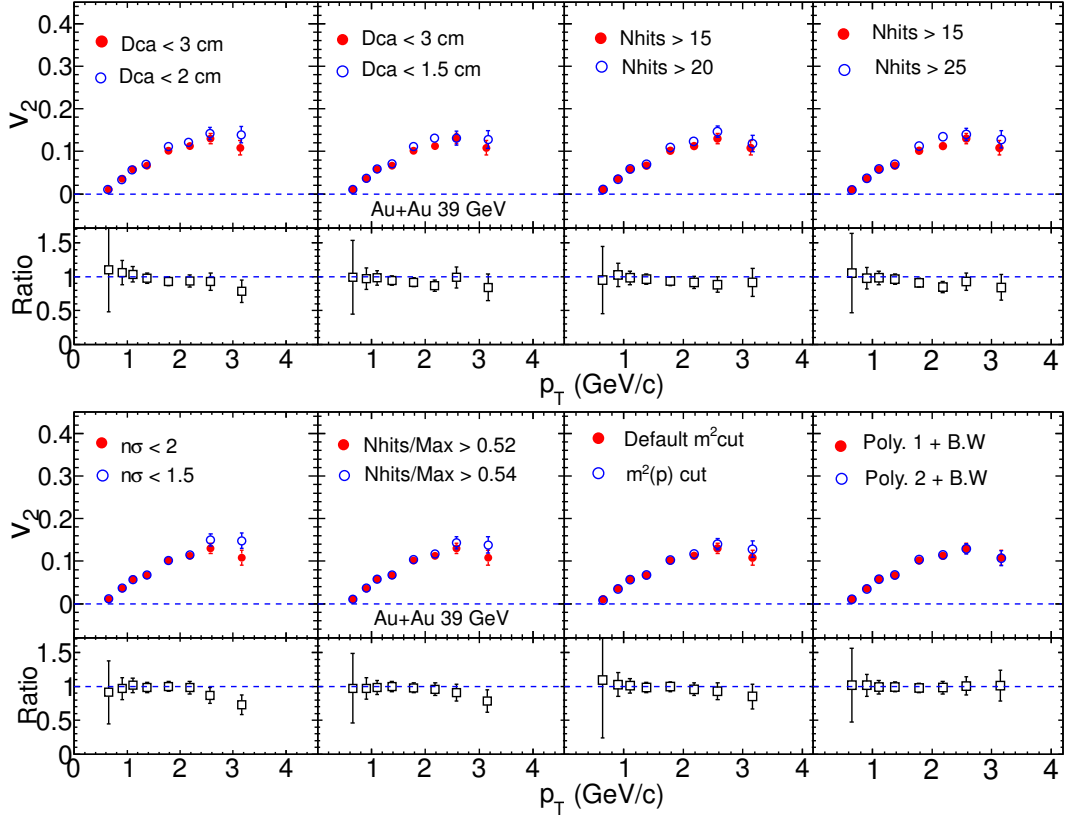


Figure 3.12: (Color online)  $\phi$ -meson  $v_2$  using different cuts in Au+Au collisions at  $\sqrt{s_{NN}} = 39$  GeV. The ratios with default value are shown in bottom panels. Error bars are statistical.

### 3.4.1 Differential $\phi$ -meson $v_2$

The results for measurements of the  $\phi$ -meson  $v_2$  as a function of  $p_T$  are presented in the Fig. 3.13. These results are for 0-80% centrality and measured at mid-rapidity ( $|y| < 1.0$ ) [13]. The shape of  $\phi v_2(p_T)$  for  $\sqrt{s_{NN}} = 19.6$  GeV to 62.4 GeV are similar with the results of  $\phi v_2(p_T)$  at  $\sqrt{s_{NN}} = 200$  GeV [14]. But at 7.7 and 11.5 GeV, the  $\phi v_2$  values at the highest measured  $p_T$  bins are observed to be smaller than other energies. To understand these results let us discuss effect of partonic and hadronic interaction on the  $\phi$ -meson  $v_2$ . The two main possibility of  $\phi$ -meson production are (a) kaon coalescence and (b) coalescence of  $s$  and  $\bar{s}$  quarks in the medium. The recent

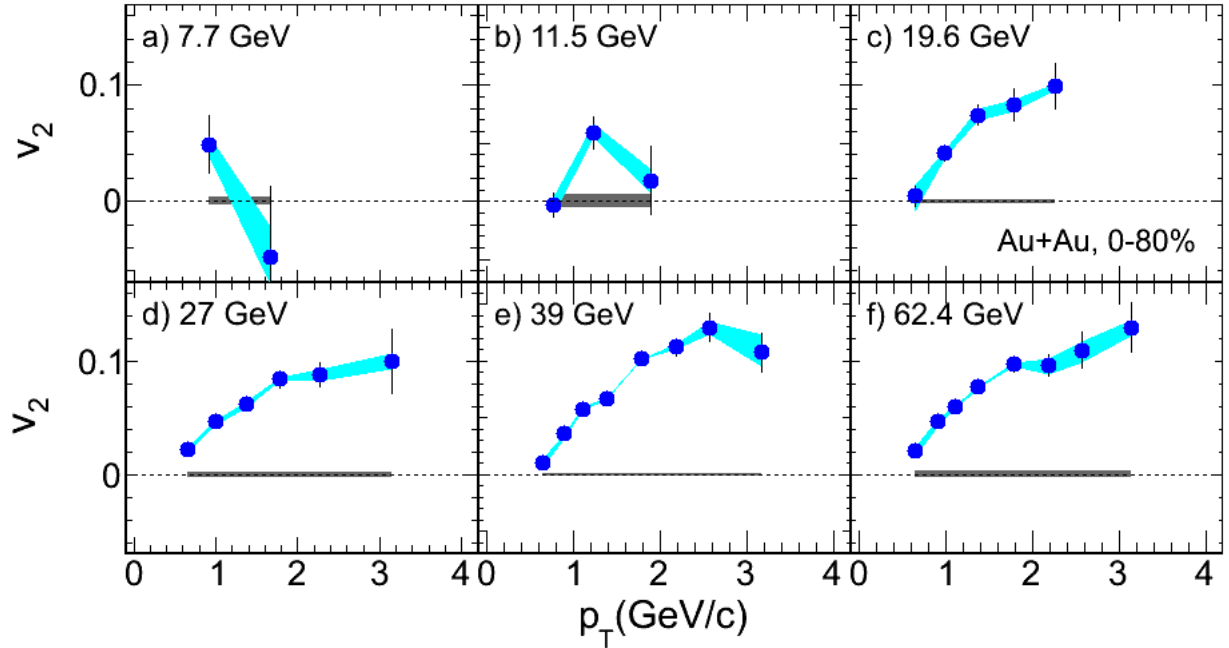


Figure 3.13: (Color online) The  $\phi$ -meson  $v_2(p_T)$  at mid-rapidity ( $|y| < 1.0$ ) in Au+Au collisions at  $\sqrt{s_{NN}} = 7.7 - 62.6$  GeV for 0-80% centrality [13]. The systematic uncertainties are shown by the shaded areas attached to the data points, while the global systematic uncertainties are shown as the shaded horizontal bar near  $v_2 = 0$  and the vertical lines are statistical uncertainties.

results from RHIC [14] and NA49 Collaboration [15] on the  $\phi$ -meson production show that the contribution from kaon coalescence should be small in this energy range and the  $\phi$ -meson production is expected to be dominated by parton recombination or coalescence. The hadronic interaction cross section of  $\phi$  mesons is much smaller compared to that of other hadrons and  $\phi$  mesons freeze out very early and close to chemical freeze-out temperature [18]. Therefore the effect of late stage hadronic interaction on  $\phi$   $v_2$  is small and most of the contribution on  $v_2$  is from partonic phase [16, 21]. So the large  $\phi$ -meson  $v_2$  at  $\sqrt{s_{NN}} \geq 15$  GeV indicates the formation

partonic matter and small  $v_2$  at  $\sqrt{s_{NN}} \leq 11.5$  could indicate dominance of hadron interactions.

### 3.4.2 Mass ordering of $\phi$ $v_2$ at low $p_T$

According to ideal hydrodynamics,  $v_2(p_T)$  follows a mass ordering, such that  $v_2$  of heavier particles is small compared to lighter hadrons [19]. In data, mass ordering was observed in the low  $p_T$  region ( $p_T < 2.0$  GeV/c) for top RHIC energy [20]. In Fig. 3.14, the  $v_2(p_T)$  values in the low transverse momentum range ( $p_T < 1.5$  GeV/c) for various identified particle species are directly compared [13]. One can see that the mass ordering is valid for all energies as was observed earlier at  $\sqrt{s_{NN}} = 200$  GeV [20]. Only the  $\phi$  meson deviate from this general trend at the lower energies. Their  $v_2(p_T)$  values are slightly smaller compared to all of the other hadrons. Starting at  $\sqrt{s_{NN}} = 39$  GeV, every  $\phi$  mesons  $v_2(p_T)$  value is smaller than the corresponding value for the heavier  $\bar{\Lambda}$ . This also supports the picture that partonic interactions become gradually smaller as the beam energy decreases.

### 3.4.3 Number-of-constituent quark scaling

The results from RHIC on the  $v_2$  for identified baryons and mesons when measured as a function of transverse kinetic energy ( $m_T - m$ ), where  $m_T = \sqrt{p_T^2 + m^2}$  is the transverse mass,  $m$  is the mass of the hadron, show a unique scaling at  $\sqrt{s_{NN}} = 200$  GeV. When  $v_2$  and  $m_T - m$  are scaled by the number-of-constituent quarks ( $n_q$ ) for a hadron, the  $v_2$  values follow a universal scaling for all the measured hadrons [21]. This observation is known as the number-of-constituent quark (NCQ) scaling. The NCQ scaling was originally predicted for  $v_2$  at intermediate transverse momenta ( $2.0 \leq p_T \leq 4.0$  GeV/c) when  $v_2/n_q$  plotted as function of  $p_T/n_q$  [22]. The observed NCQ scaling at RHIC can be explained by considering particle production mechanism via the quark recombination model and therefore it can be considered as a good signature of partonic collectivity [23]. This scaling should vanish in a hadron gas system at lower energies. Thus, the breakdown of NCQ scaling would be a necessary signature for

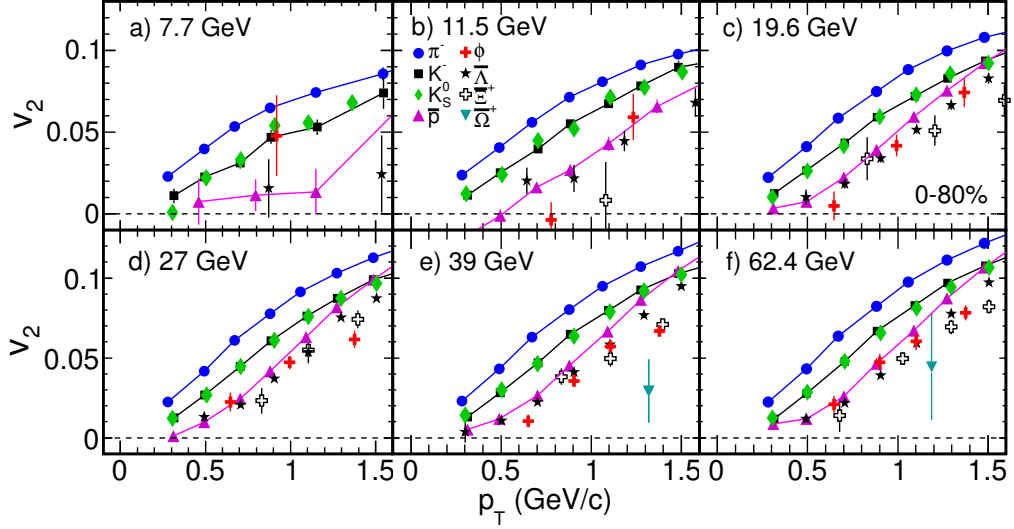


Figure 3.14: (Color online) The elliptic flow,  $v_2(p_T)$ , in 0-80% central Au+Au collisions for selected identified particles plotted only for the transverse momentum up-to 1.5 GeV/c to emphasize the mass ordering at low  $p_T$  [13]. Only statistical error bars are shown. Systematic errors are much smaller than the statistical errors. The lines connecting  $v_2(p_T)$  data points for  $\pi^-$ ,  $K^-$  and  $\bar{p}$  is just to guide the eye of the reader.

a QCD phase transition from partonic to hadronic matter. It will be interesting to investigate NCQ scaling for different beam energies. This will help us to determine the relevant degrees of freedom of the produced system in heavy-ion collision. Figure 3.15 and Fig. 3.16 presents the scaled  $v_2$  by  $n_q$  as a function of  $p_T/n_q$  and  $(m_T - m)/n_q$ , respectively, for 0-80% central Au+Au collisions for selected identified particles at various beam energies. The NCQ scaling holds fairly well for all particles including  $\phi$  mesons at  $\sqrt{s_{NN}} \geq 19.6$  GeV. This could be considered as a signature of partonic collectivity. However, at  $\sqrt{s_{NN}} = 7.7$  and 11.5 GeV, the  $\phi$ -meson  $v_2$  deviates from the trend of the other hadrons at highest measured  $p_T$  values by  $1.8\sigma$  and  $2.3\sigma$ , respectively. This could be related to the lower hadronic cross sections of particles

containing multiple strange quarks. Due to the small hadronic interaction cross-section,  $v_2$  of  $\phi$  mesons mostly reflect collectivity from the partonic phase. So the small magnitude of the  $\phi$ -meson  $v_2$  at  $\sqrt{s_{NN}} \leq 11.5$  GeV could be the effect for a system, where hadronic interactions are more important. But more statistics are needed at  $\sqrt{s_{NN}} = 7.7$  and 11.5 GeV for  $\phi$ -meson  $v_2$  measurement to draw a clear conclusion and therefore  $\phi$  meson measurement would be one of the focuses in the proposed BES phase II program.

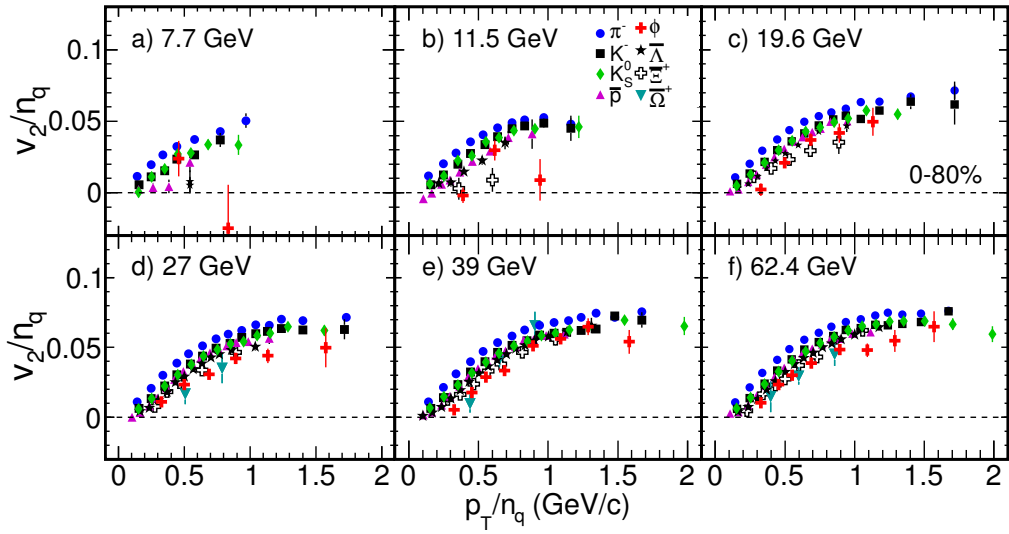


Figure 3.15: (Color online) The NCQ-scaled elliptic flow,  $v_2/n_q$ , versus  $p_T/n_q$  for 0-80% central Au+Au collisions for selected identified particles [13]. Only statistical error bars are shown.

### 3.4.4 Centrality dependence of $\phi$ -meson $v_2$

The centrality dependence of  $\phi$ -meson  $v_2(p_T)$  are presented in Fig. 3.17 for  $\sqrt{s_{NN}} = 11.5$  to 62.4 GeV. Due to very small event statistics at  $\sqrt{s_{NN}} = 7.7$  GeV the measurement for centrality dependence has not been shown. Figure 3.17 shows  $\phi$ -meson

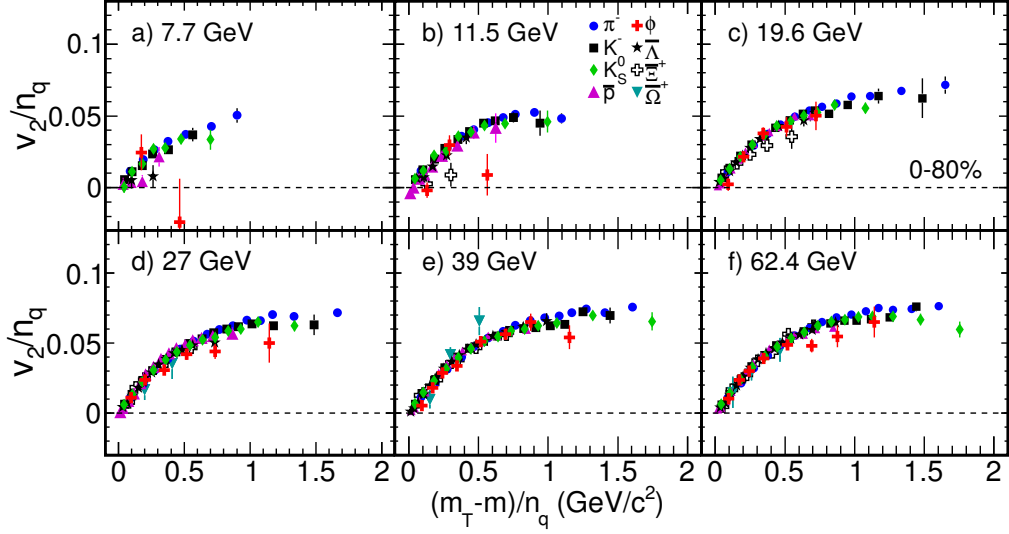


Figure 3.16: (Color online) The NCCQ-scaled elliptic flow,  $v_2/n_q$ , versus  $(m_T - m)/n_q$  for 0-80% central Au+Au collisions for selected identified particles [13]. Only statistical error bars are shown.

$v_2(p_T)$  for two different centrality bins: 0-30% and 30-80%.  $\phi$   $v_2$  values of 30 – 80% are larger than 0 – 30% collisions. This is expected as the eccentricity of the initial nuclear overlap area (reflecting initial spatial anisotropy) is larger for 30 – 80% compared to 0 – 30%.

In order to investigate the collectivity of the medium, one need to remove the effects due to the initial spatial geometry of the produced medium. This can be done by dividing the measured  $v_2$  by eccentricity of the initial spatial geometry. Here the participant eccentricity,  $\varepsilon_{part}\{2\}$ , calculated using a Monte Carlo Glauber Model, is used. Values of  $\varepsilon_{part}\{2\}$  with systematic uncertainties for 0-30% and 30-80% centrality bins at  $\sqrt{s_{NN}}= 11.5, 19.6, 27, 39$  and 62.4 GeV are shown in table 3.5. The advantage of using  $\varepsilon_{part}\{2\}$  is that this calculation of the eccentricity takes into account event-by-event fluctuations in eccentricity for a fixed impact parameter [25].

The  $v_2(p_T)/\varepsilon_{part}\{2\}$  for 0-30% and 30-80% centrality bins are presented in Fig. 3.18 for different beam energies. One can observe that  $v_2(p_T)/\varepsilon_{part}\{2\}$  is higher at 0-30% centrality than 30-80% for the energies 62.4 to 19.6 GeV. This is consistent with the picture that collective interactions are stronger in collisions with larger numbers of participants. Because of small statistics at 11.5 GeV, it is not possible to make any conclusion.

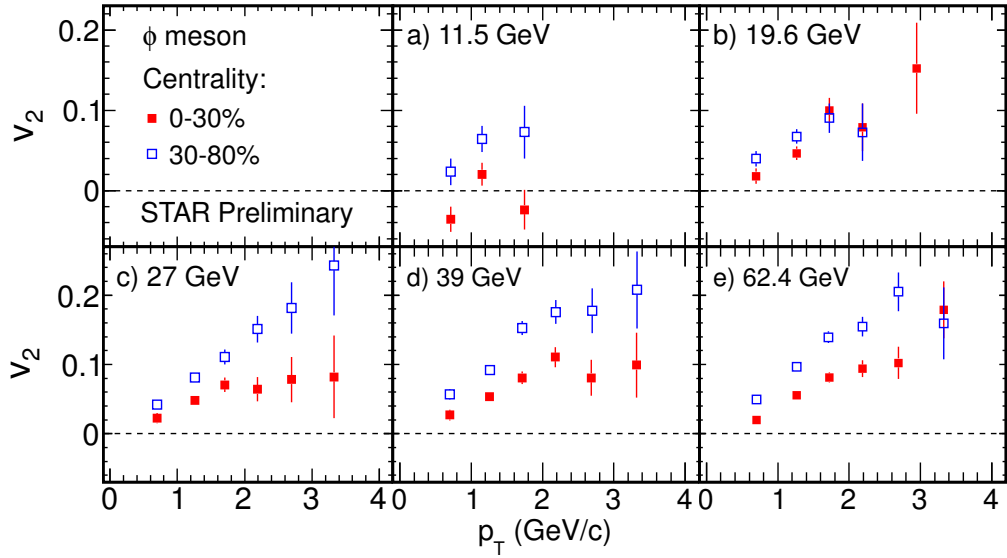


Figure 3.17: (Color online) The  $\phi$ -meson  $v_2(p_T)$  for 0-30% and 30-80% centrality bins. Error bars represent statistical errors.

### 3.4.5 $p_T$ integrated $\phi$ -meson $v_2$

The  $p_T$  integrated elliptic flow  $\langle v_2 \rangle$ , which is also an interesting observable, can be defined as:

$$\langle v_2 \rangle = \frac{\int v_2(p_T)(dN/dp_T)dp_T}{\int (dN/dp_T)dp_T}, \quad (3.26)$$

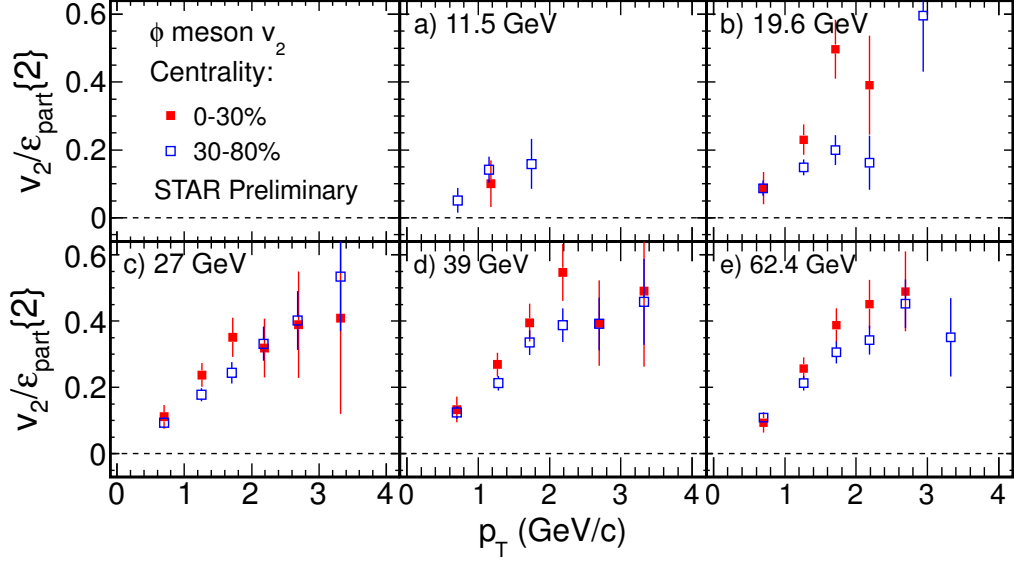


Figure 3.18: (Color online) The  $\phi$ -meson  $v_2(p_T)$  scaled by  $\varepsilon_{part}\{2\}$  for 0-30% and 30-80% centrality bins. The systematic errors on  $\varepsilon_{part}\{2\}$  are added in quadrature to the statistical error of  $v_2$ .

i.e. the  $\langle v_2 \rangle$  folds the measured  $v_2$  versus  $p_T$  with the  $p_T$  distribution ( $dN/dp_T$ ) of the particles. To calculate the  $\langle v_2 \rangle$  of  $\phi$  mesons each  $v_2(p_T)$  distribution was fitted (shown in Fig. 3.19) with function : a 3<sup>rd</sup> order polynomial function and a function of the form

$$f_{v_2}(n) = \frac{an}{1 + \exp[-(p_T/n - b)/c]} - dn, \quad (3.27)$$

where  $a$ ,  $b$ ,  $c$  and  $d$  are free parameters and  $n$  is the number of constituent quarks. This function was inspired by parameterizations of quark number scaling [24]. After that  $p_T$  distribution of the  $\phi$  mesons (details of  $p_T$  distribution will be discussed in the next chapter) has been fitted with Levy function as shown in Fig. 3.19. The functional form of Levy function is given by

$$f_{Levy}(p_T) = \frac{dN}{dy} \frac{(n-1)(n-2)}{2\pi nT(nT + m(n-2))} \left(1 + \frac{\sqrt{p_T^2 + m^2} - m}{nT}\right)^{-n}, \quad (3.28)$$

$\sqrt{s_{NN}}$ (GeV)	0 – 30%	30 – 80%
11.5	$0.2020 \pm 0.0226$	$0.4537 \pm 0.0336$
19.6	$0.2020 \pm 0.0220$	$0.4540 \pm 0.0340$
27	$0.2014 \pm 0.0210$	$0.4533 \pm 0.0329$
39	$0.2015 \pm 0.0211$	$0.4533 \pm 0.0327$
62.4	$0.2026 \pm 0.0213$	$0.4535 \pm 0.0335$

Table 3.5: Values of  $\varepsilon_{part}\{2\}$  with systematic uncertainties for 0-30% and 30-80% centrality bins at  $\sqrt{s_{NN}} = 11.5, 19.6, 27, 39$  and  $62.4$  GeV.

where  $T$  is known as the inverse slope parameter,  $dN/dy$  is the  $\phi$ -meson yield per unit rapidity,  $m$  is the rest mass of  $\phi$  meson and  $n$  is the Levy function parameter. The  $\langle v_2 \rangle$  for each choice of  $v_2(p_T)$  parameterization is given by the integral of the corresponding distributions normalized by integral of the  $p_T$  distribution. In addition the  $\langle v_2 \rangle$  has been calculated directly from measured data points of  $v_2(p_T)$  with corresponding yield obtained from the fit function to the  $p_T$  distribution. The final  $\langle v_2 \rangle$  was obtained from calculating the mean of the three  $\langle v_2 \rangle$  results and the systematic error was estimated from maximum deviation from the mean. There are two source for the statistical error, one is errors on  $p_T$  distribution and other is errors on  $v_2(p_T)$ . Since the error on  $dN/dp_T$  is very small compared to that on  $v_2(p_T)$ , one can simply neglect the error of  $dN/dp_T$ . Hence, only errors on  $v_2(p_T)$  are taken care for calculation of final statistical error on  $\langle v_2 \rangle$ . The errors on  $v_2$  are parameterized as a function of  $p_T$  and extrapolated to low and high  $p_T$  as shown in bottom panel of Fig. 3.19.

Figure 3.20 shows  $p_T$  integrated  $\phi$ -meson  $v_2$  as a function of centre of mass energy for 0-80% centrality. Due to limited statistics, results for 7.7 GeV is not shown here. One can see that  $\langle v_2 \rangle$  increases with increasing beam energy. The details of this calculation for other energies are shown in Appendix.

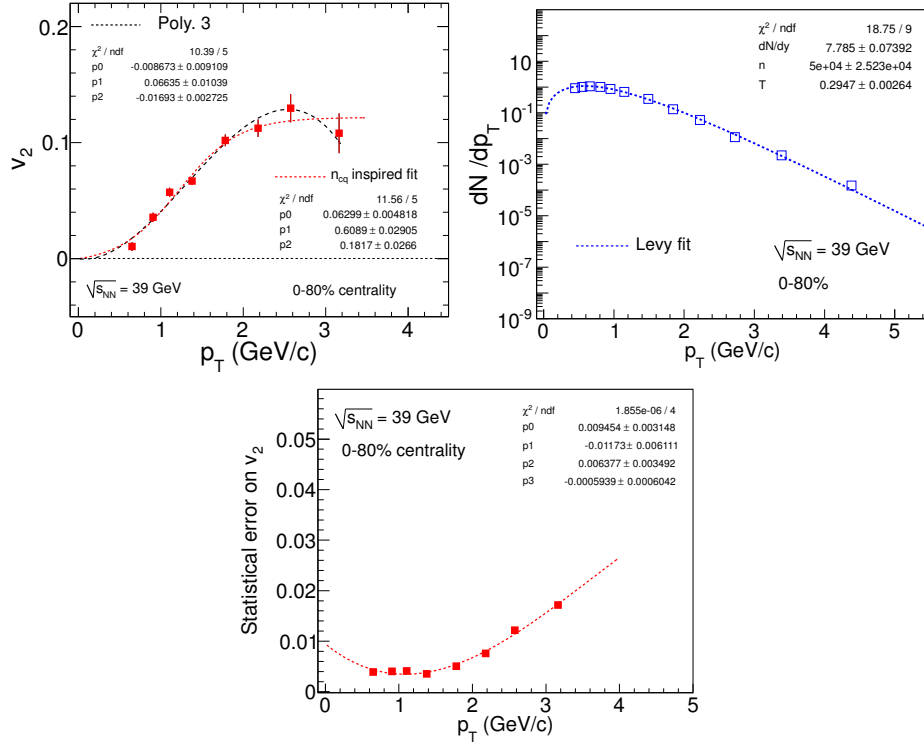


Figure 3.19: (Color online) Left panel: The  $\phi$ -meson  $v_2(p_T)$  at  $\sqrt{s_{NN}} = 39$  GeV for 0-80% centrality bin is fitted with 3<sup>rd</sup> order polynomial and with function described in Eq. 3.27. Right panel: The  $\phi$ -meson  $dN/dp_T$  vs  $p_T$  at  $\sqrt{s_{NN}} = 39$  GeV for 0-80% centrality bin is fitted with Levy function. Bottom panel: Statistical errors on  $v_2(p_T)$  at  $\sqrt{s_{NN}} = 39$  GeV for 0-80% centrality bin are fitted with 4<sup>th</sup> order polynomial.

### 3.4.6 Transport model comparison

Figure 3.21 shows the comparison of elliptic flow of  $\phi$  mesons in 0-80% minimum-bias Au+Au collisions at mid-rapidity for  $\sqrt{s_{NN}} = 7.7, 11.5, 19.6, 27, 39$  and 62.4 GeV with the corresponding results from the AMPT model (version 1.11) [22]. The measured data points are compared with both AMPT String Melting (3 and 10 mb parton-parton cross-section) and AMPT Default version. The interactions between the minijet partons in the AMPT Default model and those between partons in the

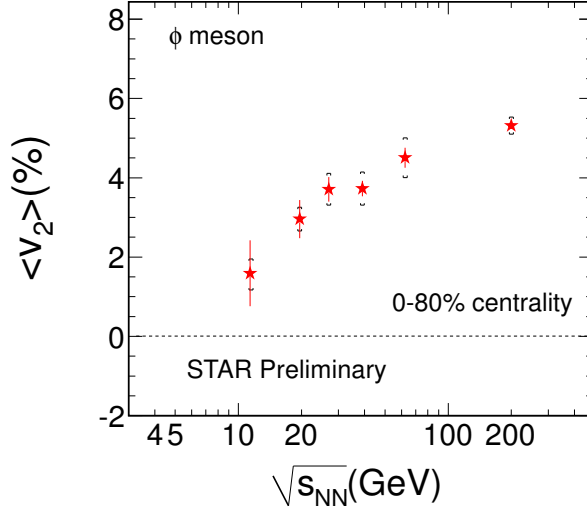


Figure 3.20: (Color online) The  $p_T$  integrated  $\phi$ -meson  $v_2$  for various centre of mass energies for 0-80% centrality in Au+Au collisions. Vertical lines are the statistical error and systematic error are shown by cap symbol. The details of  $\phi$   $v_2$  analysis at 200 GeV will be discussed in chapter 6.

AMPT-SM could give rise to substantial  $v_2$ . Therefore, agreement between the data and the results from AMPT-SM would indicate the contribution of partonic interactions to the measured  $v_2$ . At  $\sqrt{s_{NN}} = 62.4$  GeV experimental data are in a good agreement with AMPT String Melting model with 10 mb parton-parton cross-section. The measured  $\phi$   $v_2$  for  $p_T < 1.5$  GeV/c lie between the model results with 3 mb and 10 mb partonic cross sections for the energy range  $19.6 \leq \sqrt{s_{NN}} \leq 39$  GeV, but in order to explain the measurements for  $p_T > 1.5$  GeV/c a parton-parton cross-section of the order of 10 mb is required. Due to limited statistics we have 2 and 3 data points at  $\sqrt{s_{NN}} = 7.7$  and 11.5 GeV, respectively, and models can not explain the trend of  $\phi$ -meson  $v_2$ . Both AMPT-SM and AMPT Default model over predicts experimental data at intermediate  $p_T$  for  $\sqrt{s_{NN}} = 7.7$  and 11.5 GeV. As we expect that the  $\phi$ -meson  $v_2$  mostly reflect the collectivity from the partonic phase, therefore from the compar-

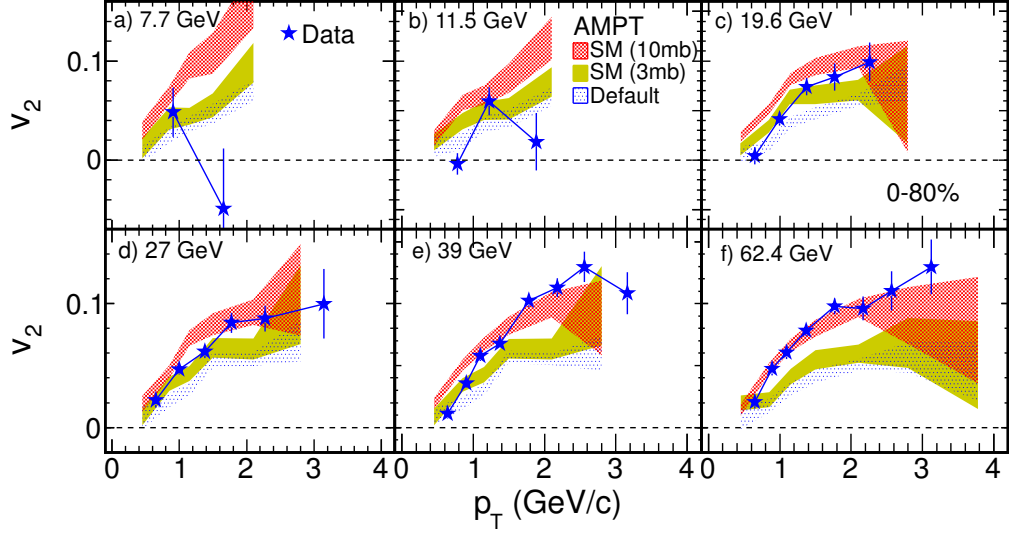


Figure 3.21: (Color online) The  $\phi$ -meson  $v_2(p_T)$  for Au+Au minimum-bias collisions at mid-rapidity ( $|\eta| < 1.0$ ) from the STAR experiment at RHIC compared to the corresponding AMPT model calculation at various beam energies. The errors shown are statistical.

Comparison of experimental data with AMPT model one can conclude that for  $\sqrt{s_{NN}} \geq 19.6$  GeV the partonic collectivity has been developed at RHIC and for  $\sqrt{s_{NN}} \leq 11.5$  GeV, the contribution to the collectivity from hadronic phase is dominant. The  $p_T$  integrated  $\phi$ -meson  $v_2$  for Au+Au minimum-bias collisions at mid-rapidity ( $|y| < 1.0$ ) are also compared to the corresponding AMPT model calculation at various beam energies and shown in Fig. 3.22. It is clear from the Fig. 3.22 that as the beam energy decreases, the contribution to the collectivity from the partonic phase decreases and for  $\sqrt{s_{NN}} \leq 11.5$  GeV, the hadronic interaction plays a dominant role.

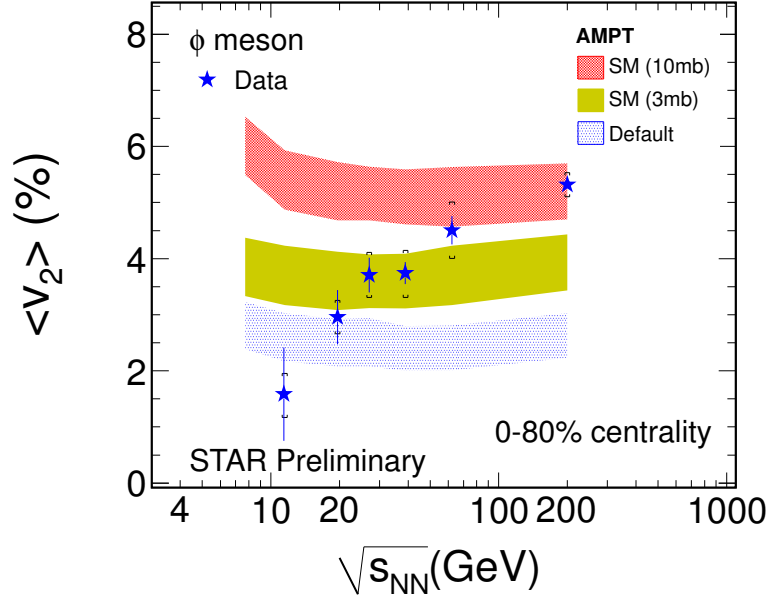


Figure 3.22: (Color online) The  $p_T$  integrated  $\phi$ -meson  $v_2$  for Au+Au minimum-bias collisions at mid-rapidity ( $|\eta| < 1.0$ ) from the STAR experiment at RHIC are compared to the corresponding AMPT model calculation at various beam energies. Details of  $\phi$   $v_2$  analysis at 200 GeV will be discussed in chapter 6.

### 3.5 Summary

The measurement of  $\phi$ -meson  $v_2$  as function of  $p_T$  and collision centrality in Au+Au collisions at  $\sqrt{s_{NN}} = 7.7, 11.5, 19.6, 27, 39$  and  $62.4$  GeV recorded by the STAR detector has been discussed.  $\phi$ -meson  $v_2(p_T)$  shows similar behaviour for  $\sqrt{s_{NN}} \geq 19.6$  GeV. The NCQ scaling holds for  $\sqrt{s_{NN}} \geq 19.6$  GeV. However at  $\sqrt{s_{NN}} = 7.7$  and  $11.5$  GeV, the  $\phi$ -meson  $v_2$  show deviation from the other hadrons at highest measured  $p_T$  values by  $1.8\sigma$  and  $2.3\sigma$ , respectively. This may indicate that the contribution to the collectivity from partonic phases decreases at lower beam energies. We also compared the measured  $\phi$ -meson  $v_2$  with AMPT model calculation. It has been observed that

the experimental data can be explained by varying parton-parton interaction cross-section from 3mb to 10mb for  $\sqrt{s_{NN}} \geq 19.6$  GeV, but models fails to explain data at  $\sqrt{s_{NN}} = 7.7$  and 11.5 GeV. This indicates that for  $\sqrt{s_{NN}} \leq 11.5$  GeV, the hadronic interaction plays a dominant role. On the experimental side, high statistics data are needed in order to further understand the results.

# Bibliography

- [1] B. I. Abelev *et al.* (STAR Collaboration), Phys. Rev. **C 79**, 034909 (2009).
- [2] D. Kharzeev and M. Nardi, Phys. Lett. **B 507**, 121 (2001).
- [3] B. B. Back *et al.* (PHOBOS Collaboration), Phys. Rev. **C 70**, 021902(R) (2004).
- [4] J. Beringer *et al.* (Particle Data Group), Phys. Rev. **D 86**, 010001 (2012).
- [5] H. Bichsel, Nucl. Instrum. Meth. **A 562** 154 (2006).
- [6]  $\phi$ -meson Production in Au+Au Collisions at the Relativistic Heavy Ion Collider. PhD thesis by Eugene Toyonari Yamamoto, UCLA (2001).
- [7] P.F. Kolb *et al.*, Nucl. Phys. **A 715**, 653c (2003).
- [8] A. M. Poskanzer and S. A. Voloshin, Phys. Rev. **C 58**, 1671 (1998).
- [9] Zi-Wei Lin and C. M. Ko, Phys. Rev. **C 65**, 034904 (2002);  
Zi-Wei Lin *et al.*, Phys. Rev. **C 72**, 064901 (2005);  
Lie-Wen Chen *et al.*, Phys. Lett. **B 605**, 95 (2005).
- [10] H. Masui and A. Schmah, arXiv: 1212.3650v1 [nucl-ex].
- [11] B.I. Abelev *et al.* (STAR Collaboration), Phys. Rev. **C 77**, 054901 (2008).
- [12] N. Borghini and J. Y. Ollitrault, Phys. Rev. **C 70**, 064905 (2004).
- [13] L. Adamczyk *et al.* (STAR Collaboration), Phys. Rev. **C 88**, 014902 (2013).
- [14] B.I. Abelev *et al.* (STAR Collaboration), Phys. Rev. **C 79**, 064903 (2009).

- [15] C. Alt *et al.* (NA49 Collaboration), Phys. Rev. **C 78**, 044907 (2008).
- [16] B. Mohanty and N. Xu , J. Phys. **G 36**, 064022 (2009).
- [17] Md. Nasim, B. Mohanty and N. Xu, Phys. Rev. **C 87**, 014903 (2013).
- [18] J. Rafelski, B. Muller, Phys. Rev. Lett. **48**, 1066 (1982);  
A. Shor, Phys. Rev. Lett. **54**,1122 (1985);  
H. van Hecke *et al.* Phys. Rev. Lett. **81**, 5764 (1998);  
A. Sibirtsev *et al.* Eur. Phys. J. **A 29**, 209 (2006).
- [19] P. Huovinen *et al.*, Phys. Lett. **B 503**, 58 (2001).
- [20] B.I. Abelev *et al.* (STAR Collaboration), Phys. Rev. **C 77**, 054901 (2008).
- [21] J. Adams *et al.* (STAR Collaboration), Phys. Rev. Lett. **95**, 122301 (2005);  
A. Adare *et al.* (PHENIX Collaboration), *ibid.* **98**, 162301 (2007).
- [22] S. A. Voloshin, Nucl. Phys. **A 715**, 379 (2003).
- [23] D. Molnar and S. A. Voloshin, Phys. Rev. Lett. **91**, 092301 (2003).
- [24] X. Dong *et al.*, Phys. Lett. **B 597**, 328 (2004).
- [25] S. Manly *et al.*, Nucl. Phys. **A 774**, 523 (2006).

## 3.6 Appendix

### 3.6.1 Centrality selection condition using $N_{ch}^{raw}$ or refmult

Values of $N_{ch}^{raw}$ or refmult for different centralities									
	Centrality								
$\sqrt{s_{NN}}$	0-5%	5-10%	10-20%	20-30%	30-40%	40-50%	50-60%	60-70%	70-80%
200 GeV	> 446	> 379	> 269	> 184	> 119	> 73	> 41	> 21	> 10
62.4 GeV	> 339	> 285	> 199	> 135	> 85	> 54	> 30	> 16	> 7
39 GeV	> 316	> 265	> 185	> 125	> 81	> 50	> 28	> 15	> 7
27 GeV	> 288	> 241	> 168	> 114	> 74	> 45	> 26	> 13	> 6
19.6 GeV	> 268	> 227	> 161	> 111	> 75	> 47	> 28	> 16	> 8
11.5 GeV	> 221	> 184	> 127	> 86	> 56	> 34	> 19	> 10	> 5
7.7 GeV	> 185	> 154	> 106	> 72	> 46	> 28	> 16	> 8	> 4

Table 3.6: Values of  $N_{ch}^{raw}$  or refmult for all the centrality classes and all energies.

### 3.6.2 Data points of $\phi$ -meson $v_2$

Centrality: 0-80%

#### 3.6.2.1 $\sqrt{s_{NN}} = 62.4$ GeV:

$p_T$  bin center[8] = {0.6515,0.9055,1.1045,1.3785,1.7835,2.1785,2.5745,3.1375}

$v_2$  values[8] = {0.020467,0.0471095,0.0598547,0.077578,0.096987,0.096019,0.109442,0.12973}

Statistical error [8] = {0.00525,0.00532,0.00535,0.00456,0.00643,0.00962,0.0158,0.022}

Systematic low error [8] = {0.00566,0.00437,0.00278,0.00122,0.00153,0.00810,0.0101,0.0073}

Systematic high error[8] = {0.00411,0.00211,0.00166,0.00102,0.00190,0.00653,0.00822,0.00615}

Global Systematic error = {0.00288575}

#### 3.6.2.2 $\sqrt{s_{NN}} = 39$ GeV:

$p_T$  bin center[8] = {0.6505,0.9055,1.1055,1.3775,1.7815,2.1805,2.5755,3.1635}

$v_2$  values[8] = {0.0104781,0.0356858,0.0572164,0.0669468,0.101966,0.112441,0.12968,0.108037}

Statistical error [8] = {0.00392,0.00402,0.00409,0.0035,0.00504,0.00757,0.0121,0.0171}

Systematic low error [8] = {0.00484,0.00319,0.00113,0.000620,0.000936,0.00211,0.00653,0.0130}

Systematic high error[8] = {0.00376,0.00220,0.0025,0.00153,0.000799,0.00270,0.00533,0.0155}

Global Systematic error = {0.00141856}

#### 3.6.2.3 $\sqrt{s_{NN}} = 27$ GeV:

$p_T$  bin center[6] = {0.6515,0.9985,1.3765,1.7825,2.2735,3.1485}

$v_2$  values[6] = {0.02202,0.04697,0.06134,0.08411,0.08797,0.09988}

Statistical error [6] = {0.005853,0.004245,0.005393,0.008058,0.01042,0.02809}

Systematic low error [6] = {0.003333,0.003721,0.002584,0.001966,0.005516,0.007288}

Systematic high error[6] = {0.00255,0.001666,0.00284935,0.001509,0.004449,0.006877}

Global Systematic error = {0.00204473}

### 3.6.2.4 $\sqrt{s_{NN}} = 19.6 \text{ GeV}$ :

$$p_T \text{ bin center}[5] = \{0.6515, 0.9975, 1.3735, 1.7775, 2.2605\}$$

$$v_2 \text{ values}[5] = \{0.00429508, 0.0416252, 0.0740384, 0.0834012, 0.0991101\}$$

$$\text{Statistical error [5]} = \{0.00881035, 0.00663025, 0.00863229, 0.0135508, 0.0197109\}$$

$$\text{Systematic low error [5]} = \{0.0128433, 0.00288614, 0.0043494, 0.00550575, 0.00324487\}$$

$$\text{Systematic high error [5]} = \{0.00919987, 0.00337382, 0.00549493, 0.00441887, 0.00261673\}$$

$$\text{Global Systematic error} = \{0.00180674\}$$

### 3.6.2.5 $\sqrt{s_{NN}} = 11.5 \text{ GeV}$ :

$$p_T \text{ bin center}[3] = \{0.7775, 1.2345, 1.8865\}$$

$$v_2 \text{ values}[3] = \{-0.00372217, 0.0591929, 0.0180024\}$$

$$\text{Statistical error [3]} = \{0.0107628, 0.0140929, 0.0290041\}$$

$$\text{Systematic low error [3]} = \{0.00654685, 0.0049599, 0.0103747\}$$

$$\text{Systematic high error [3]} = \{0.00949784, 0.00738526, 0.00932728\}$$

$$\text{Global Systematic error} = \{0.00558752\}$$

### 3.6.2.6 $\sqrt{s_{NN}} = 7.7 \text{ GeV}$ :

$$p_T \text{ bin center}[2] = \{0.9185, 1.6685\}$$

$$v_2 \text{ values}[2] = \{0.0478335, -0.049273\}$$

$$\text{Statistical error [2]} = \{0.0247765, 0.0605828\}$$

$$\text{Systematic low error [2]} = \{0.00964971, 0.0232742\}$$

$$\text{Systematic high error [2]} = \{0.00910412, 0.0277136\}$$

$$\text{Global Systematic error} = \{0.00369459\}$$

### 3.6.3 Figures and fit parameter for integrated $v_2$ calculation

#### 3.6.3.1 Au+Au 200 GeV:

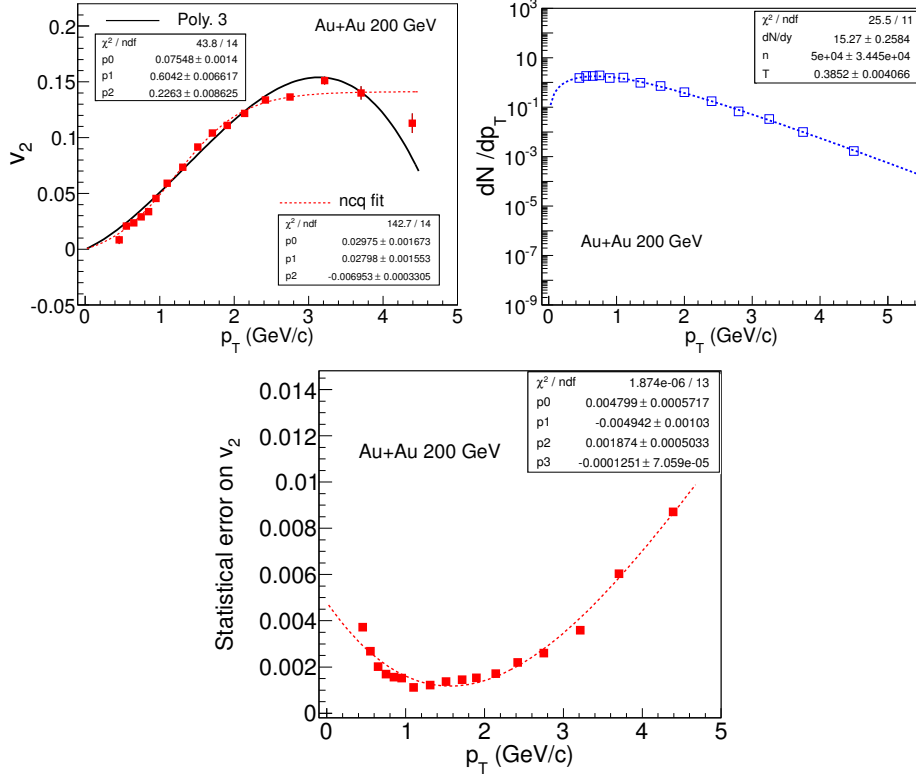


Figure 3.23: (Color online) Left panel: The  $\phi$ -meson  $v_2(p_T)$  at  $\sqrt{s_{NN}} = 200$  GeV for 0-80% centrality bin is fitted with 3<sup>rd</sup> order polynomial and with function described in Eq. 3.27. Right panel: The  $\phi$ -meson  $dN/dp_T$  vs  $p_T$  at  $\sqrt{s_{NN}} = 200$  GeV for 0-80% centrality bin is fitted with levy function. Bottom panel: Statistical errors on  $v_2(p_T)$  at  $\sqrt{s_{NN}} = 200$  GeV for 0-80% centrality bin are fitted with 4<sup>th</sup> polynomial.

### 3.6.3.2 Au+Au 62.4 GeV:

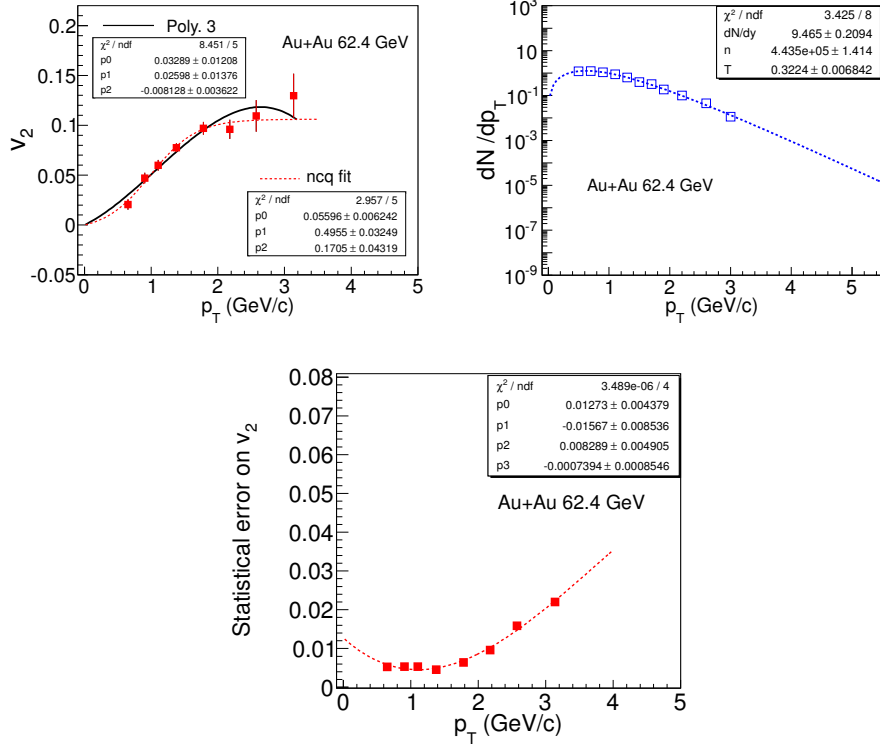


Figure 3.24: (Color online) Left panel: The  $\phi$ -meson  $v_2(p_T)$  at  $\sqrt{s_{NN}} = 62.4$  GeV for 0-80% centrality bin is fitted with 3<sup>rd</sup> order polynomial and with function described in Eq. 3.27. Right panel: The  $\phi$ -meson  $dN/dp_T$  vs  $p_T$  at  $\sqrt{s_{NN}} = 62.4$  GeV for 0-80% centrality bin is fitted with levy function. Bottom panel: Statistical errors on  $v_2(p_T)$  at  $\sqrt{s_{NN}} = 62.4$  GeV for 0-80% centrality bin are fitted with 4<sup>th</sup> order polynomial.

### 3.6.3.3 Au+Au 27 GeV:

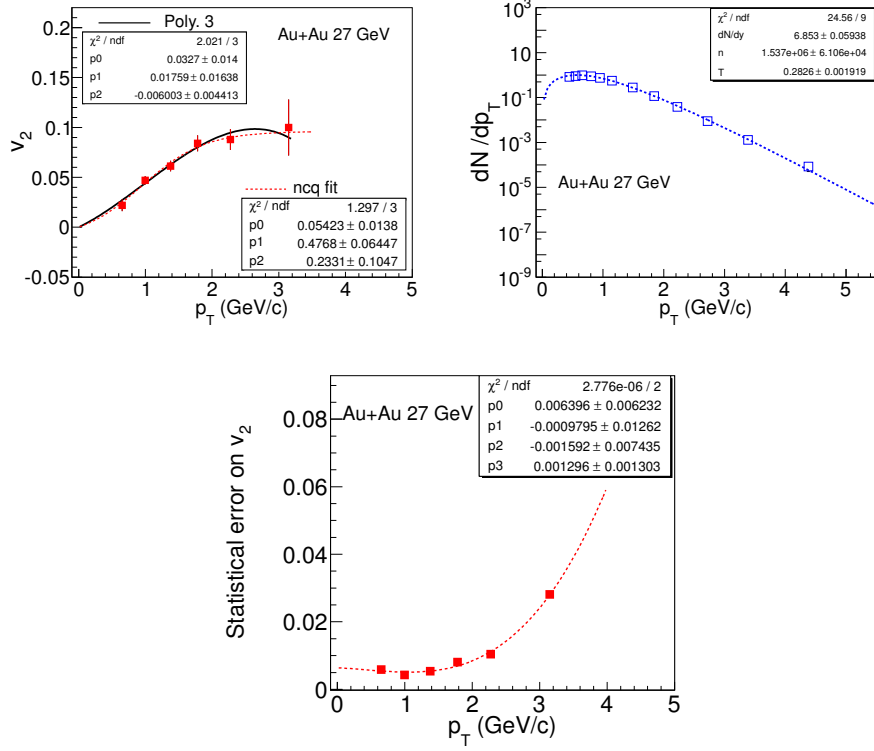


Figure 3.25: (Color online) Left panel: The  $\phi$ -meson  $v_2(p_T)$  at  $\sqrt{s_{NN}} = 19.6$  GeV for 0-80% centrality bin is fitted with 3<sup>rd</sup> order polynomial and with function described in Eq. 3.27. Right panel: The  $\phi$ -meson  $dN/dp_T$  vs  $p_T$  at  $\sqrt{s_{NN}} = 19.6$  GeV for 0-80% centrality bin is fitted with levy function. Bottom panel: Statistical errors on  $v_2(p_T)$  at  $\sqrt{s_{NN}} = 19.6$  GeV for 0-80% centrality bin are fitted with 4<sup>th</sup> order polynomial.

### 3.6.3.4 Au+Au 19.6 GeV:

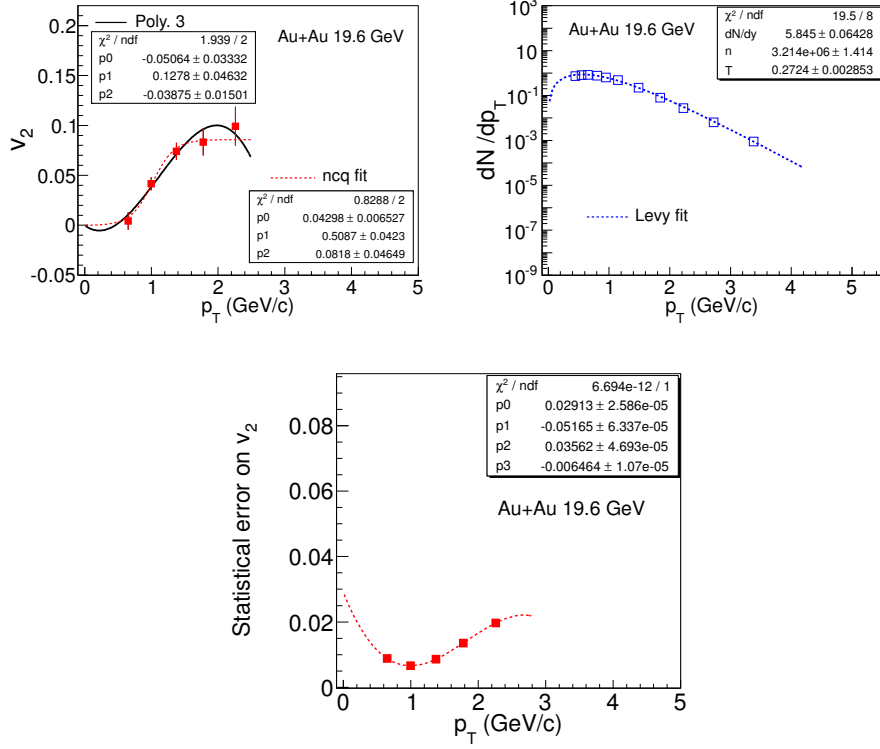


Figure 3.26: (Color online) Left panel: The  $\phi$ -meson  $v_2(p_T)$  at  $\sqrt{s_{NN}} = 19.6$  GeV for 0-80% centrality bin is fitted with 3<sup>rd</sup> order polynomial and with function described in Eq. 3.27. Right panel: The  $\phi$ -meson  $dN/dp_T$  vs  $p_T$  at  $\sqrt{s_{NN}} = 19.6$  GeV for 0-80% centrality bin is fitted with levy function. Bottom panel: Statistical errors on  $v_2(p_T)$  at  $\sqrt{s_{NN}} = 19.6$  GeV for 0-80% centrality bin are fitted with 4<sup>th</sup> order polynomial.

### 3.6.3.5 Au+Au 11.5 GeV:

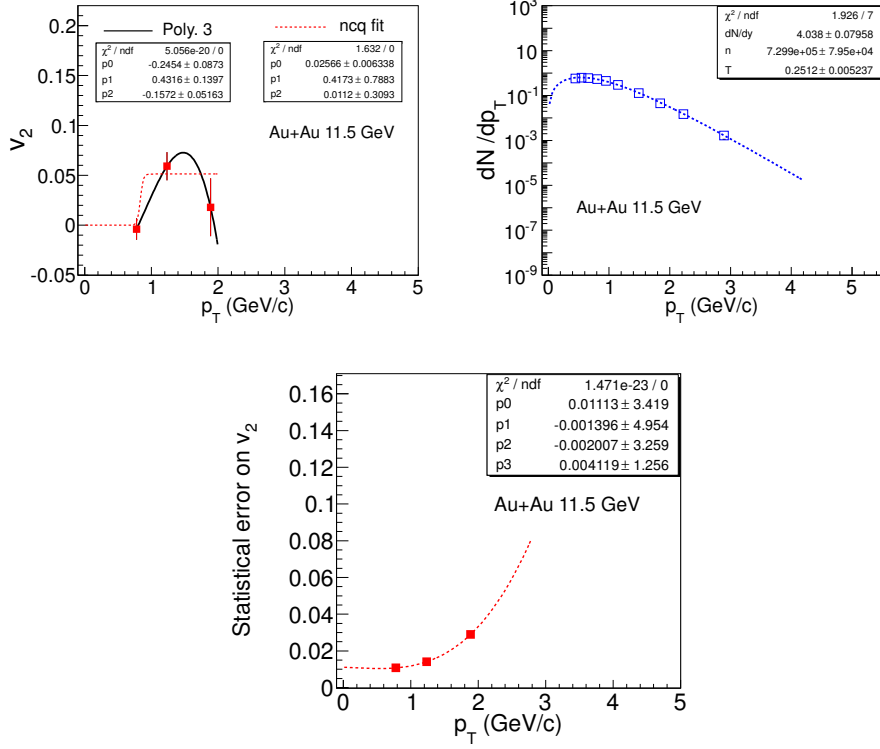


Figure 3.27: (Color online) Left panel: The  $\phi$ -meson  $v_2(p_T)$  at  $\sqrt{s_{NN}} = 11.5$  GeV for 0-80% centrality bin is fitted with 3<sup>rd</sup> order polynomial and with function described in Eq. 3.27. Right panel: The  $\phi$ -meson  $dN/dp_T$  vs  $p_T$  at  $\sqrt{s_{NN}} = 11.5$  GeV for 0-80% centrality bin is fitted with levy function. Bottom panel: Statistical errors on  $v_2(p_T)$  at  $\sqrt{s_{NN}} = 11.5$  GeV for 0-80% centrality bin are fitted with 4<sup>th</sup> order polynomial.

### 3.6.4 TPC event plane distributions

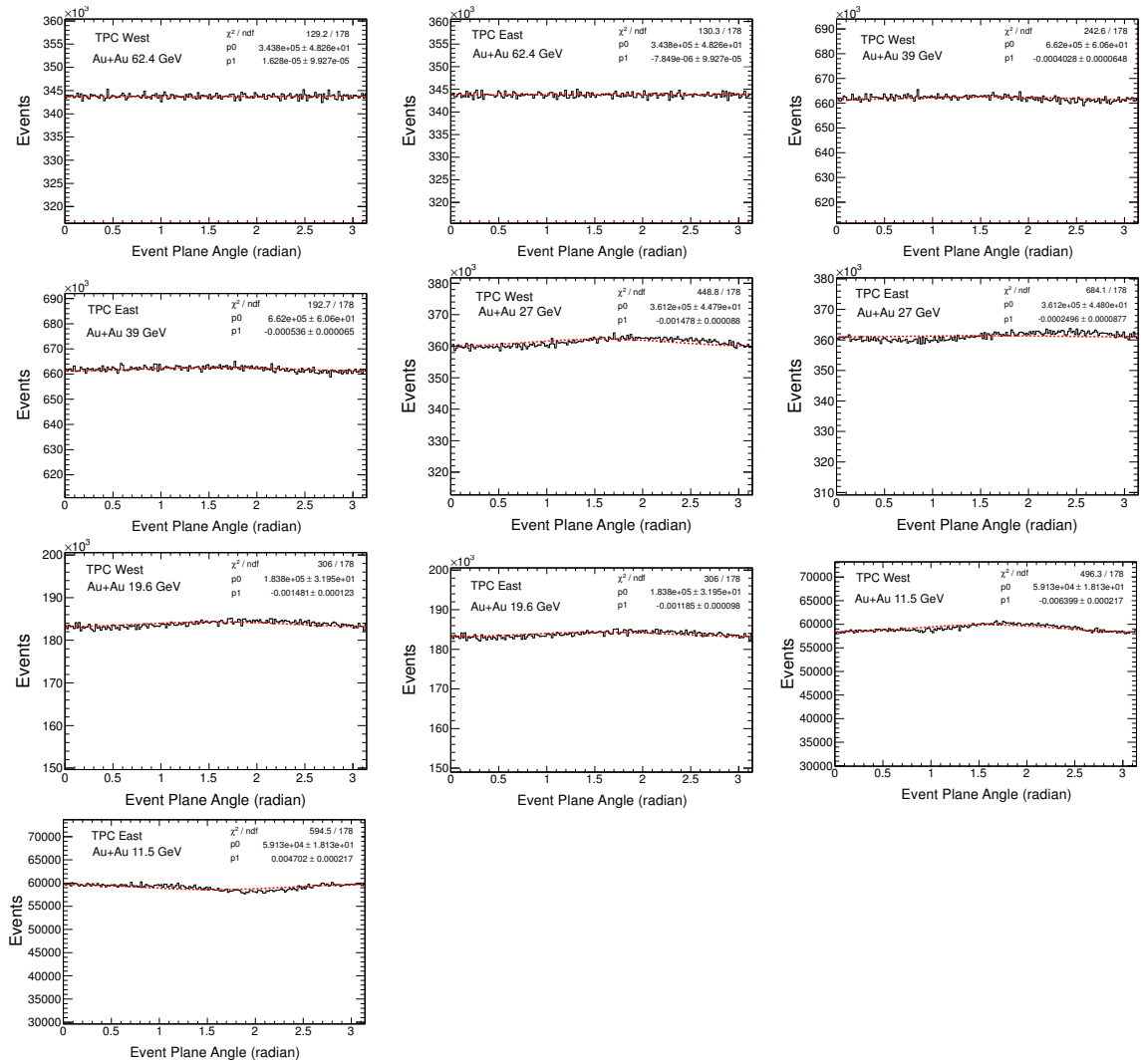


Figure 3.28: (Color online) TPC event plane distributions in Au+Au collisions at  $\sqrt{s_{NN}} = 11.5, 19.6, 27, 39$  and  $62.4$  GeV.

# Chapter 4

## Energy Dependence of $\phi$ -meson

### Invariant Yields

In this chapter the results of  $\phi$ -meson transverse momentum distributions measured at mid-rapidity ( $|y| < 0.50$ ) for RHIC Beam Energy Scan data are presented.

#### 4.1 Data Sets and Cuts

The results presented in this chapter are based on data collected from Au+Au collisions at  $\sqrt{s_{NN}} = 7.7, 11.5, 19.6, 27$  and  $39$  GeV with the STAR detector for minimum bias trigger in the years of 2010 and 2011. The minimum-bias trigger condition for all six energies was based on a coincidence of the signals from the zero-degree calorimeters, vertex position detectors, and/or beam-beam counters. The event selection, centrality selection, track selection and other kinematic cuts are same as used for  $\phi$ -meson  $v_2$  analysis and already discussed in chapter 3. Only difference is that, in spectra analysis, information only from the Time Projection Chamber (TPC) was used for kaon identification.

## 4.2 Transverse Momentum Spectra Measurement

### Methods

#### 4.2.1 $\phi$ -meson reconstruction

$\phi$  meson were reconstructed through their decays to two charged kaons ( $\phi \rightarrow K^+ + K^-$ ). Since there is no way to distinguish kaons track-by-track from  $\phi$  meson decay, all the kaons from each event are combined into unlike-sign pairs to calculate invariant mass ( $m_{inv}$ ) distribution, called as same-event or signal distribution. The invariant mass for the kaon pair with momentum  $\vec{p}_{K^+}$  and  $\vec{p}_{K^-}$  is then calculated based on the 2-body decay kinematics as:

$$m_{K^+K^-} = \sqrt{(E_{K^+} + E_{K^-})^2 - (\vec{p}_{K^+} + \vec{p}_{K^-})^2}, \quad (4.1)$$

where  $E_{K^{+/-}} = \sqrt{\vec{p}_{K^{+/-}}^2 + m_{K^{+/-}}^2}$  and  $m_{K^{+/-}} = 0.4936 \text{ GeV}/c^2$ . Since all kaons in a event are not daughters of  $\phi$  mesons, the  $\phi$ -meson signal sits on the top of combinatorial background of uncorrelated unlike-sign kaon pairs as shown in Fig. 4.1. The  $\phi$ -meson signal can be extracted by removing the combinatorial background.

#### 4.2.2 Combinatorial background estimation

Mixed event technique has been used to estimate the combinatorial background. It is based on the fact that there are no physical correlations to produce a  $\phi$  meson between unlike-sign tracks in artificially mixed events formed by combining positive charged tracks from one event and negative charged tracks from a different event [1, 2]. Under appropriate constraints of *event similarity* the mixed event technique allows to reproduce the shape of the uncorrelated part of the combinatorial background. An invariant mass distribution is constructed using all positively charged kaon candidates from one event mixed with all negatively charged kaon candidates from 5 other events. One can use more than 5 events to reconstruct the mixed event background but as the mixing of 5 events successfully reproduced the shape of combinatorial background we did not use more events just to save computing time. Event mixing was done by

dividing events into a nine centrality classes and only mixing events with the same classes to minimize the effects of multiplicity fluctuation. Again in order to minimize distortions due to acceptance effects, each centrality class was further sub-divided in 10 bins according to vertex Z position. The final mixed events distribution for each centrality class was obtained by adding all invariant mass from each z-vertex bin. Figure 4.1 shows the mixed event invariant mass distribution (red curve) after proper normalisation with same event invariant mass distribution (black curve) for different  $p_T$  bins at  $\sqrt{s_{NN}}=39$  GeV and for 60-80% collision centrality. The normalization was done in the mass range from 1.04 to 1.06 GeV/c<sup>2</sup> since this region is  $5\Gamma$  away from signal.  $\Gamma$  is the width of  $\phi$ -mesons peak.

### 4.2.3 Extraction of raw $\phi$ -meson yield

The raw  $\phi$  yields are extracted after subtracting the scaled mixed events background distributions from the same event distributions for each centrality and each  $p_T$  window. Figure 4.2 shows  $\phi$ -meson signal after combinatorial background subtraction in Au+Au collision at  $\sqrt{s_{NN}}=39$  GeV for different  $p_T$  window and for 60-80% centrality. The  $\phi$ -meson signal is fitted with Briet-Wigner function and 1st order polynomial for residual background to extract raw  $\phi$ -meson yield.

$$BW(m_{inv}) = \frac{1}{2\pi} \frac{A\Gamma}{(m_{inv} - m_\phi)^2 + (\Gamma/2)^2}, \quad (4.2)$$

where A is the area of the distribution,  $\Gamma$  is the width of the distribution and  $m_\phi$  is the mass of the  $\phi$  meson. Both  $\Gamma$  and  $m_\phi$  were taken as free parameters. The extra peak on the invariant mass distribution at high  $p_T$  ( $p_T > 1.2$  GeV/c in Fig. 4.2 ) is due to the misidentification of pions (daughters of  $K_S^0$ ) as kaon candidates. If both pions of  $K_S^0$  decay are misidentified as kaons, then they will contribute a true  $K_S^0$  mass peak which will be shifted from its proper position in invariant mass distribution due to kaon's mass being attributed to the pions [3].

The ratios of (signal+background)/background for  $\phi$  mesons in Au+Au collisions at  $\sqrt{s_{NN}} = 39$  GeV for different centrality classes and  $p_T$  bins are shown in Fig 4.3. The ratios of (signal+background)/background is poor for  $p_T > 1.0$  GeV/c, since in TPC

dE/dX plot the kaon band starts overlap with pion after  $p_T \sim 0.6$  GeV/c. On the other hand as the number of possible  $K^+K^-$  combination are less in peripheral collisions than central, the background level is low causing higher signal to background ratio. Ratios for other energies are shown in Appendix section.

#### 4.2.4 Efficiency and acceptance corrections

In the high multiplicity environment of heavy-ion collisions the track reconstruction efficiency of detector is less than 100% and decreases with increasing detector occupancy (or centrality). Therefore the extracted raw  $\phi$  yield need to be corrected for tracking inefficiencies and detector acceptance.  $\phi$ -meson reconstruction efficiency is obtained from the single kaon counting efficiency.

##### 4.2.4.1 Kaon efficiency from embedding :

Simulated kaon tracks were generated using a flat  $p_T$  and  $y$  distribution and passed through STAR GEANT and TPC Response Simulator (TRS). This whole process is known as embedding. TRS consists of simulation programs which simulate the response of the TPC detector to the passage of particles. The output of TRS was then combined with the raw data. After that the combination of real and simulated data were passed through the standard STAR reconstruction chain. Once the reconstruction is done for a complete event, the Monte-Carlo (MC) tracks were correlated to reconstructed (RC) tracks. The detectors efficiency is defined as the ratio of reconstructed tracks to the input Monte-Carlo tracks for a given kinematic acceptance as used in the analysis. Figure 4.4 shows the distributions of Z-vertex and uncorrected reference multiplicity from Au+Au embedding data at  $\sqrt{s_{NN}} = 7.7$  GeV. Different centrality bins are shown by different color in right plot of Fig. 4.4. Figure 4.5 shows the distribution of DCA and TPC hits of  $K^+$  tracks reconstructed from matched MC kaon tracks and kaon candidates from real data. The distributions have been normal-

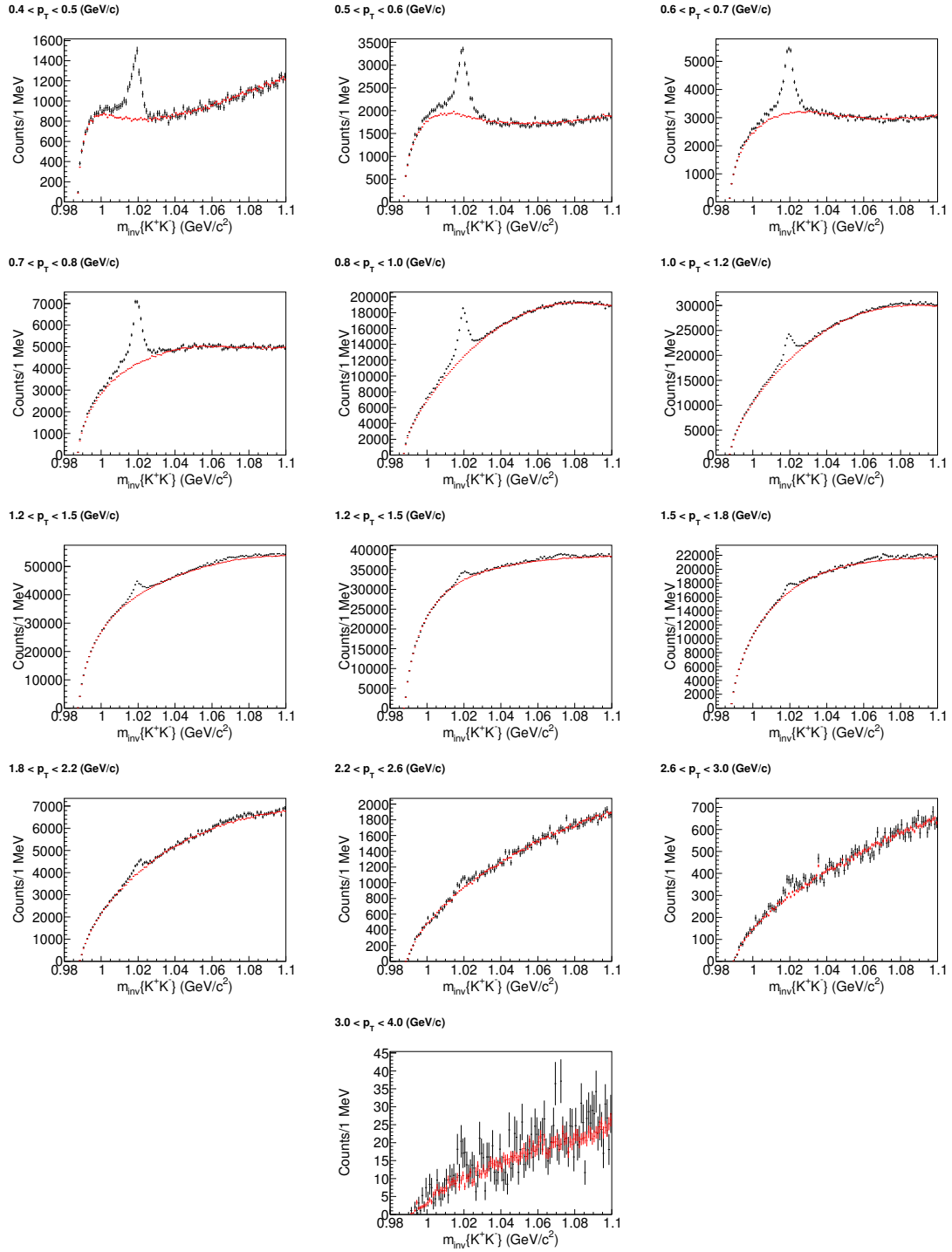


Figure 4.1: (Color online) Same event invariant mass distribution (black curve) and mixed event invariant mass distribution (red curve) after proper normalisation in Au+Au collision (60-80%) at  $\sqrt{s_{NN}} = 39$  GeV for different  $p_T$  bins.

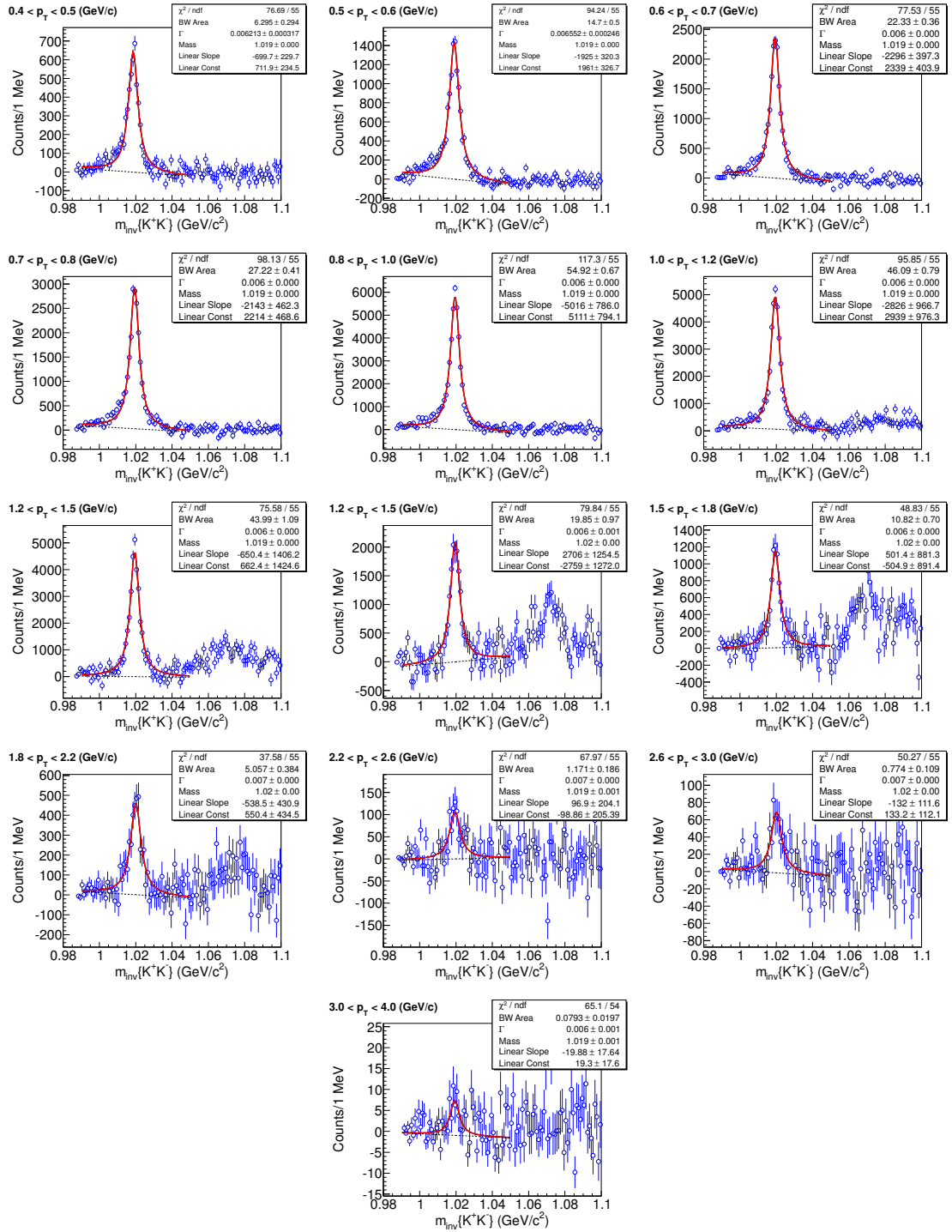


Figure 4.2: (Color online)  $\phi$ -mesons signal after combinatorial background subtraction in Au+Au collision (60-80%) at  $\sqrt{s_{NN}} = 39$  GeV for different  $p_T$  bins.

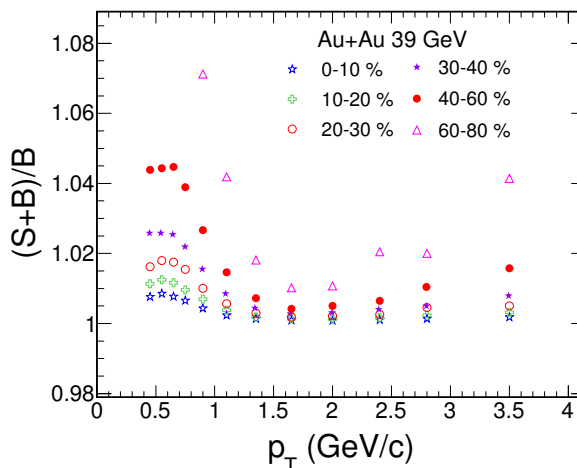


Figure 4.3: (Color online) Values of (signal+background)/background for  $\phi$  mesons in Au+Au collisions at  $\sqrt{s_{NN}} = 39$  GeV for different centrality classes and  $p_T$  bins.

ized to unit area to only compare the shapes. Both the distributions in embedding data are qualitatively consistent with the real data.

The transverse momentum and pseudo-rapidity distribution of Monte-Carlo and reconstructed tracks are shown in Fig. 4.6. The Monte-Carlo and reconstructed tracks are shown by red and blue marker, respectively. Number of reconstructed tracks are less than that of input Monte-Carlo tracks indicating efficiency less than unity. The  $K^+$  reconstruction efficiency as function  $p_T$  is shown Fig. 4.7 for 0-80% minimum bias Au+Au system at  $\sqrt{s_{NN}} = 7.7$  GeV. We can see that the efficiency is very poor for low  $p_T$  region and then increasing with increase in  $p_T$ .

#### 4.2.4.2 Short lived resonance efficiency from single particle embedding:

The method of obtaining short lived resonance efficiency from single particle embedding as follows:

1. Create a Monte Carlo resonance sample with flat (or realistic)  $p_T$  distributions and resonance mass from relativistic Breit Wigner using peak and width from PDG.
2. Then decay the resonance into daughters with given momenta.
3. Smear momentum components  $p_x$ ,  $p_y$  and  $p_z$  of daughters with actual distribution

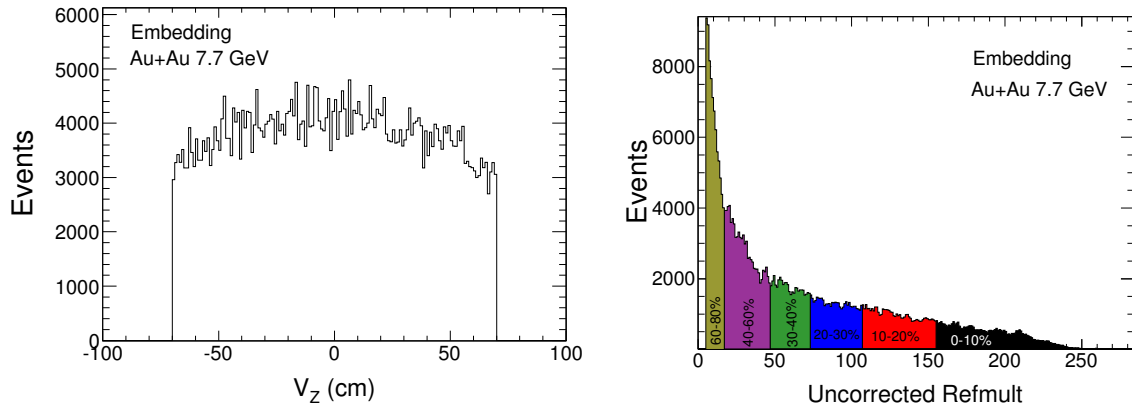


Figure 4.4: (Color online) Distributions of Z-vertex and uncorrected reference multiplicity from Au+Au embedding data at  $\sqrt{s_{NN}} = 7.7$  GeV.

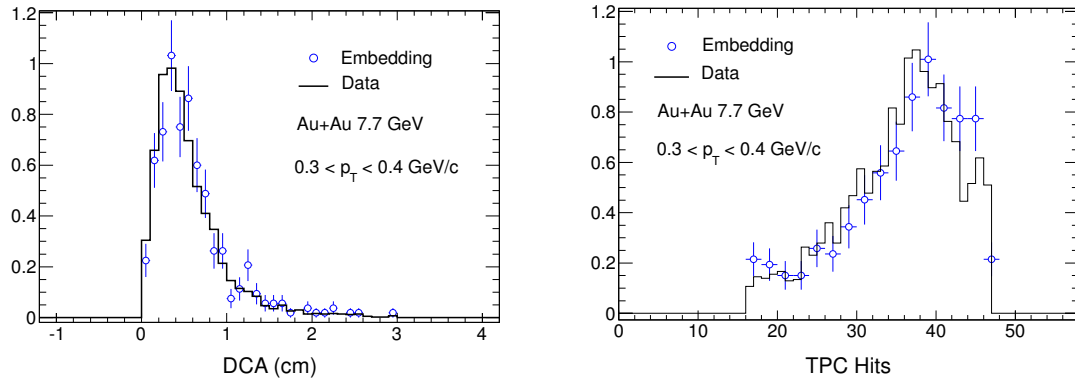


Figure 4.5: (Color online) Distributions DCA and TPC hits of  $K^+$  tracks in Au+Au embedding data (open blue circle) and real data (solid black line) at  $\sqrt{s_{NN}} = 7.7$  GeV for  $0.3 < p_T < 0.4$  GeV/c. The distributions have been normalized to unit area.

from the embedding.

4. Fill histogram of reconstructed resonances

-  $\text{histR} \rightarrow \text{Fill}(p_T, \epsilon_1(p_T, \eta) * \epsilon_2(p_T, \eta))$

where  $\epsilon_1$  and  $\epsilon_2$  are the efficiencies of daughters.

5. Mimic reconstruction/acceptance effect.

6. Reconstructed resonance created.

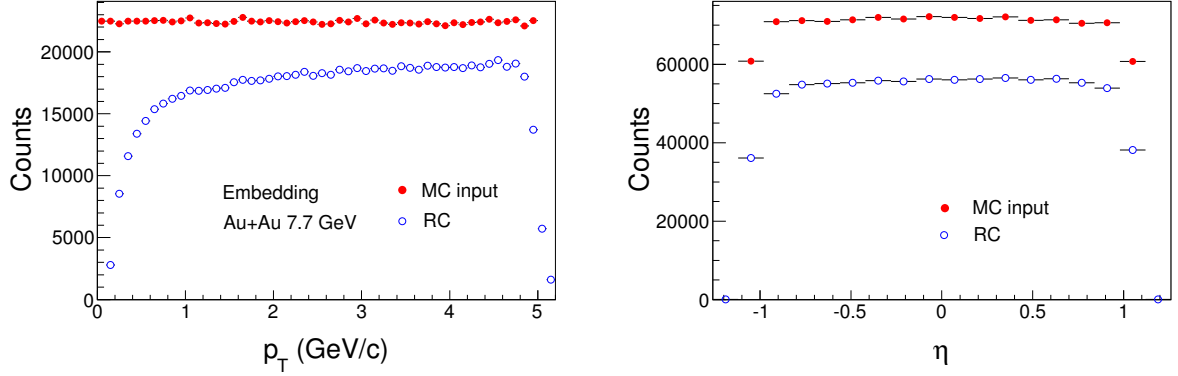


Figure 4.6: (Color online) Transverse momentum and pseudo-rapidity distribution of Monte-Carlo (MC) and reconstructed (RC) tracks in Au+Au embedding data (0-80%) at  $\sqrt{s_{NN}} = 7.7$  GeV. Error bars are statistical.

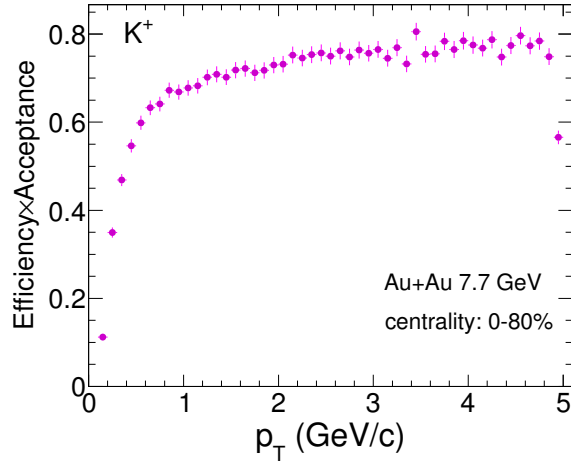


Figure 4.7: (Color online) Efficiency  $\times$  Acceptance of  $K^+$  in Au+Au embedding data at  $\sqrt{s_{NN}} = 7.7$  GeV for 0-80% centrality. Error bars are statistical.

7. Now calculate the efficiency of short lived resonances which is defined as the number of reconstructed resonances divided by number resonances created as input.

Before we use this new method, it is necessary to check its consistency with the measurements from direct  $\phi$ -meson embedding data. Figure 4.8 shows a comparison of  $\phi$ -meson efficiency from single kaon efficiency and from embedding production

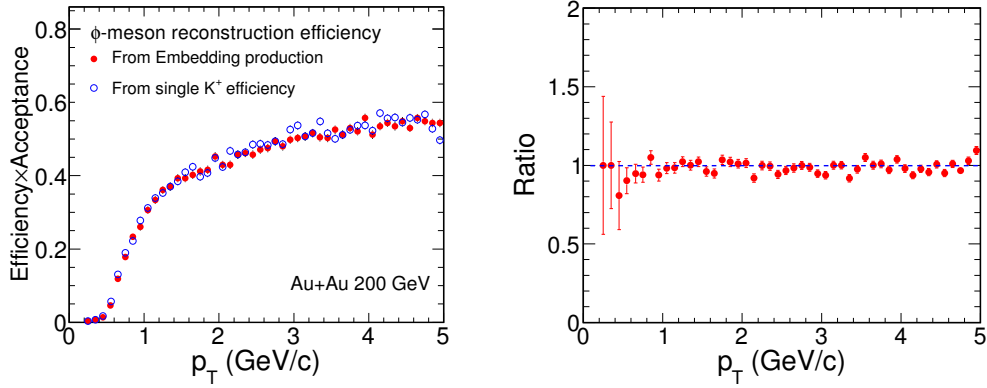


Figure 4.8: (Color online) Left panel shows a comparison of  $\phi$ -meson efficiency from single kaon efficiency and from embedding production in Au+Au collisions at 200 GeV and ratio of them are shown in right panel.

in Au+Au collision at 200 GeV where  $\phi$  mesons are embedded directly, decayed to kaons as per the branching fraction and reconstructed following the usual procedure of embedding [3]. One can see the ratios, shown in the right panel of Fig.4.8, are close to unity indicating that both results are matching very well. Having established the procedure, we show the  $p_T$  dependence of  $\phi$ -meson efficiency ( $|y| < 0.5$ ) obtained from single kaon efficiency as a function of centrality at all the beam energies studied in Fig.4.9. The efficiency  $\times$  acceptance increases with  $p_T$  and from central to peripheral collisions.

#### 4.2.4.3 Energy loss correction for kaon:

Low momentum particles lose energy while traversing the detector material [4]. This energy loss is significant for heavier particles ( $K^\pm$ ,  $p$  and  $\bar{p}$ ) [5] and therefore correction is needed. The correction is obtained from embedding. Figure 4.10 shows the difference between the reconstructed transverse momentum and the MC input transverse momentum,  $p_T^{RC} - p_T^{MC}$ , versus the reconstructed transverse momentum,  $p_T^{RC}$ , for kaons within  $|y| < 0.5$ . The profile can be parametrized to provide the correction

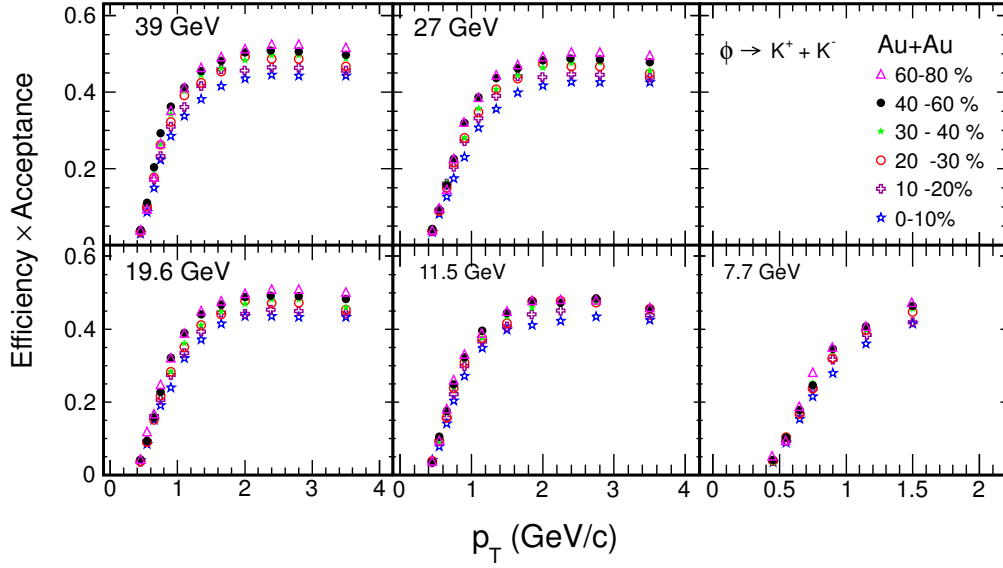


Figure 4.9: (Color online) Efficiency $\times$ Acceptance for  $\phi$  mesons as a function of  $p_T$  calculated for different centralities in Au+Au collisions at  $\sqrt{s_{NN}}=7.7 - 39$  GeV.

function for the measured momentum:

$$p_T^{RC} - p_T^{MC} = p_0 + p_1 \left(1 + \frac{m^2}{(p_T^{RC})^2}\right)^{p_2}, \quad (4.3)$$

where  $m$  is the mass of the kaon, and  $p_0$ ,  $p_1$ , and  $p_2$  are the fit parameters. The energy loss correction is applied for all the kaon tracks using the correction formula given in Eq. 4.3. The values of all the parameters in Eq. 4.3 are approximately equal for all the centre-of-mass energies of BES program, since for all the energies, detectors setup and amount of material was same in STAR. For all the results presented in this chapter, the corrected  $p_T$  was used.

### 4.3 Systematic Error Study

The main sources of systematic uncertainty are followings:

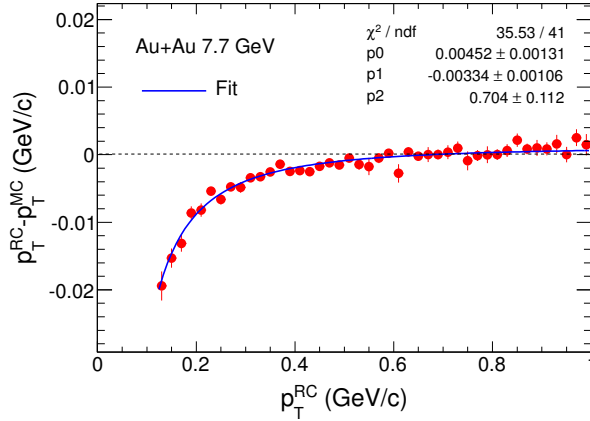


Figure 4.10: (Color online) Energy loss effect for  $K^+$  as a function of reconstructed transverse momentum at mid-rapidity ( $|y| < 0.5$ ) in 7.7 GeV 0-80% minimum bias collisions. Errors shown are statistical only.

### 4.3.1 Uncertainty in particle identification

For systematic study, following cuts has been varied for kaon selection.

Number of fit points	$\geq 15$	$\geq 20$	$\geq 25$
Dca	$\leq 3.0$ cm	$\leq 2.0$ cm	$\leq 1.5$ cm
Ratio of fit points to possible points	$\geq 0.52$	$\geq 0.54$	
$n\sigma$ cut on kaon $dE/dx$	$\leq 2.0  \sigma $	$\leq 1.5  \sigma $	

### 4.3.2 Uncertainty from residual background

The shape of residual background after mixed event subtraction varies with  $p_T$ . This is because of contamination in kaon selection using the  $dE/dx$  information. Using only  $dE/dx$  information one can identify kaon with high purity up-to momentum 0.6 GeV/ $c$ . So with increase in  $p_T$ , the contamination in kaon sample from pion and proton increases. To estimate the effect different methods has been used for raw  $\phi$  yield extraction.

1. Varying fit function range for residual background.
2. Using different fit function for residual background
  - 1st order polynomial
  - 2nd order polynomial
3. Bin counting

### 4.3.3 Statistical uncertainty on efficiency

This is done by propagating of  $K^+$  efficiency uncertainty to  $\phi$  efficiency determination [5]. Systematic error on  $\phi$ -meson spectra due to statistical uncertainty on efficiency is found to be  $\sim 5\%$ .

Total systematic error was obtained by adding errors in quadrature from different sources. The contribution from the each source to the final systematic error for most central 0-10% and most peripheral 60-80% centrality at  $\sqrt{s_{NN}} = 39$  GeV are shown in the panel (a) and (b) of Fig. 4.11, respectively. The systematic errors from the residual background is dominant at very low  $p_T$  ( $p_T < 0.8$  GeV/c) in the 0-10% central collisions. However at the high  $p_T$  region, the main source of systematic errors is due to the variation of tracks selection cuts. This is mainly because of misidentification of kaon tracks in that momentum region where the  $dE/dx$  band of pions and kaons are not separated. The panel (c) of Fig. 4.11, shows the total systematic errors for six different centrality classes at  $\sqrt{s_{NN}} = 39$  GeV. Total systematic errors are approximately similar (within 10 -16%) for all the centrality classes, however we observed 2 to 3% higher systematic errors in 0-10% central collisions than 60-80% peripheral collisions. This is also true for other beam energies. In the panel (d) of Fig. 4.11, systematic errors for different beam energies are compared for fixed 0-10% most central events. We observed that at  $\sqrt{s_{NN}} = 11.5, 19.6, 27$  and  $39$  GeV, systematic errors are within 10-16%. But in case of  $\sqrt{s_{NN}} = 7.7$  GeV, systematic errors are higher than other energies and it is  $\sim 17-21\%$

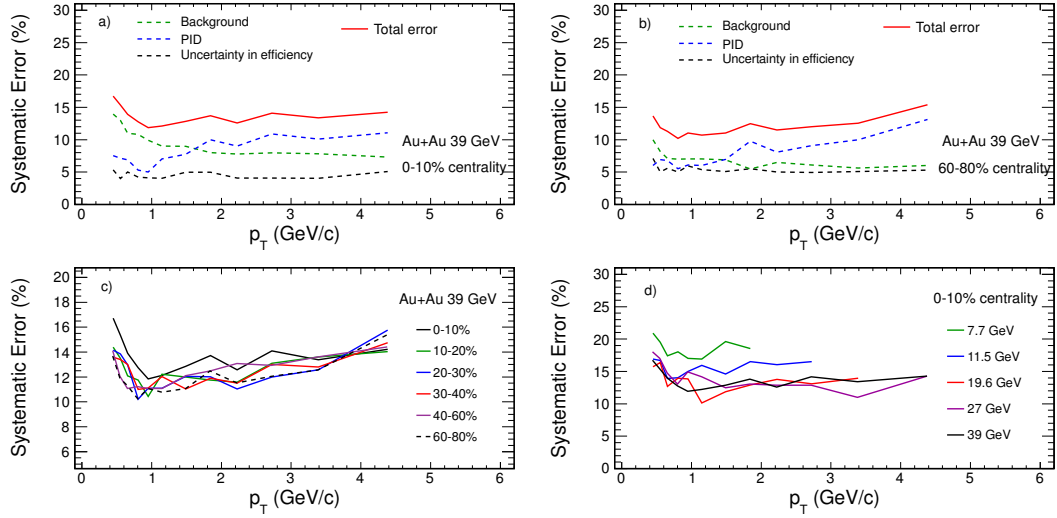


Figure 4.11: (Color online) Systematic errors due to residual background, particle identification (PID), uncertainty in efficiency and total systematic errors in Au+Au collisions at  $\sqrt{s_{NN}} = 39$  GeV for (a) 0-10% and (b) 60-80% centrality. Panel (c): Total systematic error for six different centrality at  $\sqrt{s_{NN}} = 39$  GeV. Panel (d): Total systematic error for different centre-of-mass energies for 0-10% centrality.

## 4.4 Results & Discussion

### 4.4.1 Mass and width of $\phi$ meson

The mass of  $\phi$  mesons, obtained from BW fit, as a function of  $p_T$  at  $\sqrt{s_{NN}} = 39$  GeV for 0-10% centrality are shown in Fig. 4.12. Open black and blue filled triangle corresponds to the mass of  $\phi$  mesons before and after kaon energy loss correction, respectively. We can see that there is drop in mass for  $p_T$  below 600 MeV. This drop in mass decreases after taking into account the energy loss by kaon in the detector materials. For  $p_T > 600$  MeV measured  $\phi$  masses are consistent with the PDG value of  $\phi$  mass (shown by red line). The left panel of Fig. 4.13 show centrality dependence of  $\phi$  mass for fixed beam energy  $\sqrt{s_{NN}} = 39$  GeV and energy dependence are shown

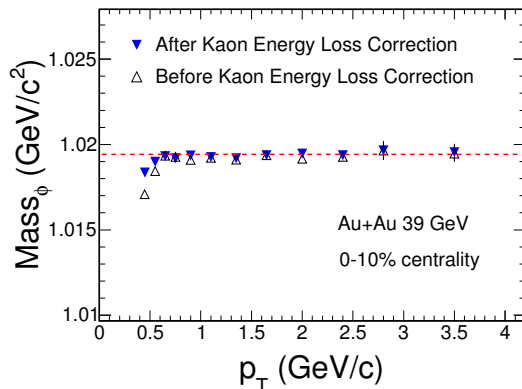


Figure 4.12: (Color online) Mass of  $\phi$  meson in Au+Au collisions at  $\sqrt{s_{NN}} = 39$  GeV for 0-10% centrality before and after kaon energy loss correction. The error bars are statistical uncertainties. Red dashed line is the PDG mass value for  $\phi$  meson [4].

in the right panel for 0-10% centrality. The black dashed lines are the PDG value for  $\phi$  mass. One can see that for  $p_T$  above 600 MeV/c, there is good agreement between data and PDG value for all energies and all centralities.

Figure 4.14 shows the width of reconstructed  $\phi$ -meson peak as a function of  $p_T$ . Both centrality and energy dependence are shown in left and right panel, respectively. The PDG value for  $\phi$  meson width are shown by dashed black lines. The measured widths are observed to be higher than PDG value. This could be due to finite momentum resolution of TPC. To check this we have studied  $\phi$  meson in AMPT model. In AMPT, input of both width and mass of the  $\phi$  meson are given exactly same as corresponding PDG value. We reconstructed  $\phi$ -meson signal using  $K^+$  and  $K^-$  decay channel using simulated AMPT data in Au+Au collisions at  $\sqrt{s_{NN}} = 39$  GeV as shown in panel (a) of Fig.4.15. We obtained the value of  $\phi$  mass and width as  $1.02 \pm 0.0012$  GeV/c<sup>2</sup> and  $0.004342 \pm 0.00031$  GeV/c<sup>2</sup>, respectively, after fitting with Breit-Wigner function. Those two values are consistent with PDG values. Now, since the momentum resolution of TPC detector is  $\sim 2\%$  for kaon in the range  $p_T < 0.5$  GeV [6], we introduced 2% momentum resolution in the AMPT data and reconstructed  $\phi$ -meson signal as shown in panel (b) of Fig.4.15. We can see that width of the  $\phi$  meson

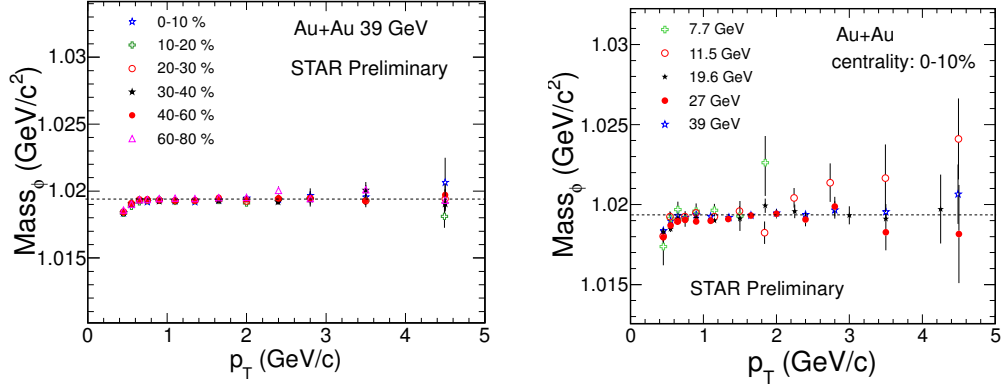


Figure 4.13: (Color online) Left panel: Mass of  $\phi$  meson in Au+Au collisions at  $\sqrt{s_{NN}} = 39$  GeV for various centralities. Right panel: Mass of  $\phi$  meson in Au+Au collisions (0-10%) for different beam energies. The error bars are statistical uncertainties. Dashed line is the PDG mass value for  $\phi$  meson [4].

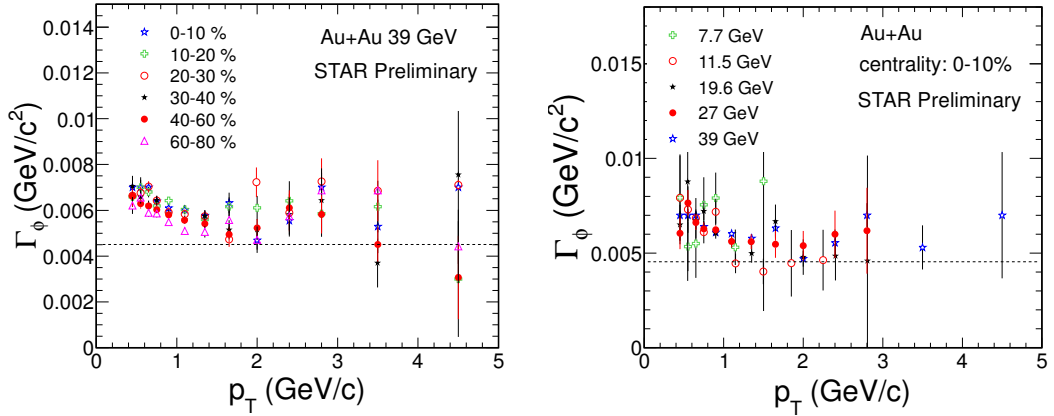


Figure 4.14: (Color online) Left panel: Width of  $\phi$  meson in Au+Au collisions at  $\sqrt{s_{NN}} = 39$  GeV for various centralities. Right panel: Width of  $\phi$  meson in Au+Au collisions (0-10%) for different beam energies. The error bars are statistical uncertainties. Dash line is the PDG width value for  $\phi$  meson [4].

changes from  $0.004342 \pm 0.00031$  GeV/c<sup>2</sup> to  $0.007097 \pm 0.00058$  GeV/c<sup>2</sup> and this value is consistent with the experimentally measured values. This study tells that,

the observed difference in width of  $\phi$  meson between experimentally measured value and PDG value is due to the finite momentum resolution of TPC detector.

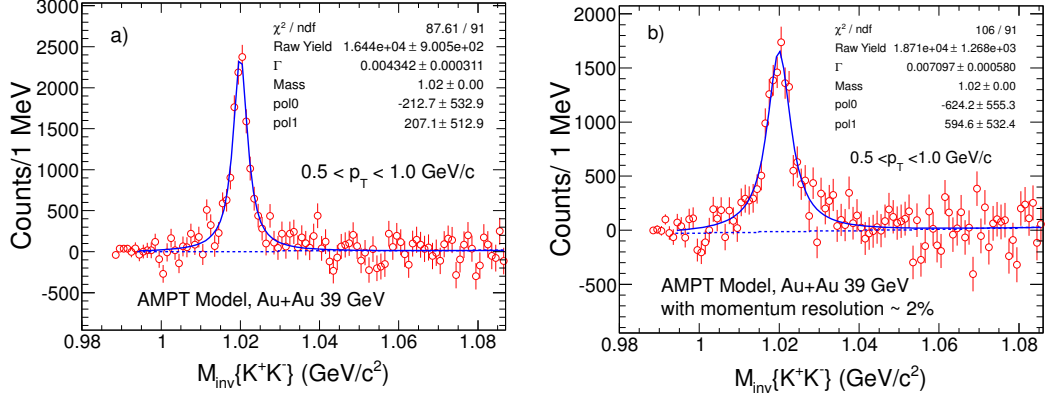


Figure 4.15: (Color online) Panel (a): Reconstructed  $\phi$ -meson signal using  $K^+$  and  $K^-$  decay channel using AMPT data in Au+Au collisions at  $\sqrt{s_{NN}} = 39$  GeV. Panel (b): Reconstructed  $\phi$ -meson signal using  $K^+$  and  $K^-$  decay channel using AMPT data with momentum resolution  $\sim 2\%$  in Au+Au collisions at  $\sqrt{s_{NN}} = 39$  GeV.

#### 4.4.2 Invariant transverse momentum spectra

The invariant  $\phi$ -meson yield per event in each  $p_T$  bin is given by:

$$\frac{1}{2\pi p_T} \frac{d^2 N}{dp_T dy} = \frac{\Delta N_{raw}^\phi}{2\pi N_{evt} p_T \Delta p_T \Delta y \varepsilon_{eff} BR}, \quad (4.4)$$

where:

- $\Delta N_{raw}^{phi}$  is the raw  $\phi$  yield.
- $N_{evt}$  number of analyzed events.
- $\Delta p_T$  is the bin size in  $p_T$ .
- $\Delta y$  is the bin size in rapidity.
- $BR$  is the branching ratio which is 0.491 for  $\phi \rightarrow K^+ + K^-$  [4].
- $\varepsilon_{eff}$  is the correction factor to account for detector acceptance and reconstruction efficiency.

The corrected invariant  $p_T$  spectra of the  $\phi$  meson measured in Au+Au collisions at

$\sqrt{s_{NN}} = 7.7, 11.5, 19.6, 27$  and  $39$  GeV are shown in Fig. 4.16 for six different collision centrality (0-10%,10-20%,20-30%,30-40%,40-60% and 60-80%). The statistical errors are indicated by the bars and the systematic errors are represented by the shaded green bands. The solid lines in Fig. 4.16 are Levy fits with the functional form:

$$\frac{1}{2\pi p_T} \frac{d^2 N}{dy dp_T} = \frac{dN}{dy} \frac{(n-1)(n-2)}{2\pi n T (nT + m(n-2))} \left(1 + \frac{\sqrt{p_T^2 + m^2} - m}{nT}\right)^{-n}. \quad (4.5)$$

$T$  is known as the inverse slope parameter,  $dN/dy$  is the  $\phi$ -meson yield per unit rapidity,  $m$  is the rest mass of  $\phi$  meson and  $n$  is the Levy function parameter. Levy function is similar in shape to an exponential at low  $p_T$  and has a power-law-like shape at higher  $p_T$ . The dashed lines in Fig. 4.16 are exponential fits of the form:

$$\frac{1}{2\pi p_T} \frac{d^2 N}{dy dp_T} = \frac{dN/dy}{2\pi T(m+T)} \exp\left[-\frac{\sqrt{m^2 + p_T^2} - m}{T}\right] \quad (4.6)$$

In fact, the exponential function is the limit of the Levy function as  $n$  approaches infinity. From Fig. 4.16, it can be seen that the exponential and Levy functions fit the central collision data equally well. However, with decreasing centrality, the exponential fits diverge from the data at higher transverse momentum and the Levy function fits the data better. This evolution in the shape of the spectra from exponential-like in central collisions to more power-law-like in peripheral collisions reflects the increasing contribution from pQCD (hard) processes to  $\phi$ -meson production in more peripheral collisions at higher  $p_T$ . Since at the low  $p_T$  part, both exponential and Levy functions fit the data for all centralities, one can say the particle production at low  $p_T$  is expected to be due to non-perturbative soft processes. Values of all fit parameters for Levy and exponential function are listed in the Appendix section at the end of this chapter.

### 4.4.3 $\phi$ -meson yield per unit rapidity

Figure 4.17 presents the  $\phi$  meson mid-rapidity  $p_T$  integrated yield per participant pair  $(dN/dy)/(0.5N_{part})$  as a function of number of participant ( $N_{part}$ ) in Au+Au collisions at  $\sqrt{s_{NN}} = 7.7, 11.5, 19.6, 27, 39$  and  $62.4$  GeV. The value of  $dN/dy$  has

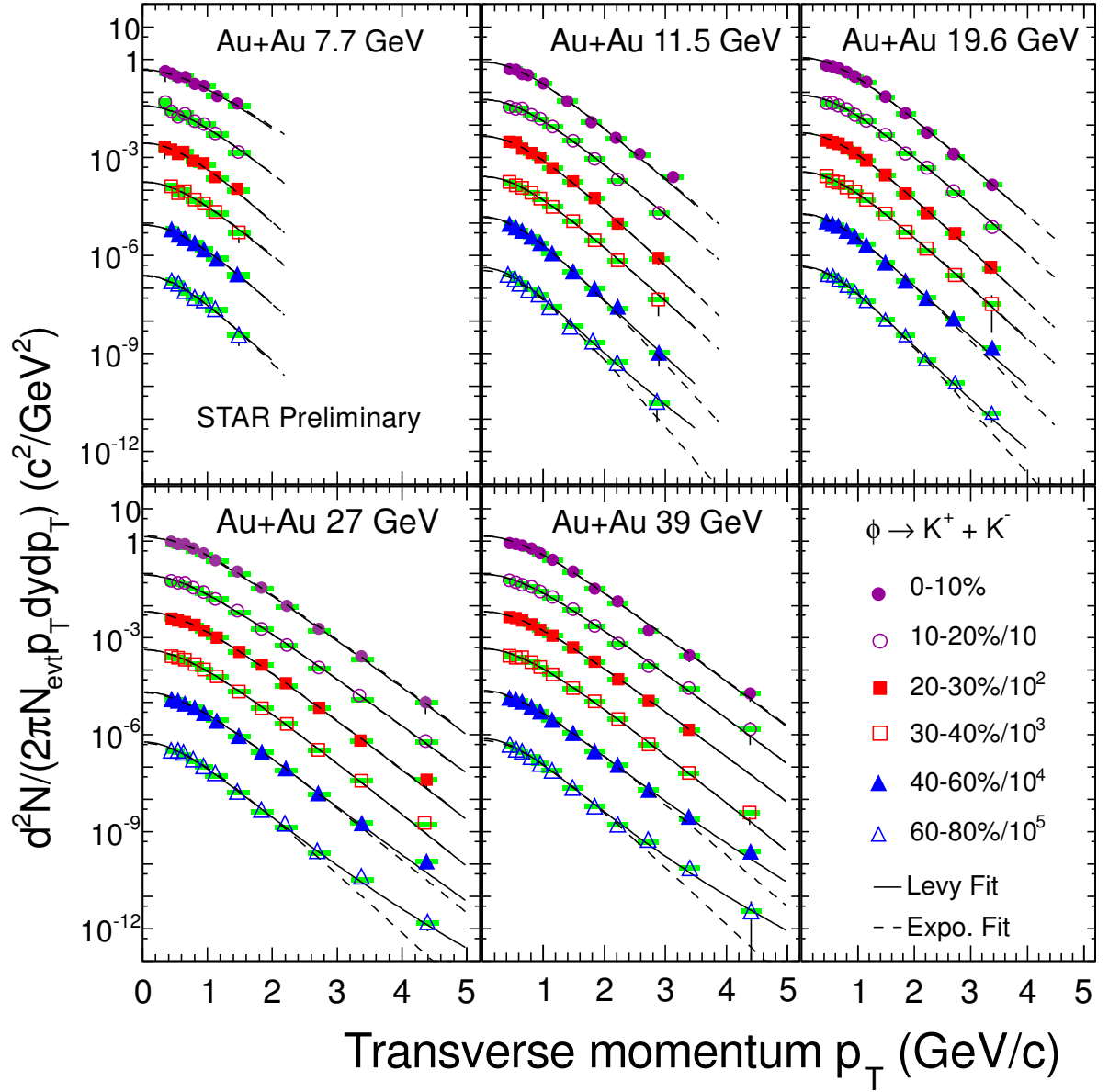


Figure 4.16: (Color online) The invariant yield of  $\phi$ -mesons as a function of  $p_T$  measured for different centralities in Au+Au collision at  $\sqrt{s_{NN}} = 7.7 - 39$  GeV. Shaded green bands are systematic errors, while the statistical errors are represented by error bars. The dashed(solid) line represents an exponential(Levy) function fit to the data.

been calculated using data points in the measured  $p_T$  region plus from extrapolation of the fit to the data using Levy functions for the region where data points does not exists. We also used exponential function for extrapolation and differences in the results are taken as part of systematic error on  $dN/dy$ . The data points for 62.4 GeV are taken from Ref. [7] for comparison. The measured mid-rapidity yield per participant pair increases nonlinearly with centrality and for the same  $N_{part}$ ,  $(dN/dy)/(0.5N_{part})$  increases with the collision energy of the Au+Au collisions. The former suggests particle production does not scale with  $N_{part}$  and the later is expected because of the increase of energy available to produce the  $\phi$  mesons. The centrality and energy dependences of the enhancement of  $\phi$ -meson production relative to  $p+p$  collisions can reflect the mechanism of strangeness enhancement in a dense medium formed in high energy heavy-ion collisions [8]. Due to lack of data in  $p+p$  collisions this result is not presented in this thesis.

Figure 4.18 shows the comparison of  $\phi$ -meson  $dN/dy$  in STAR in central Au+Au collisions with central Pb+Pb collisions of NA49 results [9]. Data points for STAR experiments are for 0-10% centrality while for NA49, data points are for 0-7.2% except  $\sqrt{s_{NN}} = 17.6$  GeV where the measurements was done for 0-5% centrality. STAR BES measurements are consistent with NA49 results within error.

#### 4.4.4 Nuclear modification factor

In order to understand parton energy loss in the medium created in high energy heavy-ion collisions for different centralities in Au+Au collisions, the nuclear modification factor ( $R_{CP}$ ) is measured which is defined as follows:

$$R_{CP} = \frac{Yield_{central}}{Yield_{peripheral}} * \frac{\langle N_{bin} \rangle_{peripheral}}{\langle N_{bin} \rangle_{central}}. \quad (4.7)$$

Where  $\langle N_{bin} \rangle$  is the is the average number of binary collisions to the corresponding centrality. The value of  $N_{bin}$  is calculated from the Monte Carlo Glauber simulation [10]. The values of  $N_{bin}$  for different centralities at different centre-of-mass energies are listed in Appendix section. If nucleus-nucleus collisions are simply a superposition of nucleon-nucleon collisions then  $R_{CP}$  is equal to one. Deviation of  $R_{CP}$

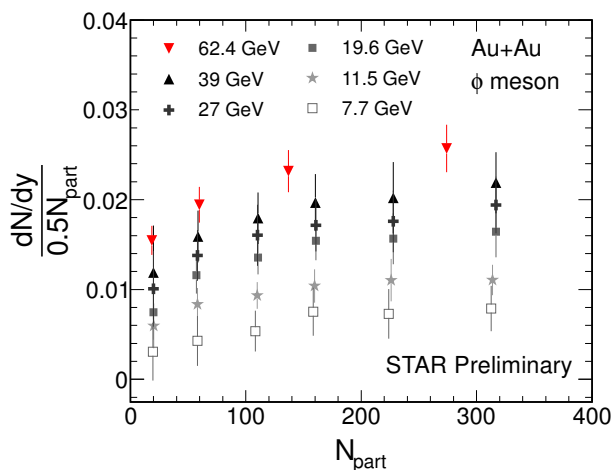


Figure 4.17: (Color online) The  $\phi$  meson mid-rapidity yield per participant pair  $(dN/dy)/(0.5N_{part})$  as a function of number of participant ( $N_{part}$ ) in Au+Au collisions at  $\sqrt{s_{NN}} = 7.7, 11.5, 19.6, 27, 39$  and  $62.4$  GeV. The results at  $\sqrt{s_{NN}} = 62.4$  GeV are taken from previous STAR measurements [7]. Systematic errors are added in quadrature with statistical errors.

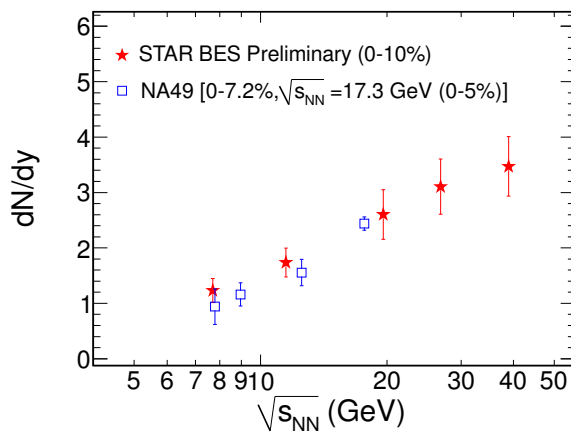


Figure 4.18: (Color online) The  $\phi$  meson mid-rapidity yield  $(dN/dy)$  as a function of  $\sqrt{s_{NN}}$  in central Au+Au collisions in STAR and in central Pb+Pb collisions in NA49 [9]. Systematic errors are added in quadrature with statistical errors.

from the unity would imply contribution from the nuclear medium effects specifically jet-quenching [11].

Figure 4.19 shows  $R_{CP}(0 - 10\%/40 - 60\%)$  measurement of  $\phi$  mesons at mid-

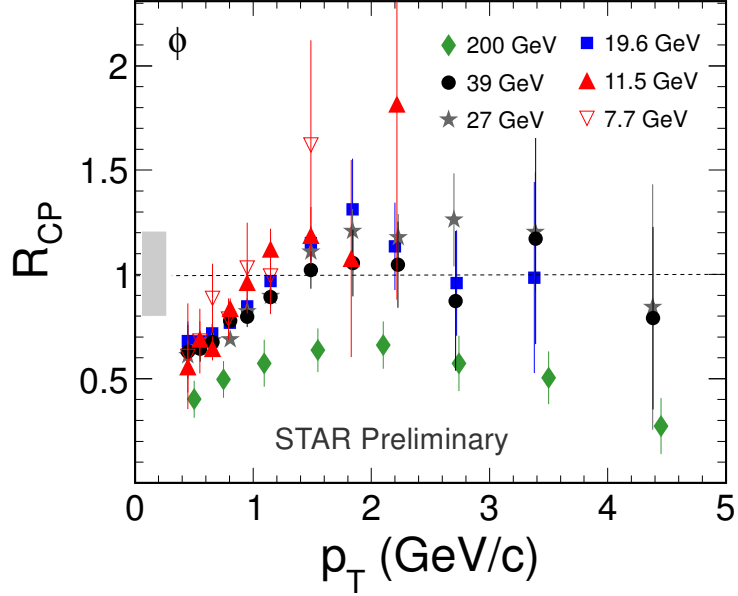


Figure 4.19: (Color online) The  $\phi$ -meson  $R_{CP}$  as function of  $p_T$  in the Au+Au collision at various beam energies. The  $R_{CP}(0 - 05\%/40 - 60\%)$  at  $\sqrt{s_{NN}} = 200$  GeV are taken from previous STAR measurements [7]. Error bars are only statistical uncertainties. Gray bands represents normalization error from  $N_{bin}$  which is approximately 20% for all energies.

rapidity ( $|y| < 0.5$ ) in Au+Au collisions at  $\sqrt{s_{NN}} = 7.7 - 39$  GeV. The  $\phi$ -meson  $R_{CP}(0 - 05\%/40 - 60\%)$  at 200 GeV measured by STAR experiments are also shown for comparison. The data points for 200 GeV are taken from Ref. [7]. Because of the energy loss of the partons traversing the high density QCD medium, the  $R_{CP}$  of  $\phi$  mesons goes below unity at 200 GeV. From Fig. 4.19, one can see at the intermediate  $p_T$  ( $p_T > 1.5$  GeV/c),  $R_{CP} \geq 1.0$  for  $\sqrt{s_{NN}} \leq 39$  GeV. This indicates that at low beam energy the parton energy loss effect is less important and this may hint for the formation of hadron dominated matter. In Fig. 4.20,  $\phi$ -meson  $R_{CP}(0 - 10\%/40 - 60\%)$

are compared with that of  $K_S^0$  for  $\sqrt{s_{NN}} = 7.7, 11.5, 19.6, 27$  and  $39$  GeV in Au+Au collisions. One can see that, similar to  $\phi$  meson  $R_{CP}$  of  $K_S^0$  goes above unity with decreasing beam energies.

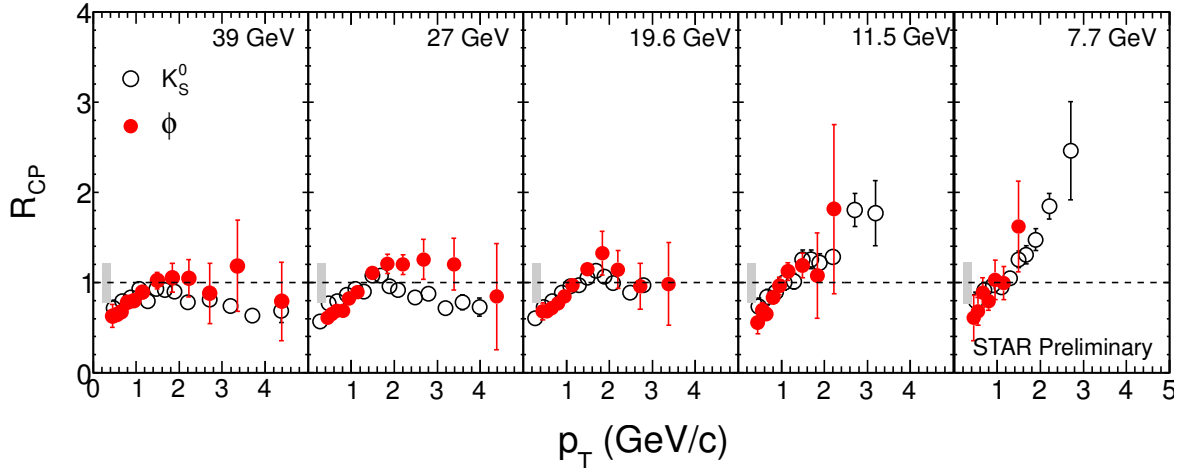


Figure 4.20: (Color online)  $R_{CP}$  of  $\phi$  mesons and  $K_S^0$  as function of  $p_T$  in Au+Au collisions at  $\sqrt{s_{NN}} = 7.7-39$  GeV. Error bars are statistical uncertainty. Gray bands represents normalization error from  $N_{bin}$ .

## 4.4.5 Particle ratios

### 4.4.5.1 $\phi/\pi^-$ :

The yield ratio  $N(\phi)/N(\pi^-)$  as a function of number of participants ( $N_{part}$ ) are presented in left panel of Fig. 4.21 for  $\sqrt{s_{NN}} = 7.7, 11.5, 39$  and  $200$  GeV in Au+Au collisions. The data points for  $200$  GeV are taken from Ref. [7]. The  $N(\phi)/N(\pi^-)$  ratios first increases with  $N_{part}$  then seems to be saturated in the high  $N_{part}$  region for all energies. These indicate that the yield of the  $\phi$  increases faster than that of  $\pi^-$  from peripheral to central collisions i.e. central collisions (highly dense and hot matter) provide a more advantageous environment for the production of  $\phi$  mesons

than peripheral collisions (less dense and less hot matter). Figure 4.21 shows that the  $N(\phi)/N(\pi^-)$  ratios also increases with centre-of-mass energy.

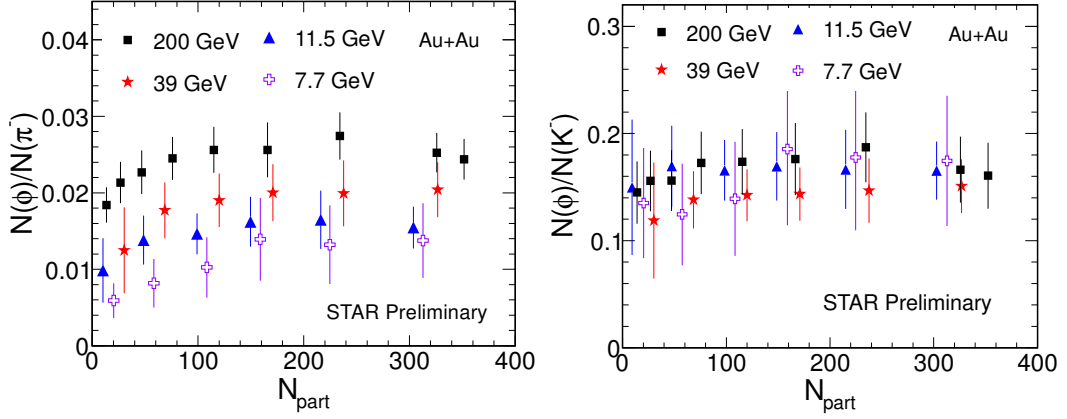


Figure 4.21: (Color online) Left panel:  $N_{part}$  dependence of ratio  $N(\phi)/N(\pi^-)$  in Au+Au collisions at different centre-of-mass energies. Systematic errors are added in quadrature with statistical errors. Right panel:  $N_{part}$  dependence of ratio  $N(\phi)/N(K^-)$  in Au+Au collisions at different centre-of-mass energies. Systematic errors are added in quadrature with statistical errors. In both panels, data points are shifted towards left and right by  $N_{part}$  value 10 for 11.5 and 39 GeV, respectively .

#### 4.4.5.2 $\phi/K^-$ :

In order to shed light on  $\phi$ -meson production mechanism, yield ratio of  $N(\phi)/N(K^-)$  as function of  $N_{part}$  are shown in the right panel of Fig. 4.21 for  $\sqrt{s_{NN}} = 7.7, 11.5, 39$  and 200 GeV in Au+Au collisions. The data points for 200 GeV are taken from Ref. [7]. One can see from Fig. 4.21 that  $N(\phi)/N(K^-)$  is almost constant as a function of centrality and centre-of-mass energy. This effectively rule out kaon coalescence as the dominant production mechanism for the  $\phi$  meson [7]. Because kaon coalescence mechanism predict an increasing  $N(\phi)/N(K^-)$  with centrality [7].

#### 4.4.6 $\phi$ -meson $\langle p_T \rangle$

The average transverse momentum,  $\langle p_T \rangle$ , of  $\phi$  meson as a function of  $N_{part}$  in Au+Au collisions at  $\sqrt{s_{NN}} = 11.5, 39, 62.4$  and  $200$  GeV are shown in Fig. 4.22. The  $\langle p_T \rangle$  is extracted from the best fit to the  $p_T$  spectra of  $\phi$  meson. The mean value of the measured  $p_T$  of the  $\phi$  meson increases from peripheral to mid-central collisions and then saturates for all the energies. But due to large error (mainly systematic error) it is not possible to make any strong conclusion. The data points for  $200$  GeV and  $62.4$  GeV are taken from Ref. [7]. Results for other energies ( $\sqrt{s_{NN}} = 7.7, 19.6$  and  $27$  GeV) are not shown for clarity of figure and the values of  $\langle p_T \rangle$  were found to be consistent with energy dependence trend.

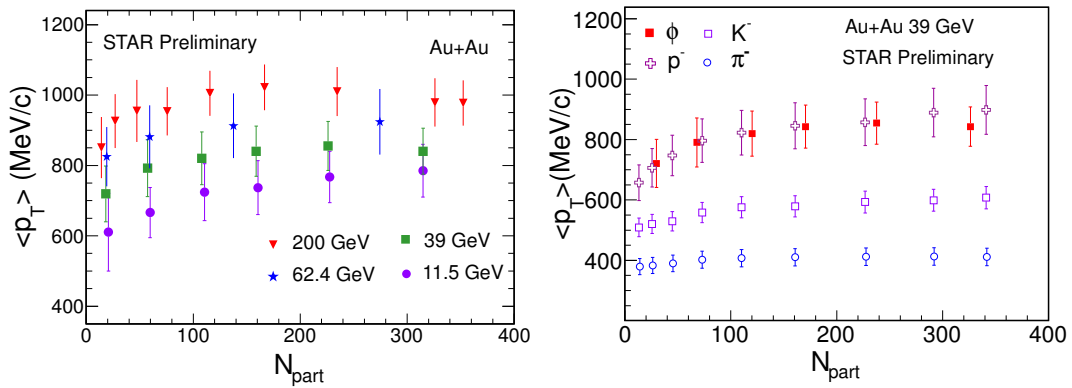


Figure 4.22: (Color online) Left panel:  $N_{part}$  dependence of  $\langle p_T \rangle$  of  $\phi$  mesons in Au+Au collisions at different centre-of-mass energies. Systematic errors are added in quadrature with statistical errors. The  $\langle p_T \rangle$  values at  $\sqrt{s_{NN}} = 62.4$  and  $200$  GeV are taken from previous STAR measurements [7]. Right panel:  $\langle p_T \rangle$  of  $\phi$ ,  $\pi^-$ ,  $K^-$  and  $p^-$  in Au+Au collisions at  $\sqrt{s_{NN}} = 39$  GeV. Systematic errors are added in quadrature with statistical errors. The data points of  $\phi$  are shifted towards right by  $N_{part}$  value of 10 in X-axis.

Right panel of Fig. 4.22 shows comparison of  $\langle p_T \rangle$  of  $\phi$  meson with that of

$\pi^-$ ,  $K^-$  and  $p^-$  in Au+Au collisions at  $\sqrt{s_{NN}} = 39$  GeV. The measured  $\langle p_T \rangle$  of  $\phi$  show similar values as that of  $p^-$ . This is expected because of their almost similar rest mass.

#### 4.4.7 Strange quark dynamics

Strange ( $s$ ) quarks in the heavy ion collision are entirely produced after the collision since the colliding nuclei only contain  $u$  and  $d$  quarks. Thus study related to strange quarks can be considered as good probes for particle production mechanism in the system created in the collision. To study the strange quark dynamics,  $\phi$  meson is considered as one of the best probe. The ratio of  $\phi$ -mesons yield with that of  $\Omega$  baryons can be used to explore the strange quark dynamics. The panel (a) of Fig. 4.23 shows the baryon-to-meson ratio,  $N(\Omega^- + \bar{\Omega}^+)/2N(\phi)$ , as a function of  $p_T$  in Au+Au collisions at  $\sqrt{s_{NN}} = 11.5$  GeV to 200 GeV. The data points for 200 GeV are taken from Ref. [7]. The dashed lines are the results from the recombination model calculation by Hwa and Yang for  $\sqrt{s_{NN}} = 200$  GeV [12]. In this model the  $\phi$  and  $\Omega$  yields in the measured  $p_T$  region are mostly from the recombination of thermal strange quarks, which were assumed to follow an exponential  $p_T$  distribution. In Au+Au central collisions at  $\sqrt{s_{NN}} = 200$  GeV, the ratios of  $N(\Omega^- + \bar{\Omega}^+)/2N(\phi)$  in the intermediate  $p_T$  range are explained by the recombination model with thermal strange quarks. The ratios  $N(\Omega^- + \bar{\Omega}^+)/2N(\phi)$  for  $\sqrt{s_{NN}} \geq 19.6$  GeV show similar trend. But at  $\sqrt{s_{NN}} = 11.5$  GeV, the ratio at the highest measured  $p_T$  shows a deviation from the trend of other energies. The  $\chi^2/\text{ndf}$  for deviation between 11.5 and 19.6 GeV is  $\sim 8.3/2$  for  $p_T > 2.4$  GeV/c. This may suggest a change in  $\Omega$  and/or  $\phi$  production mechanism at  $\sqrt{s_{NN}} = 11.5$  GeV.

The panel (b) of Fig. 4.23 shows derived strange quark  $p_T$  distribution by following the procedure developed in the paper [13]. The basic assumptions are that  $\Omega$  baryons are formed from coalescence of three strange quarks of equal momentum and the  $\phi$  mesons are from two strange quarks of equal momentum. Therefore, the  $\Omega$  baryon production probability is proportional to the local strange quark density,  $f_s^3(p_T^s)$ , and the  $\phi$  meson is proportional to  $f_s^2(p_T^s)$ , where  $f_s$  is the quark  $p_T^s$  distributions at

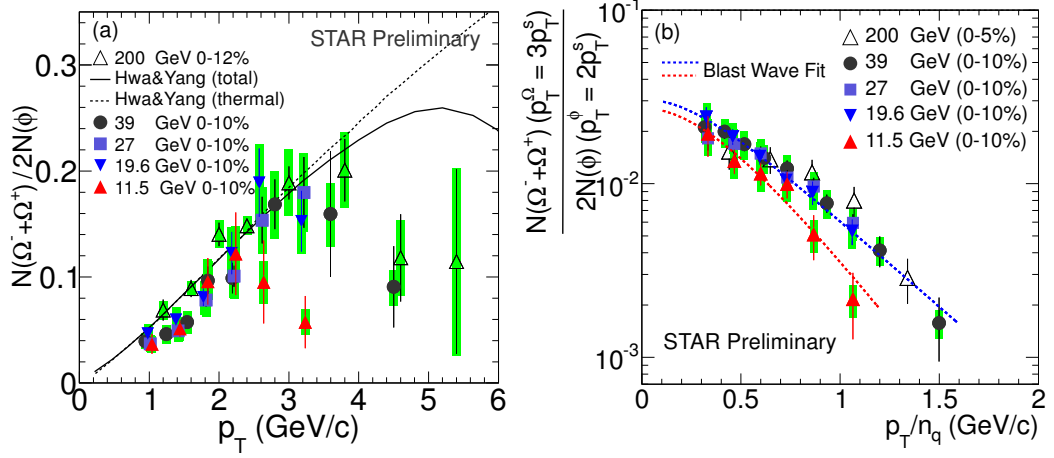


Figure 4.23: (Color online) Left panel: The baryon-to-meson ratio,  $N(\Omega^- + \bar{\Omega}^+)/2N(\phi)$ , as a function of  $p_T$  in mid-rapidity ( $|y| < 0.5$ ) from central Au+Au collisions at  $\sqrt{s_{NN}} = 11.5$ -200 GeV. Green bands denote systematical errors. The solid and dashed lines represent recombination model calculations for central collisions at  $\sqrt{s_{NN}} = 200$  GeV with total and thermal strange quark contributions, respectively [12]. Right panel: Number-of-constituent-quark scaled  $N(\Omega^- + \bar{\Omega}^+)/2N(\phi)$  ratios, as a function of  $p_T/n_q$  in mid-rapidity ( $|y| < 0.5$ ) from central Au+Au collisions at  $\sqrt{s_{NN}} = 11.5$  -200 GeV. Here  $n_q$  is the number of constituent quarks of each hadron. Green bands denote systematical errors. Dashed lines are blast-wave fits with fixed slope parameter  $T = 0.268$  GeV to data at 11.5 and 19.6 GeV, respectively.

hadronization. Now further assuming that strange quarks and anti-strange quarks have the same  $f_s$  shape, the number-of-quark scaled ratio  $\frac{N(\Omega^- + \Omega^+) |_{p_T^\Omega = 3p_T^s}}{2N(\phi) |_{p_T^\phi = 2p_T^s}}$ , which is shown in panel (b) of Fig. 4.23, could reflect the shape of strange quark distribution at the hadronization. The strange quark distributions for data from 19.6, 27, 39 and 200 GeV beam energies are similar where as data at 11.5 seems to show different trend. The dashed blue and red lines are the fit to the quark distributions at 19.6 and 11.5 GeV, respectively, with a blast-wave function [14]. In this blast-wave fit the

slope parameter  $T$  at 0.268 GeV has been fixed to make the radial velocity parameter  $v_T \sim 0$  at 11.5 GeV, and then we obtained a  $v_T$  of  $(0.41 \pm 0.08)c$  and  $(0.46 \pm 0.05)c$  for 19.6 and 27 GeV data respectively. This tells that there is difference in the shape of the strange quark  $p_T^s$  distribution between 11.5 GeV and higher energy data. These data are indicative of a possible transition from hadron dominated dynamics at the low beam energy to a partonic phase above  $\sqrt{s_{NN}} = 19.6$  GeV. Therefore, this measurements point to a beam energy region between 11.5 and 19.6 GeV for further investigation of the transition or find the onset of de-confinement transition.

## 4.5 Summary

We have presented the measurements of  $\phi$ -meson production at mid-rapidity ( $|y| < 0.5$ ) in Au+Au collisions collected by the STAR experiment at  $\sqrt{s_{NN}} = 7.7, 11.5, 19.6, 27$  and 39 GeV. Mass of the  $\phi$  meson was found to be consistent with PDG value and previous STAR measurements at top RHIC energies [7]. Width of the  $\phi$  meson was observed to be higher than PDG value and this is because of finite momentum resolution of TPC detectors. Transverse momentum spectra of  $\phi$  meson for different centralities (0-10%, 10-20%, 20-30%, 30-40%, 40-60% and 60-80%) are presented at  $\sqrt{s_{NN}} = 7.7, 11.5, 19.6, 27$  and 39 GeV. The  $p_T$  integrated yield per unit rapidity ( $dN/dy$ ) are measured for all the six centralities and all the centre-of-mass energies and compared with previous measurement by STAR and NA49 experiments. We observed a increasing trend in  $dN/dy$  with increase in beam energies. The measured mid-rapidity yield per participant pair ( $(dN/dy)/(0.5N_{part})$ ) increases nonlinearly with centrality. This suggests particle production does not scale with  $N_{part}$ . For a given  $N_{part}$ ,  $(dN/dy)/(0.5N_{part})$  increases with the collision energy, which is expected because of the increase of energy available to produce the  $\phi$  mesons.

The nuclear modification factors at the intermediate  $p_T$  are observed to be equal or higher than unity at  $\sqrt{s_{NN}} \leq 39$  GeV, indicating parton energy loss effect is less important at low beam energies and could be the hint for the formation of hadron dominated matter. We also presented particle ratios  $N(\phi)/N(\pi^-)$ ,  $N(\phi)/N(K^-)$ ,

$N(\Omega)/N(\phi)$  as function of  $N_{part}$  for different centre-of-mass energies. The ratios  $N(\phi)/N(K^-)$  are almost constant as a function of centrality and centre-of-mass energy. This effectively rule out kaon coalescence as the dominant production mechanism for the  $\phi$  meson. The ratios of  $N(\Omega^- + \bar{\Omega}^+)/2N(\phi)$  show similar trend for  $\sqrt{s_{NN}} \geq 19.6$  GeV, where as at  $\sqrt{s_{NN}} = 11.5$  GeV, the ratio at the highest measured  $p_T$  shows a deviation from the trend of other energies. This may suggest a change in  $\Omega$  and/or  $\phi$  production mechanism at  $\sqrt{s_{NN}} = 11.5$  GeV.

# Bibliography

- [1] D. Drijard *et al.*, Nucl. Instr. Meth. **A225**, 367 (1984).
- [2] D. L'Hote, Nucl. Instr. Meth. **A 337**, 544 (1994).
- [3] Using the  $\phi$ -meson to probe the medium created in Au+Au collisions at RHIC.  
PhD thesis of Sarah-Louise Blyth, UCT (2007).
- [4] J. Beringer *et al.* (Particle Data Group), Phys. Rev. **D 86**, 010001 (2012).
- [5] B. I. Abelev *et al.* (STAR Collaboration), Phys. Rev. **C 79**, 034909 (2009).
- [6] M. Anderson *et al.*, Nucl. Instr. Meth. **A 499**, 659 (2003).
- [7] B. I. Abelev *et al.* (STAR Collaboration), Phys. Rev. **C 49**, 064903 (2009).
- [8] B. I. Abelev *et al.* (STAR Collaboration), Phys. Lett. **B 673**, 183 (2009).
- [9] C. Alt *et al.* (NA49 Collaboration), Phys. Rev. **C 78**, 044907 (2008).
- [10] B. I. Abelev *et al.* (STAR Collaboration), Phys. Rev. **C 79**, 034909 (2009).
- [11] X. N. Wang and M. Gyulassy, Phys. Rev. Lett. **68**, 1480 (1992).
- [12] R.C. Hwa and C.B. Yang, Phys. Rev. **C 75**, 054904 (2007).
- [13] J. H. Chen *et al.*, Phys. Rev. **C 78**, 034907 (2008).
- [14] R. J. Fries *et al.*, Phys. Rev. Lett. **90**, 202303 (2003);  
Phys. Rev. **C 68**, 044902 (2003).

## 4.6 Appendix

### 4.6.1 (signal+background)/background ratio

(signal+background)/background						
$p_T$ bin (GeV/c)	0-10%	10-20%	20-30%	30-40%	40-60%	60-80%
0.4-0.5	1.00761	1.01136	1.01624	1.02554	1.04385	1.11554
0.5-0.6	1.00857	1.01251	1.01797	1.02548	1.04433	1.12697
0.6-0.7	1.00773	1.01163	1.01754	1.02523	1.04471	1.1195
0.7-0.8	1.00652	1.00963	1.01545	1.02182	1.03892	1.11451
0.8-1.0	1.00435	1.00692	1.01007	1.01551	1.02669	1.07121
1.0-1.2	1.0024	1.00385	1.00562	1.00838	1.01464	1.04186
1.2-1.5	1.00135	1.00194	1.00295	1.00432	1.00722	1.01811
1.5-1.8	1.00092	1.00138	1.00186	1.00257	1.00421	1.0102
1.8-2.2	1.00087	1.00129	1.00222	1.00304	1.005	1.01075
2.2-2.6	1.00111	1.00179	1.00262	1.00405	1.0065	1.02046
2.6-3.0	1.00138	1.00236	1.00457	1.00494	1.0104	1.02003
3.0-4.0	1.0018	1.00318	1.00507	1.00765	1.01578	1.04142
4.0-5.0	1.00452	1.00673	1.00945	1.002337	1.003023	1.012961

Table 4.1: Values of (signal+background)/background for  $\phi$  mesons in Au+Au collisions at  $\sqrt{s_{NN}} = 39$  GeV for different centrality classes and  $p_T$  bins.

<b>(Signal+background)/background</b>						
$p_T$ bin (GeV/c)	0-10%	10-20%	20-30%	30-40%	40-60%	60-80%
0.4-0.5	1.00786	1.00476	1.0138	1.01837	1.03541	1.14622
0.5-0.6	1.00622	1.00945	1.01757	1.0239	1.03688	1.13175
0.6-0.7	1.00582	1.00997	1.01521	1.02378	1.04584	1.14598
0.7-0.8	1.00637	1.0092	1.01693	1.02441	1.04377	1.12572
0.8-1.0	1.0046	1.00774	1.01152	1.01824	1.0338	1.10035
1.0-1.2	1.00256	1.00475	1.00702	1.00852	1.01438	1.0482
1.2-1.5	1.00152	1.00213	1.00294	1.0048	1.00622	1.00928
1.5-1.8	1.00096	1.00165	1.00115	1.00266	1.00225	1.00345
1.8-2.2	1.00103	1.00117	1.00223	1.00308	1.00304	1.00186
2.2-2.6	1.00163	1.00197	1.00464	1.00628	1.0075	1.01389
2.6-3.0	1.00228	1.0017	1.00188	1.00424	1.01239	1.02689
3.0-4.0	1.00246	1.00128	1.00399	1.00484	1.018	1.03447

Table 4.2: Values of (signal+background)/background for  $\phi$  mesons in Au+Au collisions at  $\sqrt{s_{NN}} = 27$  GeV for different centrality classes and  $p_T$  bins.

<b>(Signal+background)/background</b>						
$p_T$ bin (GeV/c)	0-10%	10-20%	20-30%	30-40%	40-60%	60-80%
0.4-0.5	1.00621	1.00886	1.01851	1.02743	1.05696	1.10768
0.5-0.6	1.00807	1.00995	1.01792	1.01981	1.04406	1.19493
0.6-0.7	1.0069	1.00978	1.01949	1.03253	1.04762	1.15939
0.7-0.8	1.00795	1.01047	1.01729	1.0264	1.04331	1.18004
0.8-1.0	1.00509	1.00903	1.01239	1.0225	1.036	1.10747
1.0-1.3	1.00272	1.00406	1.0056	1.00911	1.01439	1.03475
1.3-1.7	1.00123	1.00140	1.00287	1.00308	1.00208	1.00181
1.7-2.0	1.00039	1.00133	1.00166	1.00128	1.00332	1.00738
2.0-2.5	1.00092	1.00130	1.00369	1.00128	1.01151	1.0068
2.5-3.5	0.999723	1.0010	1.00489	1.00434	1.01151	0.999582

Table 4.3: Values of (signal+background)/background for  $\phi$  mesons in Au+Au collisions at  $\sqrt{s_{NN}} = 19.6$  GeV for different centrality classes and  $p_T$  bins.

<b>(Signal+background)/background</b>						
$p_T$ bin (GeV/c)	0-10%	10-20%	20-30%	30-40%	40-60%	60-80%
0.4-0.5	1.01308	1.01495	1.02296	1.03582	1.05036	1.14553
0.5-0.6	1.01058	1.01599	1.02844	1.03573	1.05962	1.14275
0.6-0.7	1.00955	1.01745	1.02218	1.0302	1.05684	1.14913
0.7-0.8	1.00798	1.01223	1.01752	1.02678	1.04393	1.11877
0.8-1.0	1.00532	1.00816	1.01165	1.01502	1.02609	1.06999
1.0-1.3	1.00217	1.00284	1.00461	1.00616	1.01067	1.02377
1.3-1.7	1.00114	1.00196	1.00243	1.00336	1.00383	1.00725
1.7-2.0	1.00094	1.00135	1.0022	1.00264	1.00225	1.00623
2.0-2.5	1.00166	1.00129	1.0018	1.00289	1.00645	1.008
2.5-3.0	1.0013	1.00325	1.00233	1.00431	1.00671	1.02314

Table 4.4: Values of (signal+background)/background for  $\phi$  mesons in Au+Au collisions at  $\sqrt{s_{NN}} = 11.5$  GeV for different centrality classes and  $p_T$  bins.

<b>(Signal+background)/background</b>						
$p_T$ bin (GeV/c)	0-10%	10-20%	20-30%	30-40%	40-60%	60-80%
0.4-0.5	1.01087	1.01834	1.0214	1.03309	1.08741	1.30276
0.5-0.6	1.01954	1.01631	1.03139	1.04115	1.06774	1.14183
0.6-0.7	1.01003	1.0228	1.03048	1.04135	1.0646	1.13654
0.7-0.8	1.01146	1.0154	1.02427	1.02948	1.05606	1.14316
0.8-1.0	1.00629	1.01175	1.01227	1.0199	1.03293	1.08332
1.0-1.3	1.0034	1.00367	1.0045	1.00755	1.01302	1.01838
1.3-1.7	1.00178	1.00151	1.00322	1.00173	1.00541	1.00505
1.7-2.0	0.999514	1.00212	0.999184	1.00214	1.00508	1.01384

Table 4.5: Values of (signal+background)/background for  $\phi$  mesons in Au+Au collisions at  $\sqrt{s_{NN}} = 7.7$  GeV for different centrality classes and  $p_T$  bins.

## 4.6.2 $\phi$ -meson yield per unit rapidity

<b>Au+Au collisions at <math>\sqrt{s_{NN}} = 39</math> GeV</b>			
Centrality	$dN/dy$ ( $ y  < 0.5$ )	Statistical Error	Systematic Error
0 - 10%	3.4996	0.0693	0.5373
10 - 20%	2.3237	0.0454	0.4491
20 - 30%	1.6223	0.0301	0.2551
30 - 40%	1.0527	0.0195	0.1578
40 - 60%	0.4673	0.0074	0.0843
60 - 80%	0.1298	0.0033	0.0524

<b>Au+Au collisions at <math>\sqrt{s_{NN}} = 27</math> GeV</b>			
Centrality	$dN/dy$ ( $ y  < 0.5$ )	Statistical Error	Systematic Error
0 - 10%	3.0570	0.0323	0.4965
10 - 20%	2.0270	0.0240	0.3887
20 - 30%	1.4041	0.0155	0.2335
30 - 40%	0.8781	0.0095	0.1866
40 - 60%	0.4145	0.0052	0.0821
60 - 80%	0.0954	0.0015	0.0422

<b>Au+Au collisions at <math>\sqrt{s_{NN}} = 19.6</math> GeV</b>			
Centrality	$dN/dy$ ( $ y  < 0.5$ )	Statistical Error	Systematic Error
0 - 10%	2.5850	0.0335	0.4478
10 - 20%	1.7919	0.0262	0.3210
20 - 30%	1.1662	0.01742	0.1697
30 - 40%	0.7644	0.0107	0.1019
40 - 60%	0.3431	0.0057	0.0572
60 - 80%	0.0738	0.0060	0.0307

<b>Au+Au collisions at <math>\sqrt{s_{NN}} = 11.5</math> GeV</b>			
Centrality	$dN/dy$ ( $ y  < 0.5$ )	Statistical Error	Systematic Error
0 - 10%	1.7582	0.0454	0.2609
10 - 20%	1.2659	0.0333	0.2644
20 - 30%	0.8568	0.0217	0.1466
30 - 40%	0.5057	0.0149	0.0806
40 - 60%	0.2385	0.0030	0.0519
60 - 80%	0.0612	0.0026	0.0249

<b>Au+Au collisions at <math>\sqrt{s_{NN}} = 7.7</math> GeV</b>			
Centrality	$dN/dy$ ( $ y  < 0.5$ )	Statistical Error	Systematic Error
0 - 10%	1.2099	0.0435	0.4478
10 - 20%	0.8266	0.0371	0.3210
20 - 30%	0.4794	0.0327	0.1697
30 - 40%	0.3265	0.0165	0.1019
40 - 60%	0.1496	0.0068	0.0572
60 - 80%	0.0377	0.0060	0.0307

### 4.6.3 Parameters of Levy and exponential fit to the $\phi$ -meson $p_T$ spectra

#### 4.6.3.1 Levy fit parameters:

Au+Au at $\sqrt{s_{NN}} = 39$ GeV				
Centrality	$T$ (GeV)	$n$	$dN/dy$	$\chi^2/ndf$
0-10%	$0.299543 \pm 0.01611$	$6.619e^{10} \pm 8.931e^{05}$	$3.402 \pm 0.8129$	1.645/9
10-20%	$0.3131 \pm 0.03514$	$1.108e^{07} \pm 1.414e^{04}$	$2.216 \pm 0.2744$	1.046/9
20-30%	$0.2996 \pm 0.01301$	$1.532e^{08} \pm 6.651e^{05}$	$1.597 \pm 0.15$	0.155/8
30-40%	$0.2957 \pm 0.04906$	$945 \pm 356$	$1.019 \pm 0.07738$	1.047/9
40-60%	$0.2363 \pm 0.03561$	$24.47 \pm 14.96$	$0.4562 \pm 0.05774$	0.6383/9
60-80%	$0.211 \pm 0.034$	$20.2 \pm 10.72$	$0.1285 \pm 0.01813$	0.705/9

Au+Au at $\sqrt{s_{NN}} = 27$ GeV				
Centrality	$T$ (GeV)	$n$	$dN/dy$	$\chi^2/ndf$
0-10%	$0.2861 \pm 0.007709$	$89.17 \pm 78.22$	$3.051 \pm 0.1783$	3.719/9
10-20%	$0.2851 \pm 0.0039$	$56.62 \pm 38.42$	$2.004 \pm 0.03578$	10.05/9
20-30%	$0.2747 \pm 0.01754$	$46.3 \pm 32.98$	$1.345 \pm 0.08244$	12.85/9
30-40%	$0.2574 \pm 0.01741$	$40.36 \pm 30.44$	$0.8464 \pm 0.05332$	14.06/9
40-60%	$0.2114 \pm 0.01696$	$19.3 \pm 6.155$	$0.4041 \pm 0.02639$	2.573/9
60-80%	$0.1901 \pm 0.01368$	$23.34 \pm 7.753$	$0.1076 \pm 0.00748$	15.946/9

Au+Au at $\sqrt{s_{NN}} = 19.6$ GeV				
Centrality	$T$ (GeV)	$n$	$dN/dy$	$\chi^2/ndf$
0-10%	$0.2803 \pm 0.00466$	$87.17 \pm 69.63$	$2.603 \pm 0.0519$	10.28/8
10-20%	$0.2676 \pm 0.01202$	$59.38 \pm 47.27$	$1.786 \pm 0.0379$	10.96/8
20-30%	$0.2367 \pm 0.01038$	$32.32 \pm 13.11$	$1.263 \pm 0.02903$	9.75/8
30-40%	$0.2397 \pm 0.01144$	$33.25 \pm 26.33$	$0.7595 \pm 0.01835$	8.804/8
40-60%	$0.1947 \pm 0.00865$	$15.19 \pm 2.743$	$0.3364 \pm 0.007881$	14.31/8
60-80%	$0.193 \pm 0.00553$	$15.76 \pm 2.849$	$0.08021 \pm 0.00196$	7.346/8

Au+Au at $\sqrt{s_{NN}} = 11.5$ GeV				
Centrality	$T$ (GeV)	$n$	$dN/dy$	$\chi^2/ndf$
0-10%	$0.2662 \pm 0.009276$	$100.73 \pm 75.39$	$1.733 \pm 0.1127$	6.694/7
10-20%	$0.2653 \pm 0.01187$	$60.29 \pm 42.09$	$1.121 \pm 0.07665$	8.171/7
20-30%	$0.2282 \pm 0.02887$	$37.3 \pm 32.05$	$0.7722 \pm 0.05479$	4.599/7
30-40%	$0.2353 \pm 0.03014$	$34.36 \pm 30.39$	$0.4676 \pm 0.03447$	10.18/7
40-60%	$0.1846 \pm 0.0225$	$18.9 \pm 10.09$	$0.2059 \pm 0.01574$	2.898/7
60-80%	$0.1438 \pm 0.01981$	$11.31 \pm 3.681$	$0.05699 \pm 0.00512$	1.034/7

Au+Au at $\sqrt{s_{NN}} = 7.7$ GeV				
Centrality	$T$ (GeV)	$n$	$dN/dy$	$\chi^2/ndf$
0-10%	$0.3082 \pm 0.03636$	$90.33 \pm 79.97$	$1.21 \pm 0.09845$	0.5978/4
10-20%	$0.2419 \pm 0.02615$	$64.29 \pm 40.33$	$0.7199 \pm 0.06104$	2.8/4
20-30%	$0.1639 \pm 0.07128$	$50.19 \pm 35.39$	$0.5181 \pm 0.09124$	2.946/4
30-40%	$0.2039 \pm 0.02201$	$63.3 \pm 39.39$	$0.2759 \pm 0.02447$	1.299/4
40-60%	$0.1562 \pm 0.04774$	$7.1 \pm 6.67$	$0.1397 \pm 0.01566$	1.833/4
60-80%	$0.1423 \pm 0.0842$	$15.02 \pm 52.03$	$0.0336 \pm 0.007307$	2.816/4

#### 4.6.3.2 Exponential fit parameters:

Au+Au at $\sqrt{s_{NN}} = 39$ GeV			
Centrality	$T$ (GeV)	$dN/dy$	$\chi^2/ndf$
0-10%	$0.3015 \pm 0.0052$	$3.549 \pm 0.0703$	10.36/10
10-20%	$0.3019 \pm 0.00522$	$2.347 \pm 0.0456$	15.54/10
20-30%	$0.3004 \pm 0.005711$	$1.618 \pm 0.03005$	3.946/9
30-40%	$0.2826 \pm 0.00398$	$1.067 \pm 0.0199$	12.57/10
40-60%	$0.267 \pm 0.00362$	$0.498 \pm 0.00662$	20.62/10
60-80%	$0.2371 \pm 0.00501$	$0.1246 \pm 0.002717$	21.08/10

Au+Au at $\sqrt{s_{NN}} = 27$ GeV			
Centrality	$T$ (GeV)	$dN/dy$	$\chi^2/ndf$
0-10%	$0.29 \pm 0.00245$	$3.46 \pm 0.0368$	26.13/10
10-20%	$0.2873 \pm 0.00227$	$2.152 \pm 0.02315$	32.3/10
20-30%	$0.2766 \pm 0.00236$	$1.471 \pm 0.01649$	24.93/10
30-40%	$0.2645 \pm 0.00225$	$0.9267 \pm 0.0105$	13.57/10
40-60%	$0.2601 \pm 0.00217$	$0.4224 \pm 0.00450$	25.19/10
60-80%	$0.2296 \pm 0.00250$	$0.1004 \pm 0.00116$	71.08/10

Au+Au at $\sqrt{s_{NN}} = 19.6$ GeV			
Centrality	$T$ (GeV)	$dN/dy$	$\chi^2/ndf$
0-10%	$0.2805 \pm 0.003265$	$2.609 \pm 0.0389$	28.87/9
10-20%	$0.2788 \pm 0.003722$	$1.817 \pm 0.02621$	15.28/9
20-30%	$0.2608 \pm 0.003246$	$1.187 \pm 0.01775$	13.63/9
30-40%	$0.2652 \pm 0.003917$	$0.7633 \pm 0.01107$	7.811/9
40-60%	$0.2404 \pm 0.003352$	$0.3453 \pm 0.004779$	17.78/9
60-80%	$0.2142 \pm 0.003558$	$0.07281 \pm 0.00127$	10.06/9

Au+Au at $\sqrt{s_{NN}} = 11.5$ GeV			
Centrality	$T$ (GeV)	$dN/dy$	$\chi^2/ndf$
0-10%	$0.2621 \pm 0.006674$	$1.754 \pm 0.0479$	11.5/8
10-20%	$0.265 \pm 0.006731$	$1.281 \pm 0.03328$	9.638/8
20-30%	$0.2359 \pm 0.006009$	$0.8435 \pm 0.02279$	6.885/8
30-40%	$0.2453 \pm 0.005765$	$0.5066 \pm 0.01387$	1.946/8
40-60%	$0.2071 \pm 0.00545$	$0.2352 \pm 0.00599$	2.862/8
60-80%	$0.1947 \pm 0.00888$	$0.0515 \pm 0.001855$	11.12/8

Au+Au at $\sqrt{s_{NN}} = 7.7$ GeV			
Centrality	$T$ (GeV)	$dN/dy$	$\chi^2/ndf$
0-10%	$0.3082 \pm 0.03087$	$1.207 \pm 0.06977$	3.36/5
10-20%	$0.2553 \pm 0.01811$	$0.7833 \pm 0.03676$	10.46/5
20-30%	$0.2207 \pm 0.0141$	$0.4711 \pm 0.0239$	9.767/5
30-40%	$0.2375 \pm 0.01926$	$0.3295 \pm 0.01742$	4.177/5
40-60%	$0.2195 \pm 0.01467$	$0.1474 \pm 0.007184$	0.4763/5
60-80%	$0.1992 \pm 0.02282$	$0.0358 \pm 0.00282$	3.958/5

#### 4.6.4 Results from Glauber model simulation

Table 4.6: Summary of centrality bins, average number of participants  $\langle N_{\text{part}} \rangle$ , and number of binary collisions  $\langle N_{\text{coll}} \rangle$ , from MC Glauber simulations at  $\sqrt{s_{NN}} = 7.7, 11.5, 19.6, 27, 39$  and  $62.4$  GeV. The errors are systematic uncertainties.

Au+Au at $\sqrt{s_{NN}} = 7.7$ GeV			Au+Au at $\sqrt{s_{NN}} = 11.5$ GeV		
Centrality	$\langle N_{\text{part}} \rangle$	$\langle N_{\text{coll}} \rangle$	Centrality	$\langle N_{\text{part}} \rangle$	$\langle N_{\text{coll}} \rangle$
0-5%	$337 \pm 2$	$774 \pm 28$	0-5%	$338 \pm 2$	$784 \pm 27$
5-10%	$290 \pm 6$	$629 \pm 20$	5-10%	$290 \pm 6$	$635 \pm 20$
10-20%	$226 \pm 8$	$450 \pm 22$	10-20%	$226 \pm 8$	$453 \pm 23$
20-30%	$160 \pm 10$	$283 \pm 24$	20-30%	$160 \pm 9$	$284 \pm 23$
30-40%	$110 \pm 11$	$171 \pm 23$	30-40%	$110 \pm 10$	$172 \pm 22$
40-50%	$72 \pm 10$	$96 \pm 19$	40-50%	$73 \pm 10$	$98 \pm 18$
50-60%	$45 \pm 9$	$52 \pm 13$	50-60%	$44 \pm 9$	$52 \pm 14$
60-70%	$26 \pm 7$	$25 \pm 9$	60-70%	$26 \pm 7$	$25 \pm 9$
70-80%	$14 \pm 4$	$12 \pm 5$	70-80%	$14 \pm 6$	$12 \pm 6$

Au+Au at $\sqrt{s_{NN}} = 19.6$ GeV			Au+Au at $\sqrt{s_{NN}} = 27$ GeV		
Centrality	$\langle N_{\text{part}} \rangle$	$\langle N_{\text{coll}} \rangle$	Centrality	$\langle N_{\text{part}} \rangle$	$\langle N_{\text{coll}} \rangle$
0-5%	$338 \pm 2$	$800 \pm 27$	0-5%	$343 \pm 2$	$841 \pm 28$
5-10%	$289 \pm 6$	$643 \pm 20$	5-10%	$299 \pm 6$	$694 \pm 22$
10-20%	$225 \pm 9$	$458 \pm 24$	10-20%	$233 \pm 9$	$497 \pm 26$
20-30%	$158 \pm 10$	$284 \pm 26$	20-30%	$166 \pm 11$	$312 \pm 28$
30-40%	$108 \pm 10$	$170 \pm 23$	30-40%	$114 \pm 11$	$188 \pm 25$
40-50%	$71 \pm 10$	$96 \pm 18$	40-50%	$75 \pm 10$	$106 \pm 20$
50-60%	$44 \pm 9$	$51 \pm 13$	50-60%	$47 \pm 9$	$56 \pm 15$
60-70%	$25 \pm 7$	$25 \pm 8$	60-70%	$27 \pm 8$	$27 \pm 10$
70-80%	$14 \pm 5$	$12 \pm 5$	70-80%	$14 \pm 6$	$12 \pm 6$

Au+Au at $\sqrt{s_{NN}} = 39$ GeV			Au+Au at $\sqrt{s_{NN}} = 62.4$ GeV		
Centrality	$\langle N_{\text{part}} \rangle$	$\langle N_{\text{coll}} \rangle$	Centrality	$\langle N_{\text{part}} \rangle$	$\langle N_{\text{coll}} \rangle$
0-5%	$342 \pm 2$	$853 \pm 27$	0-5%	$344 \pm 2$	$903 \pm 27$
5-10%	$294 \pm 6$	$687 \pm 21$	5-10%	$296 \pm 6$	$726 \pm 20$
10-20%	$230 \pm 9$	$492 \pm 26$	10-20%	$232 \pm 8$	$518 \pm 25$
20-30%	$162 \pm 10$	$306 \pm 27$	20-30%	$164 \pm 9$	$321 \pm 27$
30-40%	$111 \pm 11$	$183 \pm 24$	30-40%	$113 \pm 10$	$192 \pm 25$
40-50%	$74 \pm 10$	$104 \pm 20$	40-50%	$75 \pm 10$	$108 \pm 20$
50-60%	$46 \pm 9$	$55 \pm 14$	50-60%	$46 \pm 9$	$56 \pm 15$
60-70%	$26 \pm 7$	$27 \pm 9$	60-70%	$26 \pm 7$	$27 \pm 9$
70-80%	$14 \pm 5$	$12 \pm 6$	70-80%	$13 \pm 5$	$12 \pm 5$

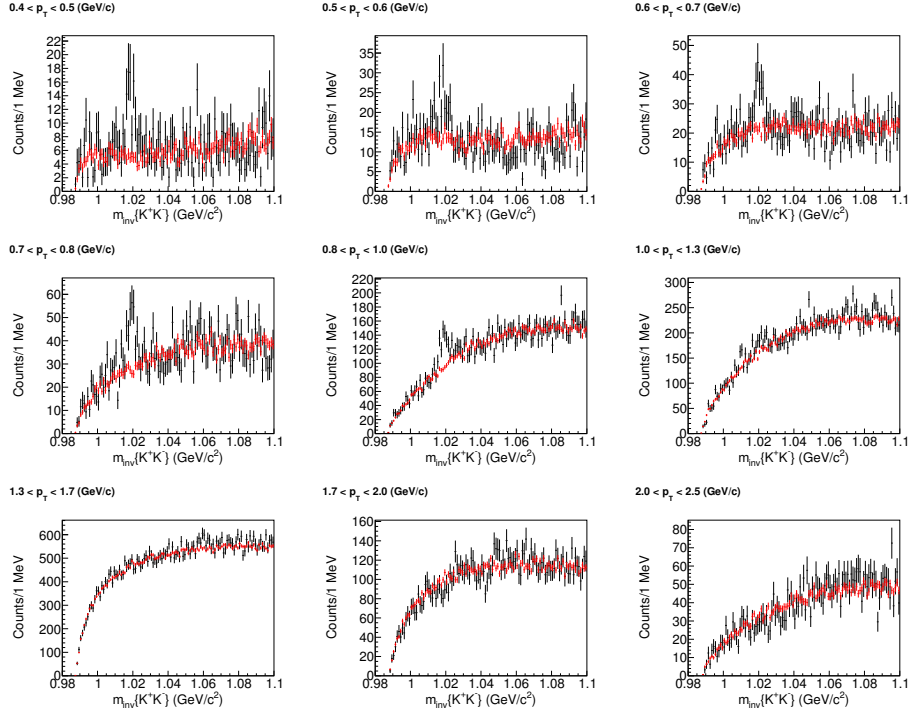


Figure 4.24: (Color online) Same event invariant mass distribution (black curve) and mixed event invariant mass distribution (red curve) after proper normalisation in Au+Au collision (60-80%) at  $\sqrt{s_{NN}} = 7.7$  GeV for different  $p_T$  bins.

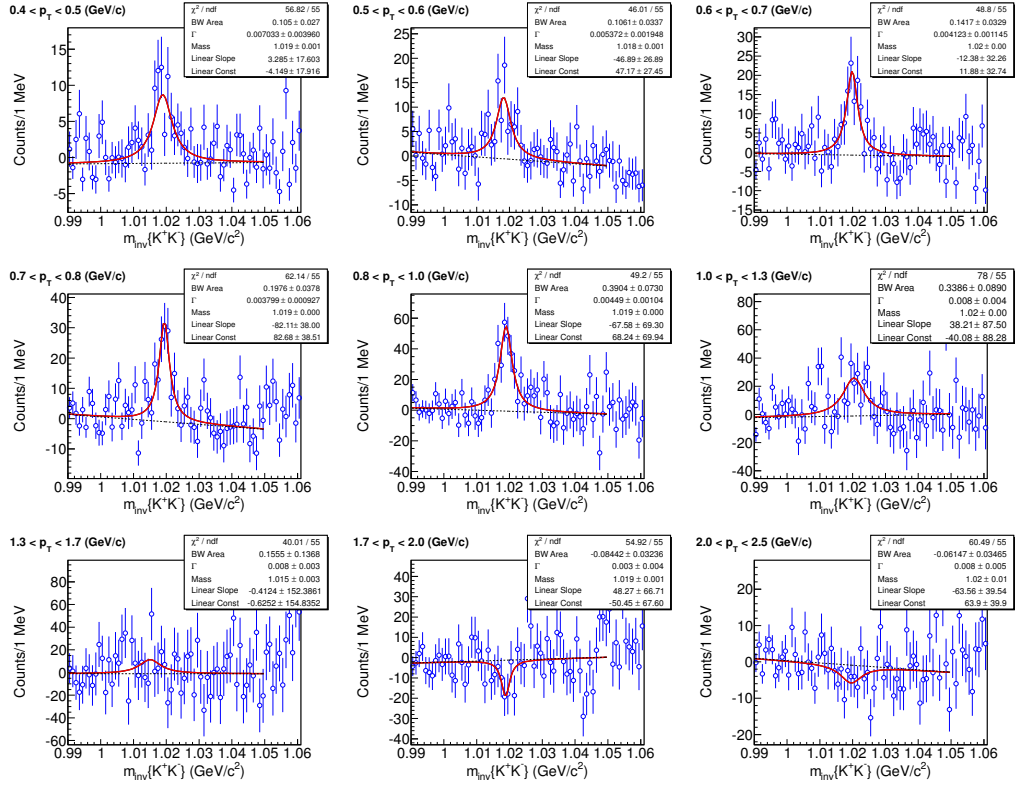


Figure 4.25: (Color online)  $\phi$ -mesons signal after combinatorial background subtraction in Au+Au collision (60-80%) at  $\sqrt{s_{NN}} = 7.7$  GeV for different  $p_T$  bins.

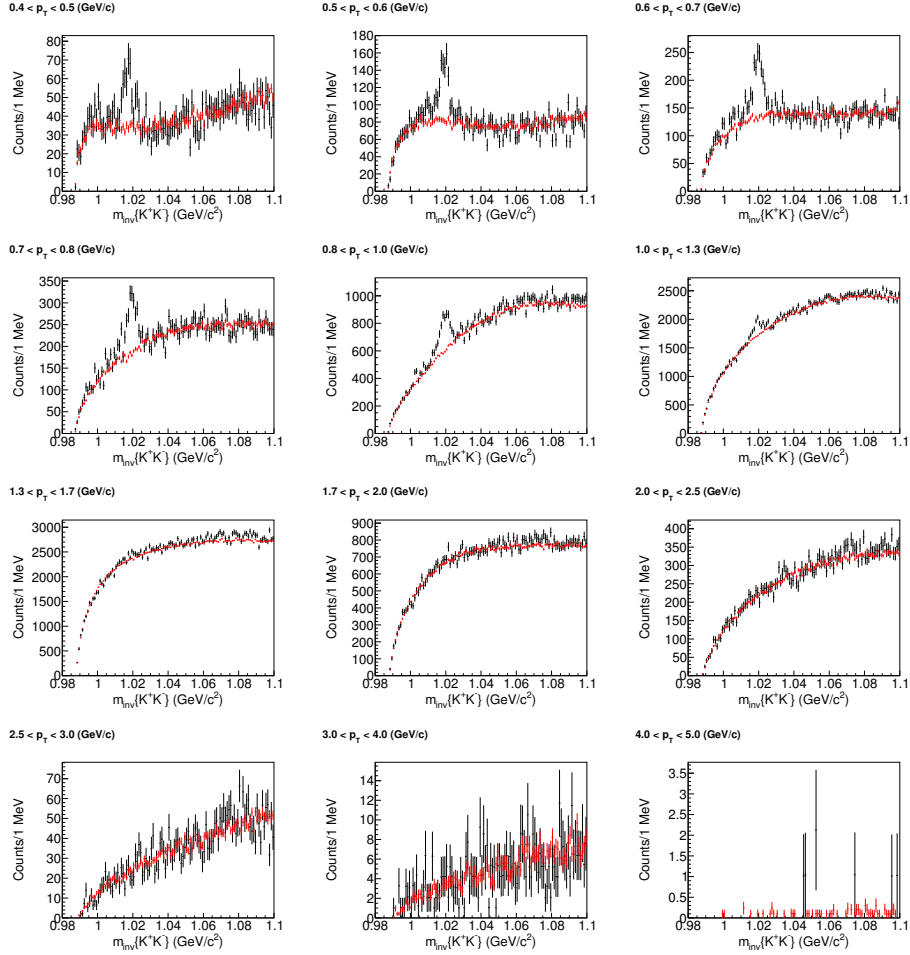


Figure 4.26: (Color online) Same event invariant mass distribution (black curve) and mixed event invariant mass distribution (red curve) after proper normalisation in Au+Au collision (60-80%) at  $\sqrt{s_{NN}} = 11.5$  GeV for different  $p_T$  bins.

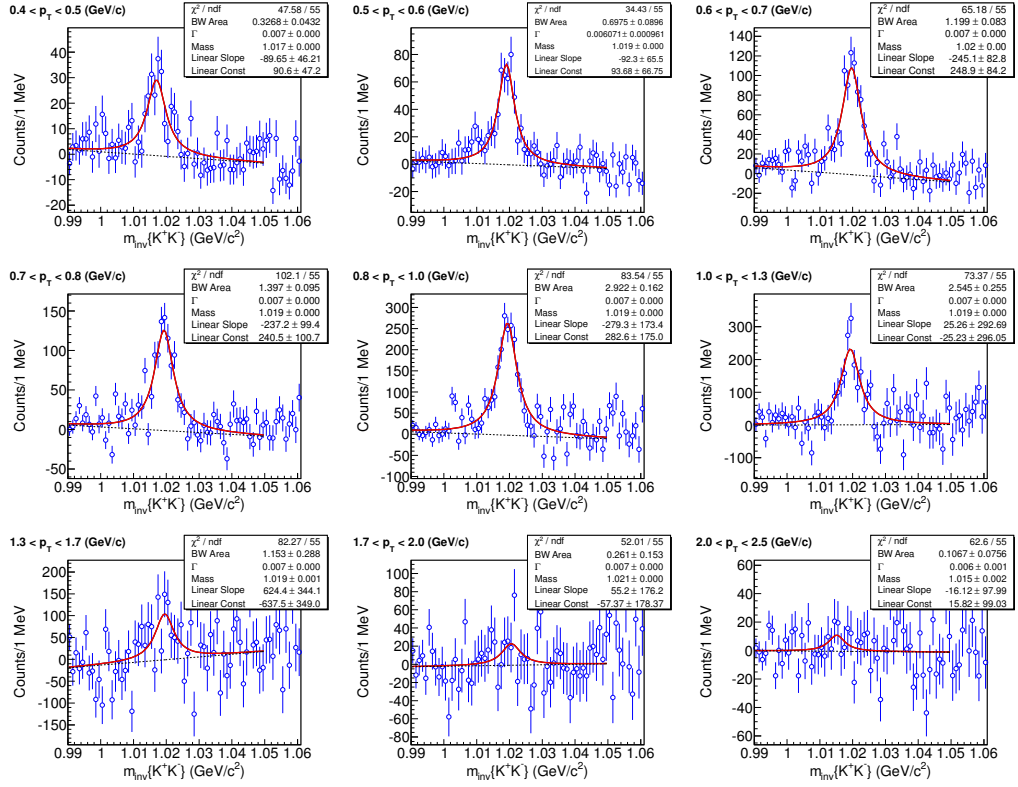


Figure 4.27: (Color online)  $\phi$ -mesons signal after combinatorial background subtraction in Au+Au collision (60-80%) at  $\sqrt{s_{NN}} = 11.5$  GeV for different  $p_T$  bins.

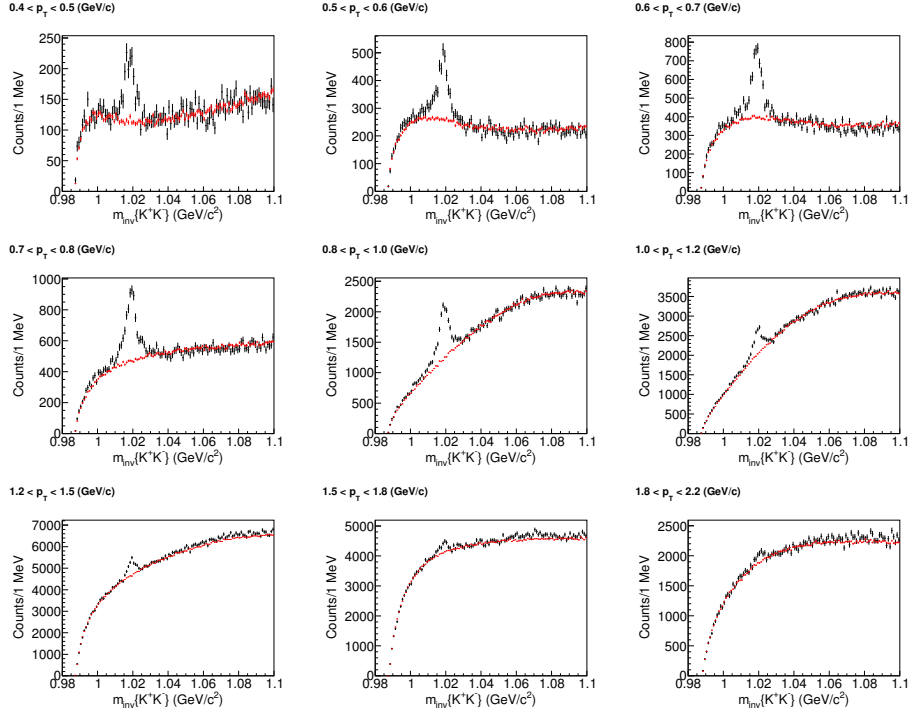


Figure 4.28: (Color online) Same event invariant mass distribution (black curve) and mixed event invariant mass distribution (red curve) after proper normalisation in Au+Au collision (60-80%) at  $\sqrt{s_{NN}} = 19.6$  GeV for different  $p_T$  bins.

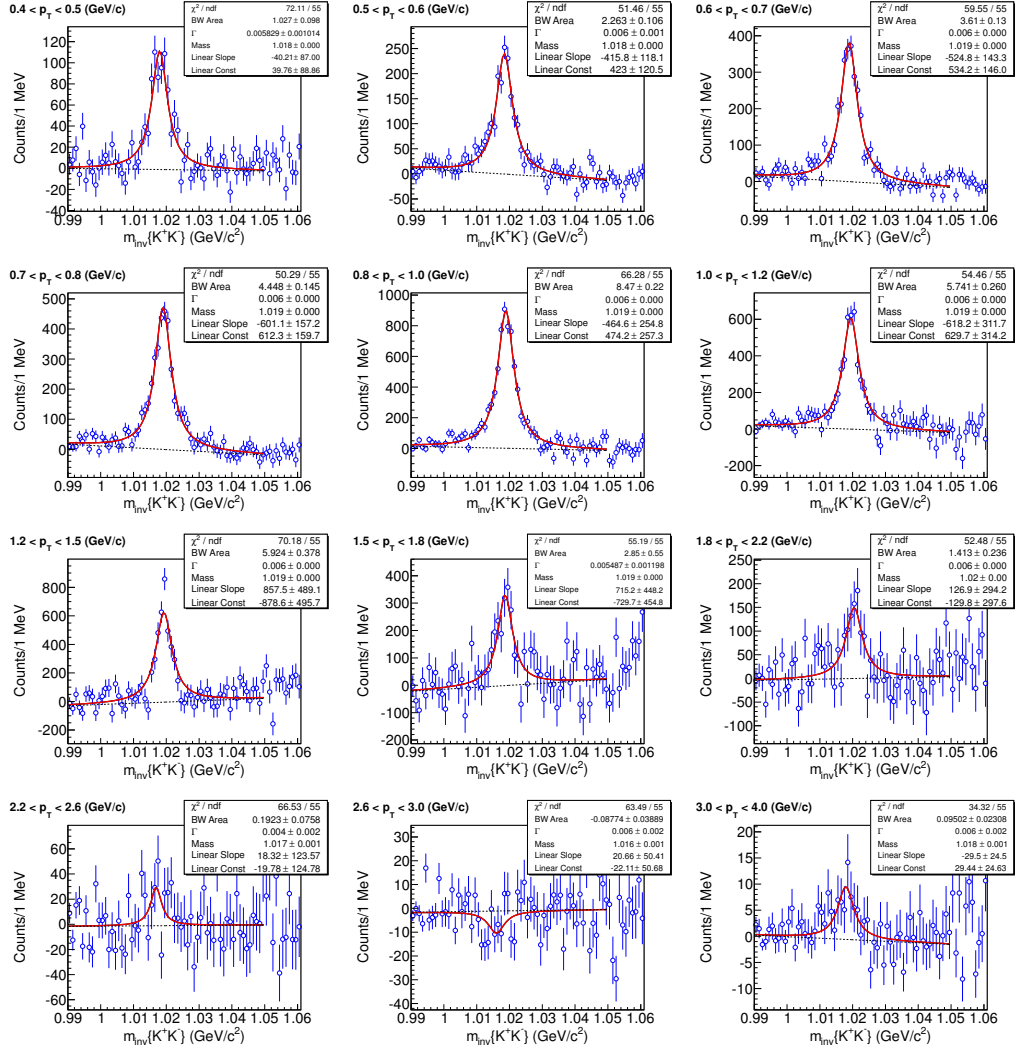


Figure 4.29: (Color online)  $\phi$ -mesons signal after combinatorial background subtraction in Au+Au collision (60-80%) at  $\sqrt{s_{NN}} = 19.6$  GeV for different  $p_T$  bins.

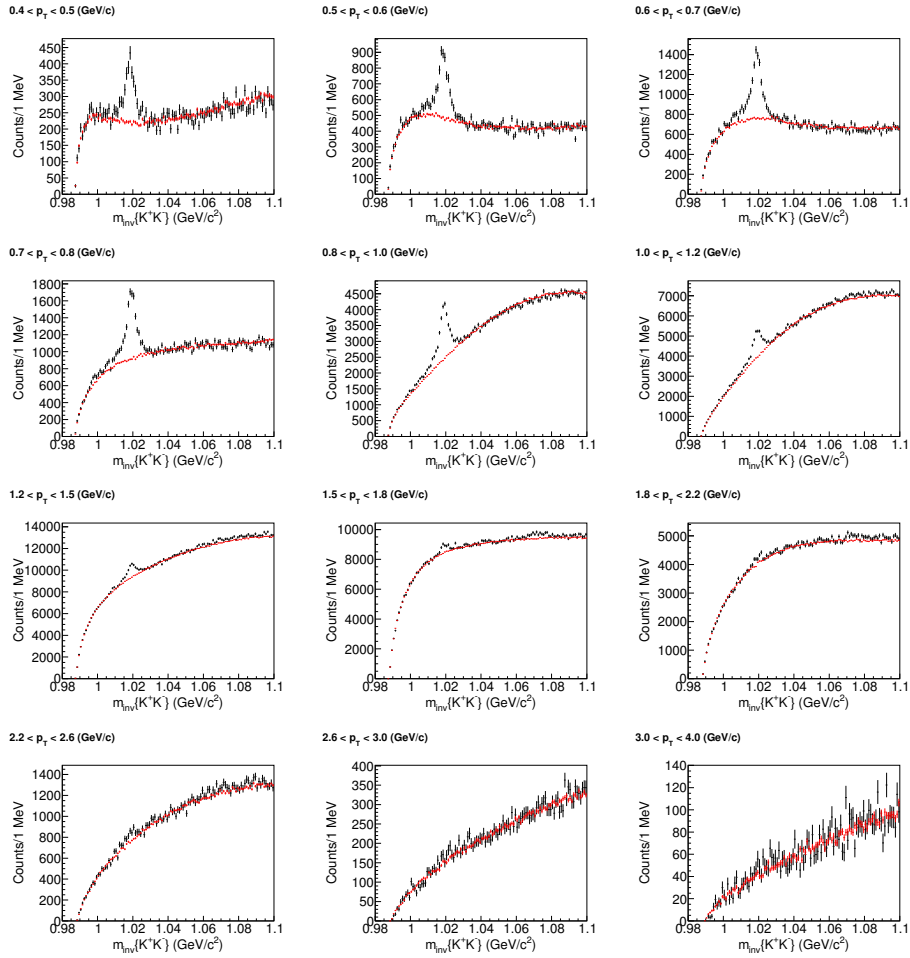


Figure 4.30: (Color online) Same event invariant mass distribution (black curve) and mixed event invariant mass distribution (red curve) after proper normalisation in Au+Au collision (60-80%) at  $\sqrt{s_{NN}} = 27$  GeV for different  $p_T$  bins.

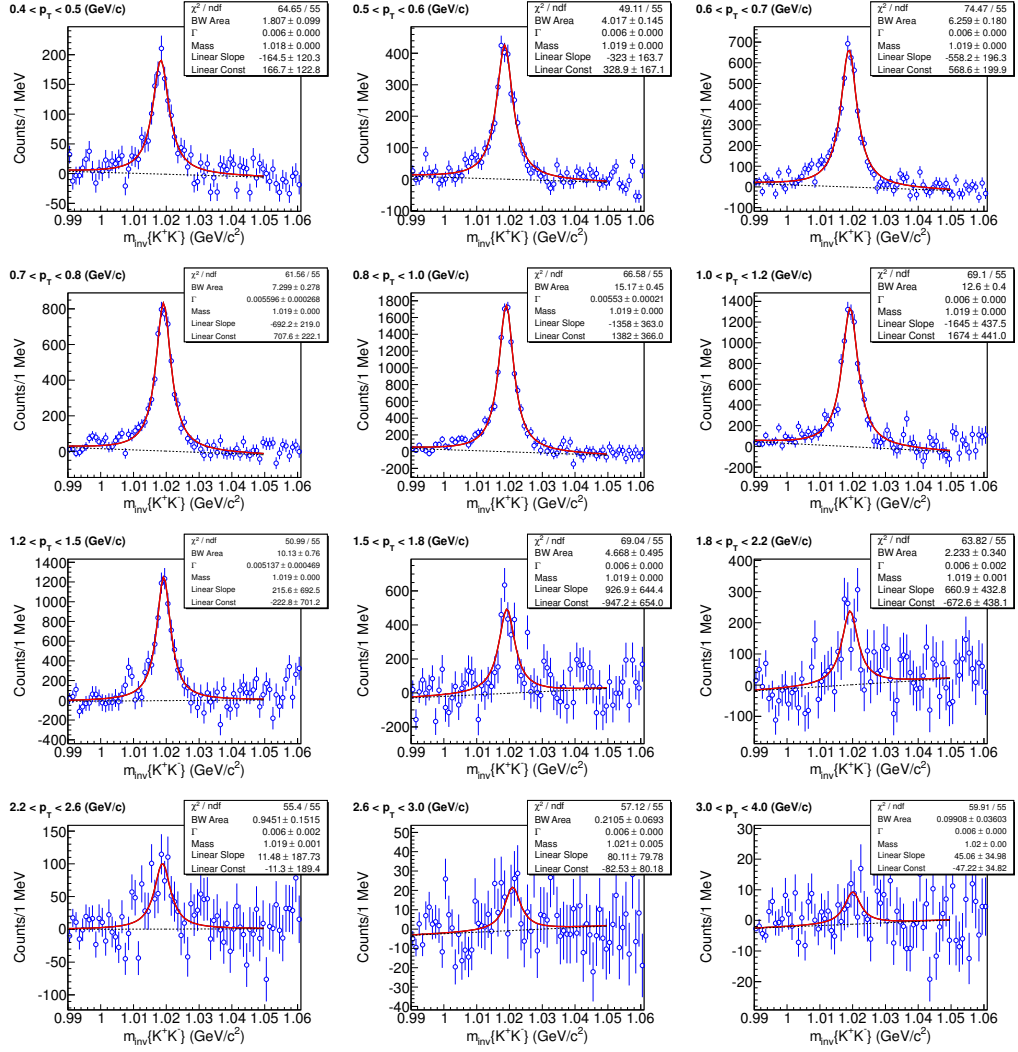


Figure 4.31: (Color online)  $\phi$ -mesons signal after combinatorial background subtraction in Au+Au collision (60-80%) at  $\sqrt{s_{NN}} = 27$  GeV for different  $p_T$  bins.

# Chapter 5

## Energy Dependence of Charged Hadron Elliptic Flow and Heavy-Ion Collision Model Results

The systematic study on inclusive charged hadrons  $v_2$  at various beam energy including the new measurements using BES data taken by STAR experiment has been presented and discussed in this chapter. The experimental results are compared with various heavy-ion collisions models. Specifically we have used the UrQMD and AMPT models which uses transport based microscopic approach and a macroscopic hydrodynamic based model for comparison with experimental data.

### 5.1 Data Sets

We present measurements of the second harmonic azimuthal anisotropy of inclusive charged hadron using data taken in the BES program from  $\sqrt{s_{NN}} = 7.7, 11.5, 19.6, 27$  and  $39$  GeV. Event selection and centrality selection cuts are same as used for

$\phi$ -meson  $v_2$  analysis and already discussed in chapter 3. A variety of track quality cuts are used to select good charged particle tracks reconstructed using information from the TPC. The distance of closest approach (DCA) of the track to the primary vertex is taken to be less than 2 cm. We require that the TPC have a number of fit points used for reconstruction of the tracks to be  $> 15$  and the ratio of the number of fit points to maximum possible hits is  $> 0.52$ . Motivation of choice of such cuts are similar to that discussed for tracks selection for  $\phi$ -meson analysis.

## 5.2 Elliptic Flow Measurement Methods

The standard event plane method for  $v_2$  measurements has already been discussed in chapter 3. The cumulant method and scalar product method are discussed in this section.

### 5.2.1 The cumulant method

One of the widely used method for measuring flow is the use of the multi-particle azimuthal correlations. The advantage of this method is that it is not required to know the reaction plane. Further the advantage of the cumulant method is that the multi-particle correlations removes the contribution of non-flow correlations (correlations not related to reaction plane and/or genuine multi-particle bulk process) [1, 2]. In the cumulant method instead of event plane one needs a different kind of reference, know as reference flow. The approach is to make a flow measurement over a large part of phase space, and then use that as a reference for the differential flow measurement. This could be as a function of transverse momentum or pseudo-rapidity. The measured 2-particle correlations can be expressed with flow and non-flow components:

$$\begin{aligned} \langle 2 \rangle &= \langle e^{in(\phi_1 - \phi_2)} \rangle = \langle e^{in(\phi_1 - \Psi_r)} \rangle \langle e^{in(\Psi_r - \phi_2)} \rangle + \delta_n \\ &= v_n^2 + \delta_n \end{aligned} \tag{5.1}$$

Here  $\Psi_r$  is the reaction plane angle,  $\phi$ 's are azimuthal angle,  $n$  is the harmonic number and  $\delta_n$  denotes the non-flow contribution. The average is taken for all pairs of particles

in a certain rapidity and transverse momentum region. The measured 4-particle correlations can be expressed as:

$$\langle 4 \rangle = \langle e^{in(\phi_1+\phi_2-\phi_3-\phi_4)} \rangle = v_n^4 + 2 \cdot 2 \cdot v_n^2 \delta_n + 2\delta_n^2 \quad (5.2)$$

Thus the flow contribution can be obtained by subtracting the 2-particle correlation from the 4-particle correlation:

$$\begin{aligned} \langle\langle 4 \rangle\rangle &= \langle\langle e^{in(\phi_1+\phi_2-\phi_3-\phi_4)} \rangle\rangle \\ &= \langle e^{in(\phi_1+\phi_2-\phi_3-\phi_4)} \rangle - 2\langle e^{in(\phi_1-\phi_3)} \rangle^2 = -v_n^4 \end{aligned} \quad (5.3)$$

where  $\langle\langle \dots \rangle\rangle$  denotes average over all events i.e cumulant. There are two types of approach for cumulants measurements, generating functions method and Q-cumulants method.

#### 5.2.1.1 The cumulant method with generating function:

In this methods, described by Borghini et al., the cumulant is computed from a generating function [2]

$$G_n(z) = \prod_{j=1}^M \left[ 1 + \frac{w_j}{M} (z^* e^{in\phi_j} + z e^{-in\phi_j}) \right] \quad (5.4)$$

Here  $z$  is an arbitrary complex number,  $z^*$  denotes its complex conjugate,  $M$  denotes the multiplicity in each event, and  $w_j$  is the weight (transverse momentum, rapidity etc.). The event-wise averaged generating function then can be expanded in powers of  $z$  and  $z^*$  where the coefficients of expansion yield the correlations of interest:

$$\begin{aligned} \langle G_n(z) \rangle &= 1 + z \langle e^{-in\phi_1} \rangle + z^* \langle e^{in\phi_1} \rangle + \\ &\quad \frac{M-1}{M} \left( \frac{z^2}{2} \langle e^{-in(\phi_1+\phi_2)} \rangle + \frac{z^{*2}}{2} \langle e^{in(\phi_1+\phi_2)} \rangle \right) \\ &\quad + z z^* \langle e^{in(\phi_1-\phi_2)} \rangle + \dots \end{aligned} \quad (5.5)$$

Using this correlations one can construct the cumulants [2].

#### 5.2.1.2 The Q-cumulant method:

This is a new approach has been developed by Ante Bilandzic and others [3] without using nested loops over tracks and without generating functions. Therefore using the

Q-cumulant method one can do the analysis very fast in terms of computing speed. The Q-cumulant is defined as:

$$Q_n \equiv \sum_{i=1}^M e^{in\phi_i}, \quad (5.6)$$

where M denotes the multiplicity in each event and therefore  $Q_n$  can be calculated with a single loop over all the particles.

**Reference flow:**

The Eq. 5.1 and Eq. 5.2 can be written as

$$\langle 2 \rangle = \frac{|Q_n|^2 - M}{M(M-1)} \quad (5.7)$$

$$\langle 4 \rangle = \frac{|Q_n|^4 + |Q_{2n}|^2 - 2\text{Re}[Q_{2n}Q_n^*Q_n^*]}{M(M-1)(M-2)(M-3)} - 2\frac{2(M-2) \cdot |Q_n|^2 - M(M-3)}{M(M-1)(M-2)(M-3)} \quad (5.8)$$

where the  $\langle 2 \rangle$  and  $\langle 4 \rangle$  denote single event average of 2- and 4-particle azimuthal correlations. The next step is to average  $\langle 2 \rangle$  and  $\langle 4 \rangle$  over all (N) events:

$$\langle\langle 2 \rangle\rangle \equiv \langle\langle e^{in(\phi_1-\phi_2)} \rangle\rangle \equiv \frac{\sum_{i=1}^N (W_{\langle 2 \rangle})_i \langle 2 \rangle_i}{\sum_{i=1}^N (W_{\langle 2 \rangle})_i} \quad (5.9)$$

$$\langle\langle 4 \rangle\rangle \equiv \langle\langle e^{in(\phi_1+\phi_2-\phi_3-\phi_4)} \rangle\rangle \equiv \frac{\sum_{i=1}^N (W_{\langle 4 \rangle})_i \langle 4 \rangle_i}{\sum_{i=1}^N (W_{\langle 4 \rangle})_i} \quad (5.10)$$

while the weights are the number of two- and four-particle combinations:

$$W_{\langle 2 \rangle} \equiv M(M-1), \quad (5.11)$$

$$W_{\langle 4 \rangle} \equiv M(M-1)(M-2)(M-3). \quad (5.12)$$

Choosing the multiplicity as weights, one can make the final multi-particle azimuthal correlations free of multiplicity fluctuations [4].

The second order cumulant is then simply:

$$c_n\{2\} = \langle\langle 2 \rangle\rangle - \langle\langle \cos n\phi_1 \rangle\rangle^2 - \langle\langle \sin n\phi_1 \rangle\rangle^2, \quad (5.13)$$

where the last two terms are to counter bias from correlations due to non-uniform azimuthal coverage. They are defined as:

$$\langle\langle \cos n\phi_1 \rangle\rangle^2 \equiv \frac{\sum_{i=1}^N (Re[Q_n])_i}{\sum_{i=1}^N M_i} \quad (5.14)$$

and

$$\langle\langle \sin n\phi_1 \rangle\rangle^2 \equiv \frac{\sum_{i=1}^N (Im[Q_n])_i}{\sum_{i=1}^N M_i} \quad (5.15)$$

Here  $Re$  and  $Im$  denotes the real and imaginary part, respectively. The  $n^{th}$  order reference flow can be estimated from 2-particle cumulants as

$$v_n\{2\} = \sqrt{c_n\{2\}}. \quad (5.16)$$

The fourth order cumulant then follows as:

$$\begin{aligned} c_n\{4\} &= \langle\langle 4 \rangle\rangle - 2\langle\langle 2 \rangle\rangle^2 - 4.\langle\langle \cos n\phi_1 \rangle\rangle\langle\langle \cos n(\phi_1 - \phi_2 - \phi_3) \rangle\rangle \\ &+ 4.\langle\langle \sin n\phi_1 \rangle\rangle\langle\langle \sin n(\phi_1 - \phi_2 - \phi_3) \rangle\rangle - \langle\langle \cos n(\phi_1 + \phi_2) \rangle\rangle^2 - \langle\langle \sin n(\phi_1 + \phi_2) \rangle\rangle^2 \\ &+ 4.\langle\langle \cos n(\phi_1 + \phi_2) \rangle\rangle[\langle\langle \cos n\phi_1 \rangle\rangle^2 - \langle\langle \sin n\phi_1 \rangle\rangle^2] \\ &+ 8.\langle\langle \cos n(\phi_1 - \phi_2) \rangle\rangle[\langle\langle \cos n\phi_1 \rangle\rangle^2 + \langle\langle \sin n\phi_1 \rangle\rangle^2] \\ &+ 8.\langle\langle \sin n(\phi_1 + \phi_2) \rangle\rangle\langle\langle \sin n\phi_1 \rangle\rangle\langle\langle \cos n\phi_1 \rangle\rangle - 6.[\langle\langle \cos n\phi_1 \rangle\rangle^2 + \langle\langle \sin n\phi_1 \rangle\rangle^2], \end{aligned} \quad (5.17)$$

where all the terms except the first two terms are to correct for bias from non-uniform azimuthal coverage. These new terms are defined as:

$$\langle\langle \cos n(\phi_1 + \phi_2) \rangle\rangle \equiv \frac{\sum_{i=1}^N (Re[Q_n Q_n - Q_{2n}])_i}{\sum_{i=1}^N M_i (M_i - 1)} \quad (5.18)$$

$$\langle\langle \sin n(\phi_1 + \phi_2) \rangle\rangle \equiv \frac{\sum_{i=1}^N (Im[Q_n Q_n - Q_{2n}])_i}{\sum_{i=1}^N M_i (M_i - 1)} \quad (5.19)$$

$$\langle\langle \cos n(\phi_1 - \phi_2) \rangle\rangle \equiv \frac{\sum_{i=1}^N (Re[Q_n Q_n^* Q_n^* - Q_n Q_{2n}^*] - 2(M-1)Re[Q_n^*])_i}{\sum_{i=1}^N M_i (M_i - 1)(M_i - 2)} \quad (5.20)$$

$$\langle\langle \sin n(\phi_1 - \phi_2) \rangle\rangle \equiv \frac{\sum_{i=1}^N (Im[Q_n Q_n^* Q_n^* - Q_n Q_{2n}^*] - 2(M-1)Im[Q_n^*])_i}{\sum_{i=1}^N M_i(M_i-1)(M_i-2)} \quad (5.21)$$

Now the  $n_{th}$  order reference flow can be calculated from 4-particle cumulants as

$$v_n\{4\} = \sqrt[4]{-c_n\{4\}} \quad (5.22)$$

### Differential flow:

Once the reference flow is estimated, the next step is to calculate differential flow (e.g. as a function of  $p_T$ ) of the particle of interest (POI), which needs another two vectors  $\vec{p}$  and  $\vec{q}$ . Particles used to estimate reference flow are called reference particles (REP). For particles labeled as POI:

$$p_n \equiv \sum_{i=1}^{m_p} e^{in\psi_i}. \quad (5.23)$$

For particles labeled as both POI and REP:

$$q_n \equiv \sum_{i=1}^{m_q} e^{in\psi_i}. \quad (5.24)$$

Then the reduced single-event average 2- and 4-particle correlations are:

$$\langle 2' \rangle = \frac{p_n Q_n^* - m_q}{m_p M - m_q} \quad (5.25)$$

$$\begin{aligned} \langle 4' \rangle = & [p_n Q_n Q_n^* Q_n^* - q_{2n} Q_n^* Q_n^* - p_n Q_n Q_{2n}^* \\ & - 2 \cdot M p_n Q_n^* - 2 \cdot m_q |Q_n|^2 + 7 \cdot q_n Q_n^* \\ & - Q_n q_n^* + q_{2n} Q_{2n}^* + 2 \cdot p_n Q_n^* + 2 \cdot m_q M \\ & - 6 \cdot m_q] / [(m_p M - 3m_q)(M-1)(M-2)], \end{aligned} \quad (5.26)$$

where  $m_p$  is the total particles of interest in an event and total number of particles which can be marked as both POI and REP are  $m_q$ . Now the average over  $N$  events can be obtained as follows:

$$\langle\langle 2' \rangle\rangle \equiv \frac{\sum_{i=1}^N (W_{\langle 2' \rangle})_i \langle 2' \rangle_i}{\sum_{i=1}^N (W_{\langle 2' \rangle})_i} \quad (5.27)$$

$$\langle\langle 4' \rangle\rangle \equiv \frac{\sum_{i=1}^N (W_{\langle 4' \rangle})_i \langle 4' \rangle_i}{\sum_{i=1}^N (W_{\langle 4' \rangle})_i} \quad (5.28)$$

Here weights factors are

$$w_{\langle 2' \rangle} \equiv m_p M - m_q \quad (5.29)$$

$$w_{\langle 4' \rangle} \equiv (m_p M - m_q)(M - 1)(M - 2) \quad (5.30)$$

The second order differential Q-cumulant is then:

$$d_n\{2\} = \langle\langle 2' \rangle\rangle - \langle\langle \cos n\psi_1 \rangle\rangle \langle\langle \cos n\phi_2 \rangle\rangle - \langle\langle \sin n\psi_1 \rangle\rangle \langle\langle \sin n\phi_1 \rangle\rangle. \quad (5.31)$$

The last two terms are due to correct for non-uniformity of detectors.

The fourth order differential Q-cumulant is then obtained as:

$$\begin{aligned} d_n\{4\} &= \langle\langle 4' \rangle\rangle - 2.\langle\langle 2' \rangle\rangle \langle\langle 2 \rangle\rangle \\ &\quad - \langle\langle \cos n\psi_1 \rangle\rangle \langle\langle \cos n(\phi_1 - \phi_2 - \phi_3) \rangle\rangle + \langle\langle \sin n\psi_1 \rangle\rangle \langle\langle \sin n(\phi_1 - \phi_2 - \phi_3) \rangle\rangle \\ &\quad - \langle\langle \cos n\phi_1 \rangle\rangle \langle\langle \cos n(\psi_1 - \phi_2 - \phi_3) \rangle\rangle + \langle\langle \sin n\phi_1 \rangle\rangle \langle\langle \sin n(\psi_1 - \phi_2 - \phi_3) \rangle\rangle \\ &\quad - 2.\langle\langle \cos n\phi_1 \rangle\rangle \langle\langle \cos n(\psi_1 + \phi_2 - \phi_3) \rangle\rangle - 2.\langle\langle \sin n\phi_1 \rangle\rangle \langle\langle \sin n(\psi_1 + \phi_2 - \phi_3) \rangle\rangle \\ &\quad - \langle\langle \cos n(\psi_1 + \phi_2) \rangle\rangle \langle\langle \cos n(\phi_1 + \phi_2) \rangle\rangle - \langle\langle \sin n(\psi_1 + \phi_2) \rangle\rangle \langle\langle \sin n(\phi_1 + \phi_2) \rangle\rangle \\ &\quad + 2.\langle\langle \cos n(\phi_1 + \phi_2) \rangle\rangle [\langle\langle \cos n\psi_1 \rangle\rangle \langle\langle \cos n\phi_1 \rangle\rangle - \langle\langle \sin n\psi_1 \rangle\rangle \langle\langle \sin n\phi_1 \rangle\rangle] \\ &\quad + \langle\langle \sin n(\phi_1 + \phi_2) \rangle\rangle [\langle\langle \cos n\psi_1 \rangle\rangle \langle\langle \sin n\phi_1 \rangle\rangle - \langle\langle \sin n\psi_1 \rangle\rangle \langle\langle \cos n\phi_1 \rangle\rangle] \\ &\quad + 4.\langle\langle \cos n(\phi_1 - \phi_2) \rangle\rangle [\langle\langle \cos n\psi_1 \rangle\rangle \langle\langle \cos n\phi_1 \rangle\rangle + \langle\langle \sin n\psi_1 \rangle\rangle \langle\langle \sin n\phi_1 \rangle\rangle] \\ &\quad + 2.\langle\langle \cos n(\psi_1 + \phi_2) \rangle\rangle [\langle\langle \cos n\phi_1 \rangle\rangle^2 - \langle\langle \sin n\phi_1 \rangle\rangle^2] \\ &\quad + 4.\langle\langle \sin n(\psi_1 + \phi_2) \rangle\rangle \langle\langle \cos n\phi_1 \rangle\rangle \langle\langle \sin n\phi_1 \rangle\rangle \\ &\quad + 4.\langle\langle \cos n(\psi_1 - \phi_2) \rangle\rangle [\langle\langle \cos n\phi_1 \rangle\rangle^2 + \langle\langle \sin n\phi_1 \rangle\rangle^2] \\ &\quad - 6. [\langle\langle \cos n\phi_1 \rangle\rangle^2 - \langle\langle \sin n\phi_1 \rangle\rangle^2] [\langle\langle \cos n\psi_1 \rangle\rangle \langle\langle \cos n\phi_1 \rangle\rangle - \langle\langle \sin n\psi_1 \rangle\rangle \langle\langle \sin n\phi_1 \rangle\rangle] \\ &\quad - 12.\langle\langle \cos n\phi_1 \rangle\rangle \langle\langle \sin n\phi_1 \rangle\rangle [\langle\langle \sin n\psi_1 \rangle\rangle \langle\langle \cos n\phi_1 \rangle\rangle - \langle\langle \cos n\psi_1 \rangle\rangle \langle\langle \sin n\phi_1 \rangle\rangle], \end{aligned} \quad (5.32)$$

where everything except first two terms is to correct for non-uniform azimuthal acceptance of the detectors. Finally the  $n^{\text{th}}$  order differential flow from 2- and 4-particle cumulants can be defined as

$$v'_n\{2\} = \frac{d_n\{2\}}{\sqrt{c_n\{2\}}} \quad (5.33)$$

$$v'_n\{4\} = \frac{d_n\{4\}}{-c_n\{2\}^{3/4}}. \quad (5.34)$$

### 5.2.2 The scalar product method

In a scalar product method [5] each event is partitioned into two sub-events, labeled by the superscripts A and B. The  $Q_n^A$  and  $Q_n^B$  are the flow vectors of sub-events A and B for  $n^{th}$  harmonic then the correlation between two sub-events is

$$\langle Q_n^A Q_n^{B*} \rangle = \langle v_n^2 M^A M^B \rangle, \quad (5.35)$$

where  $M^A$  and  $M^B$  are the multiplicities for sub-events A and B, respectively. Elliptic flow in this method can be calculated as

$$v_2(SP) = \frac{\langle Q_2 u_2^* \rangle}{\sqrt{\langle Q_2^A Q_2^{B*} \rangle}}. \quad (5.36)$$

Here  $Q_2 = \sum u_2^i$  and  $u_2^i$  is a unit vector associated with the  $i^{th}$  particle. The scalar-product method always yields the root-mean-square  $v_2$ , regardless of the details of

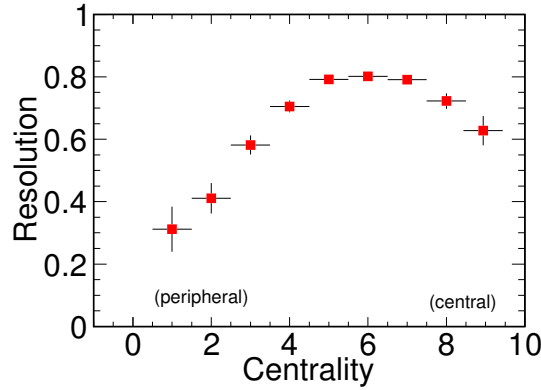


Figure 5.1: (Color online) Second order event plane resolution as a function of centrality in Au+Au collisions at 200 GeV from AMPT model.

the analysis [6].

$$v_2(SP) = \frac{\langle Q_2 u_2^* \rangle}{\sqrt{\langle Q_2^A Q_2^{B*} \rangle}} = \sqrt{\langle v_2^2 \rangle}. \quad (5.37)$$

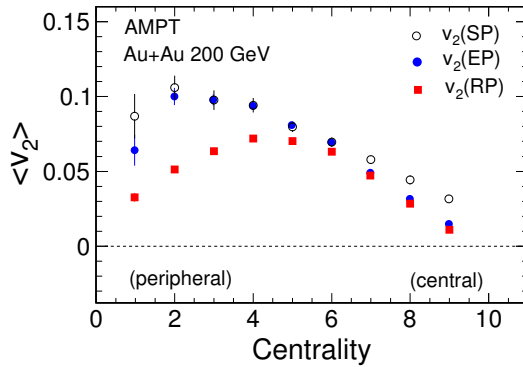


Figure 5.2: (Color online) The elliptic flow of charged particle as a function of centrality in Au+Au collisions at 200 GeV from AMPT model.

But this is not true for  $v_2(EP)$  measured by conventional event plane method. In the limit of perfect resolution (i.e.  $R \rightarrow 1$ )

$$v_2(EP) \rightarrow \langle v_2 \rangle, \quad (5.38)$$

and in the limit of low resolution

$$v_2(EP) \rightarrow \sqrt{\langle v_2^2 \rangle}. \quad (5.39)$$

We have investigated this aspect using AMPT model where the actual  $\langle v_2 \rangle$  is known. The event plane resolution from AMPT model is shown in Fig. 5.1 for nine centrality bin. Resolution is poor for peripheral centrality and maximum at mid-central and then slightly decreases in most central collisions. Figure 5.2 shows charged particle  $v_2$  as a function of centrality in Au+Au collisions at 200 GeV from AMPT model using scalar product, event plane and reaction plane method. One can see that for peripheral collision where resolution is poor,  $v_2(EP)$  and  $v_2(SP)$  are very close to each other that means  $v_2(EP)$  is equivalent to root-mean-square  $v_2$ . However for central to mid-central where resolution is high,  $v_2(EP)$  is closer to  $v_2(RP)$  or  $\langle v_2 \rangle$ . These results show consistency with Eq. 5.38 and 5.39 .

## 5.3 Results & Discussion

### 5.3.1 Energy dependence of charged hadron $v_2$

One of the most important experimental observations at RHIC is the significant  $v_2$  signal at the top energy of Au+Au collisions [7, 8]. The measured  $v_2$  at top RHIC energy is more than 50% higher than at the SPS [9]. This could be due to higher energy density and pressure gradients at higher energy than at lower collision energies. The BES program at STAR-RHIC experiment allow us to measure the  $v_2$  as function of various centre-of-mass energy. Figure 5.3 shows the  $p_T$  dependence of  $v_2\{4\}$  from  $\sqrt{s_{NN}} = 7.7$  GeV to 2.76 TeV in 10 – 20% (a1), 20 – 30% (b1) and 30 – 40% (c1) centrality bins [10], where the ALICE results in Pb+Pb collisions at  $\sqrt{s_{NN}} = 2.76$  TeV are taken from Ref. [11]. The 200-GeV data are empirically fitted by a fifth-order polynomial function and ratio with this fit to other energies are shown in the corresponding bottom panels of Fig. 5.3. The parameters for the fit function are listed in Table 5.1. For  $p_T$  below 2 GeV/ $c$ , the  $v_2$  values rise with increasing collision energy. Beyond  $p_T = 2$  GeV/ $c$  the  $v_2$  results show comparable values within statistical errors. The increase of  $v_2(p_T)$  as a function of energy could be due to the change of particle composition from low to high energies [12] and/or larger collectivity at the higher collision energy. The baryonic chemical potential varies a lot (20 - 400 MeV) from 200 to 7.7 GeV [12]. The baryon over meson ratio is larger in lower collision energies [13]. The difference of  $v_2$  for baryon and meson, for example proton  $v_2 <$  pion  $v_2$  for  $p_T$  below 2 GeV/ $c$ , could partly explain the collision energy dependence at low  $p_T$ .

The  $p_T$  integrated charged hadron elliptic flow ( $\langle v_2 \rangle$ ) as function of beam energy are shown in Fig. 5.4. A non-monotonic dependence of  $\langle v_2 \rangle$  versus  $\sqrt{s_{NN}}$  is observed. At lower energies, the negative  $\langle v_2 \rangle$  is attributed to out-of-plane squeeze-out phenomena [14]. In this case, the elliptical shape of the particle transverse momentum distribution at mid-rapidity is elongated in the direction perpendicular to the reaction plane and interpreted as due to shadowing by spectator nucleons. At high energies, the longitudinal size of the Lorentz contracted nuclei becomes negligible compared

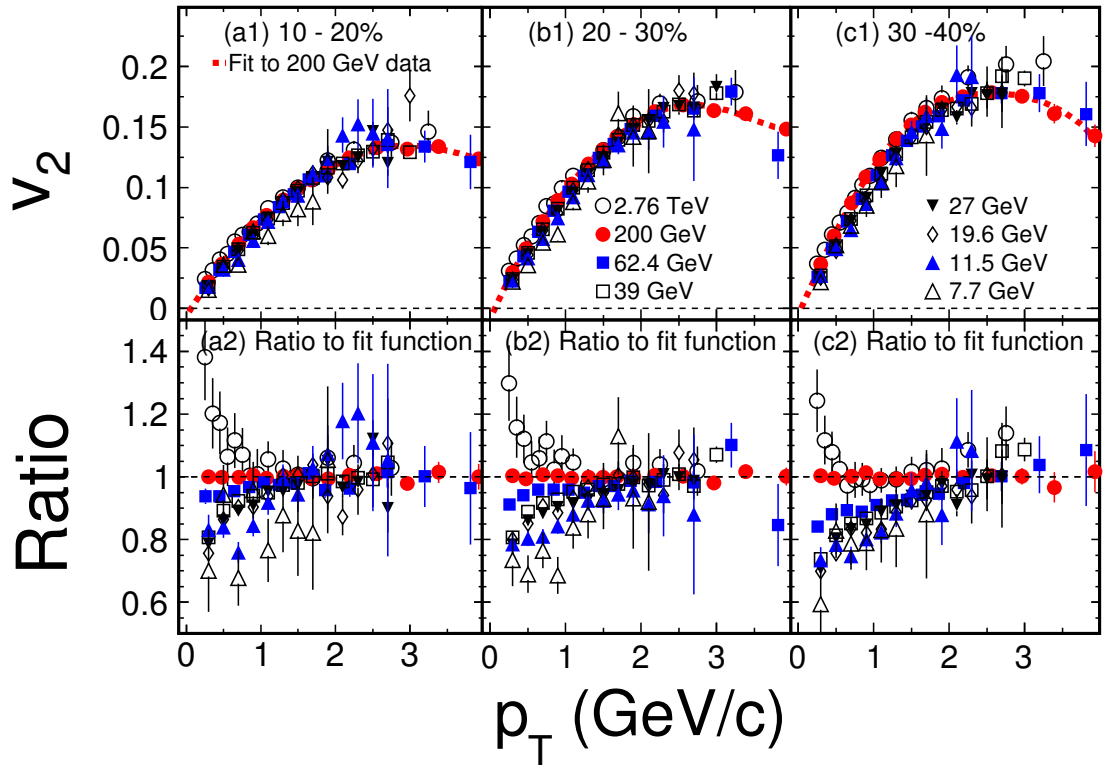


Figure 5.3: (Color online) The top panels show  $v_2\{4\}$  vs.  $p_T$  at mid-rapidity for various collision energies ( $\sqrt{s_{NN}} = 7.7$  GeV to 2.76 TeV). The results for  $\sqrt{s_{NN}} = 7.7$  to 200 GeV are for Au+Au collisions and those for 2.76 TeV are for Pb+Pb collisions. The dashed red curves show the empirical fits to the results from Au+Au collisions at  $\sqrt{s_{NN}} = 200$  GeV. The bottom panels show the ratio of  $v_2\{4\}$  vs.  $p_T$  for all  $\sqrt{s_{NN}}$  with respect to the fit curve. The results are shown for three collision centrality classes: 10 – 20% (a1), 20 – 30% (b1) and 30 – 40% (c1). Error bars are shown only for the statistical uncertainties.

to their transverse size. This decreases the crossing time scales of the two nuclei. The shadowing effect goes away and elliptic flow fully develops in plane, leading to a

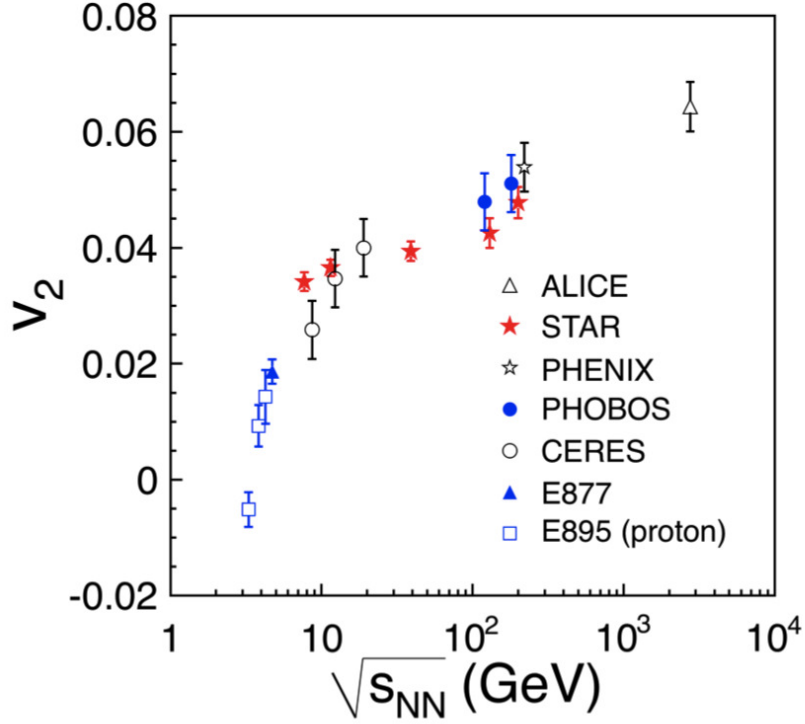


Figure 5.4: (Color online) Average elliptic flow ( $\langle v_2 \rangle$ ) as a function of beam energy. The results are shown for charged particles from, LHC experiments of ALICE [11], RHIC experiments of STAR [15], PHENIX [16] and PHOBOS [17], SPS experiments of CERES [18], AGS experiments of E877 [19] and E895 [20] (proton).

positive value of  $\langle v_2 \rangle$ .

### 5.3.2 Centrality dependence of charged hadron $v_2(p_T)$

The centrality dependence of  $p_T$  differential  $v_2$  over eccentricity ( $\varepsilon_{\text{part}}\{2\}$ ) is shown for Au+Au collisions at  $\sqrt{s_{NN}} = 7.7, 11.5, 19.6, 27$  and  $39$  GeV in Figs. 5.5 and 5.6. The root-mean-square of participant eccentricity has been used here to subtract the effect of initial geometry. For the  $v_2$  measurements the event plane is constructed

Parameters	$p_0$	$p_1$	$p_2$	$p_3$	$p_4$	$p_5$
10 – 20%	$-0.00730 \pm 0.00114$	$0.10785 \pm 0.00598$	$-0.03941 \pm 0.01038$	$0.01508 \pm 0.00767$	$-0.00411 \pm 0.00246$	$0.00041 \pm 0.00028$
20 – 30%	$-0.00890 \pm 0.00096$	$0.14250 \pm 0.00500$	$-0.05206 \pm 0.00869$	$0.02156 \pm 0.00642$	$-0.00685 \pm 0.00206$	$0.00077 \pm 0.00023$
30 – 40%	$-0.00581 \pm 0.00206$	$0.14526 \pm 0.01089$	$-0.00529 \pm 0.01910$	$-0.02409 \pm 0.01419$	$0.00797 \pm 0.00456$	$-0.00084 \pm 0.00052$

Table 5.1: Summary of the parameters for the fit functions to the results of  $v_2\{4\}$  vs.  $p_T$  in Au+Au collisions at  $\sqrt{s} = 200$  GeV.

from hadrons which have their origin in participant nucleons and at the same time, the event plane resolution ( $\eta$  sub-event) is less than 0.5 [10]. Thus, what we actually measure is the root-mean-square of  $v_2$  with respect to the participant plane [21]. In this case,  $\varepsilon_{\text{part}}\{2\}$  is the appropriate measure of the initial geometric anisotropy taking the event-by-event fluctuations into account [22, 23, 21]. The root-mean-square participant eccentricity,  $\varepsilon_{\text{part}}\{2\}$ , is calculated from the Monte Carlo Glauber model [24, 25] and Color Glass Condensate (CGC) model [26, 27, 28, 29]. The values of  $\varepsilon_{\text{part}}\{2\}$  for different centrality classes and for different centre-of-mass energies are listed in Appendix section. One can see from Figs. 5.5 and 5.6 that the  $v_2/\varepsilon_{\text{part}}\{2\}$  is higher in central collisions than peripheral collisions and this is consistent with the picture that collective interactions are stronger in collisions with larger numbers of participants. For all five collision energies, the centrality dependence of  $v_2(p_T)$  is observed to be similar to that at higher collision energies (62.4 and 200 GeV) [30, 31].

### 5.3.3 Model comparison

Various observables are compared to theoretical calculations to understand the physical mechanism behind the measurements. Some of the frequently used models in heavy-ion collisions are transport models (UrQMD [23], AMPT [22]) and Hydrodynamic models [34]. To investigate the partonic and hadronic contribution to the final  $v_2$  results from different collision energies, transport model calculations from AMPT default (ver. 1.11), AMPT string-melting (ver. 2.11) and UrQMD (ver. 2.3) are compared with the data and are presented. The initial-parameter settings for the models follow the recommendation in the cited references and shown in Appendix. The AMPT default and UrQMD models only take the hadronic interactions into con-

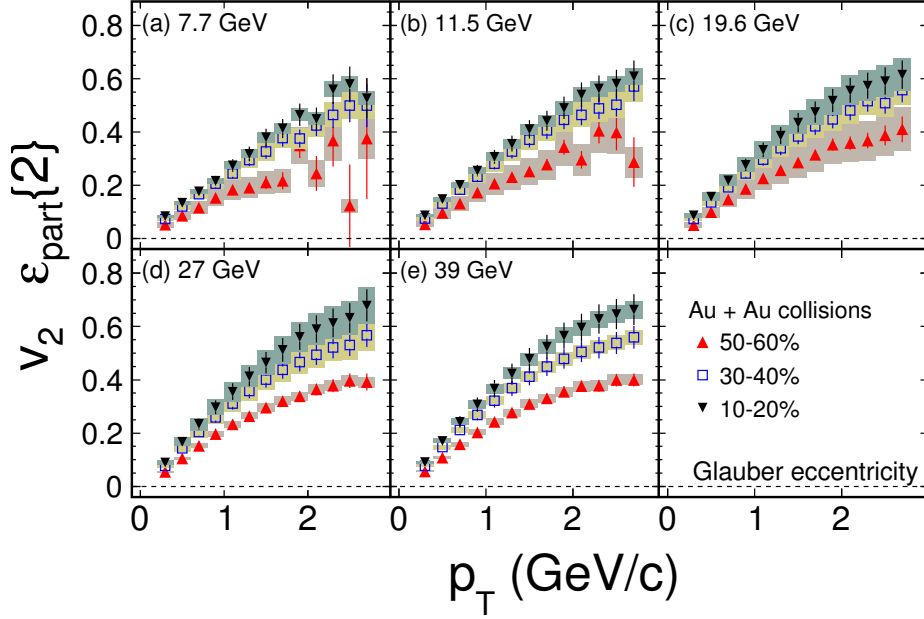


Figure 5.5: (Color online) The  $v_2$  over  $\epsilon_{\text{part}}\{2\}$  (Glauber) as a function of  $p_T$  for various collision centralities (10 – 20%, 30 – 40% and 50 – 60%) in Au + Au collisions at mid-rapidity. Panels (a), (b), (c), (d) and (e) show the results for  $\sqrt{s_{NN}} = 7.7, 11.5, 19.6, 27$  and  $39$  GeV respectively. The data are from  $v_2\{\text{EtaSubs}\}$ . The error bars and shaded boxes represent the statistical and systematic uncertainties respectively..

sideration, while the AMPT string-melting version incorporates both partonic and hadronic interactions. Figure 5.7 shows the comparison of  $p_T$  differential  $v_2\{4\}$  between model and data in the 20 – 30% centrality bin. The centrality selection is same for data and the models. The figure shows that UrQMD under-predicts the measurements at  $\sqrt{s_{NN}} = 39$  and  $200$  GeV in the  $p_T$  range studied. The differences are reduced as the collision energy decreases. That the ratio of data to UrQMD results are closer to 1 at the lower collision energy indicates that the contribution of hadronic interactions becomes more significant at lower collision energies. The AMPT model with string-melting version with 3 and 10 mb parton cross sections over-predicts the results at all collision energies from 7.7 to 200 GeV. A larger parton cross section means stronger partonic interactions which translate into a larger magnitude of  $v_2$ .

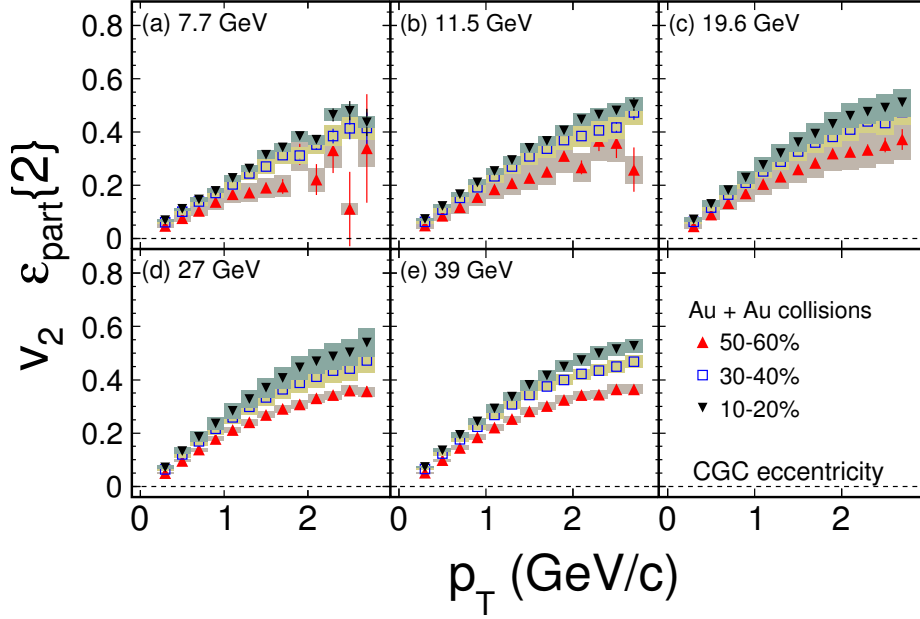


Figure 5.6: (Color online) The  $v_2$  over  $\varepsilon_{\text{part}}\{2\}$  (CGC) as a function of  $p_T$  for various collision centralities (10 – 20%, 30 – 40% and 50 – 60%) in Au + Au collisions at mid-rapidity. Panels (a), (b), (c), (d) and (e) show the results for  $\sqrt{s_{NN}} = 7.7, 11.5, 19.6, 27$  and  $39$  GeV respectively. The data are from  $v_2\{\text{EtaSubs}\}$ . The error bars and shaded boxes represent the statistical and systematic uncertainties respectively.

The difference between data and these AMPT model calculations seems to show no significantly systematic change with the collision energies. A recent study with the AMPT model suggests hadronic potentials affect the final  $v_2$  results significantly when the collision energy is less than  $\sqrt{s_{NN}} = 39$  GeV [35].

Further, in Fig. 5.8 we compare the experimental data from Fig. 5.3 (b2) to the viscous hydrodynamic calculations [36]. As the collision energy varies from  $\sqrt{s_{NN}} = 7.7$  to  $2760$  GeV, the experimental data show larger differences in the lower  $p_T$  region and converge at the intermediate range ( $p_T \sim 2$  GeV/c); while, in the pure viscous hydrodynamic simulations, the differences tends to increases with  $p_T$ . The  $p_T$  dependence of the  $v_2$  ratio cannot be reproduced by pure viscous hydrodynamic simulations with a constant shear viscosity to entropy density ratio ( $\eta/s$ ), and zero net baryon density.

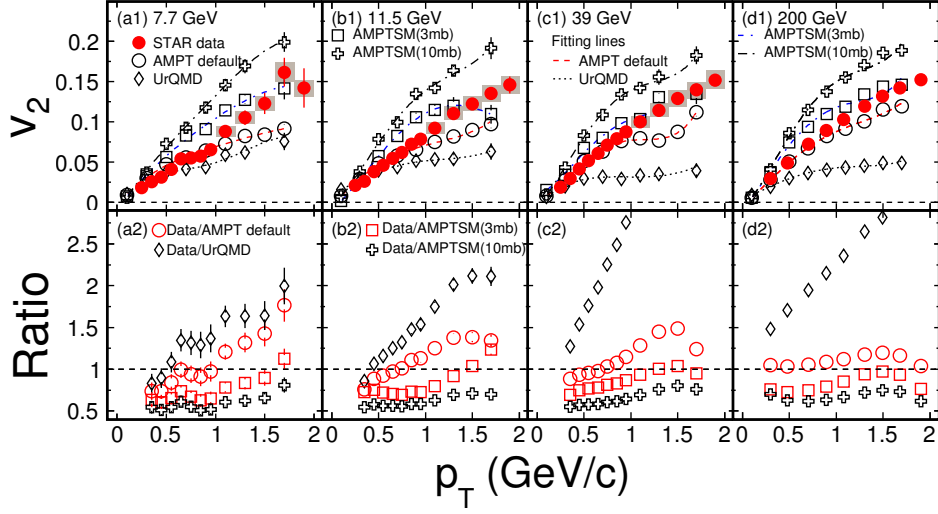


Figure 5.7: (Color online) The  $v_2\{4\}$  as a function of  $p_T$  for 20 – 30% Au + Au collisions at  $\sqrt{s_{NN}} = 7.7, 11.5, 39$  and 200 GeV compared to corresponding results from UrQMD, AMPT default version, and AMPT with string melting version (3 and 10 mb). The shaded boxes show the systematic uncertainties for the experimental data of 7.7, 11.5 and 39 GeV. The bottom panels show the ratio of data to the fit results of the models.

The comparison suggests that a quantitative study at lower collision energies requires a more serious theoretical approach, like 3+1D viscous hydro + UrQMD with an appropriate equation of state.

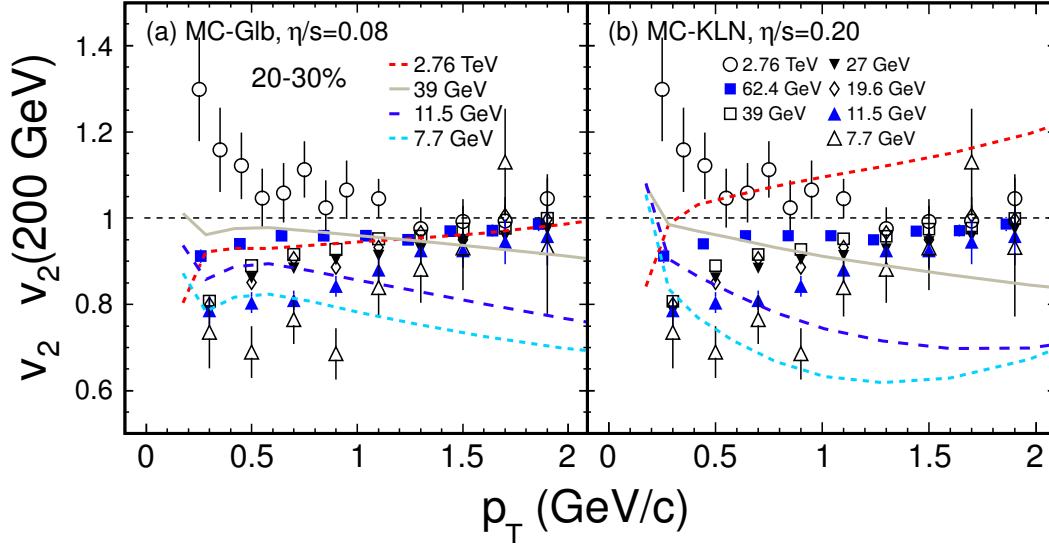


Figure 5.8: (Color online) The experimental data (symbols) are the same as in Fig. 5.3 (b2). The lines represent the viscous hydrodynamic calculations from Ref. [36] based on (a) MC-Glauber initial conditions and  $\eta/s = 0.08$  (b) MC-KLN initial conditions and  $\eta/s = 0.20$ .

## 5.4 Systematic Study on $v_2$ Using Transport Models

### 5.4.1 Longitudinal scaling of $v_2$ :

Longitudinal scaling of pseudo-rapidity distribution of charged particles ( $dN_{\text{ch}}/d\eta$ ) is observed when presented as a function of pseudo-rapidity ( $\eta$ ) shifted by the beam rapidity ( $\eta - y_{\text{beam}}$ ) for a wide range of collision systems ( $e^+ + e^-$ ,  $p+p$ ,  $d+A$  and  $A+A$ ) and beam energies [39, 40]. This phenomena is often called limiting fragmentation. Such a scaling is also observed for the elliptic flow ( $v_2$ ) of charged hadrons in  $A+A$  collisions [41]. This is a striking observation, as  $v_2$  is expected to be sensitive to the

initial conditions, the expansion dynamics and the degrees of freedom of the system, all of which potentially varies with collision system and colliding energies. Recent studies [42] suggest that the simultaneous observation of longitudinal scaling of  $v_2$  and  $dN_{\text{ch}}/d\eta$  can be reconciled only if the system formed in heavy-ion collisions are weakly coupled. This is contrary to other indirect estimations of the shear viscosity to entropy ratio which suggests the system is strongly coupled [43]. The longitudinal scaling of  $dN_{\text{ch}}/d\eta, \langle p_T \rangle$  and  $v_2$  using models AMPT and UrQMD for charged particles has been studied in Au+Au collisions at  $\sqrt{s_{\text{NN}}} = 19.6, 62.4, 200$  GeV and Pb+Pb collisions at 2760 GeV [44]. The aim being to see if these models also exhibit such longitudinal scalings and hence provide a physical insight behind the phenomena.

Figure 5.9 shows the  $dN_{\text{ch}}/d\eta$  versus  $\eta-y_{\text{beam}}$  for 0-6% central Au+Au collisions at  $\sqrt{s_{\text{NN}}} = 19.6, 62.4$  and 200 GeV from (a) the PHOBOS experiment at RHIC [39], (b) UrQMD, (c) AMPT and (d) AMPT-SM models. Also shown are the results from the models for Pb+Pb collisions at  $\sqrt{s_{\text{NN}}} = 2760$  GeV. The  $y_{\text{beam}}$  values for  $\sqrt{s_{\text{NN}}} = 19.6, 62.4, 200$  and 2760 GeV are 3.03, 4.19, 5.36 and 7.98 respectively. The longitudinal scaling observed in  $dN_{\text{ch}}/d\eta$  in the data (Fig. 5.9(a)) is also observed in all the models studied.

Figure 5.10 shows the  $\langle p_T \rangle$  for the charged particles versus  $\eta-y_{\text{beam}}$  for minimum bias Au+Au collisions at  $\sqrt{s_{\text{NN}}} = 19.6, 62.4$  and 200 GeV from (a) the UrQMD, (b) AMPT and (c) AMPT-SM models. Also shown are the results from the models for minimum bias Pb+Pb collisions at  $\sqrt{s_{\text{NN}}} = 2760$  GeV. There are no experimental data available at RHIC for  $\langle p_T \rangle$  versus  $\eta-y_{\text{beam}}$  hence not shown in the figure. The longitudinal scaling is observed in all the models studied.

These results then sets the stage for studying the longitudinal scaling in  $v_2$ . Note that the goal here is not to have a quantitative comparison with data on the scalings in  $dN_{\text{ch}}/d\eta$  and  $v_2$ , but to see if the observations are qualitatively reproduced in the models. Figure 5.11 shows the  $v_2$  for charged particles versus  $\eta-y_{\text{beam}}$  in Au+Au collisions at  $\sqrt{s_{\text{NN}}} = 19.6, 62.4$  and 200 GeV [41]. The results from the models for Pb+Pb collisions at  $\sqrt{s_{\text{NN}}} = 2760$  GeV are also shown. The collision centrality is 0-40% central and is different for that shown for  $dN_{\text{ch}}/d\eta$  in Fig. 5.9. The choice of centrality

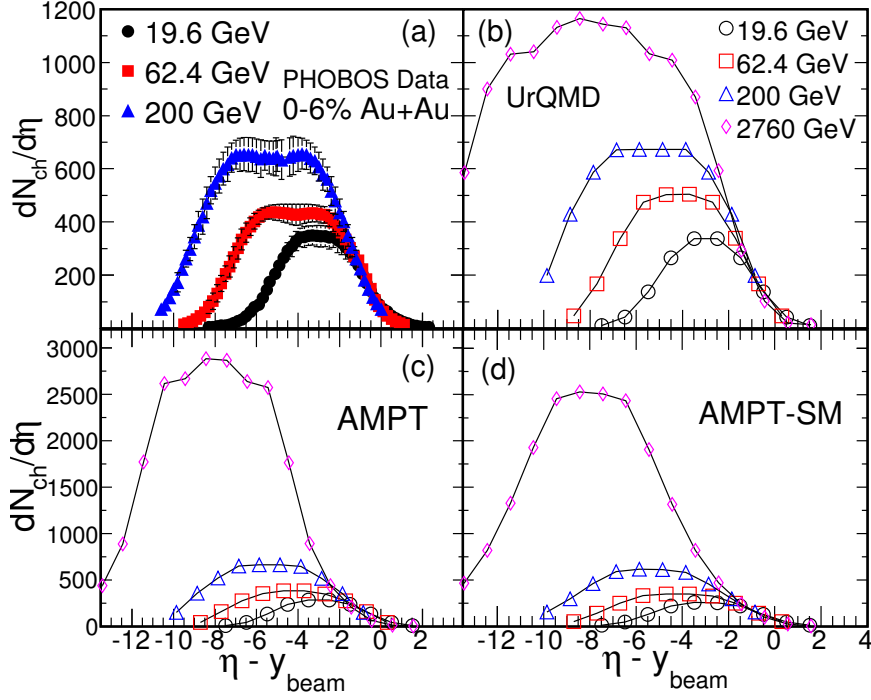


Figure 5.9: (Color online)  $dN_{\text{ch}}/d\eta$  versus  $\eta - y_{\text{beam}}$  for 0–6% central Au+Au collisions at  $\sqrt{s_{\text{NN}}} = 19.6, 62.4$  and 200 GeV from (a) the PHOBOS experiment at RHIC [39], (b) UrQMD, (c) AMPT default and (d) AMPT-SM. Also shown are the model results from Pb+Pb collisions at  $\sqrt{s_{\text{NN}}} = 2760$  GeV.

is based on availability of the  $v_2$  data for charged particles in the experiment as a function of rapidity. Figure 5.11 (a) shows the longitudinal scaling of  $v_2$  as measured by the PHOBOS experiment [41]. Fig. 5.11 (b) shows the  $v_2$  vs.  $\eta - y_{\text{beam}}$  from UrQMD model, in (c) the corresponding results from AMPT default are shown and in (d) the same results from AMPT-SM are presented. It is observed that the UrQMD and the AMPT default models do not show the longitudinal scaling as observed in the data (Fig. 5.11 (a)). Only the AMPT model with string melting qualitatively reproduces the observed longitudinal scaling of  $v_2$ .

It is worthwhile to now discuss briefly the differences in these transport models. The main difference between UrQMD and AMPT lies in the initial conditions (for AMPT

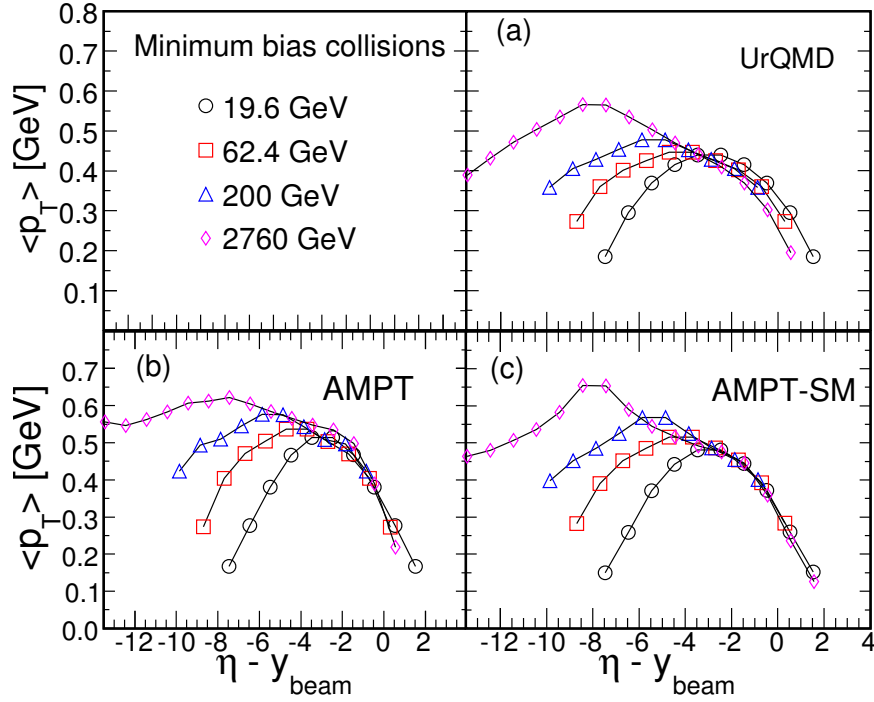


Figure 5.10: (Color online)  $\langle p_T \rangle$  versus  $\eta - y_{\text{beam}}$  for minimum bias Au+Au collisions at  $\sqrt{s_{\text{NN}}} = 19.6, 62.4$  and  $200$  GeV from (a) the UrQMD, (b) AMPT default and (c) AMPT-SM. Also shown are the model results from Pb+Pb collisions at  $\sqrt{s_{\text{NN}}} = 2760$  GeV.

taken from HIJING [45]) and additional initial state rescatterings in AMPT. The main difference between AMPT default and AMPT-SM lies in the following: The string melting version of the AMPT model is formulated on the idea that for energy densities beyond a critical value of  $\sim 1 \text{ GeV}/fm^3$ , it is difficult to visualize the co-existence of strings (or hadrons) and partons. Hence the need to melt the strings to partons. This is done by converting the mesons to a quark and anti-quark pair, baryons to three quarks etc. The scattering of the quarks are then carried out based on parton cascade [22]. The parton-parton cross section taken here is  $10 \text{ mb}$ . Once the interactions stop, the partons then hadronizes through the mechanism of partonic coalescence. While for the AMPT default case the scattering occurs for minijet

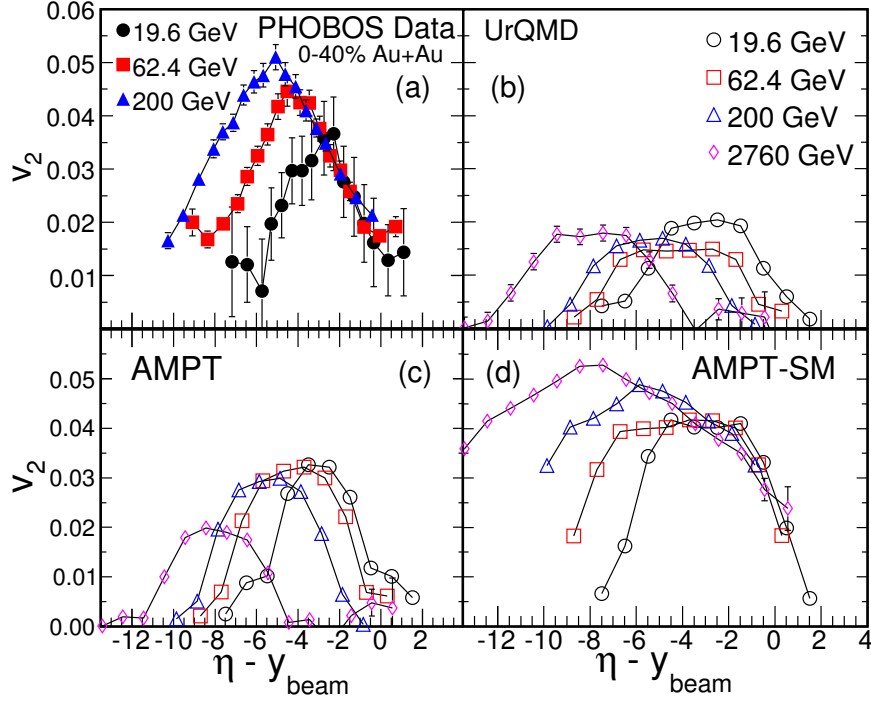


Figure 5.11: (Color online)  $v_2$  for charged particles versus  $\eta - y_{\text{beam}}$  for 0–40% central Au+Au collisions at  $\sqrt{s_{\text{NN}}} = 19.6, 62.4$  and 200 GeV from (a) the PHOBOS experiment at RHIC [41], (b) UrQMD, (c) AMPT default and (d) AMPT-SM. Also shown are the model results from Pb+Pb collisions at  $\sqrt{s_{\text{NN}}} = 2760$  GeV.

partons (no melting of strings to partons) and hadronization occurs through fragmentation process [46]. This model based study then suggests that partonic interactions in high energy density matter is essential to qualitatively reproduced the simultaneous observation of the longitudinal scalings in  $dN_{\text{ch}}/d\eta$  and  $v_2$  in experiment. If this is the actual cause then it will be interesting to have experimental measurements of  $v_2$  vs.  $\eta$  for lower beam energies where we do not expect to create a sufficiently high energy density system to see the breakdown of such a  $v_2$  longitudinal scaling.

There are some other possibilities which could explain the longitudinal scaling of  $v_2$ . One of them is based on the arguments whether the system is weakly coupled or strongly coupled. A weakly coupled system has been argued to favor the combined

$v_2$  and  $dN_{\text{ch}}/d\eta$  scaling behavior [42]. It has been suggested that for systems where the interactions among the constituent particles are small, or the system is close to free streaming, called the collision less limit [47], the  $v_2 \sim \frac{dN}{d\eta} \frac{\langle v\sigma \rangle}{\pi R_x R_y}$ . Where  $v$  is the relative velocity of the particles,  $\sigma$  is the momentum transfer interaction cross section and the product  $\pi R_x R_y$  is the transverse overlap area for the two nuclei. In this model, one can easily see that  $v_2$  should exhibit a longitudinal scaling similar to  $dN_{\text{ch}}/d\eta$  provided  $\langle v\sigma \rangle$  does not change with beam energy. A linear dependence of  $v_2$  with change in  $\frac{1}{\pi R_x R_y} \frac{dN}{d\eta}$  has been observed in experiments over a wide collision systems [15]. In the event of  $\langle v\sigma \rangle$  changing with beam energy, possibly due to change in the relevant degrees of freedom (hadronic or partonic), there would be a breakdown of the longitudinal scaling of  $v_2$ . This is consistent with the conclusions from our model study. Now let us move to the other extreme limit, where the re-scattering among the constituent particles are abundant leading to the hydrodynamic limit [47]. In such a model the  $v_2$  is proportional to the average transverse momentum of the particles among several other quantities as discussed in [48]. If the  $\langle p_T \rangle$  also exhibits a longitudinal scaling then  $v_2$  in the hydrodynamic limit scenario should also exhibit the scaling. Measuring  $\langle p_T \rangle$  vs.  $\eta$  could help address the cause of the longitudinal scaling of  $v_2$ . However we have seen in Fig. 5.10 that the models based on transport approach also exhibit longitudinal scaling of  $\langle p_T \rangle$ . The model study for all the three observables indicates that observing longitudinal scaling in  $dN_{\text{ch}}/d\eta$  and/or  $\langle p_T \rangle$  does not necessarily implies we should see a similar scaling in  $v_2$ .

### 5.4.2 Effect of centrality determination procedure on measured $v_2$ :

It is very important to know how the measured  $v_2$  depend on centrality determination procedure, because different experiments follow different methods for centrality selection. To check this effect, AMPT model is used to measure  $v_2$  in three possible way of centrality selection in the experiment. The most common method for centrality selections are follows: centrality using charged particle multiplicity within

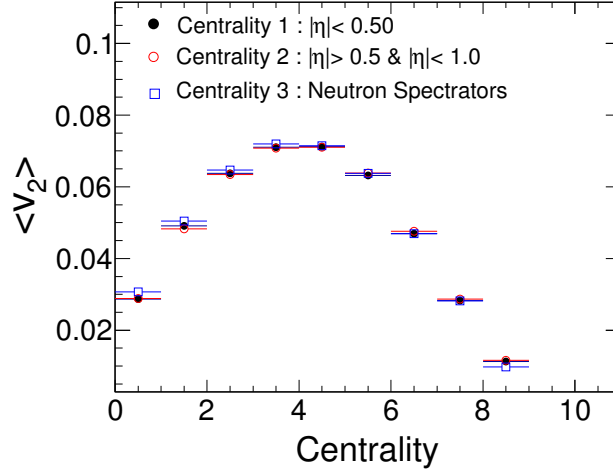


Figure 5.12: (Color online) The elliptic flow of charged particles as function of centrality in Au + Au collisions from AMPT model. The black solid circle, red open circle and blue open square represents the charged particles  $v_2$  corresponding centrality 1, 2 and 3, respectively.

$|\eta| < 0.5$  (labeled as centrality 1), centrality using charged particle multiplicity within  $|\eta| > 0.5$  and  $|\eta| < 1.0$  (labeled as centrality 2) and using neutron spectators (labeled as centrality 3). Figure 5.12 shows average  $v_2$  of charged particles measured at mid-rapidity ( $|\eta| < 0.5$ ) as function of centrality for three different cases using AMPT model. Good agreement among the results from three different cases are observed. The maximum difference in  $v_2$  for a particular centrality is found to be  $\sim 2\%$ . The agreement between the result from centrality 1 and centrality 2 also tells that there is no auto-correlation effect on  $v_2$  due to the centrality determination.

### 5.4.3 Effect of detector efficiency on measured $v_2$

As the particle track reconstruction efficiency in a detector varies with the occupancy, therefore this efficiency is not same for all centralities; efficiency is poor for central col-

lisions than the peripheral collisions. This centrality dependence of track reconstruction efficiency could bias the measured  $v_2$  for wide centrality bin towards the events with higher reconstruction efficiency i.e towards peripheral collisions. This is specifically true if we are combining events of widely different multiplicities/centralities to present the results. This effect has been investigated with the help of AMPT model. To do that, the experimental  $\pi$  meson reconstruction efficiency from the embedding from the STAR experiment [49] were used to modify the output of AMPT model. This has been done both as function of  $p_T$  and centrality. After this modification,  $v_2$  of charged particles were calculated for 0-80% centrality and compared with real  $v_2$  from AMPT model, i.e. with 100% efficiency. Figure 5.13 (left panel) shows the comparison of  $v_2$  with and without efficiency effect. As expected,  $v_2$  with detector inefficiency biased the  $v_2$  towards peripheral collisions and overall  $v_2$  for 0-80% centrality is found to be higher than original input  $v_2$  from AMPT. The ratios between these two results are shown in the right panel of Fig. 5.13. The change in  $v_2$  is of the order of 2 to 4 %. This effect can be large for particles, like  $\Xi$  and  $\Omega$ , having three decay daughters. Therefore it is necessary to correct for this effect.

This effect can be corrected by weighting the  $v_2$  for each centrality with the inverse of efficiency of the corresponding centrality. The final efficiency corrected  $v_2$  are shown in Fig. 5.14 and compared with input  $v_2$ . One can see from ratios, shown in right panel of Fig. 5.14, that the charged particle  $v_2$  after efficiency correction are consistent with true initial  $v_2$  within the statistical error. Therefore one should use this method to measure  $v_2$  in real experiment data.

The effect discussed above is due to centrality dependence of efficiency. Now question is that whether the measured  $v_2$  depends on absolute magnitude of  $v_2$ . If we recall the basic definition of  $v_2$  which is as follows:

$$\langle v_2 \rangle = \left\langle \frac{p_x^2 - p_y^2}{p_x^2 + p_y^2} \right\rangle \quad (5.40)$$

The  $\langle \rangle$  denotes average of all particles in all events. So  $\langle v_2 \rangle$  will not change and if we remove few particles randomly from the total number of particles in all events. But situation will not be same if we remove particle randomly for event by event basis. This is more important for events with small multiplicities. Using AMPT model and

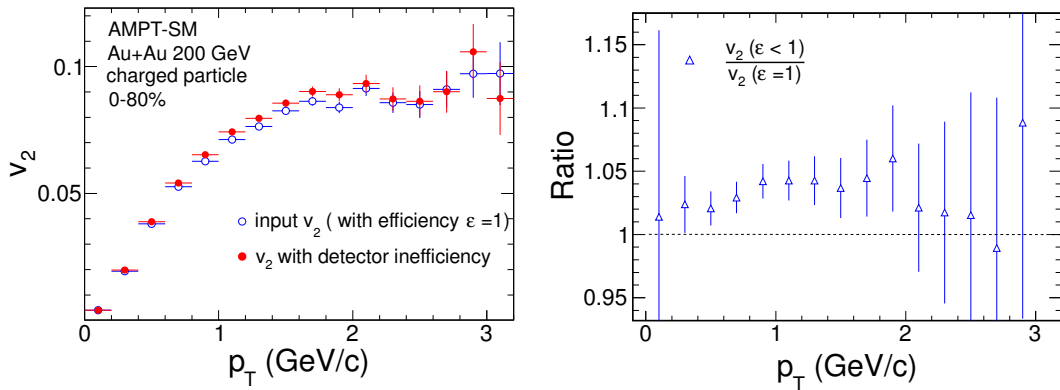


Figure 5.13: (Color online) Left panel: Charged particles  $v_2$  from AMPT model with finite particle track reconstruction efficiency  $\varepsilon$  (as a function of  $p_T$  and centrality) are compared with default  $v_2$  ( $\varepsilon=1$ ) of AMPT. Centre-of-mass energy is 200 GeV and centrality is 0-80%. Right panel: Ratios of the  $v_2$  as function of  $p_T$ .

realistic detector efficiency this effect has been studied. The realistic track reconstruction efficiency of charged kaons and  $K_S^0$  as function of  $p_T$  are shown in the left panel of Fig. 5.15. Based on the value of efficiency, kaon tracks are removed from AMPT output. The aim was to measure kaon  $v_2$  with charged kaon reconstruction efficiency and also with  $K_S^0$  reconstruction efficiency to see the change in measured  $v_2$ , if any. The yield of kaon from AMPT model with and without considering reconstruction efficiency are shown in the right panel of Fig. 5.15, the red line shows kaon yield as function of  $p_T$  from AMPT without any modification where as black line shows kaon yield after modification with reconstruction efficiency of  $K_S^0$ . The two distributions have been normalised at their respective yield values at  $p_T = 1$  GeV/c. The effect of finite particle reconstruction efficiency can be seen from the shape of yield vs.  $p_T$  distribution below  $p_T = 1$  GeV/c and as the efficiency values are constant with  $p_T$  beyond 1 GeV/c the spectra shape are similar at high  $p_T$  (consistent with Fig. 5.15). The elliptic flow of charged kaons has been calculated in three different condition: with 100% efficiency (labeled as default), with kaon track reconstruction efficiency

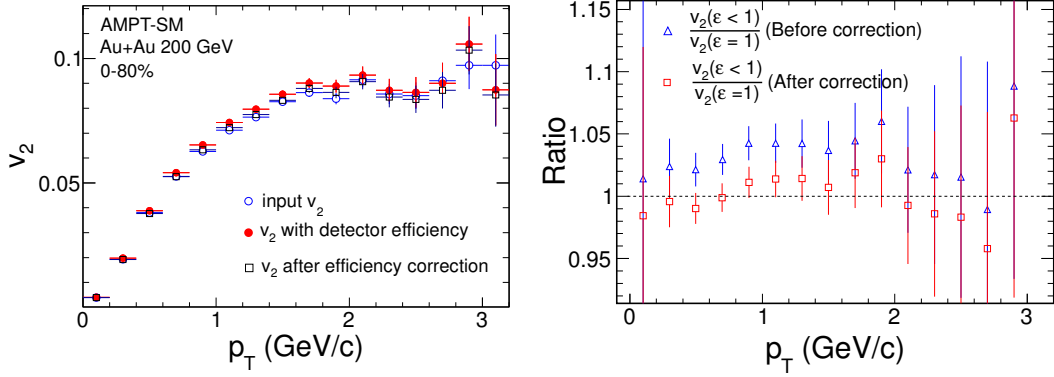


Figure 5.14: (Color online) Left panel: Charged particles  $v_2$  from AMPT model with finite particle track reconstruction efficiency  $\epsilon$  (as a function of  $p_T$  and centrality) and after efficiency correction are compared with default  $v_2$  value ( $\epsilon = 1$ ) of AMPT. Centre-of-mass energy is 200 GeV and centrality is 0-80%. Right panel: Ratios of the  $v_2$  as function of  $p_T$ .

and with  $K_S^0$  reconstruction efficiency. Figure 5.16 shows the comparison of charged kaons  $v_2$  for three different cases. The charged kaons  $v_2$  from AMPT with default setting, with charged kaon reconstruction efficiency and with  $K_S^0$  reconstruction efficiency has been shown by solid black circle, open blue square and open red circle, respectively. The bottom panel of Fig. 5.16 shows the ratios of  $v_2$  with default kaon  $v_2$ . From the ratios one can see that there is a change due to finite track reconstruction efficiency on the measured  $v_2$ . The change in  $v_2$  due to  $K_S^0$  reconstruction efficiency is about 10% to 30% while for charged kaon reconstruction efficiency the change is less than 5%. The change is large at low  $p_T$  since efficiency is poor in the low  $p_T$  region. A method to correct for this effect is still not obtained.

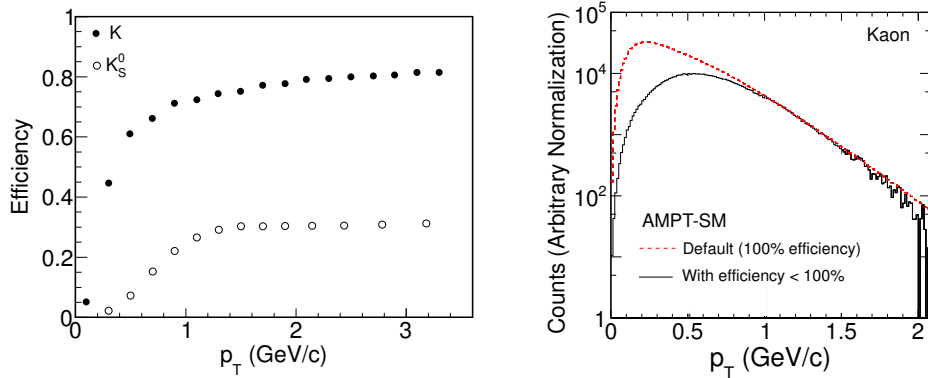


Figure 5.15: (Color online) Left panel: Track reconstruction efficiency as function of  $p_T$  for charged kaon and  $K_S^0$ . Open symbol is for  $K_S^0$  and filled symbol for charged kaons. Right panel: Yield as function of  $p_T$  for kaon. Red line is yield of kaon directly obtained from AMPT model and black line correspond kaon yield obtained after modification with  $K_S^0$  reconstruction efficiency values. Y-axis has arbitrary normalization.

#### 5.4.4 Resonance decay effect

In the heavy ion collision a large fraction of stable hadrons such as pions, kaons, and protons are from resonance decays. Azimuthal anisotropy of the resonance decay daughters are not expected to be the same as direct produced particles. Therefore this will change the average  $v_2$  of corresponding particle. To study the effect of resonance decays on the elliptic flow of stable hadrons UrQMD model has been used. The main aim is to study how the elliptic flows of pions, kaons and protons are affected by decays of resonances, such as  $\rho$ ,  $\Lambda$ ,  $\phi$ ,  $\eta$ ,  $\Omega$ ,  $\Sigma$  and  $\Delta$ . UrQMD model allow us to measure  $v_2$  with resonance decay on and off condition. Figure 5.17 shows  $v_2$  of  $\pi$ ,  $K$  and  $p$  as function of  $p_T$  with decay off and decay on condition in Au+Au collision from UrQMD model. From the ratios shown in the lower panels of Fig 5.17, one can see that there is change of 10% to 15% in pions  $v_2$ , less than 5% in kaons  $v_2$  and protons are almost unaffected. Also we can see that there is a overall decrease in  $v_2$  values due

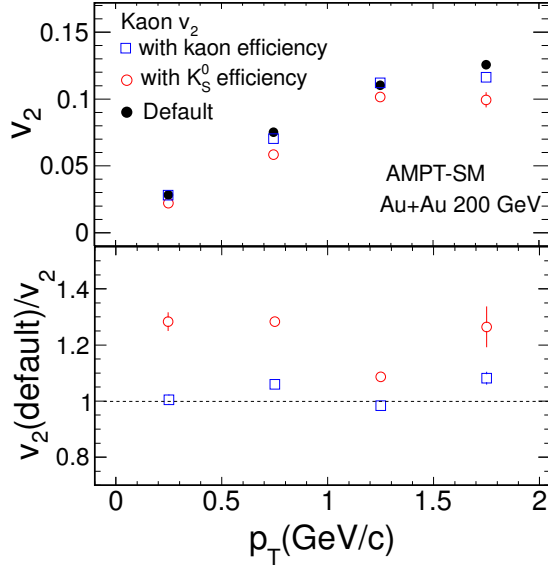


Figure 5.16: (Color online) The elliptic flow of kaon as function of  $p_T$  in Au+Au collision for 0-80% from AMPT model in three different condition: with 100% efficiency (labeled as default), with kaon reconstruction efficiency and with  $K_S^0$  reconstruction efficiency. The centre-of-mass energy is 200 GeV per nucleon.

to decay of resonances. But in general one could expect a higher elliptic flow from decay of resonances since a decay particle at given transverse momentum arises from a resonance at higher momentum with higher elliptic flow. However, the decay process, which is isotropic in the rest frame of the resonance, reduces the elliptic flow [50]. To understand the result the effect of pions  $v_2$  from decay of  $\rho \rightarrow \pi^+ + \pi^-$  has been studied. This decay process is almost isotropic in the rest frame of the resonance and hence one can expect reduction in the momentum anisotropy of daughter pions.

Figure 5.18 shows the pions  $v_2$  as a function of  $p_T$  in Au+Au collisions from UrQMD model with three different cases: (1) Decay of all resonances are on (shown by red triangle) (2) Decay of  $\rho$ ,  $\Lambda$ ,  $\eta$ ,  $\Sigma$  and  $\Delta$  are off ( shown by blue circle). (3)

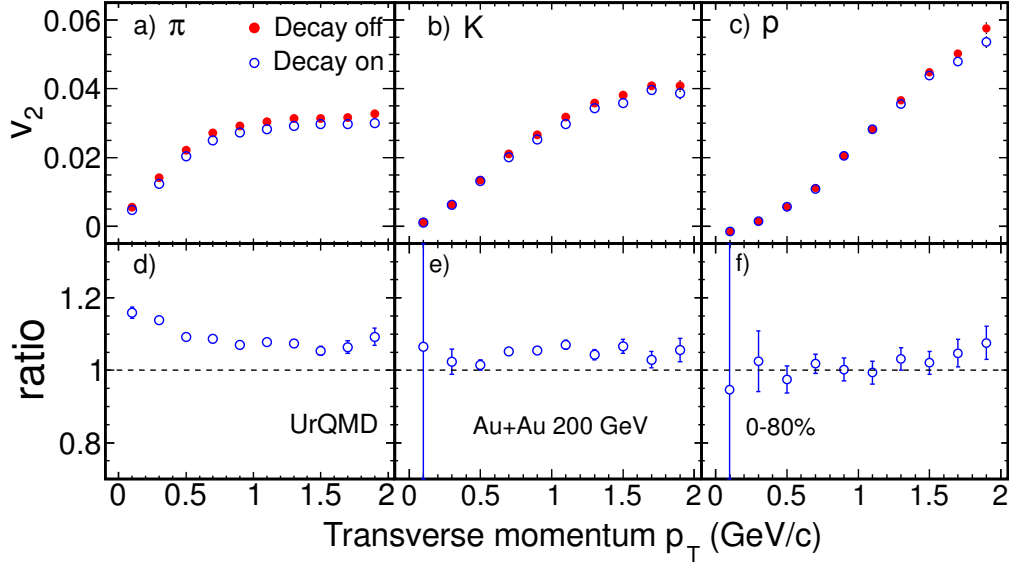


Figure 5.17: (Color online) The  $v_2$  of  $\pi$ ,  $K$  and  $p$  as function of  $p_T$  at 0-80% centrality with decay off and decay on condition in Au+Au collision at 200 GeV from UrQMD model.

Decay of  $\Lambda$ ,  $\eta$ ,  $\Sigma$  and  $\Delta$  off (shown by black triangle). Now if we compare result from case 2 and case 3, we can see that there is decrease in pions  $v_2$  due to decay of  $\rho \rightarrow \pi^+ + \pi^-$  which is expected from the decay kinematics. Now if we compare case 1 and case 3, one can see that pions  $v_2$  increases and that is because of contributions from the decay of  $\Lambda$ ,  $\eta$ ,  $\Sigma$  and  $\Delta$ . This is also expected from as discussed before. Similarly we have observed that the decrease in kaons  $v_2$  is due to  $\phi \rightarrow K^+ + K^-$  decay. This study using UrQMD model shows that there is an overall decrease in pions and kaons  $v_2$  due to decay of resonances.

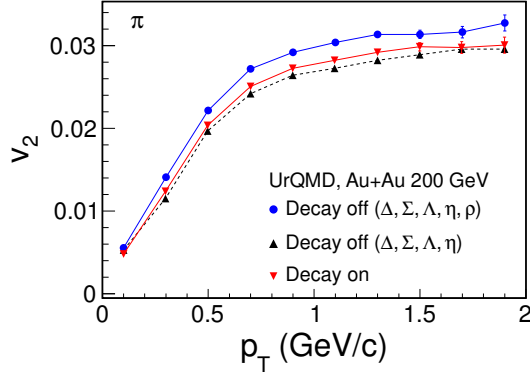


Figure 5.18: (Color online) The elliptic flow of pions as a function of  $p_T$  in Au+Au collisions at 200 GeV for 0-80% centrality from UrQMD model.

## 5.5 Summary

We have presented elliptic flow,  $v_2$ , measurements from Au + Au collisions at  $\sqrt{s_{NN}} = 7.7, 11.5, 19.6, 27$  and  $39$  GeV for inclusive charged hadrons at mid-rapidity. The centrality and  $p_T$  dependence of  $v_2$  are similar to that observed at higher RHIC collision energies. The comparison with Au + Au collisions at higher energies at RHIC ( $\sqrt{s_{NN}} = 62.4$  and  $200$  GeV) and at LHC (Pb+Pb collisions at  $\sqrt{s_{NN}} = 2.76$  TeV) shows the  $v_2\{4\}$  values at low  $p_T$  ( $p_T < 2.0$  GeV/ $c$ ) increase with increase in collision energy implying an increase of collectivity. The current viscous hydrodynamic simulations [36] cannot reproduce the trend of the energy dependence of  $v_2(p_T)$ . The agreement between the data and UrQMD, which is based on hadronic rescatterings, is observed at lower collision energies, consistent with an increasing role of the hadronic stage at these energies. These results sets the stage for understanding the collision energy dependence of  $v_2$  in the regime where the relative contribution of baryon and mesons vary significantly.

We have also presented some systematic study to improve our knowledge on  $v_2$  estimates. The observed longitudinal scaling of  $v_2$  in data was also reproduced by AMPT model with string melting, where as UrQMD and AMPT default model fails to re-

produce such a scaling of  $v_2$ . This model based study then suggests that partonic interactions in high energy density matter is essential to qualitatively reproduced longitudinal scaling of  $v_2$ . We showed that measured  $v_2$  is not affected by the method fo centrality determination procedure. The effect of finite track reconstruction efficiency in detectors on measured  $v_2$  was also discussed in details. The measured  $v_2$  depends on both centrality dependence of the reconstruction efficiency as well as the magnitude. Using UrQMD model, we have showed that the pion  $v_2$  is largely effected by resonance decay contribution.

# Bibliography

- [1] N. Borghini, P. M. Dinh, and J.-Y. Ollitrault, Phys. Rev. **C 63**, 054906 (2001).
- [2] N. Borghini, P. M. Dinh, and J.-Y. Ollitrault, Phys. Rev. **C 64**, 054901 (2001).
- [3] A. Bilandzic, R. Snellings, S. Voloshin, Phys. Rev. **C 83**, 044913 (2011).
- [4] A. Bilandzic, PhD. thesis, Nikhef and Utrecht University, (2011).
- [5] C. Adler *et al.* (STAR Collaboration) Phys. Rev. **C 66**, 034904 (2002).
- [6] M. Luzum and J. Ollitrault, Phys. Rev. **C 87**, 044907 (2013).
- [7] K. H. Ackermann *et al.* (STAR Collaboration), Phys. Rev. Lett. **86**, 402 (2001).
- [8] J. Adams *et al.* (STAR Collaboration), Phys. Rev. **C 72**, 014904 (2005).
- [9] A. M. Poskanzer and S. A. Voloshin (NA49 Collaboration), Nucl. Phys. **A 661**, 341c (1999).
- [10] L. Adamczyk *et al.* (STAR Collaboration), Phys. Rev. **C 86**, 054908 (2012).
- [11] K. Aamodt *et al.* (ALICE Collaboration), Phys. Rev. Lett. **105**, 252302 (2010).
- [12] L. Kumar (For STAR Collaboration), J. Phys. **G 38**, 124145 (2011).
- [13] S. Das (for the STAR Collaboration), Nucl. Phys. **A 904-905**, 891c (2013).
- [14] H. H. Gutbord *et al.* Phys. Lett. **B 216**, 267 (1989).

- [15] J. Adams *et al.* ( STAR Collaboration), Phys. Rev. **C 72**, 014904 (2005);  
 B. I. Abelev *et al.* ( STAR Collaboration), Phys. Rev. **C 75**, 054906 (2007);  
 B. I. Abelev *et al.* ( STAR Collaboration), Phys. Rev. **C 77**, 054901 (2007).
- [16] S. Afanasiev *et al.* (PHENIX Collaboration), Phys. Rev. **C 80**, 024909 (2009);  
 A. Adare *et al.* (PHENIX Collaboration), Phys. Rev. Lett. **105**, 062301 (2010);  
 S. Afanasiev *et al.* (PHENIX Collaboration), Phys. Rev. Lett. **99**, 052301 (2007).
- [17] B. B. Back *et al.* (PHOBOS Collaboration), Phys. Rev. Lett. **94**, 122303 (2005).
- [18] H. Appelshauser *et al.* (CERES Collaboration), Nucl. Phys. **A 698**, 253c (2002).
- [19] C. Pinkenburg *et al.* Phys. Rev. Lett. **83**, 1295 (1999).
- [20] P. Braun-Munzinger, J. Stachel, Nucl. Phys. **A 638**, 3c (1998).
- [21] J. Y. Ollitrault *et al.* Phys. Rev. **C 80**, 014904 (2009).
- [22] S. Voloshin, nucl-th/0606022 (2006).
- [23] B. Alver *et al.* (PHOBOS Collaboration), Phys. Rev. **C 77**, 014906 (2008).
- [24] M. Miller and R. Snellings, nucl-ex/0312008 (2003).
- [25] M. L. Miller *et al.* Ann. Rev. Nucl. Part. Sci. **57**, 205 (2007).
- [26] A. Adil *et al.* Phys. Rev. **C 74**, 044905 (2006).
- [27] H. J. Drescher and Y. Nara, Phys. Rev. **C 76**, 041903 (2007).
- [28] H. J. Drescher and Y. Nara, Phys. Rev. **C 75**, 034905 (2007).
- [29] T. Hirano and Y. Nara, Phys. Rev. **C 79**, 064904 (2009).
- [30] B. I. Abelev *et al.* (STAR Collaboration), Phys. Rev. **C 77**, 054901 (2008).
- [31] B. I. Abelev *et al.* (STAR Collaboration), Phys. Rev. **C 81**, 044902 (2010).
- [32] S. A. Bass *et al.* Prog. Part. Nucl. Phys. **41**, 255 (1998);  
 M. Bleicher *et al.* J. Phys. **G 25**, 1859 (1999).

- [33] Zi-Wei Lin, C. M. Ko, Phys. Rev. **C 65**, 034904 (2002);  
Zi-Wei Lin *et al.* Phys. Rev. **C 72**, 064901 (2005);  
Lie-Wen Chen *et al.* Phys. Lett. **B 605**, 95 (2005).
- [34] J. Y. Ollitrault, Phys. Rev. **D 46**, 229 (1992).
- [35] J. Xu *et al.* Phys. Rev. **C 85**, 041901 (2012).
- [36] C. Shen and U. Heinz, Phys. Rev. **C 85**, 054902 (2012).
- [37] Md. Nasim *et al.* Phys. Rev. **C 82**, 054908 (2010).
- [38] B. I. Abelev *et al.* (STAR Collaboration), Phys. Rev. **C 81**, 024911 (2010).
- [39] B. Alver, *et al.* (PHOBOS Collaboration), Phys. Rev. Lett **102**, 142301 (2009);  
B. B. Back, *et al.* (PHOBOS Collaboration), Phys. Rev. Lett **91**, 052303 (2003);  
J. Adams, *et al.* (STAR Collaboration), Phys. Rev. Lett **95**, 062301 (2005);  
J. Adams, *et al.* (STAR Collaboration), Phys. Rev. **C 73**, 034906 (2006);  
B. I. Abelev, *et al.* (STAR Collaboration), Nucl. Phys. **A 832**, 134 (2010).
- [40] B. B. Back, *et al.* (PHOBOS Collaboration), Phys. Rev. **C 74**, 021902(R) (2006);  
B. B. Back, *et al.* (PHOBOS Collaboration), Phys. Rev. **C 72**, 031901(R) (2005).
- [41] B. B. Back, *et al.* (PHOBOS Collaboration), Phys. Rev. Lett **94**, 122303 (2005).
- [42] G. Torrieri, Phys. Rev. **C 82**, 054906 (2010).
- [43] R. A. Lacey *et al.* Phys. Rev. Lett. **98**, 092301 (2007);  
S. Gavin and M. Abdel-Aziz, Phys. Rev. Lett. **97**, 162302 (2006);  
A Adare *et al.* (PHENIX Collaboration) Phys. Rev. Lett. **98**, 172301 (2007);  
H-J. Drescher *et al.* Phys. Rev. **C 76**, 024905 (2007).
- [44] Md. Nasim *et al.* Phys. Rev. **C 83**, 054902 (2011).
- [45] X. N. Wang and M. Gyulassy, Phys. Rev. **D 44**, 3501 (1991).
- [46] B. Andersson *et al.* Phys. Rep. **97**, 31 (1983).

- [47] H. Heiselberg and A. M. Levy, Phys. Rev. **C 59**, 2716 (1999).
- [48] S. Voloshin, Y. Zhang, Z. Phys. **C 70**, 665 (1996);  
S. A. Voloshin, A. M. Poskanzer and R. Snellings, arXiv:0809.2949.
- [49] B. I. Abelev *et al.* (STAR Collaboration), Phys. Rev. **C 79**, 034909 (2009).
- [50] T. Hirano, Phys. Rev. Lett. **86**, 2754 (2001).

## 5.6 Appendix

### 5.6.1 Color Glass Condensate Simulation

Table 5.2: The  $\varepsilon_{part}\{2\}$  and transverse area  $\langle S_{part} \rangle$  from the Color Glass Condensate (CGC) model [26, 27, 28, 29] calculations in Au + Au collisions at  $\sqrt{s_{NN}} = 7.7, 11.5, 19.6, 27, 39, 62.4$  and 200 GeV. The errors are systematic uncertainties.

Centrality (%)	0 – 5%	5 – 10%	10 – 20%	20 – 30%	30 – 40%	40 – 50%	50 – 60%	60 – 70%	70 – 80%
Au+Au at $\sqrt{s_{NN}} = 7.7$ GeV									
$\varepsilon_{part}\{2\}$	$0.104 \pm 0.005$	$0.19 \pm 0.01$	$0.29 \pm 0.01$	$0.39 \pm 0.02$	$0.47 \pm 0.02$	$0.54 \pm 0.03$	$0.59 \pm 0.03$	$0.62 \pm 0.03$	$0.51 \pm 0.02$
$\langle S_{part} \rangle$ (fm <sup>2</sup> )	$25.9 \pm 1.3$	$21.8 \pm 1.1$	$17.5 \pm 0.9$	$13.4 \pm 0.7$	$10.2 \pm 0.5$	$7.7 \pm 0.4$	$5.5 \pm 0.3$	$3.6 \pm 0.2$	$1.8 \pm 0.1$
Au+Au at $\sqrt{s_{NN}} = 11.5$ GeV									
$\varepsilon_{part}\{2\}$	$0.104 \pm 0.005$	$0.19 \pm 0.01$	$0.29 \pm 0.01$	$0.39 \pm 0.02$	$0.47 \pm 0.02$	$0.53 \pm 0.03$	$0.59 \pm 0.03$	$0.62 \pm 0.03$	$0.51 \pm 0.02$
$\langle S_{part} \rangle$ (fm <sup>2</sup> )	$25.2 \pm 1.2$	$21.2 \pm 1.1$	$17.0 \pm 0.9$	$13.0 \pm 0.7$	$9.9 \pm 0.5$	$7.5 \pm 0.4$	$5.4 \pm 0.3$	$3.5 \pm 0.2$	$1.8 \pm 0.1$
Au+Au at $\sqrt{s_{NN}} = 19.6$ GeV									
$\varepsilon_{part}\{2\}$	$0.105 \pm 0.005$	$0.19 \pm 0.01$	$0.29 \pm 0.01$	$0.39 \pm 0.02$	$0.47 \pm 0.02$	$0.53 \pm 0.03$	$0.58 \pm 0.03$	$0.61 \pm 0.03$	$0.51 \pm 0.02$
$\langle S_{part} \rangle$ (fm <sup>2</sup> )	$24.4 \pm 1.2$	$20.6 \pm 1.0$	$16.6 \pm 0.9$	$12.6 \pm 0.7$	$9.7 \pm 0.5$	$7.3 \pm 0.4$	$5.3 \pm 0.3$	$3.5 \pm 0.2$	$1.8 \pm 0.1$
Au+Au at $\sqrt{s_{NN}} = 27$ GeV									
$\varepsilon_{part}\{2\}$	$0.105 \pm 0.005$	$0.19 \pm 0.01$	$0.29 \pm 0.01$	$0.39 \pm 0.02$	$0.47 \pm 0.02$	$0.53 \pm 0.03$	$0.58 \pm 0.03$	$0.61 \pm 0.03$	$0.51 \pm 0.02$
$\langle S_{part} \rangle$ (fm <sup>2</sup> )	$24.1 \pm 1.2$	$20.3 \pm 1.0$	$16.4 \pm 0.8$	$12.5 \pm 0.6$	$9.6 \pm 0.5$	$7.2 \pm 0.4$	$5.3 \pm 0.3$	$3.5 \pm 0.2$	$1.8 \pm 0.1$
Au+Au at $\sqrt{s_{NN}} = 39$ GeV									
$\varepsilon_{part}\{2\}$	$0.105 \pm 0.005$	$0.19 \pm 0.01$	$0.29 \pm 0.01$	$0.39 \pm 0.02$	$0.47 \pm 0.02$	$0.53 \pm 0.03$	$0.58 \pm 0.03$	$0.61 \pm 0.03$	$0.50 \pm 0.02$
$\langle S_{part} \rangle$ (fm <sup>2</sup> )	$23.9 \pm 1.2$	$20.1 \pm 1.0$	$16.2 \pm 0.8$	$12.4 \pm 0.6$	$9.5 \pm 0.5$	$7.2 \pm 0.4$	$5.3 \pm 0.3$	$3.5 \pm 0.2$	$1.8 \pm 0.1$
Au+Au at $\sqrt{s_{NN}} = 62.4$ GeV									
$\varepsilon_{part}\{2\}$	$0.105 \pm 0.005$	$0.19 \pm 0.01$	$0.29 \pm 0.01$	$0.39 \pm 0.02$	$0.47 \pm 0.02$	$0.53 \pm 0.03$	$0.58 \pm 0.03$	$0.61 \pm 0.03$	$0.50 \pm 0.02$
$\langle S_{part} \rangle$ (fm <sup>2</sup> )	$23.7 \pm 1.2$	$20.0 \pm 1.0$	$16.1 \pm 0.8$	$12.3 \pm 0.6$	$9.4 \pm 0.5$	$7.2 \pm 0.4$	$5.3 \pm 0.3$	$3.5 \pm 0.2$	$1.8 \pm 0.1$
Au+Au at $\sqrt{s_{NN}} = 200$ GeV									
$\varepsilon_{part}\{2\}$	$0.104 \pm 0.005$	$0.19 \pm 0.01$	$0.29 \pm 0.01$	$0.39 \pm 0.02$	$0.47 \pm 0.02$	$0.53 \pm 0.03$	$0.57 \pm 0.03$	$0.60 \pm 0.03$	$0.49 \pm 0.02$
$\langle S_{part} \rangle$ (fm <sup>2</sup> )	$23.7 \pm 1.2$	$20.0 \pm 1.0$	$16.1 \pm 0.8$	$12.3 \pm 0.6$	$9.4 \pm 0.5$	$7.2 \pm 0.4$	$5.3 \pm 0.3$	$3.6 \pm 0.2$	$1.9 \pm 0.1$

## 5.6.2 Glauber Model Simulation

Table 5.3: The  $\varepsilon_{part}\{2\}$  and transverse area  $\langle S_{part} \rangle$  from the Glauber model calculations in Au + Au collisions at  $\sqrt{s_{NN}} = 7.7, 11.5, 19.6, 27, 39, 62.4$  and 200 GeV. The errors are systematic uncertainties.

Centrality (%)	0 – 5%	5 – 10%	10 – 20%	20 – 30%	30 – 40%	40 – 50%	50 – 60%	60 – 70%	70 – 80%
Au+Au at $\sqrt{s_{NN}} = 7.7$ GeV									
$\varepsilon_{part}\{2\}$	$0.117 \pm 0.003$	$0.16 \pm 0.01$	$0.24 \pm 0.01$	$0.32 \pm 0.02$	$0.39 \pm 0.02$	$0.46 \pm 0.03$	$0.53 \pm 0.03$	$0.53 \pm 0.03$	$0.72 \pm 0.02$
$\langle S_{part} \rangle$ (fm <sup>2</sup> )	$25.5 \pm 0.4$	$23.0 \pm 0.3$	$19.5 \pm 0.4$	$15.7 \pm 0.7$	$12.6 \pm 0.8$	$10.0 \pm 0.9$	$7.8 \pm 1.0$	$5.8 \pm 1.1$	$3.6 \pm 1.0$
Au+Au at $\sqrt{s_{NN}} = 11.5$ GeV									
$\varepsilon_{part}\{2\}$	$0.116 \pm 0.005$	$0.16 \pm 0.01$	$0.24 \pm 0.01$	$0.32 \pm 0.02$	$0.39 \pm 0.02$	$0.46 \pm 0.03$	$0.53 \pm 0.03$	$0.53 \pm 0.03$	$0.71 \pm 0.02$
$\langle S_{part} \rangle$ (fm <sup>2</sup> )	$25.6 \pm 0.4$	$23.0 \pm 0.3$	$19.5 \pm 0.5$	$15.7 \pm 0.7$	$12.6 \pm 0.5$	$10.1 \pm 0.6$	$7.8 \pm 0.7$	$5.8 \pm 1.0$	$3.7 \pm 1.2$
Au+Au at $\sqrt{s_{NN}} = 19.6$ GeV									
$\varepsilon_{part}\{2\}$	$0.117 \pm 0.005$	$0.16 \pm 0.01$	$0.24 \pm 0.01$	$0.32 \pm 0.02$	$0.40 \pm 0.02$	$0.46 \pm 0.03$	$0.53 \pm 0.03$	$0.62 \pm 0.04$	$0.71 \pm 0.05$
$\langle S_{part} \rangle$ (fm <sup>2</sup> )	$25.6 \pm 1.2$	$23.0 \pm 1.0$	$19.5 \pm 0.9$	$15.6 \pm 0.7$	$12.5 \pm 0.5$	$10.0 \pm 0.4$	$7.8 \pm 0.3$	$5.8 \pm 0.2$	$3.7 \pm 0.1$
Au+Au at $\sqrt{s_{NN}} = 27$ GeV									
$\varepsilon_{part}\{2\}$	$0.114 \pm 0.005$	$0.16 \pm 0.01$	$0.23 \pm 0.01$	$0.32 \pm 0.02$	$0.39 \pm 0.02$	$0.46 \pm 0.03$	$0.53 \pm 0.03$	$0.61 \pm 0.03$	$0.71 \pm 0.02$
$\langle S_{part} \rangle$ (fm <sup>2</sup> )	$25.8 \pm 1.2$	$23.4 \pm 1.0$	$19.8 \pm 0.8$	$15.9 \pm 0.6$	$12.8 \pm 0.5$	$10.2 \pm 0.4$	$7.9 \pm 0.3$	$5.8 \pm 0.2$	$3.6 \pm 0.1$
Au+Au at $\sqrt{s_{NN}} = 39$ GeV									
$\varepsilon_{part}\{2\}$	$0.115 \pm 0.005$	$0.16 \pm 0.01$	$0.23 \pm 0.01$	$0.32 \pm 0.02$	$0.39 \pm 0.02$	$0.46 \pm 0.03$	$0.53 \pm 0.03$	$0.53 \pm 0.03$	$0.71 \pm 0.02$
$\langle S_{part} \rangle$ (fm <sup>2</sup> )	$25.9 \pm 1.2$	$23.3 \pm 1.0$	$19.8 \pm 0.8$	$16.0 \pm 0.6$	$12.8 \pm 0.5$	$10.3 \pm 0.4$	$8.0 \pm 0.3$	$5.9 \pm 0.2$	$3.8 \pm 0.1$
Au+Au at $\sqrt{s_{NN}} = 62.4$ GeV									
$\varepsilon_{part}\{2\}$	$0.112 \pm 0.005$	$0.157 \pm 0.01$	$0.229 \pm 0.01$	$0.313 \pm 0.02$	$0.385 \pm 0.02$	$0.453 \pm 0.03$	$0.525 \pm 0.03$	$0.609 \pm 0.03$	$0.707 \pm 0.02$
$\langle S_{part} \rangle$ (fm <sup>2</sup> )	$26.0 \pm 1.2$	$23.5 \pm 1.0$	$20.0 \pm 0.8$	$16.1 \pm 0.6$	$13.0 \pm 0.5$	$10.4 \pm 0.4$	$8.1 \pm 0.3$	$5.9 \pm 0.2$	$3.7 \pm 0.1$
Au+Au at $\sqrt{s_{NN}} = 200$ GeV									
$\varepsilon_{part}\{2\}$	$0.112 \pm 0.005$	$0.154 \pm 0.01$	$0.225 \pm 0.01$	$0.306 \pm 0.02$	$0.378 \pm 0.02$	$0.445 \pm 0.03$	$0.516 \pm 0.03$	$0.601 \pm 0.03$	$0.695 \pm 0.02$
$\langle S_{part} \rangle$ (fm <sup>2</sup> )	$26.6 \pm 1.2$	$24.1 \pm 1.0$	$20.6 \pm 0.8$	$16.7 \pm 0.6$	$13.5 \pm 0.5$	$10.8 \pm 0.4$	$8.4 \pm 0.3$	$6.2 \pm 0.2$	$3.9 \pm 0.1$

## 5.6.3 Inputs Parameters of AMPT and UrQMD Model

### 5.6.3.1 Inputs parameters of AMPT model:

200  $\rightarrow$  EFRM ( $\sqrt{s_{NN}}$  in GeV)  
CMS  $\rightarrow$  FRAME  
A  $\rightarrow$  PROJ  
A  $\rightarrow$  TARG  
197  $\rightarrow$  IAP (projectile A number)  
79  $\rightarrow$  IZP (projectile Z number)  
197  $\rightarrow$  IAT (target A number)  
79  $\rightarrow$  IZT (target Z number)  
10000  $\rightarrow$  NEVNT (total number of events)  
0.  $\rightarrow$  BMIN (minimum impact parameter in fm)  
15.0  $\rightarrow$  BMAX (maximum impact parameter in fm, also see below)  
4  $\rightarrow$  ISOFT (D=1): select Default AMPT or String Melting  
150  $\rightarrow$  NTMAX: number of timesteps (D=150),  
0.2  $\rightarrow$  DT: timestep in fm (hadron cascade time= DT\*NTMAX) (D=0.2)  
2.2  $\rightarrow$  PARJ(41): parameter a in Lund symmetric splitting function  
0.5  $\rightarrow$  PARJ(42): parameter b in Lund symmetric splitting function  
1  $\rightarrow$  (D=1,yes;0,no) flag for popcorn mechanism(netbaryon stopping)  
1.0  $\rightarrow$  PARJ(5) to control BMBbar vs BBbar in popcorn (D=1.0)  
1  $\rightarrow$  shadowing flag (Default=1,yes; 0,no)  
0  $\rightarrow$  quenching flag (D=0,no; 1,yes)  
1.0  $\rightarrow$  quenching parameter -dE/dx (GeV/fm) in case quenching flag=1  
2.0  $\rightarrow$  p0 cutoff in HIJING for minijet productions (D=2.0)  
1.76717d0  $\rightarrow$  parton screening mass in fm<sup>(-1)</sup>(D = 3.2264d0)  
0 $\rightarrow$  IZPC: (D=0 forward-angle parton scatterings; 100,isotropic)  
0.47140452d0  $\rightarrow$  alpha in parton cascade  
1d6  $\rightarrow$  dpcoal in GeV  
1d6  $\rightarrow$  drcoal in fm

11 → ihjseed: take HIJING seed from below (D=0)or at runtime(11)  
53153511 → random seed for HIJING  
8 → random seed for parton cascade  
0 → flag for Ks0 weak decays (D=0,no; 1,yes)  
0 → optional OSCAR output (D=0,no; 1,yes)

### 5.6.3.2 Inputs parameters of UrQMD model:

pro 197 79  
tar 197 79  
nev 10000  
imp -14.  
ecm 200.  
tim 100 100  
eos 0  
f13  
#f14  
f15  
f16  
f19  
f20

# Chapter 6

## Centrality Dependence of Multi-strange Hadron $v_2$ in Au+Au Collisions at 200 GeV

In this chapter the centrality dependence of multi-strange hadron ( $\phi$ ,  $\Xi$ ,  $\Omega$ )  $v_2$  measured at mid-rapidity ( $|y| < 1.0$ ) in Au+Au collisions at  $\sqrt{s_{NN}} = 200$  GeV are presented.

### 6.1 Data Sets and Event Selection Cuts

The results presented in this chapter are based on data collected from Au+Au collisions at  $\sqrt{s_{NN}} = 200$  GeV with the STAR detector for minimum bias trigger in the years of 2010 and 2011. The minimum-bias trigger condition was based on a coincidence of the signals from the zero-degree calorimeters, vertex position detectors, and/or beam-beam counters [1]. The final results are presented by combining data sets of the years 2010 and 2011. Total number of events analyzed for 0-80% centrality

is about 750 Million (250 M and 500 M from years the 2010 and 2011, respectively) after all event selection cuts. The events were selected within the vertex range  $\pm 30$  cm in the Z (beam) direction. In addition, less than 2 cm cuts on vertex radii were applied to remove contamination from beam pipe. Figure 6.1 shows the distribution of uncorrected reference multiplicity and Z position of vertex in Au+Au collisions at  $\sqrt{s_{NN}} = 200$  GeV. One can see that the values of uncorrected multiplicity is less in Run 10 than Run 11. This is due one dead sector of TPC during Run 10.

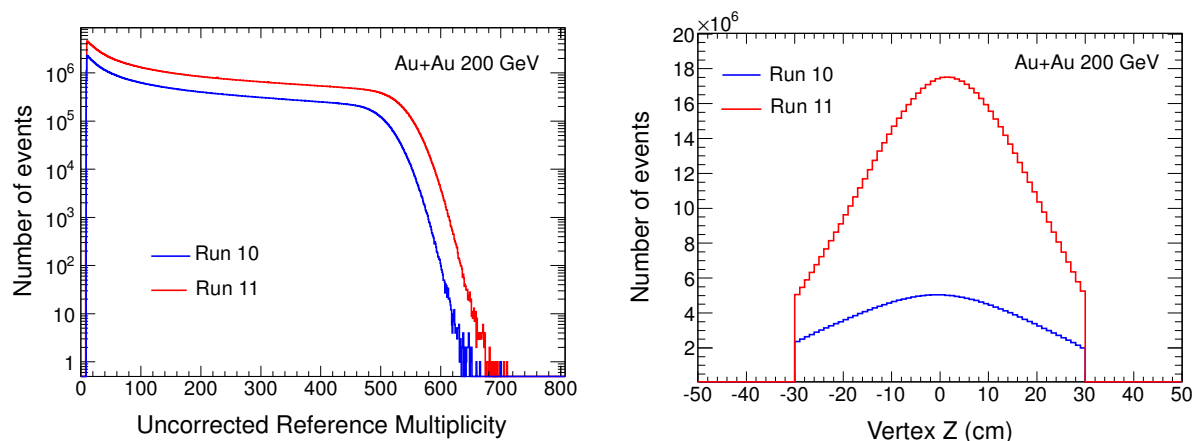


Figure 6.1: (Color online) Distribution of uncorrected reference multiplicity (left panel) and Z position of vertex (right panel) in Au+Au collisions at  $\sqrt{s_{NN}} = 200$  GeV. Blue and Red line corresponds to the data sets collected in the years 2010 (labeled as Run 10) and 2011 (labeled as Run 11), respectively.

## 6.2 Procedure to obtain multi-strange hadron $v_2$

### 6.2.1 Multi-strange hadron reconstruction

Multi-strange hadrons ( $\phi\{s\bar{s}\}, \Xi\{dss\}, \Omega\{sss\}$ ) were reconstructed by invariant mass technique through their following decay channel:  $\phi \rightarrow K^+ + K^-$  (Branching ratio =  $48.9 \pm 0.5\%$ ),  $\Xi^- \rightarrow \Lambda + \pi^-$  ( $\Xi^+ \rightarrow \bar{\Lambda} + \pi^+$ ) (Branching ratio =  $99.887 \pm 0.035\%$ ) and  $\Omega^- \rightarrow \Lambda + K^-$  ( $\bar{\Omega}^+ \rightarrow \bar{\Lambda} + K^+$ ) (Branching ratio =  $67.8 \pm 0.7\%$ ). The details

of  $\phi$ -meson reconstructions has already been discussed in chapters 3 and 4. In this section only the reconstruction of  $\Xi$  and  $\Omega$  will be discussed in detail.

A multi-strange baryon decays into a charged meson and a neutral  $\Lambda$  baryon, which again decays into a pion and a proton as shown in Fig. 6.2. The track information for the multi-strange baryon is carried by the three daughter tracks and therefore one need to calculate decay kinematics to reconstruct them. The decay topology is shown in Fig. 6.3 for  $\Xi$  as an example. The reconstruction of multi-strange baryon involve

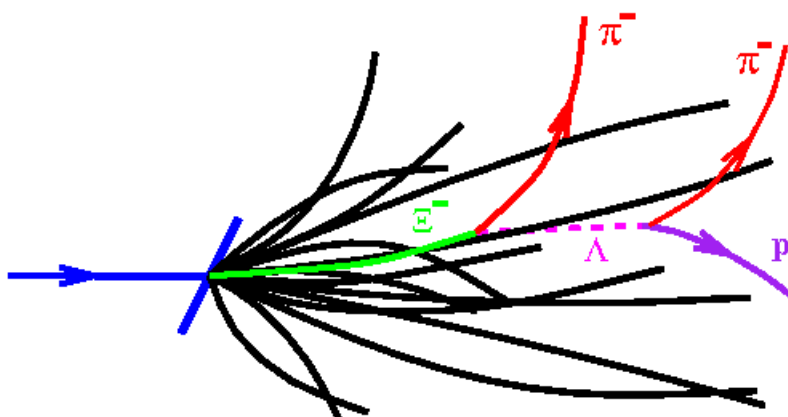


Figure 6.2: (Color online) Decay diagram of  $\Xi$  baryon.

two steps, first finding a suitable neutral  $\Lambda$  candidate and then finding  $\Xi$  or  $\Omega$  using a matching meson. Thus this involves reconstruction of two secondary decay vertex as shown in Fig. 6.3. This vertex type is called a *cascade* because of the multi-stage decay process.

### 6.2.1.1 $\Lambda$ reconstruction:

The  $\Lambda^0$  particle decays into  $p^+$  and  $\pi^-$  with branching ratio  $63.9 \pm 0.5$  %. The decay of a  $\Lambda^0$  occurs via the weak interaction. The  $p^+$  and  $\pi^-$  tracks were identified by the ionization energy loss in TPC and information of mass square ( $m^2$ ) from TOF. The basic cuts for track selection using TPC and TOF are listed in the table 6.1. After that  $V0$  topology was used to reconstruct the  $\Lambda^0$ . A simple diagram of  $V0$  topology

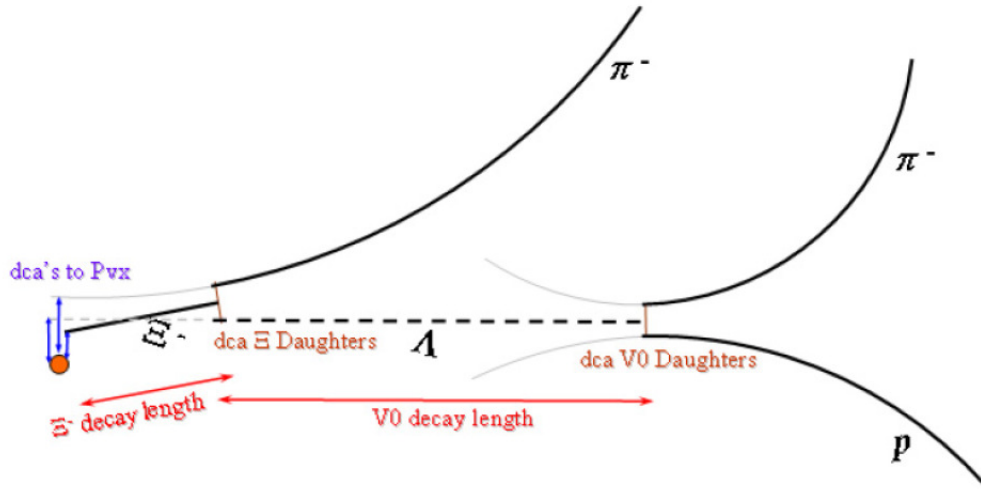


Figure 6.3: (Color online) The topology of a  $\Xi$  decay. The charged tracks are represented in the figure by solid lines, and the neutral  $\Lambda$  track by a dashed line. All the geometrical variables used for  $\Xi$  topological reconstruction are represented.

is shown in Fig. 6.4. The distance of closest approach (dca) between two daughter tracks is the parameter to determine the point of the decay vertex. Dca1 and Dca2 are the dca of the two daughters from the primary vertex. These Dca1 and Dca2 should not be very close to primary vertex if they are daughters of  $\Lambda^0$ . The parameter  $b$  is the dca from the primary vertex to the direction of  $V0$  momentum. Ideally,  $b$  should be equal to zero. The decay length of lambda is shown by parameter  $rv$  in Fig. 6.4.

### 6.2.1.2 $\Xi$ and $\Omega$ reconstruction:

After finding  $\Lambda^0$  i.e.  $V0$  vertex, next job is to find a meson which is the daughter of  $\Xi$  or  $\Omega$ . The possible topological criteria for  $\Xi$  and/or  $\Omega$  reconstruction are [2]:

- Distance of closest approach of the multi-strange baryon to the primary vertex (dca  $\Xi(\Omega)$  to Pvx)
- Distance of closest approach of the  $\Lambda$  daughter to the primary vertex (dca  $\Lambda$  to Pvx).

Number of fit points in TPC (nHits)	$\geq 15$
Ratio of fit points to possible points (nHits/Max. nHits)	$\geq 0.52$
Dca from primary vertex	$\leq 3.0$ cm
$n\sigma$ dE/dx of $p^+$ and $\pi^-$	$\leq 2.0$
$p_T$	$\geq 0.15$ GeV/c
pseudo-rapidity ( $\eta$ )	$\leq 1.0$
$m^2$ for $p^+$	$0.6 \leq m^2 \leq 1.15$ (GeV/c <sup>2</sup> )
$m^2$ for $\pi^-$	$0.0 \leq m^2 \leq 0.2$ (GeV/c <sup>2</sup> )

Table 6.1: Track selection cuts using TPC and TOF for  $\Lambda^0$  reconstruction.

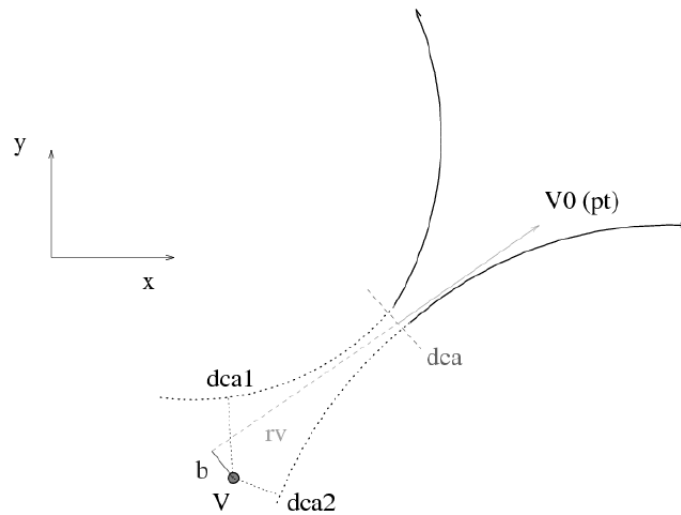


Figure 6.4: The topology of  $V0$  decay.

- Distance of closest approach of the bachelor  $\pi(K)$  to the primary vertex (dca Bach. to Pvx).
- $\Xi(\Omega)$  baryon decay length.
- $\Lambda$  daughter decay length.
- Distance of closest approach between  $\Xi(\Omega)$  daughters,  $\Lambda$  and the bachelor  $\pi(K)$ .

- Distance of closest approach between  $\Lambda$  daughters, the  $p^+$  and the  $\Lambda$  daughter  $\pi^-$ .

All the above parameters were varied to get best significance of the  $\Xi$  and  $\Omega$  signal. The significance ( $S_g$ ) is defined as  $S_g = \frac{S}{\sqrt{S+B}}$ , where  $S$  and  $B$  are the signal and background, respectively. Table 6.2 lists all the optimized cuts for  $\Xi$  (a) and  $\Omega$  (b) in Au+Au collisions at  $\sqrt{s_{NN}} = 200$  GeV.

## 6.2.2 Combinatorial background estimation

Rotational background technique was used to estimate the combinatorial background [3]. The whole idea was to rotate one decay daughter by  $180^\circ$  in azimuthal direction. This breaks the correlation between the two decay daughters and therefore if we reconstruct the invariant mass, we will not get any signal for parent particles but reproduce the shape of the combinatorial background. In this analysis, momentum vector of  $\Lambda$  was rotated by  $180^\circ$  in azimuthal direction to reproduce the combinatorial background for  $\Xi$  and  $\Omega$ . As the number of tracks used to reconstruct signal and combinatorial background are same, therefore we do not need to normalise the combinatorial background distribution. Figure 6.5 and 6.6 show reconstructed signal of  $\Xi$  and  $\Omega$ , respectively, for 0-30% and 30-80% centrality in Au+Au collisions at  $\sqrt{s_{NN}} = 200$  GeV integrated over  $0 < p_T < 10$  GeV/c. The upper panel of Fig. 6.5 and 6.6 show signal before combinatorial background subtraction. The background distribution from rotational technique, which nicely explain the combinatorial background, are shown by red marker. The signals of  $\Xi$  and  $\Omega$  after subtraction of combinatorial background are shown in bottom panel of Fig. 6.5 and 6.6, respectively. The raw yields are then extracted from the invariant mass distribution by counting the number of entries in the mass peak after background subtraction. The amount of combinatorial background is higher in 0-30% central event than that of 30-80% peripheral events. This is because of high multiplicity in central events than that of peripheral events. The residual bump at lower invariant mass, left of the peak in Fig. 6.5 can be understood as fake  $\Xi$  candidates being reconstructed as  $\Xi_{fake}(\pi_\Lambda, \Lambda_{fake}(\pi_{random}, p_\Lambda))$ , where  $\pi_\Lambda$  and  $p_\Lambda$  are the daughters of a real  $\Lambda$  and  $\pi_{random}$  from a random  $\pi$ . The real correlation between

<b>(a) <math>\Xi</math> selection cuts</b>	
dca $\Xi$ to Pvx	$\leq 0.55$ cm
dca bachelor ( $\pi$ ) to Pvx	$\geq 0.6$ cm
dca $\Lambda$ to Pvx	$\geq 0.1$ cm
dca $\Lambda$ to bachelor	$\leq 0.7$ cm
dca $p^+$ to $\pi^-$ daughter	$\leq 0.8$ cm
decay length (dl) $\Xi$	$\geq 3.0$ cm
decay length (dl) $\Lambda$	$\geq$ dl $\Xi$
nHits bachelor $\pi$	$\geq 15$
$n\sigma$ dE/dx of bachelor $\pi$	$\leq 2.0$
$m^2$ for bachelor $\pi$	$0.0 \leq m^2 \leq 0.2$ (GeV/ $c^2$ )
<b>(b) <math>\Omega</math> selection cuts</b>	
dca $\Omega$ to Pvx ( $dca_\Omega$ )	$\leq 0.4$ cm
dca bachelor ( $\pi$ ) to Pvx	$\geq 0.6$ cm
dca $\Lambda$ to Pvx	$\geq 0.5 \times \sqrt{dca_\Omega} + 0.2$ cm
dca $\Lambda$ to bachelor	$\leq 0.5$ cm
dca $p^+$ to $\pi^-$ daughter	$\leq 0.8$ cm
decay length (dl) $\Omega$	$\geq 2.0$ cm
decay length (dl) $\Lambda$	$\geq$ dl $\Omega$
nHits bachelor	$\geq 15$
$n\sigma$ dE/dx of bachelor $K$	$\leq 2.0$
$m^2$ for bachelor $K$	$0.16 \leq m^2 \leq 0.36$ (GeV/ $c^2$ )

Table 6.2: Track selection cuts for  $\Xi$  and  $\Omega$  reconstruction.

$\pi_\Lambda$  and  $p_\Lambda$  remains in the  $\Xi_{fake}$  reconstruction resulting in the observed bump in the  $\Xi$  invariant mass distribution. But this residual correlation does not affect the signal peak [3].

For  $\phi$  meson, mixed event technique were used to estimate combinatorial background. The details of mixed event technique has already been discussed in chapter

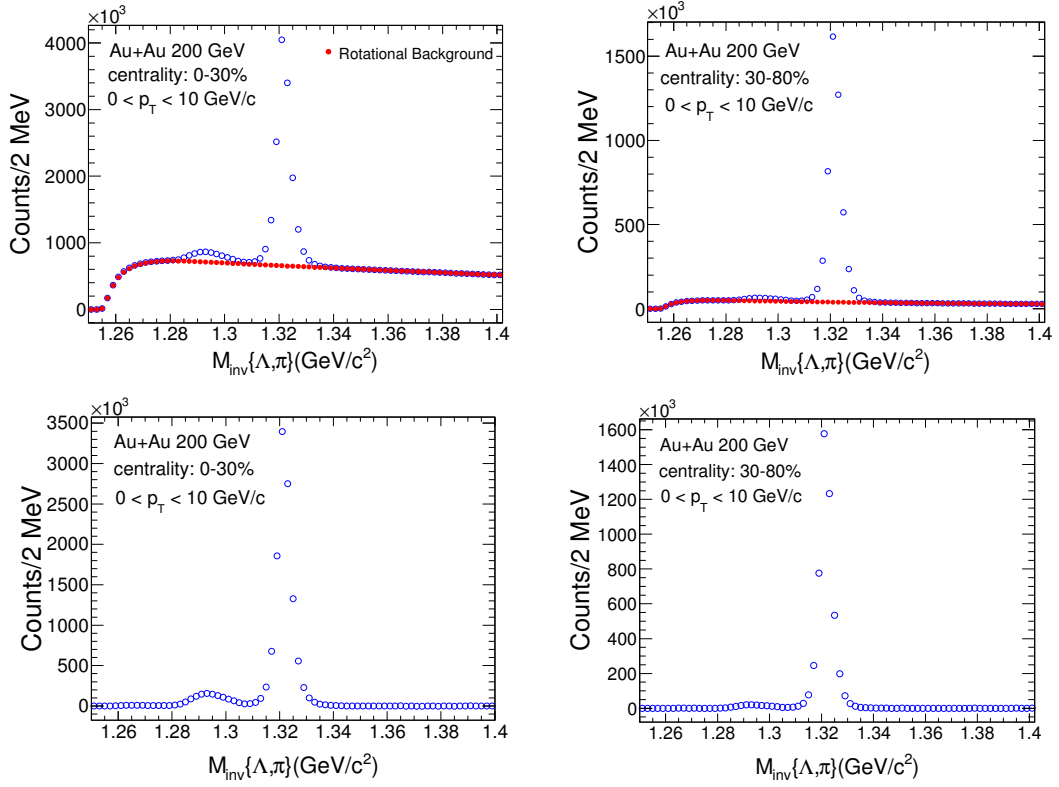


Figure 6.5: (Color online) Reconstructed signal of  $\Xi$  from  $\Lambda$  and  $\pi$  decay channel for 0-30% and 30-80% centrality in Au+Au collisions at  $\sqrt{s_{NN}} = 200$  GeV integrated over  $0 < p_T < 10$  GeV/c. In the upper panel red circles show rotational background. Background subtracted signal are shown in the bottom panel. Results obtained by combining both year 2010 and 2011 data sets.

4. Figure 6.7 shows invariant mass distribution of  $K^+$  and  $K^-$  pair with  $\phi$ -meson signal for 0-30% and 30-80% centrality in Au+Au collisions at  $\sqrt{s_{NN}} = 200$  GeV integrated over  $0 < p_T < 10$  GeV/c. Upper panel and bottom panel shows before and after combinatorial background subtraction, respectively.

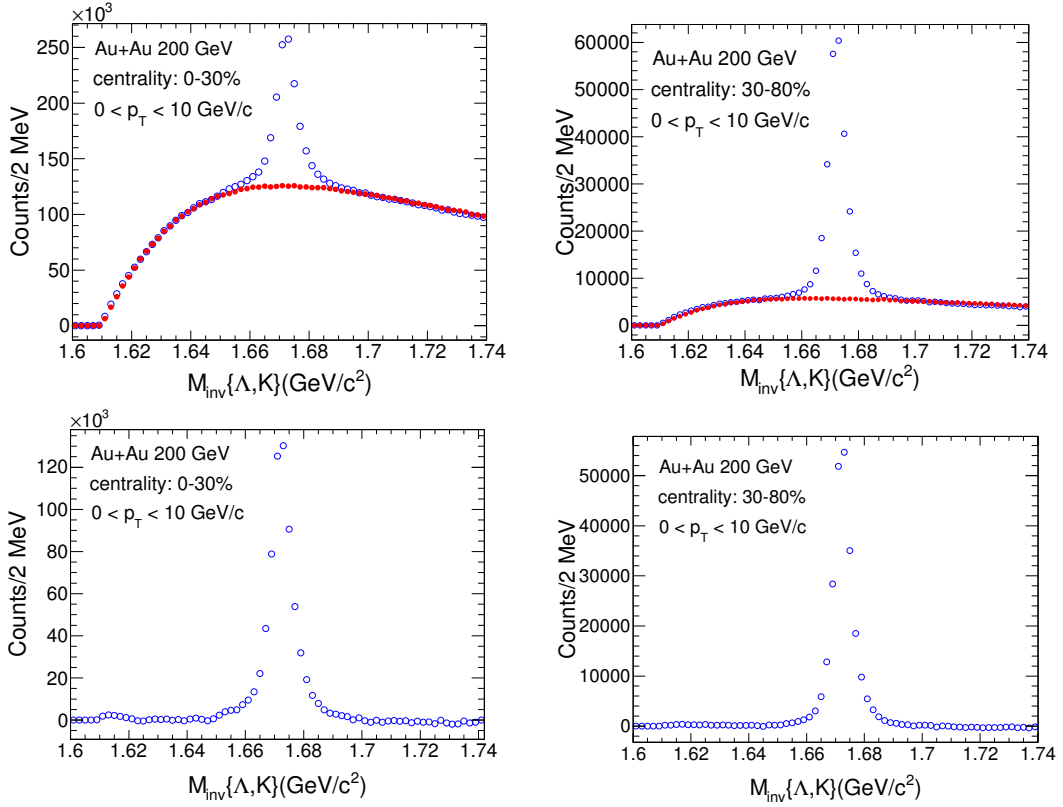


Figure 6.6: (Color online) Reconstructed signal of  $\Omega$  from  $\Lambda$  and  $K$  decay channel for 0-30% and 30-80% centrality in Au+Au collisions at  $\sqrt{s_{NN}} = 200$  GeV integrated over  $0 < p_T < 10$  GeV/c. In the upper panel red circles show rotational background. Background subtracted signal are shown in the bottom panel. Results obtained by combining both year 2010 and 2011 data sets.

### 6.2.3 Elliptic flow measurement methods

The  $\eta$ -sub event plane method [4] was used to calculate elliptic flow ( $v_2$ ) of multi-strange hadrons. As discussed in chapter 3, it helps to reduce the contribution from non-flow effects (mostly due to short-range correlations). An  $\eta$  gap of  $|\eta| < 0.05$  between positive and negative pseudo-rapidity sub-events has been used for event plane reconstruction, similar to that carried out for the BES energies. The TPC

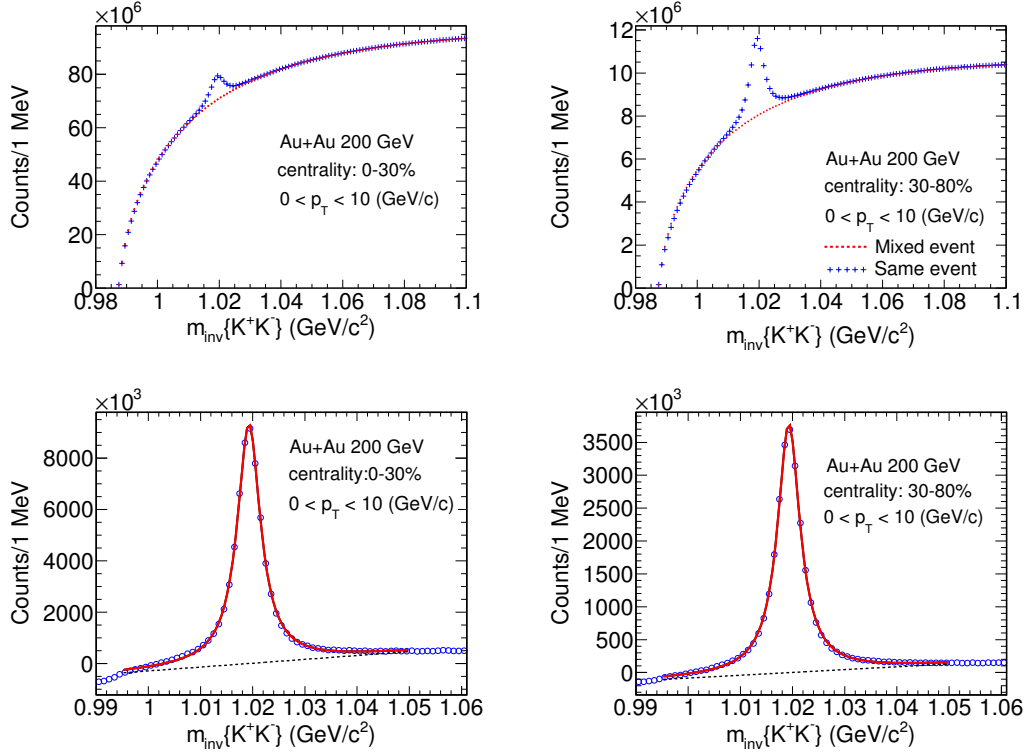


Figure 6.7: (Color online) Reconstructed signal of  $\phi$  meson from  $K^+$  and  $K^-$  decay channel for 0-30% and 30-80% centrality in Au+Au collisions at  $\sqrt{s_{NN}} = 200$  GeV integrated over  $0 < p_T < 10$  GeV/c. In the upper panel red circles show mixed event background. Background subtracted signal are shown in the bottom panel. Results obtained by combining both year 2010 and 2011 data sets.

event plane angle distributions for both eta sub-event are shown in Fig. 6.8. These are corrected by re-centre and shift methods [4].

The  $v_2$  vs.  $m_{inv}$  method [5] was used to extract the  $v_2$  of  $\phi$ ,  $\Xi$  and  $\Omega$ . As discussed in chapter 3, the first step of this method is to calculate the  $v_2^{S+B} = \langle \cos[2(\phi - \Psi_2)] \rangle$  as a function of invariant mass  $m_{inv}$ . Then the  $v_2^{S+B}(m_{inv})$  can be decompose as

$$v_2^{S+B}(m_{inv}) = v_2^S \frac{S}{S+B}(m_{inv}) + v_2^B(m_{inv}) \frac{B}{S+B}(m_{inv}), \quad (6.1)$$

where  $S$  is the signal yield,  $B$  is background yield,  $v_2^S$ ,  $v_2^B$  and  $v_2^{S+B}$  are the  $v_2$  for signal, background and total particles, respectively. For  $\Xi$ , we need to add an additional term in the Eq. 6.1 due the observed bump in invariant mass distribution. The modified equation for  $\Xi$  as follows:

$$v_2^{S+S_b+B}(m_{inv}) = v_2^S \frac{S}{S+S_b+B}(m_{inv}) + v_2^B(m_{inv}) \frac{B}{S+S_b+B}(m_{inv}) + v_2^{bump} \frac{S_b}{S+S_b+B}(m_{inv}), \quad (6.2)$$

where  $S_b$  is the yield of fake  $\Xi$  in the bump region and  $v_2^{bump}$  is the contribution of  $v_2$  due to fake  $\Xi$ . The  $v_2$  vs invariant mass plots for different  $p_T$  bins in minimum bias Au+Au collisions at  $\sqrt{s_{NN}} = 200$  GeV are shown in Fig. 6.9, Fig. 6.10 and Fig. 6.11 for  $\Xi$ ,  $\Omega$  and  $\phi$ , respectively.

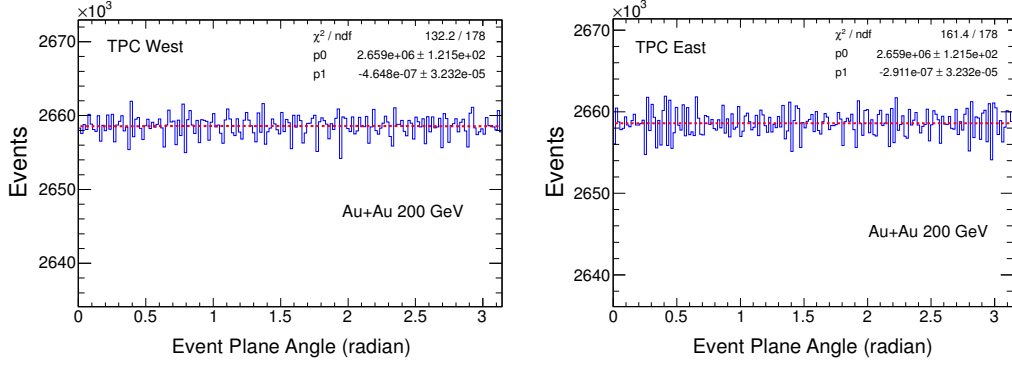


Figure 6.8: (Color online) The TPC event plane angle distribution for TPC west and TPC East eta sub-events in Au+Au collisions at  $\sqrt{s_{NN}} = 200$  GeV. Red lines are the fit function of the form  $p_0(1 + 2 \times p_1 \times \cos(2 * x))$ .

## 6.2.4 Event plane resolution correction

The event plane resolution was calculated for nine centrality bins (0–5%, 5–10%, 10–20%, 20–30%, 30–40%, 40–50%, 50–60%, 60–70% and 70–80%). After that observed  $v_2$  was corrected by event-by-event resolution correction method [6]. The values of event plane resolution for different centralities has been shown in chapter 3.

## 6.2.5 Systematic error study

The systematic uncertainties were calculated by varying the tracks cuts and using different methods to determine particle yields. For  $\Xi$  and  $\Omega$ , 23 different combinations of cuts and 13 different cuts for  $\phi$  meson were used. The point-by-point systematic uncertainties on  $v_2(p_T)$  were evaluated for all combinations by calculating the root-mean-squared value for each data point.

### 6.2.5.1 Cut details for $\Xi$ and $\Omega$ :

Following cuts were varied to estimate the systematic error on  $v_2$  of  $\Xi$  and  $\Omega$ .

- **TPC Nhits fit points :**  $\geq 15$  (Default cut),  $\geq 20$  and  $\geq 25$ .
  - **DCA of tracks:**  $\leq 3$  cm (Default cut),  $\leq 2$  cm,  $\leq 1$  cm.
  - **Both Nhits and DCA:** Nhits  $\geq 20$  & DCA  $\leq 2$  cm; Nhits  $\geq 20$  & DCA  $\leq 1$  cm; Nhits  $\geq 25$  & DCA  $\leq 2$  cm; Nhits  $\geq 25$  & DCA  $\leq 1$  cm.
  - **Particle Identification:** By varying momentum dependent mass cut using TOF information.
  - **Background subtraction:** Rotational Background (Default) and Polynomial fit function.
  - **Topology cuts:** Topology cuts were varied by changing 5% from its default value.
- In total 10 different cuts were used to estimate systematic.

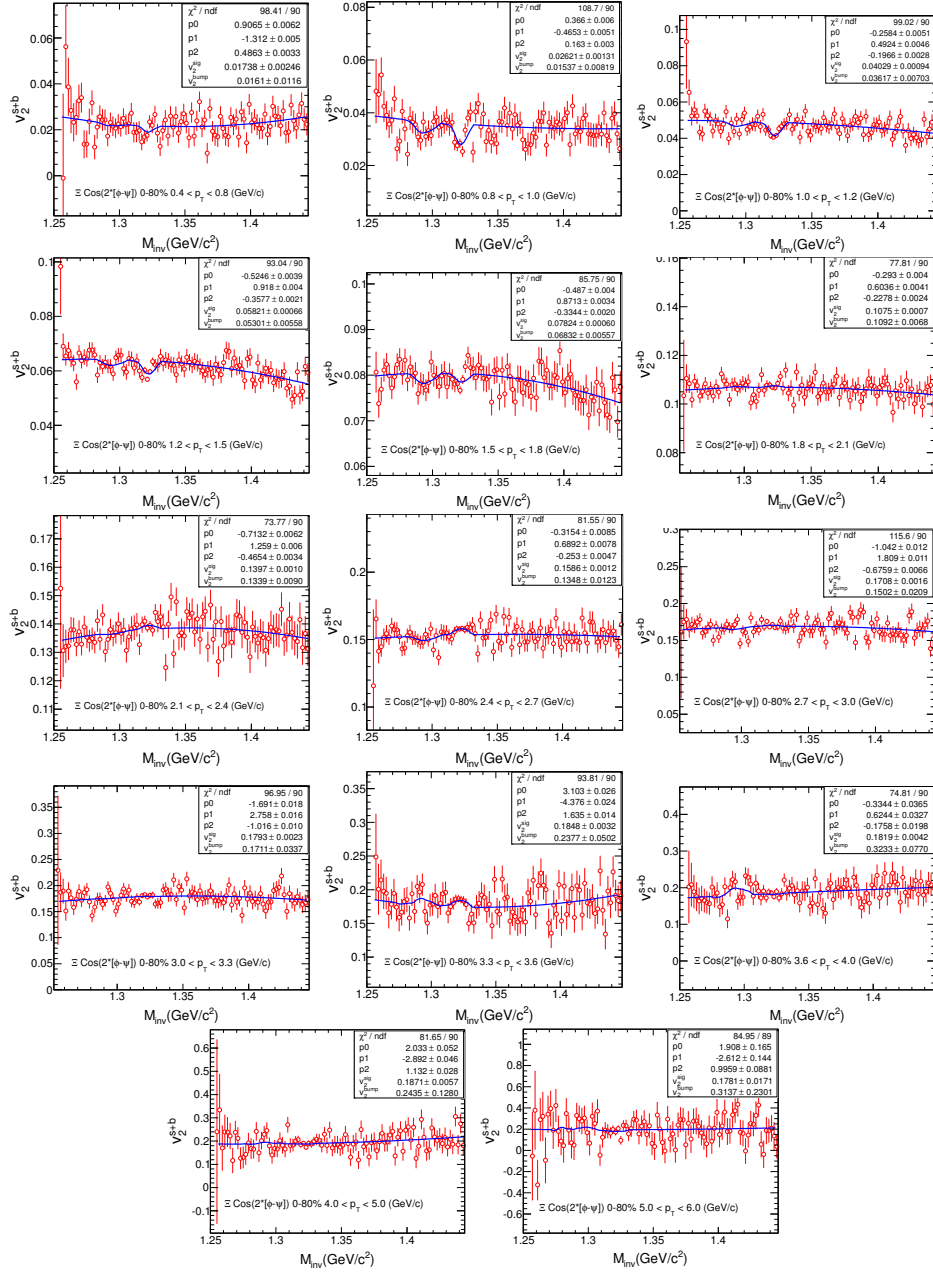


Figure 6.9: (Color online)  $v_2^{S+B}$  as function of invariant mass for  $\Xi$  in minimum bias Au+Au collisions at  $\sqrt{s_{NN}} = 200$  GeV for various  $p_T$  bins. The distributions are fitted with function shown in Eq. 6.2.

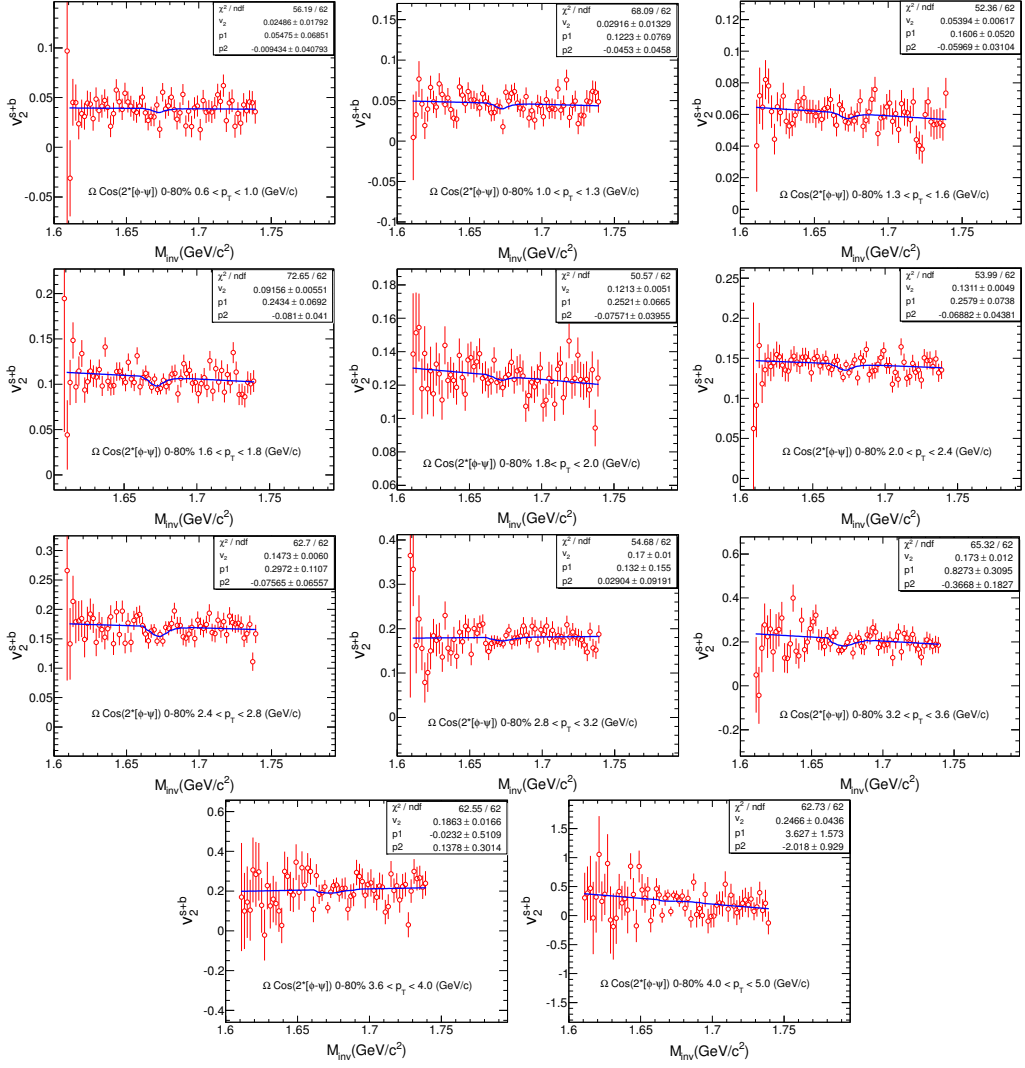


Figure 6.10: (Color online)  $v_2^{S+B}$  as function of invariant mass for  $\Omega$  in minimum bias Au+Au collisions at  $\sqrt{s_{NN}} = 200$  GeV for various  $p_T$  bins. The distributions are fitted with function shown in Eq. 6.1.

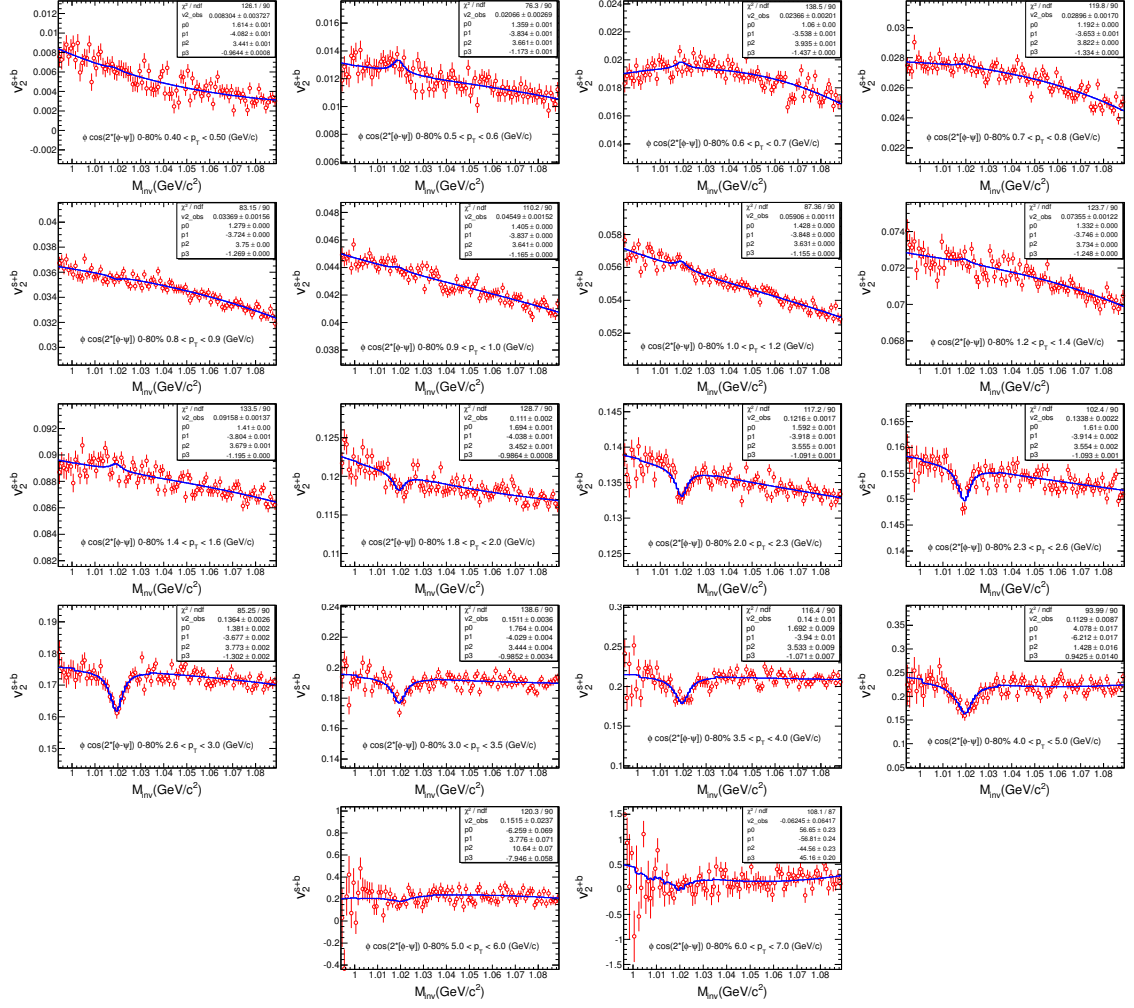


Figure 6.11: (Color online)  $v_2^{S+B}$  as function of invariant mass for  $\phi$  meson in minimum bias Au+Au collisions at  $\sqrt{s_{NN}} = 200$  GeV for various  $p_T$  bins. The distributions are fitted with function shown in Eq. 6.1.

### 6.2.5.2 Cut details for $\phi$ meson:

- TPC Nhits fit points :  $\geq 15$  (Default cut),  $\geq 20$  and  $\geq 25$ .
- DCA of tracks:  $\leq 3$  cm (Default cut),  $\leq 2$  cm,  $\leq 1$  cm.
- Both Nhits and DCA: Nhits  $\geq 20$  & DCA  $\leq 2$  cm; Nhits  $\geq 20$  & DCA  $\leq 1$  cm;

Nhits  $\geq 25$  & DCA  $\leq 2$  cm; Nhits  $\geq 25$  & DCA  $\leq 1$  cm.

- **Particle Identification:** By varying momentum dependent mass cut using TOF information.
- **Background subtraction:** First order polynomial (Default) and second order polynomial function to subtract residual background after combinatorial background subtraction by mixed event technique.

The systematic errors on  $\phi$ ,  $\Xi$  and  $\Omega$  from variation of the background and cut criteria are summarized in Table 6.3, 6.4 and 6.5, respectively.

$\phi$ meson						
	$p_T < 1.5$ GeV/c		$1.5$ GeV/c $< p_T < 4.0$ GeV/c		$p_T > 4.0$ GeV/c	
Centrality	Background	Cut criteria	Background	Cut criteria	Background	Cut criteria
0-30%	2%	5%	1%	2%	1%	8%
30-80%	1%	2%	1%	2%	1%	4%
0-80%	2%	4%	1%	2%	1%	5%

Table 6.3: Summary of systematic error on  $\phi$ -meson  $v_2$  from different sources in Au+Au collisions at  $\sqrt{s_{NN}} = 200$  GeV.

### 6.2.6 Efficiency correction

The effect of the track reconstruction efficiency has also been investigated on measured  $v_2$  in wide centrality bins. The occupancy in the TPC increases from peripheral to central collisions, causing a lower track reconstruction efficiency in central events compared to peripheral events. This may bias measured  $v_2$  towards centrality with higher track reconstruction efficiency. A model based study about the efficiency effect on measured  $v_2$  is discussed in chapter 5. This effect will be larger for particles with three daughters, such as  $\Xi$  and  $\Omega$ . This effect, which is  $\sim 5\%$  to  $8\%$  for  $\Xi$  and  $\Omega$  in 0-80% centrality, has been corrected by the method discussed in chapter 5. A

$\Xi$ baryon						
	$p_T < 1.5 \text{ GeV}/c$		$1.5 \text{ GeV}/c < p_T < 4.0 \text{ GeV}/c$		$p_T > 4.0 \text{ GeV}/c$	
Centrality	Background	Cut criteria	Background	Cut criteria	Background	Cut criteria
0-30%	2%	8%	1%	2%	1%	8%
30-80%	2%	2%	1%	2%	1%	2%
0-80%	2%	4%	1%	2%	1%	5%

Table 6.4: Summary of systematic error on  $\Xi v_2$  from different sources in Au+Au collisions at  $\sqrt{s_{NN}} = 200 \text{ GeV}$ .

$\Omega$ baryon						
	$p_T < 1.5 \text{ GeV}/c$		$1.5 \text{ GeV}/c < p_T < 4.0 \text{ GeV}/c$		$p_T > 4.0 \text{ GeV}/c$	
Centrality	Background	Cut criteria	Background	Cut criteria	Background	Cut criteria
0-30%	8%	14%	2%	5%	2%	10%
30-80%	3%	5%	1%	2%	1%	4%
0-80%	5%	10%	1%	5%	1%	6%

Table 6.5: Summary of systematic error on  $\Omega v_2$  from different sources in Au+Au collisions at  $\sqrt{s_{NN}} = 200 \text{ GeV}$ .

comparison of  $\Xi$  and  $\Omega v_2$  before and after efficiency correction is shown in Fig. 6.12 for 0-80% centrality. After efficiency correction,  $v_2$  of  $\Xi$  and  $\Omega$  becomes lower. This is expected, because track reconstruction efficiency is lower for more central collisions than that of peripheral collisions where as  $v_2$  is also lower in most central collisions. In efficiency correction method, we put more weight (inverse of efficiency) on central events than peripheral events resulting lower  $v_2$  for 0-80% centrality. In case of  $\phi$ , change in  $v_2$  due to reconstruction efficiency effect is negligible ( $\sim 2\%$ ). All  $v_2(p_T)$  data points presented in this chapter are efficiency corrected.

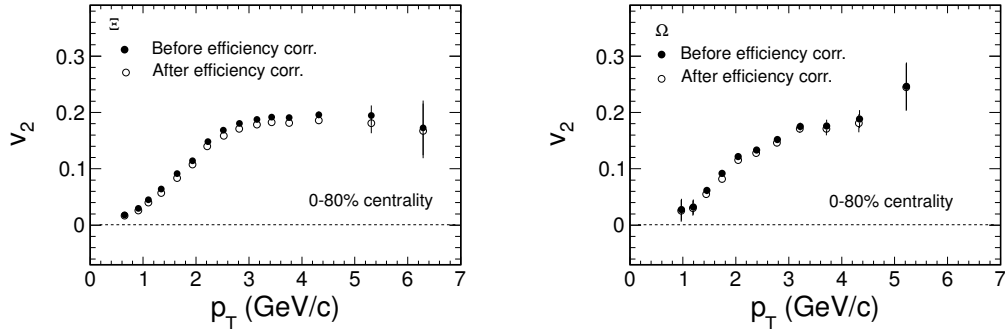


Figure 6.12: A comparison of  $\Xi$  and  $\Omega$   $v_2$  before and after efficiency correction for 0-80% centrality in Au+Au collisions at  $\sqrt{s_{NN}} = 200$  GeV. Error bars are statistical only.

### 6.2.7 Event bias correction

An additional correction has been done for obtaining the multi-strange hadrons ( $\phi$ ,  $\Xi$  and  $\Omega$ )  $v_2$ . Figure 6.13 (left panel) shows the particle yield as function of uncorrected reference multiplicity in Au+Au collisions at  $\sqrt{s_{NN}} = 200$  GeV. Since we can not calculate actual number of produced unstable particles ( $\phi$ ,  $\Xi$  and  $\Omega$ ) on an event by event basis, therefore those particle yields were calculated in a small reference multiplicity window. The bin size of reference multiplicity window was taken as 5. In the right panel of Fig. 6.13, participants eccentricity ( $\varepsilon_{part}\{2\}$ ) as a function of reference multiplicity calculated from Glauber model simulation is shown. Since  $v_2$  is driven by the anisotropy of the initial spatial geometry, therefore one can see from Fig. 6.13 that the event bias is naturally introduced when one measures the  $v_2$  in a wide centrality bin especially for the rare produced particles. As the measured  $v_2$  is particle-yield wise averaged, the average event shape depends on the particles type. The average initial participant eccentricity reflects the multi-strange hadrons production are more bias to the central events than the light and other strange hadrons. Hence, the average eccentricity for multi-strange hadrons in wide centrality is smaller than the standard eccentricity determined by the particle yield of all charged hadrons. One should take

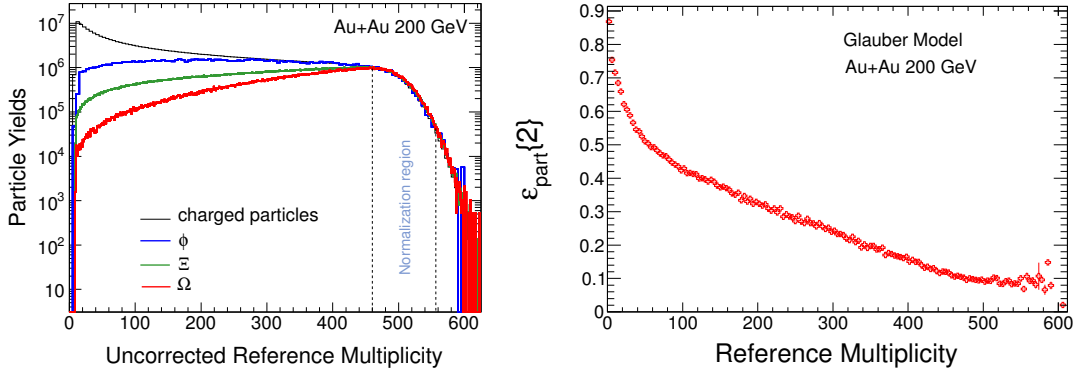


Figure 6.13: (Color online) Left panel: Particle yield as a function of uncorrected reference multiplicity in Au+Au collisions at  $\sqrt{s_{NN}} = 200$  GeV. Right panel: Participants eccentricity calculated from Glauber model simulation as function of reference multiplicity in Au+Au collisions at  $\sqrt{s_{NN}} = 200$  GeV.

this effect into consideration if any conclusion on the number of constituent quark scaling is to be addressed. This bias could be corrected by normalizing the measured  $v_2$  by the ratio of standard eccentricity to the eccentricity determined by the yield of particle of interest. The event bias correction factors for  $\phi$ ,  $\Xi$  and  $\Omega$  are shown in Table 6.6.

Correction factors	0-30%	30-80%	0-80%
$\varepsilon/\varepsilon_{\Omega}$	1.068	1.067	1.177
$\varepsilon/\varepsilon_{\Xi}$	1.019	1.054	1.091
$\varepsilon/\varepsilon_{\phi}$	1.002	1.053	1.028

Table 6.6: Event bias correction factors for different centrality in Au+Au collision at  $\sqrt{s_{NN}} = 200$  GeV.

The light and strange hadrons are not sensitive to the event bias correction (< 3%), due to their copious production in nuclear collisions at RHIC. For the later discussion on the NCQ scaling, the event bias correction is applied to the  $v_2$  of multi-

strange hadrons.

## 6.3 Results & Discussion

### 6.3.1 Comparison with previous published results

The STAR collaboration already published results on multi-strange hadron  $v_2$  for a low event statistics data set taken in the year 2004 [7]. Hence these measurements are not sufficient to make strong physics conclusion due to large statistical errors. The main goal of the present analysis is to do high precision measurements and study the centrality dependence of multi-strange hadron  $v_2$ . But at the beginning, it worth to compare new results with the corresponding published results. Figure 6.14 shows the comparison of  $\phi$ ,  $\Xi$  and  $\Omega$   $v_2$  between new analysis (using combined data sets of year 2010 and 2011, labelled as Run 10+11) and STAR published data (using data sets of year 2004, labeled as Run 4) for 0-80% centrality. Both the results are agreeing within the respective statistical uncertainties. It can be noted that using high statistics data statistical errors are significantly reduced and also the measurements of  $v_2(p_T)$  are extended up-to low and high  $p_T$ .

### 6.3.2 Signature of partonic collectivity

Figure 6.15 shows the  $v_2$  as a function of  $p_T$  for  $\pi$ ,  $p$ ,  $\phi$  and  $\Omega$  for 0-80% centrality in Au+Au collisions at  $\sqrt{s_{NN}} = 200$  GeV. Here  $\phi$  and  $\Omega$   $v_2$  are corrected by event bias correction. Panel (a) of Fig. 6.15 shows comparison between  $v_2$  of  $\pi$  and  $p$ , consisting of  $u$  and  $d$  light constituent quarks, and panel (b) shows comparison between  $v_2$  of  $\phi$  and  $\Omega$  containing heavy strange (s) constituent quarks. The  $v_2$  of  $\phi$  and  $\Omega$  follows mass ordering between them at low  $p_T$ , and a baryon-meson separation at intermediate  $p_T$ . It is clear from the Fig. 6.15 that the  $v_2(p_T)$  of pure strange quark carrying hadrons ( $\phi$  and  $\Omega$ ) is similar as that of  $\pi$  and  $p$  which is made of  $u$  and  $d$  light quarks. However the  $\phi$  and  $\Omega$  do not participates strongly in the hadronic interactions unlike  $\pi$  and

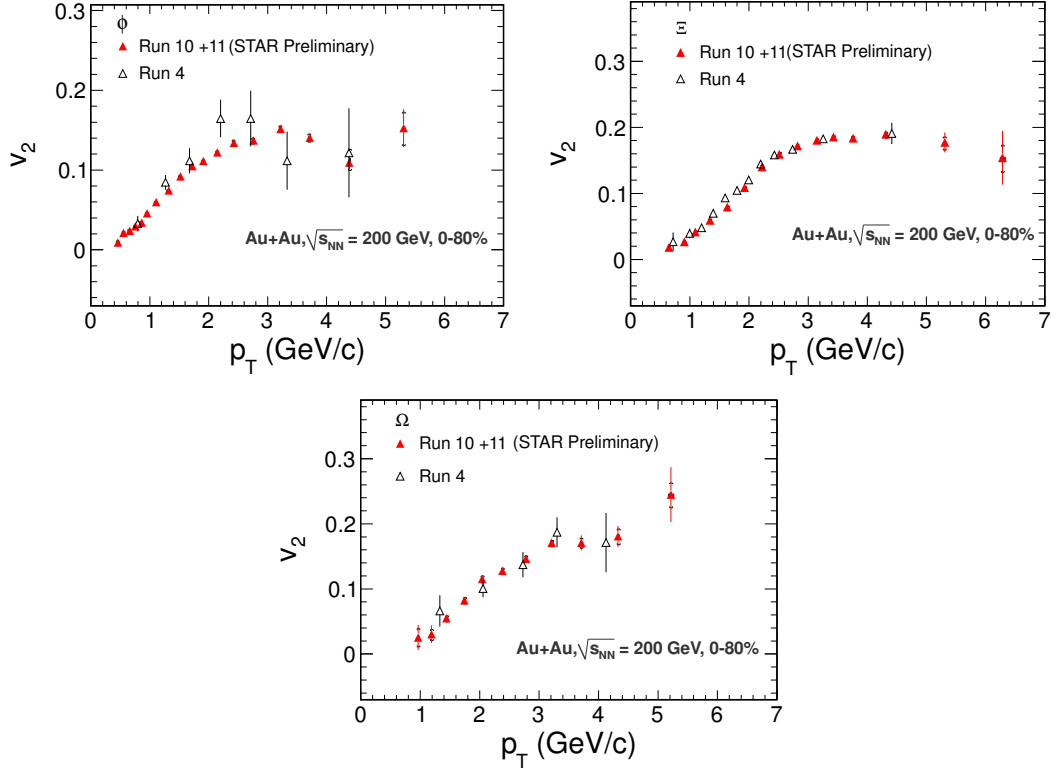


Figure 6.14: (Color online) A comparison of  $\phi$ ,  $\Xi$  and  $\Omega$   $v_2$  between new analysis (using combined data sets of year 2010 and 2011, labelled as Run 10+11) and STAR published data (using data sets of year 2004, labeled as Run 4) in Au+Au collision at  $\sqrt{s_{NN}} = 200$  GeV for 0-80% centrality. Error bars are statistical uncertainty. Systematic errors are shown by cap symbol on the new analysis.

$p$ . This tells that major part of collectivity is developed during the partonic phase in Au+Au collisions at  $\sqrt{s_{NN}} = 200$  GeV [8].

### 6.3.3 Centrality dependence of multi-strange hadron $v_2$

Figure 6.16 present the results of the elliptic flow parameter  $v_2(p_T)$  for multi-strange hadrons (a)  $\Xi^- + \bar{\Xi}^+$  (b)  $\Omega^- + \bar{\Omega}^+$  and (c)  $\phi$  in Au+Au collision at  $\sqrt{s_{NN}} = 200$

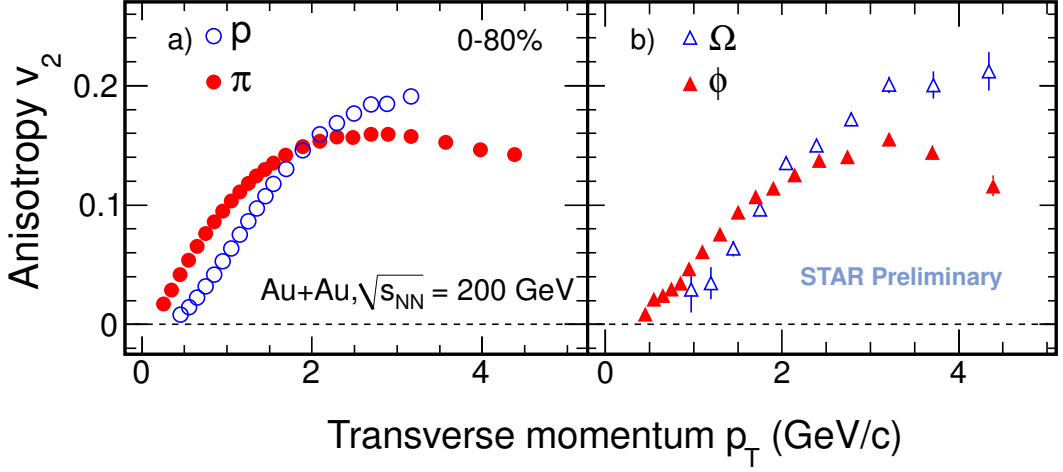


Figure 6.15: (Color online) The  $v_2$  as function of  $p_T$  for  $\pi$ ,  $p$  (panel a) and  $\phi$ ,  $\Omega$  (panel b) in Au+Au minimum-bias collisions at  $\sqrt{s_{NN}} = 200$  GeV. Only statistical errors are shown.  $\phi$  and  $\Omega$   $v_2$  are event bias corrected.

GeV for centrality 0-30% and 30-80%. Systematic error, shown by open band, based on the background evaluation and variation of the track selection criteria. Event bias correction factor has not been applied in these results shown in Fig 6.16. A clear centrality dependence of multi-strange hadrons  $v_2(p_T)$  is observed as other identified light and strange hadrons measured by STAR experiment [7]. The larger  $v_2$  values are observed in the peripheral collisions because the final momentum anisotropy is driven by the initial spatial anisotropy (higher eccentricity). This effect of initial spatial anisotropy can be removed by the dividing  $v_2$  by eccentricity of the initial spatial geometry for a given collision centrality. The  $v_2$  of multi-strange hadrons scaled by participant eccentricity  $\varepsilon_{part}\{2\}$  as a function of  $p_T$  are shown in Fig. 6.17. The participant eccentricity  $\varepsilon_{part}\{2\}$  was calculated from Glauber model simulation. After removing initial spatial anisotropy, elliptic flow becomes higher in 0-30% centrality than that of 30-80% for all the multi-strange hadrons. This is consistent with the

picture that collective interactions are stronger in collisions with larger numbers of participants. Similar results was observed when we use color glass condensate as a initial condition to calculate eccentricity.

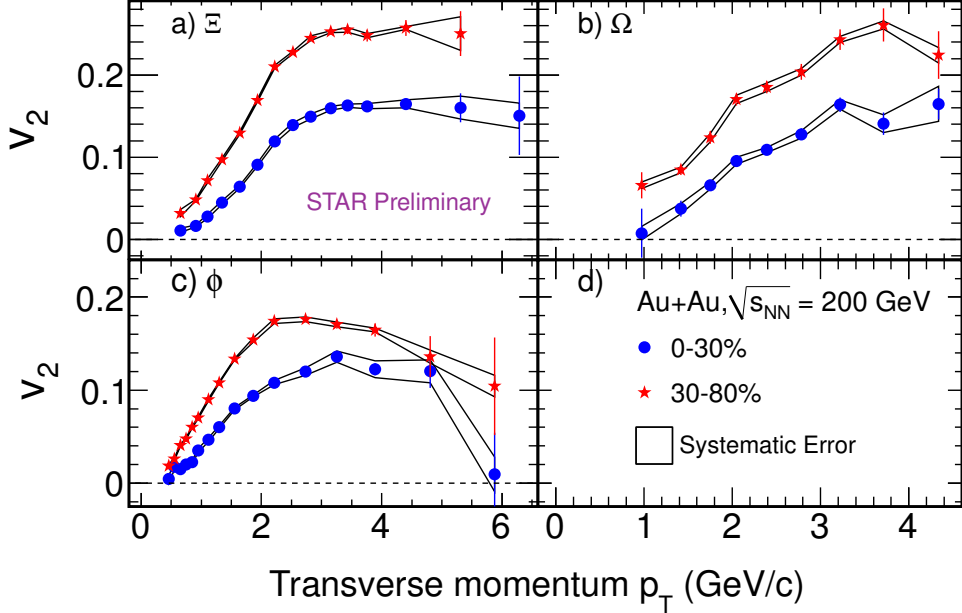


Figure 6.16: (Color online) The  $v_2$  as a function of  $p_T$  for multi-strange hadrons (a)  $\Xi^- + \Xi^+$  (b)  $\Omega^- + \Omega^+$  and (c)  $\phi$  in Au+Au collision at  $\sqrt{s_{NN}} = 200$  GeV for centrality 0-30% and 30-80%. Open bands are the systematic uncertainty and vertical lines are the statistical uncertainty.

### 6.3.4 Centrality dependence of number-of-constituent quark scaling

The observed number-of-constituents quark (NCQ) scaling of identified hadrons in experimental data can be well described by parton recombination or coalescence model [9, 10, 11]. Such scaling indicates that collective elliptic flow has been developed at the partonic phase. It has been already found by the previous measurements that

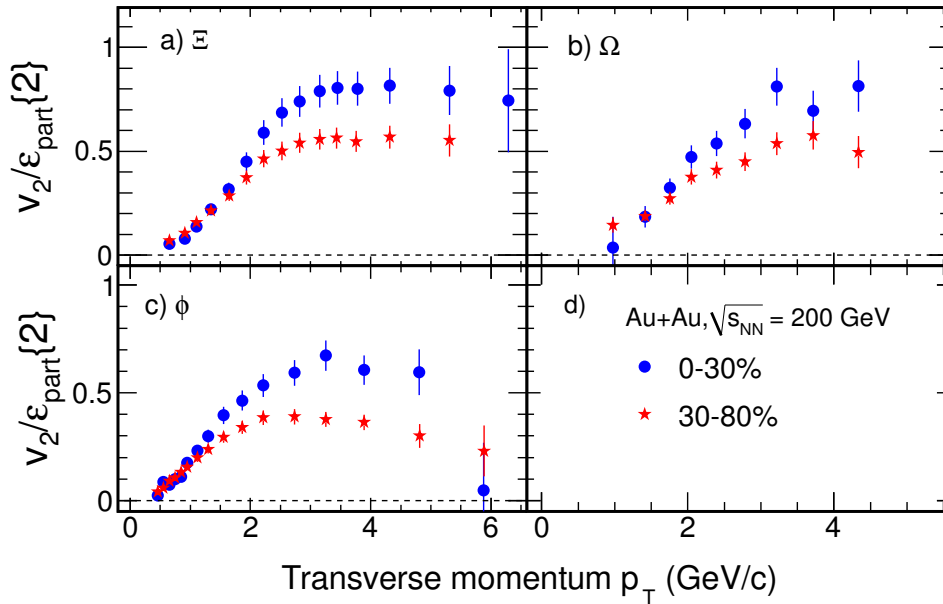


Figure 6.17: (Color online) The  $v_2$  scaled by participant eccentricity  $\varepsilon_{part}\{2\}$  as a function of  $p_T$  for multi-strange hadrons (a)  $\Xi^- + \Xi^+$  (b)  $\Omega^- + \Omega^+$  and (c)  $\phi$  in Au+Au collision at  $\sqrt{s_{NN}} = 200$  GeV for centrality 0-30% and 30-80%. The participant eccentricity  $\varepsilon_{part}\{2\}$  was calculated from Glauber model simulation. Vertical lines are the statistical uncertainty only.

$\pi$ ,  $K$ ,  $p$ ,  $K_S^0$ ,  $\Lambda$ ,  $\Xi$  and  $\phi$  follows NCQ scaling fairly well at top RHIC energy [11]. The large statistics data collected by STAR detectors in the years 2010 and 2011 allows us to measure elliptic flow of multi-strange hadrons with higher precision, especially for the  $\phi$  meson, consisting of one strange and one anti-strange constituent quarks, and  $\Omega$  baryon that is made of pure strange or anti-strange constituent quarks. Because of their large mass and small hadronic interaction cross-section, the multi-strange hadrons are expected to be less sensitive to the late stage hadronic re-scattering. In addition, a fit of the  $m_T$  spectra to a hydrodynamically inspired Blast Wave model suggests that the multi-strange hadrons freeze-out at a higher temperature, which is closer to the chemical freeze-out temperature, and with a smaller radial flow than

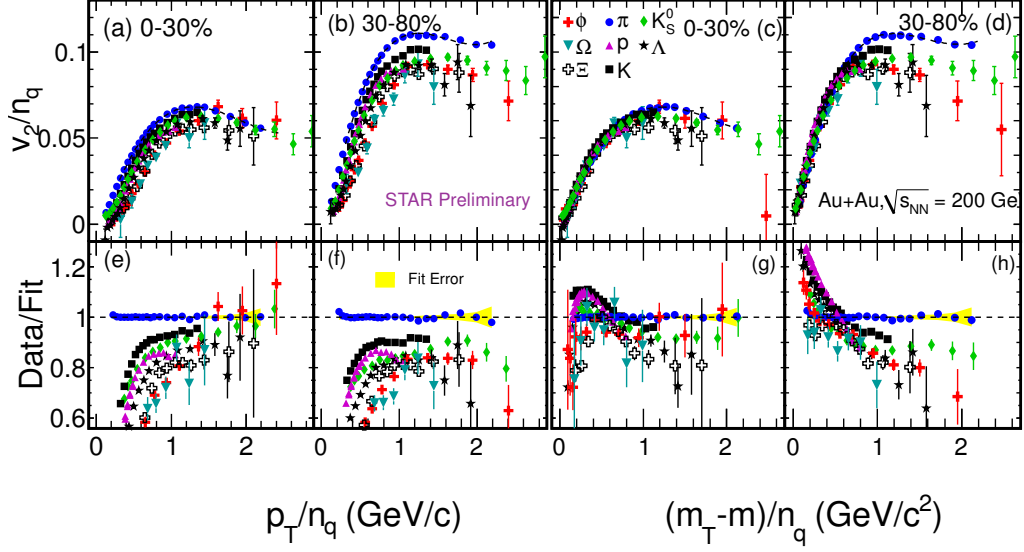


Figure 6.18: (Color online) The  $v_2$  scaled by number of constituent quarks ( $n_q$ ) as a function of  $p_T/n_q$  and  $(m_T - m)/n_q$  for identified hadrons in Au+Au collisions at  $\sqrt{s_{NN}} = 200$  GeV. The ratios with fit to  $\pi$   $v_2$  to the other hadrons  $v_2$  are shown in corresponding lower panels. Statistical and systematic error are added in quadrature and propagated for the ratios for  $\phi$ ,  $\Xi$  and  $\Omega$  but for other particles only statistical errors are shown.

the other lighter hadrons [12, 13, 14, 15, 16]. Therefore elliptic flow of multi-strange hadrons are good probes for the partonic phase of the system formed in heavy-ion collisions.

In the Fig. 6.18 the  $v_2$  scaled by number-of-constituent quarks as a function of  $p_T/n_q$  and  $(m_T - m)/n_q$  for identified hadrons in Au+Au collisions at  $\sqrt{s_{NN}} = 200$  GeV for 0-30% and 30-80% centrality has been shown. To quantify deviations from NCQ scaling, the ratios with fit to  $\pi$   $v_2(p_T)$  to the other hadrons  $v_2$  are shown in corresponding lower panels. For 0-30% centrality scaling holds within the statistical errors at the intermediate  $p_T$ . We observe the scaling breaks down for 30-80% central-

ity. The  $\phi$ ,  $K_S^0$ ,  $\Lambda$ ,  $\Xi$  and  $\Omega$  deviate from the fit line by  $17\pm 1.2\%$ ,  $13\pm 0.4\%$ ,  $16\pm 1.6\%$ ,  $19\pm 1.6\%$  and  $27\pm 9.0\%$  respectively at 30-80% centrality for the range  $(m_T - m)/n_q > 0.8$  GeV/ $c^2$ . The deviations at 0-30% centrality are  $5.5\pm 2.8\%$ ,  $6\pm 0.3\%$ ,  $10\pm 1\%$ ,  $15\pm 1.5\%$  and  $12\pm 5.4\%$  for  $\phi$ ,  $K_S^0$ ,  $\Lambda$ ,  $\Xi$  and  $\Omega$ , respectively. These observations may indicate that the contribution to the collectivity from the partonic phase decreases from central to peripheral collisions.

### 6.3.5 Hadronic re-scattering effect on $v_2$

Hydrodynamical model calculations predict that  $v_2$  as a function of  $p_T$  follows mass ordering. That is for heavier particles  $v_2$  is lower than lighter particles [17, 18, 19]. In the experimental data, the mass ordering was observed among the identified hadrons  $v_2$  in the low  $p_T$  region ( $p_T \leq 1.5$  GeV/ $c$ ) [7]. Recent phenomenological calculation based on ideal hydrodynamical model together with the later stage hadron cascade shows that the mass ordering of  $v_2$  could be broken between that of  $\phi$ -meson and proton at low  $p_T$  ( $p_T < 1.5$  GeV/ $c$ ) [20]. This is because of late stage hadronic re-scattering effects on proton  $v_2$ . The model calculation was done by considering low hadronic interaction cross-section for  $\phi$ -meson and large hadronic interaction cross-section for proton.

To further study the effect of hadronic interactions,  $v_2$  calculations are carried out for both  $\phi$  meson and proton using AMPT model. We chose protons and  $\phi$  mesons mainly for two reasons: (a) as a hadron, protons have a mass similar to that of the  $\phi$  mesons and (b) contrary to that of the  $\phi$  mesons, protons have larger hadronic interaction cross sections. Figure 6.19 (a) shows the  $\phi$  meson  $v_2$  for minimum bias Au+Au collisions at mid-rapidity versus  $p_T$  from AMPT model for parton-parton cross section of 10 mb (red solid circles) and results without any parton-parton interaction (blue solid square, obtained by setting the parton-parton cross section value to 0 mb). The hadronic cascade time is 30 fm/ $c$  for both the cases. The  $\phi$  meson  $v_2$  is consistent with zero in absence of parton-parton interactions. The panel (c) shows the difference between the two results, indicating that almost all the  $\phi$  meson  $v_2$  is generated via the partonic interactions. Figure 6.19 (b) and (d) reinforces these observations by

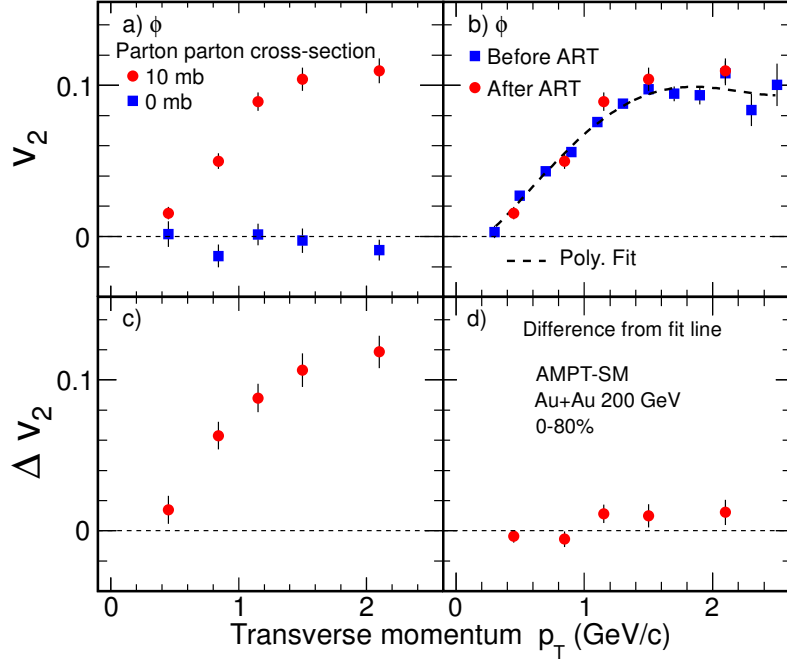


Figure 6.19: (Color online)  $\phi$  meson  $v_2$  for Au+Au minimum bias (0-80%) collisions at mid-rapidity ( $\pm 1.0$ ) at  $\sqrt{s_{NN}} = 200$  GeV from the AMPT model. Panels (a) and (b) shows the results as a function of  $p_T$  for parton-parton interaction cross section of 0 and 10 mb and calculations before and after relativistic transport (ART) calculations for hadrons, respectively. The lower panels (c) and (d) shows the difference in  $v_2$  shown in panels (a) and (b), respectively. The errors shown are statistical.

presenting the  $\phi$  meson  $v_2$  for the same system before (solid blue squares) and after (solid red circles) the relativistic transport calculations for hadrons. The results are similar between the two cases as seen from the  $p_T$  dependence of  $\phi$  meson  $v_2$  in panel (b), the difference between the two cases is shown in panel (d) is found to be consistent with zero. These results indicate that partonic interactions are essential for generating  $v_2$  of  $\phi$  mesons and contributions from hadronic interactions are minimal, within the context of the AMPT calculation.

The model simulations were also carried out for the Au+Au minimum bias collisions with parton-parton interaction cross section fixed to be 10 mb and varying the hadronic cascade time from 0.6 fm/ $c$  to 30 fm/ $c$ . Higher value of hadronic cascade time reflects larger hadronic re-scatterings. We have checked that for RHIC energies going to even longer time duration does not contribute any further to the results presented. Figure 6.20 (a) shows the  $v_2$  of protons versus  $p_T$  for 0-80% Au+Au collisions at  $\sqrt{s_{NN}} = 200$  GeV from the AMPT model with parton-parton interaction cross section of 10 mb and three different values of hadronic cascade time of 0.6 fm/ $c$  (red solid circle), 15 fm/ $c$  (black open cross) and 30 fm/ $c$  (blue solid square). With increase in hadron cascade time, which reflects increasing contributions from hadronic interactions, the proton  $v_2$  decreases at lower  $p_T$ . Implying the development of the collective expansion in the hadronic state of the system. This is more clearly illustrated in the panel (c) of the figure, which shows the ratio of the proton  $v_2$  for the hadron cascade time of 0.6 fm/ $c$  to the corresponding  $v_2$  values for time periods of 15 (open crosses) and 30 (solid squares) fm/ $c$ . Figure 6.20 (b) and (d) shows the corresponding results for  $\phi$  mesons. In marked contrast to the case for protons, the  $\phi$  meson  $v_2$  remains unaffected by the hadronic interactions, indicating that  $v_2$  is solely generated due to the partonic interactions in these model calculations.

High statistics data, collected by STAR detectors, allows for such an investigation in real data. The ratio between  $\phi$   $v_2$  and proton  $v_2$  is shown in Fig. 6.21. The ratios are larger than unity at low  $p_T$  region ( $p_T < 0.7$  GeV/ $c$ ) for 0-30% centrality although mass of the  $\phi$ -meson (1.019 GeV/ $c^2$ ) is greater than mass of the proton (0.938 GeV/ $c^2$ ). This means mass ordering between  $\phi$  and proton  $v_2$  breaks down at that

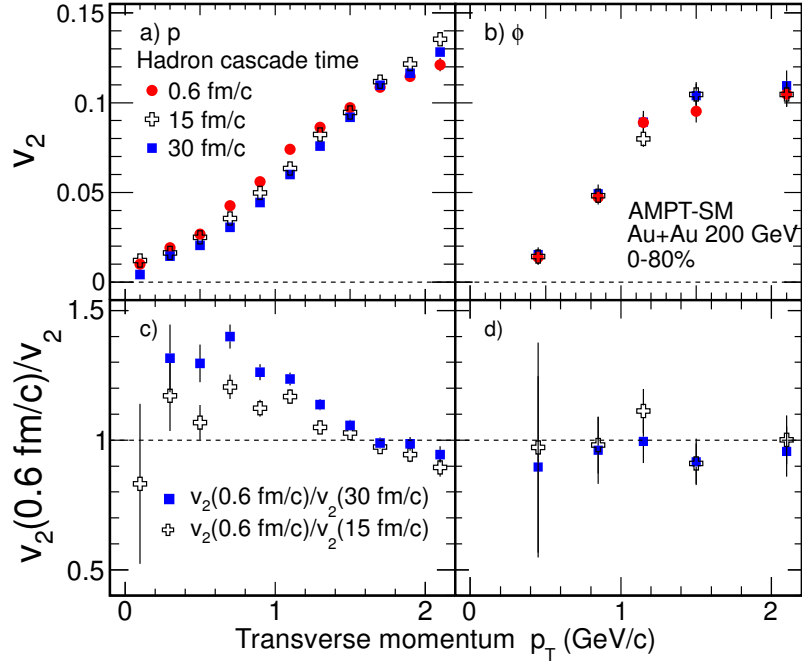


Figure 6.20: (Color online) (a)  $v_2$  of protons as a function of  $p_T$  for Au+Au 0-80% collisions at  $\sqrt{s_{NN}} = 200$  GeV from AMPT model at mid-rapidity. The results are shown for a parton-parton cross section of 10 mb and three different values of hadronic cascade time periods. (b) The same plot as (a) for the  $\phi$  mesons. (c) Ratio of  $v_2$  of protons for hadron cascade time of 0.6 fm/c to corresponding  $v_2$  for time periods of 15 and 30 fm/c, and (d) same as in (c) for the  $\phi$  mesons. The error bars shown are statistical.

momentum range. This could be because of the larger effect of hadronic re-scattering on proton  $v_2$ , which reduced proton  $v_2$ , as predicted in the theoretical model [20, 21]. Due to small hadronic interaction cross-section  $\phi$ -meson  $v_2$  is not affected by hadronic re-scattering.

Figure 6.22 shows the results from the hydrodynamic and hydrodynamic+cascade

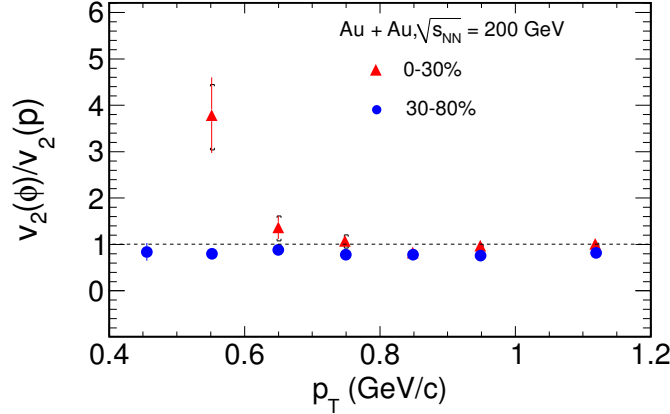


Figure 6.21: (Color online) Ratio between  $\phi$  and  $p$   $v_2$  for 0-30% and 30-80% centrality in Au+Au collisions  $\sqrt{s_{NN}} = 200$  GeV. Systematic uncertainties are shown by cap symbol and vertical lines are the statistical uncertainty.

model calculations [20] along with experimental data. The model calculation was done for the fixed range of impact parameter ( $b$ ) from 0 to 7.2 fm. According to ideal hydrodynamics model,  $v_2(\phi)/v_2(p)$  should be less than equal to unity as shown by red shaded band in Fig. 6.22. However due to the effect of hadronic cascade the ratios  $v_2(\phi)/v_2(p)$  could go above unity since hadronic re-scattering reduced proton  $v_2$ . The results from hydro+cascade model calculation (shown by blue shaded band) qualitatively explain the trend of experimental data but fails to describe quantitatively. The ratios between  $\phi$   $v_2$  and proton  $v_2$  from AMPT [22] and UrQMD [23] are shown in Fig. 6.23. The string melting version of the AMPT used in this study produces  $\phi$  mesons using a quark coalescence model in the partonic stage. On the other hand in UrQMD model,  $\phi$  meson produced from  $K^+$  and  $K^-$  coalescence. It can be seen

from Fig. 6.23 that AMPT model with hadronic cascade time equal to 0.6 fm/c gives  $v_2(\phi)/v_2(p) \leq 1.0$ . But if we increase hadronic cascade time from 0.6 fm/c to 30 fm/c, the ratios  $v_2(\phi)/v_2(p)$  goes up above unity at low  $p_T$ . This is because of later stage hadronic re-scattering due to which proton  $v_2$  gets lower where as  $\phi$ -meson  $v_2$  remain almost unaffected [21]. Due to lack of collectivity in UrQMD model,  $\phi$ -meson  $v_2$  are not developed fully and the ratios  $v_2(\phi)/v_2(p)$  remain less than unity [21].

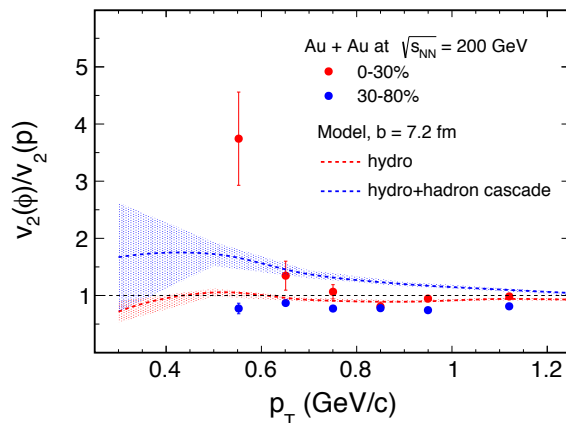


Figure 6.22: (Color online) Ratio between  $\phi$  and  $p$   $v_2$  for 0-30% and 30-80% centrality in Au+Au collisions  $\sqrt{s_{NN}} = 200$  GeV. Shaded bands are the results from the model calculations [20].

## 6.4 Summary

We have presented a systematic study on centrality dependence of multi-strange hadrons  $v_2$  at mid-rapidity using high statistics data in Au+Au collisions at  $\sqrt{s_{NN}} = 200$  GeV collected by STAR detectors in the years of 2011 and 2011. The  $p_T$  dependence of  $\phi$  and  $\Omega$   $v_2$  was observed similar as  $\pi$  and  $p$   $v_2$ , which indicates that the major parts of collectivity developed at the initial partonic phase. To investigate partonic collectivity for different system size, NCQ scaling has been shown for two different

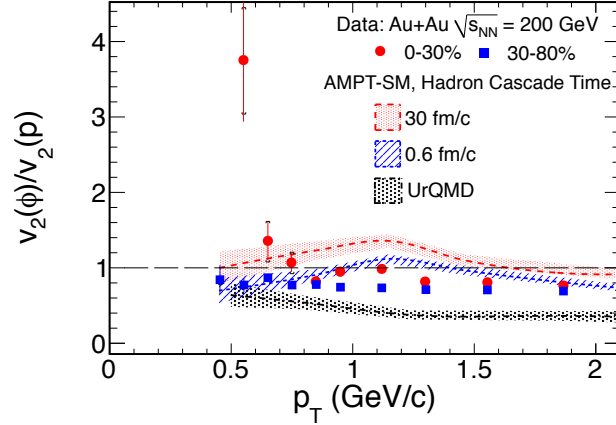


Figure 6.23: (Color online) Ratio between  $\phi$  and  $p$   $v_2$  for 0-30% and 30-80% in Au+Au collisions  $\sqrt{s_{NN}} = 200$  GeV. Shaded bands are the results from the AMPT and UrQMD model calculations for 0-30% centrality in Au+Au collisions  $\sqrt{s_{NN}} = 200$  GeV..

centralities. For 0-30% centrality, NCQ scaling holds within the statistical uncertainty where as scaling breaks down at 30-80% centrality for the range  $(m_T - m)/n_q > 0.8$  GeV/ $c^2$ . This indicates that partonic contribution to the collectivity decrease from central to peripheral collisions. The comparison between  $\phi$  and  $p$   $v_2$  shows that at low  $p_T$ , there is a violation of mass ordering between  $\phi$  and  $p$  as expected from an ideal hydrodynamic based model.. This may be due to the late hadronic interaction effect on proton  $v_2$  [20].

# Bibliography

- [1] B.I. Abelev *et al.* (STAR Collaboration), Phys. Rev. **C 81**, 024911 (2010).
- [2] *Event anisotropy  $v_2$  at STAR* - Ph.D thesis by Shusu Shi, CCNU, China.
- [3] J. Adams *et al.* (STAR Collaboration), Phys. Rev. Lett. **95**, 122301 (2005).
- [4] A. M. Poskanzer and S. A. Voloshin, Phys. Rev. **C 58**, 1671 (1998).
- [5] N. Borghini and J. Y. Ollitrault, Phys. Rev. **C 70**, 064905 (2004).
- [6] H. Masui and A. Schmah, arXiv:1212.3650.
- [7] B. I. Abelev *et al.* (STAR Collaboration), Phys. Rev. **C 77**, 054901 (2008).
- [8] B. Mohanty, New Journal of Physics **13**, 065031 (2011).
- [9] D. Molnar and S. A. Voloshin, Phys. Rev. Lett. **91**, 092301 (2003).
- [10] R. J. Fries *et al.* Phys. Rev. Lett. **90**, 202303 (2003).
- [11] B. I. Abelev *et al.* (STAR Collaboration), Phys. Rev. Lett. **99**, 112301 (2007).
- [12] C. Adler *et al.* (STAR Collaboration), Phys. Rev. Lett. **89**, 092301 (2002).
- [13] J. Adams *et al.* (STAR Collaboration), Phys. Lett. **B 595**, 143 (2004).
- [14] J. Adams *et al.* (STAR Collaboration), Phys. Rev. **C 70**, 041901 (2004).
- [15] J. Adams *et al.* (STAR Collaboration), Phys. Lett. **B 612**, 181 (2005).
- [16] J. Adams *et al.* (STAR Collaboration), Phys. Rev. Lett. **92**, 182301 (2004).

- [17] P. Huovinen *et al.* Phys. Lett. **B 503**, 58 (2001).
- [18] C. Nonaka, R. J. Fries and S. A. Bass, Phys. Lett. **B 583**, 73 (2004).
- [19] T. Hirano and Y. Nara, Phys. Rev. **C 69**, 034908 (2004).
- [20] T. Hirano *et al.* Phys. Rev. **C 77**, 044909 (2008).
- [21] Md. Nasim, B. Mohanty and N. Xu, Phys. Rev. **C 87**, 014903 (2013).
- [22] Zi-Wei Lin and C. M. Ko, Phys. Rev. **C 65**, 034904 (2002).
- [23] S. A. Bass *et al.*, Prog. Part. Nucl. Phys. **41**, 255 (1998).

## 6.5 Appendix

### 6.5.1 Data points

$\phi$ meson : 0-80% centrality			
$\langle p_T \rangle$ (GeV/c)	$v_2$	Statistical Error	Systematic Error
0.4558	0.00830374	0.00372655	0.00304749
0.5522	0.02066	0.00268552	0.00240772
0.6509	0.0236598	0.00201424	0.00184949
0.7502	0.0289574	0.00169694	0.00144949
0.8499	0.0336933	0.00156258	0.0013737
0.9496	0.0454915	0.00151742	0.0012737
1.1011	0.0590562	0.00111185	0.00132546
1.3102	0.0735464	0.00121991	0.00117415
1.5110	0.091581	0.00136516	0.00109836
1.7090	0.104109	0.00153278	0.00129961
1.9074	0.111006	0.00173928	0.00138362
2.1419	0.121649	0.00171319	0.00196714
2.4201	0.133793	0.0021925	0.00361407
2.7511	0.136365	0.00260106	0.00379211
3.2154	0.151143	0.00359409	0.00414789
3.7040	0.14004	0.00603122	0.00510761
4.3930	0.112905	0.00871456	0.0132062
5.3082	0.151547	0.023672	0.0209348

$\phi$ meson : 0-30% centrality			
$\langle p_T \rangle$ (GeV/c)	$v_2$	Statistical Error	Systematic Error
0.4558	4.64542e-03	5.28132e-03	0.003923659
0.5522	1.74716e-02	3.75883e-03	0.00323659
0.6509	1.48799e-02	2.79302e-03	0.00296174
0.7502	1.99758e-02	2.33091e-03	0.00266174
0.8499	2.23911e-02	2.11150e-03	0.0018827
0.9496	3.52984e-02	2.04508e-03	0.0019024
1.1203	4.66946e-02	1.48599e-03	0.001892
1.3011	6.03249e-02	1.60464e-03	0.00145575
1.5540	8.00755e-02	1.49447e-03	0.00136817
1.8671	9.38406e-02	1.77450e-03	0.00100574
2.2138	1.07989e-01	1.84315e-03	0.00226049
2.7302	1.19869e-01	2.84480e-03	0.00400361
3.2506	1.36109e-01	4.62965e-03	0.00601315
3.8911	1.22485e-01	6.63362e-03	0.0092109
4.8109	1.20269e-01	1.78962e-02	0.0122109
5.8810	9.52660e-03	4.48286e-02	0.018508

$\phi$ meson : 30-80% centrality			
$\langle p_T \rangle$ (GeV/c)	$v_2$	Statistical Error	Systematic Error
0.4558	1.86846e-02	4.29603e-03	0.0012008
0.5522	2.60414e-02	3.10570e-03	0.0011919
0.6509	4.08169e-02	2.34768e-03	0.0009606
0.7502	4.76868e-02	1.98742e-03	0.000918606
0.8499	6.00823e-02	1.82574e-03	0.00098621
0.9496	7.03344e-02	1.78771e-03	0.000966728
1.1201	8.96175e-02	1.32377e-03	0.00119206
1.3011	1.08113e-01	1.47485e-03	0.0008623
1.5540	1.33255e-01	1.41198e-03	0.000889513
1.8678	1.53830e-01	1.73499e-03	0.00203127
2.2136	1.74045e-01	1.81920e-03	0.00243127
2.7305	1.76001e-01	2.88235e-03	0.002401
3.2512	1.7066e-01	4.62700e-03	0.002431
3.8903	1.6459e-01	7.19459e-03	0.00222918
4.8121	1.35906e-01	2.20162e-02	0.00689527
5.8826	1.04213e-01	5.24715e-02	0.0115232

$\Xi$ : 0-80% centrality			
$\langle p_T \rangle$ (GeV/c)	$v_2$	Statistical Error	Systematic Error
0.6501	0.0173809	0.00246396	0.0020927
0.9106	0.0262127	0.0013095	0.0011599
1.1021	0.0402909	0.00106394	0.00287579
1.3410	0.0582142	0.000742142	0.00304568
1.6431	0.0782448	0.000679255	0.00240293
1.9352	0.107542	0.000721714	0.00277398
2.2251	0.139524	0.000853557	0.00335472
2.5230	0.158584	0.00108678	0.0034521
2.8225	0.170901	0.00145563	0.00322669
3.1503	0.179351	0.00200782	0.00319426
3.4312	0.185208	0.00282602	0.00244807
3.7608	0.182669	0.00373231	0.00387319
4.3201	0.188125	0.00505762	0.00446124
5.3108	0.175574	0.0150432	0.00984375
6.2912	0.152456	0.0406414	0.0207369

$\Xi$ : 0-30% centrality			
$\langle p_T \rangle$ (GeV/c)	$v_2$	Statistical Error	Systematic Error
0.6501	0.01092086	0.00366401	0.00230405
0.9106	0.0162929	0.00187728	0.00128456
1.1021	0.0279132	0.00130675	0.00249661
1.3410	0.0446335	0.000889031	0.0023886
1.6431	0.0641631	0.000802468	0.00166765
1.9352	0.0910614	0.000845921	0.00205917
2.2251	0.119421	0.000995348	0.00258902
2.5230	0.138915	0.00126402	0.00283349
2.8225	0.149552	0.00169014	0.00290068
3.1501	0.159672	0.00233397	0.00235716
3.4511	0.162747	0.00329173	0.0018617
3.7809	0.16209	0.00436376	0.00333323
4.3201	0.164912	0.00594039	0.00465178
5.3109	0.160195	0.0178316	0.013919
6.2911	0.150344	0.047823	0.0153919

$\Xi$ : 30-80% centrality			
$\langle p_T \rangle$ (GeV/c)	$v_2$	Statistical Error	Systematic Error
0.6501	0.0317862	0.00352851	0.00429859
0.9106	0.04795	0.00232595	0.000990224
1.1020	0.0712147	0.0018065	0.00237341
1.3411	0.0972982	0.00133007	0.00172324
1.6433	0.129583	0.00126028	0.001737522
1.9355	0.169002	0.00136849	0.001680824
2.2252	0.210307	0.00164225	0.0016850597
2.5231	0.227503	0.0021065	0.00163625
2.8223	0.244783	0.00283628	0.00298527
3.1503	0.25258	0.00390185	0.00104893
3.4311	0.255172	0.00545864	0.0028032
3.7607	0.247972	0.00711923	0.00249491
4.3210	0.257352	0.00950248	0.00194079
5.3108	0.250509	0.02721292	0.0204034

$\Omega$ : 0-80% centrality			
$\langle p_T \rangle$ (GeV/c)	$v_2$	Statistical Error	Systematic Error
0.97051	0.0248557	0.019158	0.014048
1.19602	0.0291605	0.0134215	0.008421
1.451031	0.0539421	0.00641376	0.00463053
1.75328	0.0818621	0.00509085	0.00476276
2.04818	0.114628	0.00489826	0.00536276
2.39078	0.127218	0.00472613	0.00468455
2.78379	0.145949	0.00578202	0.00494225
3.21871	0.16973	0.00695891	0.00489713
3.71415	0.170264	0.0113915	0.00761159
4.33813	0.180132	0.0159494	0.011961159
5.22109	0.243719	0.0421058	0.0191668

$\Omega$ : 0-30% centrality			
$\langle p_T \rangle$ (GeV/c)	$v_2$	Statistical Error	Systematic Error
0.97201	0.00736094	0.0299199	0.00826145
1.41596	0.037306	0.00979877	0.00626145
1.75328	0.0655455	0.00638481	0.00421708
2.04818	0.0956103	0.00610895	0.00427358
2.39078	0.108727	0.00577766	0.00330723
2.78379	0.127972	0.00697247	0.00457471
3.21871	0.164018	0.00879519	0.00557471
3.71415	0.140769	0.0135127	0.0107365
4.33811	0.164795	0.0189072	0.0212595

$\Omega$ : 30-80% centrality			
$\langle p_T \rangle$ (GeV/c)	$v_2$	Statistical Error	Systematic Error
0.97201	0.0657796	0.0158208	0.00419556
1.41596	0.0846872	0.00630646	0.0034331
1.75328	0.123764	0.00768447	0.0050331
2.04818	0.17037	0.00729799	0.00516744
2.39078	0.185324	0.00742395	0.00516744
2.78379	0.20402	0.0095584	0.0039031
3.21871	0.24331	0.0125765	0.0037031
3.71415	0.26103	0.0203267	0.00510621
4.33810	0.22422	0.0289560	0.00925778

# Chapter 7

## Summary and Conclusions

In this thesis we present the results on energy dependence ( $\sqrt{s_{NN}} = 7.7, 11.5, 19.6, 27, 39, 62.4$  and  $200$  GeV) of  $\phi$ -meson production (specifically the transverse momentum distributions and azimuthally anisotropy measurements) in Au+Au collisions using STAR detector at RHIC. These measurements corresponds to systems having baryonic chemical potential,  $\mu_B$ , in the range 20 to 450 MeV at chemical freeze-out. Mass of  $\phi$  meson obtained in this thesis from the decay channel  $\phi \rightarrow K^+ + K^-$  are observed to be consistent with PDG mass value for all the collisions centralities and all the centre-of-mass energies. This indicates there no medium modification on  $\phi$  mass. The measured value of  $\phi$  width is higher than that of PDG value and investigated in this thesis to be due to finite momentum resolution of TPC. Transverse momentum spectra of  $\phi$  meson for different centralities at  $\sqrt{s_{NN}} = 7.7-39$  GeV are presented. The shape of the distribution goes from exponential to Levy form as one goes from central to peripheral collisions. The  $p_T$  integrated  $\phi$ -meson yield per participant pair ( $(dN/dy)/(0.5N_{part})$ ) at mid-rapidity ( $|y| < 0.5$ ) increases nonlinearly with centrality. This suggests particle production does not scale with number of participating nucleons (estimated from Glauber model simulations at the respective beam energies) of the colliding nucleus. For a given  $N_{part}$ ,  $(dN/dy)/(0.5N_{part})$  increases with the collision energy, which is expected because of the increase of energy avail-

able to produce the  $\phi$  mesons. We have measured beam energy dependence of the nuclear modification factors of  $\phi$  meson at  $\sqrt{s_{NN}} = 7.7\text{-}39$  GeV and compared with that at higher RHIC energy. The nuclear modification factors at the intermediate  $p_T$  are observed to be equal or higher than unity at  $\sqrt{s_{NN}} \leq 39$  GeV. This indicates parton energy loss effect is less important at low beam energies and could be the hint of dominance of hadronic interactions at lower beam energies. The values of nuclear modification factors are less than unity for beam energies of 62.4 and 200 GeV indicating formation of a dense medium with color degrees of freedom. The ratios  $N(\phi)/N(K^-)$  has been presented as a function of centrality and centre-of-mass energy.  $\phi$  production from kaon coalescence mechanism (e.g. UrQMD model) predicts increase of  $N(\phi)/N(K^-)$  ratio as a function of both centrality and centre-of-mass energy. The ratios  $N(\phi)/N(K^-)$  are observed to be almost constant as a function of centrality and centre-of-mass energy, disfavoring  $\phi$ -meson production through kaon coalescence. The ratios of  $N(\Omega^- + \bar{\Omega}^+)/2N(\phi)$  versus  $p_T$  show similar trend for  $\sqrt{s_{NN}} \geq 19.6$  GeV, where as at  $\sqrt{s_{NN}} = 11.5$  GeV, the ratio at the highest measured  $p_T$  shows a deviation from the trend of other energies. This may suggest a change in  $\Omega$  and/or  $\phi$  production mechanism at  $\sqrt{s_{NN}} = 11.5$  GeV. This further emphasizes our finding that at lower beam energies the hadronic interactions are dominating.

The measurement of  $\phi$ -meson  $v_2$  as function of  $p_T$  and collision centrality has been presented. We observed that  $\phi$ -meson  $v_2$  shows similar  $p_T$  dependent values for  $\sqrt{s_{NN}} \geq 19.6$  GeV and NCQ scaling also holds for  $\sqrt{s_{NN}} \geq 19.6$  GeV. But at  $\sqrt{s_{NN}} = 7.7$  and 11.5 GeV, the  $\phi$ -meson  $v_2$  show deviation from the other hadrons at highest measured  $p_T$  values by  $1.8\sigma$  and  $2.3\sigma$ , respectively. Since the  $v_2$  of  $\phi$  mesons mostly reflect collectivity from partonic phase, therefore observed small  $\phi$   $v_2$  at  $\sqrt{s_{NN}} = 7.7$  and 11.5 GeV may indicate the smaller contribution to the collectivity from partonic phases. We find that the  $\phi$   $v_2$  can be explained by AMPT model with partonic interactions by varying parton-parton interaction cross-section from 3mb to 10mb for  $\sqrt{s_{NN}} \geq 19.6$  GeV, but models over predicts the data at  $\sqrt{s_{NN}} = 7.7$  and 11.5 GeV. This may indicate that the contribution to the collectivity from partonic phases decreases at lower beam energies and hadronic interaction plays a dominant role for

$$\sqrt{s_{NN}} \leq 11.5 \text{ GeV}.$$

We have also presented transverse momentum and centrality dependence of inclusive charged hadrons  $v_2$  in Au+Au collisions at  $\sqrt{s_{NN}} = 7.7, 11.5, 19.6, 27$  and  $39$  GeV. The centrality and  $p_T$  dependence of  $v_2$  are similar to that observed at higher RHIC collision energies. The comparison with Au+Au collisions at higher energies at RHIC ( $\sqrt{s_{NN}} = 62.4$  and  $200$  GeV) and at LHC (Pb+Pb collisions at  $\sqrt{s_{NN}} = 2.76$  TeV) shows the  $v_2\{4\}$  values at low  $p_T$  ( $p_T < 2.0$  GeV/ $c$ ) increases with increase in collision energy implying an increase of collectivity. Comparison with transport model calculation indicate that hadronic interaction increases with decrease in centre-of-mass energy. Some systematic study on  $v_2$  measurements methods has been discussed using various models of high energy heavy-ion collisions.

Centrality dependence of multi-strange hadrons( $\phi, \Xi, \Omega$ )  $v_2$  at mid-rapidity using high statistics data in Au+Au collisions at  $\sqrt{s_{NN}} = 200$  GeV are presented. We observed that the  $p_T$  dependence of  $\phi$  and  $\Omega$   $v_2$  are similar as  $\pi$  and  $p$   $v_2$ . This means heavier strange quarks flows as strongly as lighter (u, d) quarks. This could be possible only if the collectivity has been developed at the partonic level in Au+Au collisions at  $\sqrt{s_{NN}} = 200$  GeV . The number-of-constituent quark (NCQ) scaling has been investigated for different centralities. For 0-30% centrality, NCQ scaling holds within the statistical uncertainty where as scaling breaks down at 30-80% centrality for the range  $(m_T - m)/n_q > 0.8$  GeV/ $c^2$  indicating less partonic collectivity at peripheral collisions. To investigate the effect of late stage hadronic interaction on  $v_2$ , we have shown comparison between  $\phi$  and  $p$   $v_2$  at low  $p_T$ . We observed that the mass ordering between  $\phi$  and proton  $v_2$  breaks down in the lower momentum range. This could be because of the larger effect of hadronic re-scattering on proton  $v_2$ , which reduces the proton  $v_2$ .

In this thesis we have presented a systematic analysis of  $\phi$ -meson production in transverse momentum and azimuthal angular distribution for various collision centrality and beam energies for Au+Au collisions. Our measurements indicate that for beam energies of 200 GeV and central collisions we have a clear evidence of partonic collectivity. This collectivity reduces as we go to peripheral collisions and lower beam

energies. Through our measurements and comparisons to various model results we also conclude that the system formed at 7.7 and 11.5 GeV have hadronic interactions dominating while for those with  $\sqrt{s_{NN}} > 11.5$  GeV partonic interactions are required to explain the data. In addition our measurements of  $\phi$ -meson  $v_2$  with those for protons shows first experimental evidence of break of mass ordering in  $v_2$  values at low  $p_T$  due to final state hadronic interactions.